ABSTRACT

Title of dissertation: **TURBULENT TRANSPORT AND MIXING OF UNCONFINED AND SLOPED FIRE-INDUCED FLOWS USING A LASER-ASSISTED SALTWATER MODELING TECHNIQUE**

Pietro Maisto
Doctor of Philosophy, 2019

Dissertation directed by: Associate Professor Michael J. Gollner
Department of Fire Protection Engineering

The present work investigates turbulent, buoyant fire-induced flows using an experimental scaling technique known as saltwater modeling—a methodology enabling quantitative analysis of fire plumes built upon the analogy with saltwater (plume) flowing into the ambient water (air). The investigation, conducted by means of velocimetry (PIV) and concentration (PLIF) laser-based techniques, concerns unconfined plume mixing and transport, characterization of ceiling jet flows under sloped ceilings and activation of suppression devices in these sloped configurations.

Flow imaging provides detailed measurements of velocity and saltwater concentration within the entire spatial and temporal domain of a planar section of the plume. In analogy with low-pass filtering in large eddy simulation (LES), a virtual, pixel-binning grid of varying size is overlaid on images to compute statistical moments representative of the larger and smaller scales. By leveraging actual

measurements, converged statistics (first, second, higher-order) enables selection of cutoff resolutions, useful for validation and development of computational fluid dynamics (CFD) simulations.

The saltwater plume's subsequent impingement onto a sloped plate generates a ceiling jet flowing both streamwise (up- and downslope) and spanwise with respect to the impingement point. Such flow is investigated to first build correlations predicting velocity and temperature along a sloped ceiling and second to analyze slope-related suppression device (sprinkler) activation. For the first task, single-planar, streamwise measurements are employed; for the second, multiple orthogonal laser sheets crossing the plate are used to generate a virtual grid of measured points. Transport characteristics are implemented into an activation model, modified to predict a dimensionless response time spatial distribution. At increasing slopes, the delay in the activation between upslope (faster) and downslope (delayed) devices progressively increases at increasing ceiling angles. This also occurs between sprinklers symmetrically located upslope and spanwise. From the response spatial distribution, the streamwise-to-spanwise correlation for the delay time (thermal responsiveness) is determined using the saltwater front arrival times. The analysis for the lag time reveals that the delay in thermal responsiveness between two sprinklers with the same activation time located up- and downslope, respectively, increases exponentially compared to that found for sprinklers located spanwise, at a quadratic rate with increasing angles.

TURBULENT TRANSPORT AND MIXING OF UNCONFINED AND SLOPED FIRE-INDUCED FLOWS USING A LASER-ASSISTED SALTWATER MODELING TECHNIQUE

by

Pietro Maisto

Dissertation submitted to the Faculty of the Graduate School of the
University of Maryland, College Park in partial fulfillment
of the requirements for the degree of
Doctor of Philosophy
2019

Advisory Committee:
Professor Michael J. Gollner, Chair
Professor Kenneth H. Yu
Professor Marino diMarzo
Professor James A. Milke
Professor Stanislav I. Stoliarov

Dedication

Voglio dedicare questo lavoro alle persone a me piu'care che mi hanno supportato con il loro amore, la loro energia e la loro conoscenza in questo lungo percorso. La mia Famiglia: Mamma Nadia, Tata Chiara, mia sorella, e Papa'Paolo. Nonna Dora e Nonno Gigi, da cui ho ereditato la caparbieta', la determinazione e la passione che mi hanno condotto a questo traguardo. Il mio amato e mai dimenticato Prof. Ferdinando Mazza, a cui devo tutta la mia conoscenza della fisica e della matematica senza cui non sarei mai giunto qui. Rosa Iannotta, che ha nutrito questo mio sogno Americano con la fantasia, la leggerezza e il profondo amore che la contraddistinguevano. Ed infine, il Prof. Claudio Bruno, mio relatore di tesi e mentore dai tempi della Scuola di Ingegneria Aerospaziale a Roma: colui che, come me, ha creduto nel sogno Americano e ne ha fatto strumento per rendere ancora piu'grande il nome degli Italiani nel mondo.

I want to dedicate this work to my loved ones who have supported me with their love, their energy and their knowledge in this long journey. My Family: My Mother Nadia, my Sister Chiara ("Tata") and Paolo, my Father. My Grandmother Dora, and my Grandfather Luigi ("Gigi"), from whom I inherited the tenacity, the determination, and the passion for mechanics and aerospace that led me to achieve this goal. My beloved and never forgotten Prof. Ferdinando Mazza, to whom I owe all my knowledge of physics and mathematics without which I would never have come here. Rosa Iannotta, who nourished my American dream with the imagination, lightness and deep love that characterized her. Lastly, Prof. Claudio Bruno,

my former advisor and mentor since the School of Aerospace Engineering in Rome: one who, like me, believed in the American dream and made it a tool to make the name of Italians even greater in the world.

Acknowledgments

I would like to thank my advisor Dr. Michael Gollner and Dr. Andre Marshall, for at first offering me the opportunity to conduct this research project under their guidance, which has culminated into this research project for my Doctor of Philosophy degree. Their advice and support have led me to vast new knowledge, and this project would not be possible without them. I would like to thank Dr. Claudio Bruno for the knowledge he has imparted to me throughout all of my studies at the School of Aerospace Engineering of Rome at "La Sapienza" and at Virginia Tech, which has been relevant in both this project and my professional endeavors. For their vast amounts of help in running these experiments, I would like to thank Tom Layton, Fernando Raffan, Cui Wuquan, Jens Triller and Jan Zimlich. Each of whom provided useful assistance in the experimental process, and had a strong influence on these results. I want to thank my former lab mates at Virginia Tech, Tobias Ecker, Daniel Cadel, Donald Brooks, Tamara Guimarães, Marco Vietze and Roberto Bertacin from the Italian Space Agency (ASI) for their invaluable support as professionals and most of all as amazing friends. I want to thank the Department of Homeland Security (DHS/FEMA/USFA-Award EMW-2012-FP-01336) for funding this work as part of their grant on scale modeling in fire research. Thank you to all my other FPE friends for your help in one way or another. Finally, I would like to thank my Family Nadia Rita Fedeli, Chiara and Paolo Maisto, who have done so well in raising me and leading me to the achievement of my goals, along with my American Family: Lindon Rice, David Farmer, Carson Farmer and Jarrett Farmer.

Table of Contents

List of Tables

List of Figures

Nomenclature

Acronyms

ASM	Algebraic Stress Model
CCD	Charge-Coupled Device
CFD	Computational Fluid Dynamics
DNS	Direct Numerical Simulation
FDS	Fire Dynamics Simulator
FLUENT	CFD-based commercial code
F.O.V.	Field of View
GL	Grey Level
HRR	Heat Release Rate
LDV	Laser Doppler Velocimetry
LES	Large Eddy Simulation
NIST	National Institute of Standards and Technology
NFPA	National Fire Protection Association
PIV	Particle Image Velocimetry
PLIF	Planar Laser Induced Fluorescence
RANS	Reynolds Averaged Navier-Stokes
RTI	Response Time Index
SFPE	Society of Fire Protection Engineering
SGS	Sub-Grid Scale

Symbols, Roman

A	Sprinkler sensing element exposed area	$[m^2]$
a_0, a_1	Calibration coefficients	$[-]$
b	Spanwise distance where $\overline{u_3}/\overline{(u_3)}_c = 1/e$	$[m]$
B	Buoyancy flux	$[m^4/s^3]$
c, c_p	Specific heat capacity	$[J/(kg \cdot K)]$
C	Mass concentration	$[-]$
C_V	Coefficient for velocity integral solution	$[-]$
C_s	Smagorinsky constant	$[-]$
C_T	Coefficient for density difference integral solution	$[-]$
d_I	Width of the Interrogation window	$[m]$
D	Diffusivity or Diffusion coefficient;Diameter	$[m^2/s]$;$[m]$
D^*	Integral length scale	$[m]$
Ec	Eckert number	$[-]$
Eu	Euler number	$[-]$
$\overrightarrow{f}$	Forcing term	$[N]$

f	Focal length; Frequency	$[m]$;$[Hz]$
$f/\#$	Aperture	$[-]$
Fr	Froude number	$[-]$
g	Gravity	$[m/s^2]$
Gr	Grashof number	$[-]$
h	Convection heta transfer coefficient	$[kW/m^2K]$
H	Ceiling height	$[m]$
I_0	Incident laser light intensity	$[-]$
I_e	Emitted/Excited light intensity	$[-]$
k	Thermal conductivity	$[W/(m \cdot K)]$
k_t^*, k_{sgs}^*	Dimensionless turbulent kinetic energy (filtered, residual)	$[-]$
L	Characteristic length for the flow	$[m]$
L_{chip}	Camera chip size	$[m]$
$L_{F.OV.}$	Field of view size	$[m]$
L_M	Morton length	$[m]$
m	Sprinkler sensing element mass	$[kg]$
$\dot{m}$	mass release rate	$[kg/s]$
$\dot{m}_{sw}^*$	Saltwater source strength	$[-]$
M	Momentum flux; Camera Magnification	$[m^4/s^2]$;$[-]$
Ma	Mach number	$[-]$
N	Number of pixels within the interrogation window	$[-]$
N_I	Number of particles in the interrogation window	$[-]$
p	Pressure	$[Pa]$
Pr	Prandtl number	$[-]$
$\dot{q}'''$	Volumetric energy release rate	$[W/m^3]$
$\dot{q}^*$	Dimensionless volumetric energy release rate	$[-]$
$\dot{Q}$	Heat release rate (HRR)	$[W]$
Q^*	Fire source strength	$[-]$
R	Ideal gas constant	$[J/(mol \cdot K)]$
Re	Reynolds number	$[-]$
Ri	Richardson number	$[-]$
$\mathbb{R}^2$	Spatial domain representing the laser sheet plane	$[-]$
$\bar{S}$	Filtered rate of strain	$[s^{-1}]$
Sc	Schmidt number	$[-]$
t	Time	$[s]$
T	Temperature	$[K]$
u, U	Velocity	$[m/s]$
V_Ω	Spatial domain area	$[m^2]$
$\dot{w}'''$	Volumetric mass release rate	$[kg/(m^3 \cdot s)]$
$\dot{w}^*$	Dimensionless volumetric mass release rate	$[-]$

x	Space coordinate	$[m]$
$(x_3)_0$	Virtual origin	$[m]$
Y	Mass fraction	$[-]$

Symbols, Greek

α	Slope angle	$[deg.]$
β	Volumetric expansion coefficient	$[K^{-1}]$
λ	Wavelength	$[nm]$
δ	Ceiling jet boundary layer thickness	$[m]$
Δ, Δ_g	Filter grid width	$[m]$
Δz_0	Laser sheet thickness	$[m]$
ϵ	Molar extinction coefficient	$[m^2/mol]$
θ	Density difference	$[-]$
μ	Dynamic viscosity	$[(N \cdot s)/m^2]$
μ_t	Turbulent or eddy viscosity	$[m^2/s]$
ν	Kinematic viscosity	$[m^2/s]$
π	Dimensionless group	$[-]$
ρ	Density	$[kg/m^3]$
σ	Standard deviation	$[-]$
τ	Time constant	$[s]$
$\tilde{\chi}_\theta$	Density difference sub-grid fluctuation	$[-]$
$\tilde{\chi}_u$	Velocity sub-grid fluctuation	$[-]$
ξ	Standoff distance	$[m]$
Ω	Spatial domain	$[-]$

Subscripts and Superscripts

$()_c$	Centerline
$()_{det}$	Detector
$()_{downstream}$	Downstream
$()_{dye}$	Dye
$()_D$	Diameter
$()_{gas}$	Gas
$()_i$	i-direction index
$()_{inj}$	injector index
$()_j$	j-direction index
$()_{ref}$	Reference
$()_{salt}$	Salt
$()_{smoke}$	Smoke

$()_{sw}$	Saltwater
$()_T$	Thermal, fire
$()_{upstream}$	Upstream
$()_0$	Characteristic, ambient
$()^*$	Dimensionless
$< >$	Filter (spatial, temporal, ensemble)
$\tilde{()}$	Spatially filtered
$\bar{()}$	Temporally filtered
$\hat{()}$	Spatially filtered over adjacent pixels

Chapter 1: Introduction

In fire protection engineering, both active and passive fire protection systems are used to ensure life safety and the reduction of property losses. When an unwanted fire develops within a building, smoke rises and surrounding air is entrained into a fire-induced buoyant plume so that the plume temperature drops as the smoke rises. Additionally, mass flow within the plume increases as the plume rises [1]. This smoke continues to rise until it forms a smoke layer under the ceiling which rapidly fills the space below it, a location designed for occupants (e.g. the atrium of a building). With time, the smoke layer that forms under the ceiling grows thicker, and the bottom of that layer drops downward, placing the life of occupants at risk. Also, given the increasing entrainment of fresh air, the temperature of the combustion products could decrease to the point that sprinklers and fire detection devices under the ceiling may not activate on time [1]. Even if such devices activate, the delay in activation time can allow fire growth beyond the suppression capability of the sprinklers or delay egress of occupants beyond a safe point. Therefore, improved understanding of the growth and spread of a fire plume within a compartment including its influence on device activation times may help to minimize financial and life safety losses during unwanted fires.

Before activation of detectors and suppression devices occurs, plumes comprised of smoke and combustion products rise from these fires and impinge on compartment ceilings. These are driven by buoyant forces caused by large thermal gradients between a hot plume and fresh air. Transport and mixing processes, which regulate the initial growth of the plume, are pivotal in predicting early stage conditions of these fire-induced flows, before impingement with a ceiling. After impingement of the plume, a ceiling jet flow develops, which is critical in the activation of detection and suppression systems. While these processes have been well-studied over the past few decades, there still exists room for improvement and further understanding in how these mixing processes occur. Unique designs, such as inclined ceilings, also push the limits of current engineering knowledge and are important to fundamentally study for the improvement of activation system times.

This study investigates two configurations by means of the saltwater modeling technique: an unconfined plume that represents the early stage of a fire, and the jet flow developing on a sloped ceiling that reproduces the environment in which suppression devices operate [92, 93, 133]. Applications both to numerical simulations, through advanced understanding of sub-grid scale mixing process in a free plume, and applied engineering calculations, for fire activation and suppression devices along an inclined ceiling, will be addressed.

1.1 Motivation

A fire within a building is a complex event that often develops quickly and can cause damage and destruction of the structure, property as well as endangering life safety. A major goal in fire protection engineering is to mitigate the consequences of unwanted fires through knowledge of the mechanisms causing fire growth. Computational and experimental scale modeling of non-reacting buoyant plumes, for instance, has been pivotal in understanding the convective transport of turbulent fire-induced flows, without the additional cost required to model or take measurements in reacting flows. In fact, a non-reacting buoyant plume, with an equivalent Froude number to that of the fire of interest, has been shown to well represent the real-scale phenomenon of smoke transport far away from the fire [2,119]. This is due to a similar dynamics of the fire combustion products to that of the non-reacting buoyant plume.

For turbulent buoyant plumes, Large Eddy Simulations (LES) represent a cost-effective way to resolve the larger length scales typical of these flows, while modeling the smaller-scales (down to Kolmogorov scales [54]), in order to reduce the computational cost otherwise needed for the entire length-scale spectrum. To correct for the smaller-scale mixing processes that are not modeled, sub-grid models [16, 17] are implemented to re-introduce the effects of the small turbulent scales, referred as sub-grid scale effects (SGS). However, studies conducted on fire plumes using LES or LES-based codes (e.g. FDS) [13–15], reported some discrepancies in the results when compared with similar fire experiments and very fine Direct Numerical

Simulations (DNS). The likely reason of these was identified in the inability of each SGS model to fully capture the effects of SGS motions upon resolved scales. For instance, DesJardin *et al.* found that for locations very near the base of the plume, the LES model overpredicted the measured root-mean squared streamwise velocity and concentration when compared to PIV and PLIF experiments, respectively [14]. These overestimates were attributed to unresolved buoyancy-induced vorticity generation on resolved scales. In detail, this "extra"-vorticity was produced by fluid motion that is currently not explicitly treated in the SGS turbulence models used for the LES.

Bastiaans *et al.*, in an analysis regarding the free convection induced by a line heat source in a confined geometry, compared the LES results with the DNS data to investigate the performance of several sub-grid models (e.g. Smagorinsky, Buoyant Smagorinsky, Kolmogorov-Prandtl, Dynamic Model [17], etc.) [13]. The author comes to a major conclusion that in the use of these sub-grid models, tuning of the model constants (e.g. C_s in Eq. 2.1) seems to have the potential of yielding better results (i.e. in agreement with those of the DNS) [13]. As an example of such, Bastiaans compares two very similar SGS models, where one (Smagorinsky Buoyant) strongly diverges from the DNS and experimental data, while the other (Kolmogorov-Prandtl) results in a better agreement about the sub-grid statistics, based on their respective constants.

Based on these observations, it appears that most of the SGS models are largely un-validated by more refined (but computationally more expensive) DNS simulations and experimental data. In addition, the performance of these models

strictly depends on the estimate of their respective constants (e.g. C_s for Smagorinsky). The latter are artificial tools introduced with the intent to characterize the diffusion transport (mass, momentum, energy) in the small scale range (i.e. from sub-grid down to Kolmogorov scales), and eventually explain the interaction of these unresolved flows with the flow field at the grid-scale. Unfortunately, the intrinsic unresolved nature of turbulence makes these constants biased and requires validation through real experiments. Highly-resolved PIV and PLIF tests with saltwater modeling represent an inexpensive solution which can provide guidelines to probe the unresolved scales.

In this study, unconfined plume tests using saltwater modeling and advanced diagnostics were performed to evaluate centerline plume transport, mixing and time dynamics at different flow resolutions. Many experiments have studied unconfined plumes, but few have had the ability to measure velocity and density difference at a very high resolution and, to the best knowledge of the author, none to provide guidelines to probe grid resolved and sub-grid scale flow simulations. Planar Laser Induced Fluorescence (PLIF) and Particle Image Velocimetry (PIV) diagnostics were used with the saltwater modeling technique to provide highly-resolved [5] instantaneous field measurements useful for statistical analysis, physical insight, and model validation [9, 10]. The effect of the resolution was investigated employing a virtual interrogation window (of varying size) applied to the high-resolution field measurements. In particular, a dimensionless resolution threshold criterion was determined to achieve converged statistics on the filtered measurements [10]. Such a criterion was then used to establish the relative importance between large and

small-scale turbulence phenomena while investigating specific scales for the turbulent flow [10]. Both scalar and velocity scale-based first, second and higher order statistics were eventually estimated.

The complexity in the analysis of fire-driven plumes impinging onto sloped ceilings (Fig. 1.1) is another research aspect investigated here, under two different perspectives: (*i*) the physics of the ceiling jet flow developing under a sloped ceiling and (*ii*) the activation of suppression systems (e.g. sprinklers). Over the past several decades a great deal of research has been directed at making quantitative predictions of activation times of fire detection and suppression equipment to determine the egress time for the occupants of public buildings or residences. Such scenarios mostly included performance analysis of smoke detectors and sprinklers (or a combination of both) mounted on flat ceilings. Only a few concentrated on sloped ceiling scenarios [76], and the majority of those focused on residential sprinklers and compartment fire scenarios [77]. A rising interest for unexplored scenarios such as those characterizing warehouse rack-storage or tunnel sections (slope $\alpha \leq 10^{\circ}$) [78, 79], along with conflicting recommendations found in the current engineering practice for sprinkler orientation/spacing on sloped ceilings [76] has motivated a renewed focus on this research topic.

Some studies report that, between 2007 and 2011, in the United States, rack-storage fires cost over 16 million dollars (US) per month, on average [80]. Suppression systems such as automatic sprinklers are commonly used in warehouses and storage facilities, but given the challenges posed by new structural features such as increased storage heights and inclined ceilings, fire protection engineers have

continued to investigate these new operative conditions for sprinklers and fire detectors [74]. However, the difficulties related to large facility-scale testing are many. Therefore, increased fundamental understanding and improved modeling techniques can help to reduce the number of large, costly tests and overall improve safety in these facilities.

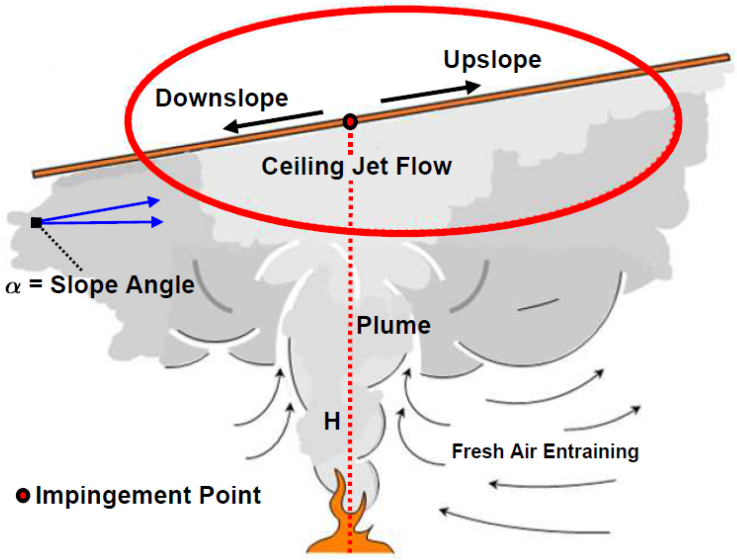

Figure 1.1: Sloped ceiling fire scenario: a buoyant plume quickly rises from a fire and impinges on an α-angled ceiling at a distance H from the source. From the impingement point, a ceiling jet flow develops both upward and downward along the slope as well as radially.

Figure 1.1 schematically illustrates a typical fire scenario investigated in this study, where an unconfined buoyant plume originating from a large point-source fire impinges on an α-angle sloped ceiling at a distance H from the source, thus generating both an upslope and a downslope ceiling jet flow. In fire protection engineering, research is currently tackling two major concerns regarding sprinkler activation for

such a fire scenario. First, possible delays in sprinkler activation can occur under sloped ceilings based on biased upslope hot ceiling jet flow [76]. Second, sprinklers further away from the fire source may activate first, causing the need for higher sprinkler densities when in the presence of larger fires [76, 81]. Over time, efforts to quantify and model fire suppression have been initiated. Several studies have shown that the intimate correlation between activation (via heat sensitive sprinklers or smoke detectors) and the ceiling jet flow field originates from the impingement of a fire plume on a ceiling [8, 78, 79, 82–87]. Therefore, experimental correlations of the fire-driven ceiling-jet flow temperatures and velocities have been used to construct engineering methods to determine heat detector spacing, sprinkler response time, and smoke detector alarm times for industrial buildings, where large undivided ceilings over storage and manufacturing [6] facilities are common. However, only a few studies approached the activation of complex configurations such as those of sloped ceilings. Both experimental and computational investigations have been challenged by the presence of inclined surfaces. CFD modelers encounter difficulties when trying to conform computational rectangular meshes over complex geometries, such as inclined ceilings. In order to model sloped ceiling jet flows, a process known as "stair stepping", or "sawtooth" geometries, consisting of jagged-step meshes [76], are often used. Recently though, the research community has raised arguments about the resolution of the sloped ceiling jet flow field [86], based upon an additional component of vorticity generated by the sharp corners of this stepped grid type. On the other hand, to date, large scale tests are limited in literature because of the excessive cost, and only a few small- or intermediate-scale experiments have been

conducted on sloped ceilings [76]. Most importantly, the majority of these studies do not highlight the correlation existing between activation models and ceiling jet characteristics [76].

In this study, an approach using saltwater modeling (discussed in Chapter 3), which draws on an analogy between buoyant smoke transport and an inverted plume of saltwater in a large freshwater tank, is utilized to model potential sprinkler head response in large compartments with sloped ceilings with slopes up to 40° [7]. As fire detection and suppression equipment activates based on heating by the near-wall flow, it is possible to use the collected data to develop estimates of response [89] time in a potential fire scenario [88]. Velocity and density difference profiles of the ceiling jet are therefore collected from experimental measurements and applied to a sprinkler detector response model [87, 89, 90] by Heskestad and Bill [91] in this work. This approach is similar to that applied in previous work using models for a ceiling jet [92,93], however this work is unique in that it is applied to sloped ceilings which have different upslope, downslope, and radial behavior that are captured in experiments. In light of this, the unexplored correlation between front arrival, delay and activation times in both spanwise and streamwise directions at increasing slope angles is the main objective for this investigation. The results later provide preliminary information useful to develop guidelines for sprinkler spacing.

Saltwater modeling, therefore, represents a valuable and efficient tool to investigate fire buoyant-driven flows. By means of this technique, a saltwater solution is injected into fresh-water and turbulently diffuses with similar characteristics to those of flows induced by a fire plume. The advantage of the saltwater modeling

technique is an accurate physical reproduction of the fire flow dispersion dynamics by means of accessible scaled experiments. Saltwater modeling has been successfully used to visualize both plume dispersion structures and ceiling jet flow over sloped surfaces using a fluorescent tracer dye (for PLIF) and micro-particles (for PIV) for flow density difference and velocity characteristics, respectively. The use of laser diagnostics is intended to provide more detailed quantitative information of the plume dynamics [94] and ceiling jet flow to build up engineering predictive tools for sprinklers activation time.

1.2 Objectives

Previous work has developed an experimental technique and an analytical framework for characterizing fire-induced flows using saltwater modeling. In this study, an approach using this scaled technique (discussed in Chapter 3), which draws on an analogy between buoyant smoke transport and an inverted plume of saltwater in a large freshwater tank, is utilized to (1) investigate turbulent mixing and transport phenomena at grid- and sub-grid scale [7] resolution in canonical free plumes, (2) analyze and characterize the ceiling jet flow developing on a sloped surface ranging the inclination from flat to a 40° angle, and (3) implement the information resulting from point (2) to build up a scaled predicting tool for real sprinkler activation times.

Saltwater modeling is therefore applied to two main fire-induced flow configurations, the unconfined free buoyant plume, and the sloped ceiling jet flow. In both

cases, measurements of velocity and dispersion (or density difference) are conducted by advanced laser diagnostics, namely PIV and PLIF, to generate a basis in order to (I) expand the analysis of free plume turbulent mixing using different orders of statistical moments at different image resolutions, and (II) to highlight the correlation between the characteristics of the ceiling jet flow and sprinkler activation times, while varying the ceiling slope angle.

Given the synopsis of the literature, the objective stated in point (I) corresponds to a systematic analysis of saltwater measurements to better understand the turbulent mixing and transport processes in fire plumes. In a fire the combustion-induced heat makes the fire plume less dense than the ambient air causing the plume to mix with the ambient air as it rises up. The generated buoyant flow is analogous to the injection of the saltwater (dense flow) into the less dense ambient environment (fresh water) [94]. Through this part of the study, a scaling approach, i.e. non-dimensional analysis of the governing equations, is adopted to ensure that similitude is maintained between the saltwater scale model and the full-scale fire plume of interest. The geometric properties as well as characteristic velocities should be utilized to establish the geometric and kinematic similarity. These will also be utilized to investigate the turbulence statistics of the flow. In particular, motivated by LES low-pass filtering concepts, the high-resolution experimental data will be analyzed within (i.e. statistics at the sub-grid scale) and on (i.e. statistics at the resolved scale) an interrogation window of variable size L [9, 10]. A dimensionless resolution threshold (L/D^*) criterion, where D^* is an integral flow length scale based on the saltwater characteristic strength ($\dot{m}^*_{sw}$), will be determined to achieve converged

statistics on the filtered measurements [9, 10].

As fire detection and suppression devices activate based on near-wall flow characteristics, it is possible to use the collected data from saltwater experiments to develop scaled estimates of response time in a potential fire scenario [88, 89]. In this work, saltwater velocity and density difference profiles of the ceiling jet are first investigated and compared with past analysis conducted using CFD models, pool fire experiments and correlations used in engineering practice, and then plugged into a validated, empirical sprinkler response model [87, 89–91]. This approach is similar to that applied by previous work using models for a ceiling jet [92, 93], however this work is unique in that it is applied to sloped ceilings which have different upslope, downslope, and radial behavior that are captured in experiments by means of a laser "multi-planar" grid. In light of this, the unexplored correlation between front arrival, delay and activation times in both spanwise and streamwise directions at increasing slope angles represents the main objective for this part of the investigation. The results later illustrated provide useful information towards the development of guidelines for sprinkler spacing.

Chapter 2: Literature Review

2.1 Unconfined Plume, Ceiling Jet Flow and Activation

The cases investigated in this study represent two different and subsequent phases of the same fire scenario: the unconfined plume rising from an early fire, and the ceiling flow jet developing under a slope, after the impingement of the plume. A third problem examined here is the activation of suppression systems (sprinklers) based on the characteristics of the ceiling jet flow. The analysis presented for all cases above is performed by means of the inverse saltwater modeling technique, where a denser saltwater source, injected into fresh water (less dense), is able to simulate the buoyant transport of a lighter hot smoke plume into cooler air (denser). Such a technique represents a validated tool [31, 53, 88, 94, 97–100, 104, 108, 109, 134] to describe the fundamental physics of the buoyant flow involved in the present work.

The transport in all of these configurations is governed by buoyancy forces, which originate from a variety of sources. In real fire scenarios, hot gases rise up from a heat source and rapidly spread into the fresh air driven by temperature (and density) gradients. Similarly, density gradients can originate by introducing one

fluid, such as saltwater, into another fluid of different density, such as fresh water. Once the fluid is set into motion by buoyant forces, both velocity and thermal fields are strongly coupled.

In regard to the unconfined plume, although the plumes recreated through experiments represent an idealization of those originating from large-scale fires, each of the dynamics is similarly independent from the source [95]. This assumption is valid (1) within the buoyancy-dominated region of the plume, and (2) as long as the density differences between the flow and the environment are small compared to some reference density in the flow. Most of the plumes generated in the laboratory (usually discharged by an injector), including those obtained with saltwater experiments, start as buoyant jets discharged into fresh air (or water) with a non-zero initial velocity, whereas, by definition, a plume has a zero initial velocity. This initial state of laminar motion is typically governed by momentum but quickly transitions to a fully turbulent regime in the far-field, when the main flow entrains the fresh fluid within it while it diffuses. In this buoyancy-dominated region (far-field), the similarity between the dynamics of a scaled plume and a real fire plume is conserved.

As a free plume rises by entering the fresh water, a process of entrainment causes an increase of the mass flux of the plume, and gradually it will continue to add fresh fluid as the plume rises, as shown in Fig. 2.1. The entrainment mechanism gradually increases the amount of fluid engulfed by the flow through large turbulent structures as shown in Fig. 2.1. Under this increasing injection of fresh fluid into the denser flow, the plume continues to spread until the buoyancy-driving

force, weakened by low concentration gradients, decreases due to adverse viscous forces. At the same time, the entrainment mechanism causes the density difference gradients to gradually decrease because of the continuous injection of the fresh fluid (mixing process).

After the impingement of the plume onto a ceiling, a new characteristic, buoyant flow, known as ceiling jet flow, develops radially below the surface. In Figure 2.1, a schematic is overlaid on a PLIF instantaneous realization which identifies both impinging plume and ceiling jet flow regions (upslope and downslope) investigated in this study.

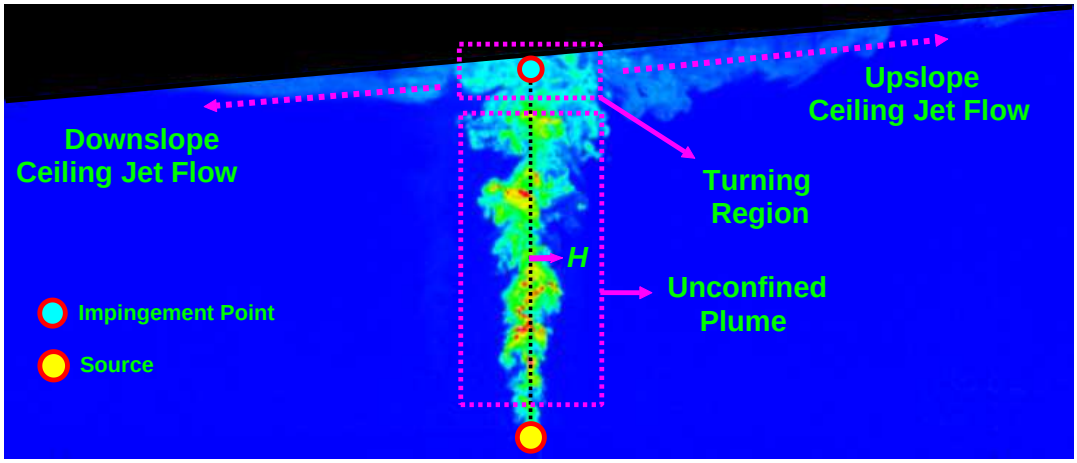

Figure 2.1: Schematic of an unconfined plume and sloped ceiling jet flow, based on an istantaneous PLIF realization: unconfined plume; turning region; upslope and downslope ceiling jet region.

From Fig. 2.1, three major regions can be identified for the impinging plume configuration: (1) plume, (2) turning region, and (3) ceiling jet flow region [94].

Except for cases where the plume is extremely weak (quick dissipation), after the transition from a momentum- to a buoyancy-driven regime, the flow exhibits fully turbulent behavior along the ceiling height at the impingement point, H (Fig. 2.1).

After impingement of the plume on the ceiling, a buoyancy-driven ceiling jet develops in a turbulent regime as well; however, far from the plume centerline, the tendency to remain turbulent can be drastically modified by the presence of density gradients in the flow (i.e. buoyancy), especially if gravitational effects are also important. One of the objectives of this study concerns the jet developing on inclined ceilings, and the balance between viscous and buoyancy forces depends on how the gravity is redistributed in the downstream direction and along the perpendicular direction, based on the slope angle [77]. The higher the slope, the less the turbulence will dissipate along the slope and the more unmixed the downstream flow will be (fire-induced or saltwater). This is consistent with the effects generated by the buoyancy components in the two directions, which depend on gravity. As the slope is increased, a higher downstream buoyancy component causes higher velocities (higher Re), whereas a lower component orthogonal to the ceiling is responsible for reduced entrainment with the fresh air (or water) and poor mixing (with consequent higher temperatures or density differences) [76, 79, 82, 83]. Given this analysis, an increasing delay in buoyant dissipation by means of turbulent mixing and smaller viscous forces (compared to buoyancy forces) are expected at higher inclinations. Based on this balance between viscous and buoyancy forces, Yao *et al.* [97] (in saltwater experiments) and Alpert [133] (in fire experiments) reported that the turbulent jet flow on a flat ceiling undergoes a process of "laminarization"

which occurs at some point downstream due to turbulence suppression. Such a phenomenon, where a stable flow stratification occurring near the ceiling was observed, was explained based on the Ri number, given as the buoyancy to the flow shear (viscous term) ratio.

The last topic examined in this study concerns the activation of sprinklers below sloped ceilings. These sprinkler systems operate based on the hot ceiling jet flow at points where these systems are mounted [85]. Usually, excess temperature and flow velocity are the main characteristics which govern the operating time of the sprinkler (activation time, t_{act}), based on one of its specific constructive parameters called the Response Time Index, RTI. Activation times are the result of the time required for the combustion products to travel to the ceiling and reach the sensitive element of the sprinkler (front arrival time, t_{FA}), plus the time required for the latter to sense the local temperature of the ceiling jet given its velocity (delay time, t_{lag}), and assuming specific properties (e.g. mass, exposed surface, heat transfer coefficient) included in the RTI, activate (activation time). Rapid activation requires that sensors to be located at optimal distances both beneath the ceiling and radially from the impingement point [81]. Ceiling jet flows are naturally affected by the ceiling slope, and this influence must be taken into account in the sprinkler design phase. At present, the practice in fire protection engineering has little information regarding the impact of sloped ceilings on sprinkler spacing strategies.

The analogy established between saltwater and fire-induced flows [31, 119], later discussed in Chapter 3, has shown to be suitable for simulating both the dynamics and the complexity of the turbulent flow within the far-field of a fire plume.

In light of this, several studies, focusing on multiple aspects involving saltwater flows (e.g. plume turbulent transport and smoke detector activation), have been published over time [88, 97, 105–107]. The results of these investigations have advanced the understanding of fire phenomena and improved the design of fire protection systems.

Nonetheless, some aspects in fire plume research, not investigated yet, could be studied by again employing the saltwater technique. On one hand, small scale resolved saltwater experiments could help to validate CFD codes (e.g. FDS) fire-induced flow simulations while on the other hand, they could result in simple engineering prediction tools for sprinkler activation strategy and spacing for sloped ceiling configurations.

2.1.1 Buoyant Plume

Buoyant plumes are encountered in a diverse range of engineering and environmental processes, including pool fires, atmospheric exhaust phenomena like smokestacks and gas releases during the event of a fire in a building [50]. In light of this, the buoyant plumes development/formation and the plumes unstable behavior are a focus in the current research. In most cases (laboratory experiments, industrial plumes) buoyant plumes originate from an initial laminar-to-turbulent transition that turns the initial buoyant-jet (momentum-driven flow at the injection) into a pure buoyant plume. The intrinsic instability related to the intrusion of one fluid into another of different characteristics (velocity, density, temperature) causes the aforementioned transition and produces turbulence. Turbulent transport

and mixing phenomena are relevant to understand the dynamics of the processes governing smoke transport and fire behavior. Although many experimental and numerical studies have revealed the physics of fire and plume dynamics occurring over a range of scales, few contributions have provided detailed information of mixing and turbulent transport at scales small enough to be sub-grid in most CFD applications [3].

Many investigators have studied the fire plume with well-designed experiments as reported in Quintiere *et al.* [32]. Among them, Morton *et al.* [120], Yokoi [23], Thomas *et al.* [102], McCaffrey [101], Zukoski *et al.* [131], Hasemi and Tokunaga [24], Cox *et al.* [25], Heskestad [26], Delichatsios [27], Kung *et al.* [28], Hamins *et al.* [29] provided a broader understanding of the plume dynamics, thus contributing to the plume theory. These studies are mostly based on Froude modeling [119] and consist of dimensional analysis to model fire buoyant flows. Most of these contributions can be found summarized in the work of Beyler [30], McCaffrey [101], Heskestad [144], Delichatsios [27], Zukoski [31], and Quintiere and Grove [32].

In detail, as summarized by Quintiere [53], fundamental contributions were provided by Rouse *et al.* [11] and Morton *et al.* [12]. Rouse *et al.* [11] described general relationships for velocity and temperature profiles resulting from turbulent plumes originating from small sources, assuming a Gaussian distribution of velocity and temperature with respect to the cross-stream direction for both scales along the plume centerline. Morton, Taylor and Turner [12] proposed approximate solutions assuming a point source, plume model.

Experimental procedures for investigating plume dynamics require detailed

measurements which can be costly and time-consuming. The improvement and the refinement of numerical methods provided better alternatives to complex fire experiments so that most research moved to CFD simulations of fire plumes. Among the modeling approaches that can be used for investigating a plume such as Direct Numerical Simulations (DNS), Reynolds Averaged Navier-Stokes (RANS) and Large Eddy Simulations (LES), the latter is often advantageous to reduce computational cost, as larger length scales are very dependent on the initial and boundary conditions, where the smaller length scales are considered isotropic based on Kolmogorov's hypotheses [54]. A filtering operation is used to separate the large scale motions, which are resolved from the small ones, which are modeled. The LES approach is characterized by a coarser grid than that used in DNS, but this allows saving in computational cost compared to DNS, where a large portion of this cost increases from resolving the dissipative scales.

In fire protection, Fire Dynamics Simulator (FDS) is the most cited CFD tool for fire investigation [41], employing Large Eddy Simulation (LES) with a Smagorinsky turbulence sub-model. The latter is used in LES to resolve the unclosed quantities at the sub-grid scale (SGS) introduced by the filtering process and which require to be modeled. The SGS Smagorinsky model uses an artificial eddy viscosity, where the effects of turbulence are lumped into a small scale eddy (or turbulent) viscosity, μ_t, given by

$$\mu_t = \bar{\rho} \left(C_s^2 \Delta_g^2 \right) |\bar{S}| \tag{2.1}$$

where $\bar{\rho}$ is the filtered density, C_s the Smagorinsky constant, $\bar{S}$ the filtered rate of strain and Δ_g the filter width of the grid.

Rehm and Baum [118] were first to develop the set of equations for the FDS, while the general use and application of the code was reported first by McGrattan *et al.* [142]. The first application of the model to plume dynamics was presented by Baum [46]. In another study, McGrattan *et al.* [42] attempted to use LES to directly simulate the large scale eddies, while modeling the effects of the small-scales using a constant value of eddy viscosity, μ_t (Eq. 2.1). The analysis of the smoke movement in an enclosure provided a validation experiment with measurements of velocity and temperature for comparison. Based on the good agreement between experimetal data and simulations carried out by using the SGS model, McGrattan *et al.* [42] concluded that a wide range of experiments could be modeled with reasonable accuracy using LES.

Ma and Quintiere [50] investigated axisymmetric fire plumes attempting to extend the work of McGrattan *et al.* [42] to unconfined fires. Using the LES approach, the standard Smagorinsky SGS model was applied with a default constant of C_s=0.2 (Eq. 2.1). The test case consisted of an unconfined, free burning pool fire and the results showed that the predicted flame heights closely matched the values obtained using the flame height correlations. Accurate predictions of temperature and velocity were also obtained in the non-combustion regions, but the temperature was over-predicted near the burner.

Zhou *et al.* [43] conducted an investigation on non-reacting turbulent buoyant jets using LES and focusing on the near-source region where the laminar to tur-

bulent transition occurs and large vortex structures are generated. The simulation assumed a fixed Smagorinsky constant of C_s=0.1 and varied the air-to-gas density ratio and compared well to equivalent experiments. In particular, the mean velocity along the centerline revealed that the plume initially accelerates under the effect of the buoyancy forces and subsequently slows down because of the turbulent mixing downstream. In a later study, Zhou *et al.* [44] applied LES to reacting plumes observing a similar flow structure in the near-field region characterized by large turbulent eddies and puffing cycles moving downstream. The axial velocity, temperature, species concentration and mixture fraction were validated by comparison with experimental results presented in one of his previous studies [45].

DesJardin *et al.* [14] published a numerical study (LES) concerning the near-field of a large turbulent helium plume and the flow instabilities rising in this region. A grid-sensitivity analysis was performed with and without the SGS model to determine velocity components and local concentrations. From the results obtained, it was concluded that the time-averaged concentration, as well as its root-mean-square (RMS), were over-predicted when no SGS model was used, and were very sensitive to the grid size.

Similar results to those of DesJardin were recently found by Maragkos *et al.* [49], who simulated a helium plume by means of FDS simulations either with, and without a SGS model. Maragkos reported that with no SGS filter, the dimensionless time-averaged mass fraction at the centerline were over-predicted if compared to both experiments and FDS simulations with a SGS model applied. This was found to be due to lack of a more accurate description of the diffusion occurring at very

fine scales (SGS). Therefore, without SGS modelling, diffusion was under-estimated and plume mixing was simulated as a turbulent-based process only. This was further shown by observing the streamwise velocity when applying the SGS filter, as following described. Simulations employing the SGS filter reduced the discrepancy between velocities (streamwise and cross-stream) based on FDS simulations and experiments. Therefore, increased entrainment (i.e. reduced mass fraction) at the centerline, when applying the SGS filter, could not simply be explained by differences in (mean) convection, but must include the effects of diffusion [49].

In previous experimental work, dimensional analysis has been extensively used, as it allows for straightforward comparison of the length and time scales as well as the source strength between scaled models (e.g. saltwater modeling) and fire full-scale phenomena. The resulting knowledge is invaluable for characterizing the underlying physics and informing the numerical models, as credibility of the simulations is strongly dependent on accurate modeling of the turbulent mixing and entrainment especially at the fuel-air interface at very fine scales. Customarily, through mathematical modeling of the integral models that account for the conservation and transport of mass, momentum, and constituents, turbulent fluxes are treated as a fixed percentage of the mean values [124]. However, the magnitude of turbulent fluxes (shear stresses, turbulent mass, and constituent's turbulent fluxes) may vary substantially, both temporally and spatially, based on the type of turbulent flow (e.g. buoyant plumes). Thus, since use of CFD methods is a common practice, particularly in fire and combustion science, as they are safer and relatively less expensive than actual full-scale experiments, it is important to accurately quantify the

contribution of these transport characteristics on a more accurate experimentally-based investigation.

Regardless of the turbulence modeling approach, the fidelity of the flow details needed for a proper characterization of the turbulent mixing and transport phenomena is often limited by the fire scale: the larger the scale, the more difficult is the prediction of the flow details. For a round buoyant plume, such as the one investigated here, the experimental investigations intended to provide support to the turbulent grid and sub-grid resolved modeling approach are relatively scarce in literature [49, 94, 100]. Most of the experimental work produced regarding buoyant plume turbulence investigated the plume transport at a "resolved" level, that is time-averaged flow transport by means of the largest turbulent scales.

By using a thin laser sheet in the probe volume, Yao [94, 97] showed that it is possible to characterize the turbulent transport and mixing down to the local Kolmogorov scales, i.e. $\approx 100\mu m$ [94], for unconfined plumes. The highly-resolved measurements were used for CFD model validation in sub-grid scale. Having demonstrated that PLIF spatial resolution can be used to validate CFD sub-grid scale estimates for unconfined saltwater plumes, Yao [94] showed that the same methodology can be used to probe the fire plume turbulent mixing and transport, and eventually validate corresponding numerical descriptions (e.g. via LES) by means of a saltwater-based probability density function. The good agreement between the second order statistics of the instantaneous mixture fraction obtained from measurements and that calculated in simulations was used to demonstrate that the sub-grid scale model can capture the turbulent mixing in the plume's region of interest.

However, not only the size of interrogation window in [94] was fixed but also the evolution of mixing was not resolved through time. Further, turbulent transport of mass and momentum were not investigated at all which are significantly important for understanding the underlying processes such as entrainment.

Given the synopsis of existing literature, the primary objective of this study is to further evaluate the use of the saltwater modeling technique and systematically analyze the measurements to better understand the turbulent mixing and transport processes in unconfined turbulent fire plumes. Planar Laser Induced Fluorescence (PLIF) and Particle Image Velocimetry (PIV) diagnostics are used with the saltwater modeling technique to provide highly-resolved instantaneous field measurements useful for statistical analysis, physical insight, and model validation. The effect of resolution is investigated employing a virtual interrogation window (of varying size) applied to the high-resolution field measurements. Inspired by LES low-pass filtering concepts, the high-resolution experimental data were analyzed within the interrogation windows (i.e. statistics at the sub-grid scale) and on interrogation windows (i.e. statistics at the resolved scale) [9, 10]. A dimensionless resolution threshold L/D^* criterion was determined to achieve converged statistics on the filtered measurements [9, 10]. Such a criterion was then used to establish the relative importance between large and small-scale turbulence phenomena while investigating specific scales for the turbulent flow [9, 10]. Both scalar and velocity scale-based first, second and higher order statistics were eventually estimated [9, 10].

2.1.2 Saltwater Modeling

The saltwater modeling approach has a rich history in both qualitative and quantitative study of buoyant flows. By means of saltwater modeling, a fire buoyant flow can be well simulated by recreating a scaled down similar configuration, where the saltwater flow employed in the experiments replaces the full-scale fire plume. This method has been used in the past to quantitatively describe fundamental physics in buoyant plumes and jets [94, 97] and as a qualitative tool to explore smoke dispersion in complex geometries [94, 102, 103, 105].

In regard to the dynamics of buoyant plumes and buoyant jets, Sangaras and Faeth [96] used saltwater modeling to study round buoyant jets and pure buoyant plumes. Flow properties were measured as a function of time for various source diameters over a wide range of *Re* number based on the source diameter. The saltwater source was prepared by adding and mixing a fluorescent dye tracer to provide flow visualization [94], and both dispersion dynamics and front arrival times were captured by a CCD camera. However, no quantitative estimate for saltwater concentration was assessed to provide insights on turbulent mixing. More recently, Yao *et al.* [94, 97–99] and Layton [100] implemented PLIF, PIV and Laser Doppler Velocimetry (LDV) laser techniques to quantitatively characterize unconfined impinging plume configurations using flow imaging data processing. Particularly, Yao *et al.* [98, 99] successfully compared saltwater data with McCaffrey's fire plume temperature measurements and point source plume theory [101] as well as Alpert's analysis of ceiling jets [92, 93].

The saltwater modelling technique has been applied to studies of complex geometries in buildings, and activation of smoke detectors within these geometries. Thomas *et al.* [102] used this technique to explore the use of vents for removing smoke from enclosures, Tangren *et al.* [103] used this approach as a way to model smoke layer migration in a ventilated compartment.

In a seminal study, Steckler *et al.* [105] visualized the smoke dispersion in a scaled multicompartment warship using a saline saltwater plume mixed with a dye tracer. They established the fire-saltwater hydrodynamic analog scaling approach through quantitative analysis of saltwater visualization experiments. Therefore, it was demonstrated that, using the appropriate scaling, the dimensionless governing equations for temperature and saltwater concentration are identical, with the exception of Re, Sc, and Pr discrepancies encountered in the diffusive term coefficients [105]. In particular, Steckler *et al.* affirmed that, for an appropriately high level of turbulence, diffusive inconsistencies in both saltwater flow and fire induced flow could be ignored, thus preserving the analogy [94]. However, as observed by Yao, near the wall the analogy between the two flows (saltwater and fire) could be compromised by larger discrepancies between the diffusion terms [94, 97]. Jankiewicz later applied saltwater modeling using PLIF to measure the smoke ceiling layer concentration for smoke detector response times in a multi-compartment model [88]. Comparison of the results with full-scale tests of the same nature suggest that saltwater modeling accurately predicts the front arrival time at different locations throughout the domain, and that front arrival time and detector activation lag time are better predictors of detectors response than gas temperature and

smoke concentration. Ling [108] then combined saltwater modeling with PIV to measure the dispersion of buoyant plumes, which are representative of smoke or other hazardous material, through cross-flow in complex domain geometries, i.e. near buildings. Also, Siang [109] studied smoke ceiling layer flows in a complex beamed ceiling utilizing PLIF and PIV techniques, where it was confirmed that saltwater model can be used for predicting front arrival times and detector response using an activation lag time.

The use of Computational Fluid Dynamics (CFD) methods is a very common practice, particularly in fire and combustion science, as they are safer and relatively less expensive than actual full-scale experiments. However, it is always necessary to quantify transport characteristics on a more accurate experimentally-based investigation, in order to probe the sensitive correlation between the initial setup (e.g. grid, initial and boundary conditions, etc.) and the numerical results obtained. In light of this, dimensional analysis of real fire phenomena, such as that presented in Sec. 3.2.2 using saltwater modelling, represents a valid alternative to real scale fire tests.

In such regard, Kelly [106] using dye visualization techniques, a salinity probe, and scaling arguments, found semi-quantitative agreement by comparing characteristic times for multi-room compartments obtained by saltwater measurements and CFD simulations [98]. Clement and Fleischman [107] also compared saltwater experiments in a two-room enclosure with the same scenario modeled using Large Eddy Simulation (LES) and Direct Numerical Simulation (DNS) methods. Their saltwater experiments were conducted using PLIF measurements enabling detailed

salt concentration data by tracking and quantifying the intensity of a fluorescent dye, which was diluted at the same rate as the saltwater. It was shown that the LES results, in cases with a highly-resolved computational grid, corroborate the saltwater measurements, whereas, DNS performed poorly primarily due to the high artificial viscosity that inhibits the turbulent mixing.

2.1.3 Ceiling Jet Flow and Activation

A number of studies have been conducted quantifying the flow in a ceiling jet generated by the impingement of a fire plume onto a ceiling. The majority of these have focused on horizontal ceiling jet flows, while only recently, a few have concentrated on plume impingement onto an inclined ceiling surface.

Alpert [92, 93, 133] developed a generalized theory for predicting the velocity, temperature rise, and thickness of an early-stage fire ceiling jet (steady) for flame heights lower than the ceiling height. Assuming an initial half Gaussian distribution for the velocity and temperature profiles, Alpert developed an integral model for the boundary layer thickness [92, 93, 133]. Although his integral model provides reasonable predictions on the temperature, the prediction of velocity from his model is somewhat inaccurate. This is mostly caused by assuming the same thickness of thermal and momentum boundary layers in his analysis (i.e., $Pr = 1$) [94].

Motevalli *et al.* [135] conducted small-scale experiments for steady fires under unconfined, horizontal ceilings, developing predicting correlations for temperature rise, velocity, and boundary layer thickness at a given position [137]. In particular,

Motevalli found results that differed from Alpert's model, namely the Gaussian momentum and thermal layers.

Kung [77] conducted early investigations on sloped ceiling jets using pool fires on three ceiling slopes: 10°, 20°, and 30°. Several experiments were conducted for smooth ceilings at different inclination angles and the additional effects of fire heat release rate and ceiling height were also investigated. Kung derived correlations for the "near-maximum" velocity and temperature (i.e. momentum and thermal boundary layers [8, 77]), based on the ceiling slope, the radial distance from the impingement point and the characteristics of the unconfined plume (before the impingement) [8, 77]. Results from this investigation were presented both in the upward and downward directions, but no correlation for the characteristic momentum or thermal Gaussian layer was investigated.

In the last two years, Chatterjee *et al.* presented a study based on FireFOAM computational analysis, which first started to focus on the relationship between sloped ceiling jet flow characteristics and sprinkler activation [76, 82]. A lack of specific guidelines for sprinkler activation patterns on sloped configurations motivated Chatterjee's research. The above studies constitute a comprehensive analysis of temperature and velocity along ceiling slopes, specifically for application in larger size fire scenarios and activation predictions. However, while the correlation between the slope angle and the momentum and thermal boundary layer has been investigated due to a particular interest on maximum velocity and temperature, such correlation has been not addressed for the whole Gaussian layer, where lower temperatures and velocities can delay the activation time of the suppression devices.

Chapter 3: Experimental Approach

This chapter details the saltwater modeling technique adopted to visualize the plume, including both the scaling analogy for a fire plume and experimental techniques used to investigate the characteristics of the saltwater source flow. Figure 3.1 shows a schematic of a free plume, including various elements analyzed in quantitative saltwater modeling. This quantitative experimental approach requires the implementation of advanced laser diagnostics to measure characteristic scales (density difference and velocity) while performing saltwater experiments. This chapter provides some basis of the scaling theory and introduces to the analogy between fire-induced and saltwater flows. A detailed discussion of the physical and analytic requirements for implementation of this quantitative technique, as well as a synopsis of the adopted scaling analysis and its limitations used to design experiments is also discussed.

3.1 Saltwater Modeling: Similitude with Fire-Driven Flows

As mentioned earlier, a flow of saltwater from an inverted source is injected downwards through fresh ambient water to model the turbulent motion and mixing of a fire-induced plume through cold ambient air. Since the buoyancy force resulting

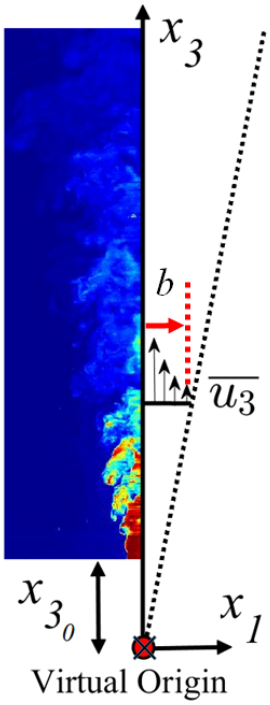

Figure 3.1: Schematic of a free plume: the coordinate system x_1 (spanwise), x_2 (cross pointing inward) and x_3 (streamwise) lays on the laser sheet plane and it is centered on the virtual origin $(x_3)_0$. The distance b from the centerline of the plume represents the point where $\overline{u_3}/\overline{(u_3)}_c = 1/e$

from density differences is the driving factor in both phenomena, these two processes can be related, provided that viscous and heat transfer effects are negligible [105]. The analogy can be made once similitude or an appropriate partial similitude is established. For complete similitude, there are three conditions that must be met: geometric, kinematic, and dynamic similarity [112, 113, 120, 121]. Once these requirements are satisfied, the solution or behavior of the non-dimensional governing equations will be the same for the prototype (fire plume) and its model (saltwater) in terms of the non-dimensional variables, i.e. similarity parameters [113].

With regard to this, depending on the choice of non-dimensional parameters and whether we are dealing with the energy (temperature) or salinity (density) equation, different non-dimensional groups may appear. A complete set of conservation equations for both fire-induced and saltwater plumes are presented in Steckler *et al.* [105]. One way of establishing partial similitude is to reduce the number of characteristic numbers (generated Π-groups) using the asymptotic behavior of the equations and solutions [114].

Before we proceed, important assumptions must be outlined. For buoyancy dominated flows, i.e. $1/Fr^2 \gg 1$ (with Froude, $Fr = u/\sqrt{gL}$, defined based on the characteristic velocity field, u, and the flow characteristic length, L), it is useful to only consider the difference of pressure and temperature from the static (reference) state (subscript $_0$) [113]. Thus, the density variations can be expanded in terms of temperature difference ($\delta T = T - T_0$) and pressure difference ($\delta p = p - p_0$) around the reference state in a Taylor Series as

$$\rho(T,p) = \rho_0 + \frac{\partial \rho}{\partial T}\delta T + \frac{\partial \rho}{\partial p}\delta p + \mathcal{O}(\delta T, \delta p)^2 + \dots \tag{3.1}$$

For an ideal gas, $\partial\rho/\partial T = -\rho_0\beta_T$ and $\partial\rho/\partial p = c_p/(c_v c^2)$, where c is the speed of sound and c_p, c_v are the specific heat capacity at constant pressure and constant volume respectively. The local temperature linearization can be performed with a reference temperature (T_0) and, after non-dimensionalizing Eq. 3.1 with a pressure perturbation term ($p^* = \frac{p-p_0}{\rho_0 U_0^2}$) you arrive at

$$\rho^*(T^*,p^*) \approx 1 - \beta_T(T^* - 1) + (\frac{c_p}{c_v})Ma^2 p^*, \tag{3.2}$$

where $\beta_T = 1/T_0$ represents the volumetric expansion coefficient, and $Ma = U_0/c$ is the Mach number. Based on Eq. 3.2, it is evident that there are two requirements that need to be met in oder to establish a model for a fire plume prototype. First, the flow should be incompressible, namely $Ma \to 0$, and secondly $T \to T_0$ everywhere in the domain, including the walls. For fire-induced plumes, the flow is often slow and not influenced by acoustics, therefore being considered incompressible. Implementing the second limit along with the first is often called the Oberbeck-Boussinesq [115, 116] or in short Boussinesq approximation, where the density differences are neglected, except for the buoyant terms for which a linear relation between the density and temperature difference is defined. The incompressible flow assumption cancels out the term proportional to Ma^2 of Eq. 3.2 and the pressure terms in the dimensionless equations. This is consistent with Lee and Chun [117] that show for a fully developed flow the pressure perturbation gradients are negligible. Therefore, preservation of the Eckert (Ec) number

$$Ec = \frac{u^2}{c_p \Delta T}, \tag{3.3}$$

representing the ratio between the flow kinetic energy, u^2, and the flow enthalpy with respect to a reference enthalpy, $c_p \Delta T = c_p(T - T_{ref})$, and Euler ($Eu$) number

$$Eu = \frac{p_{upstream} - p_{downstream}}{\rho u^2}, \tag{3.4}$$

representing the relationship between a local pressure drop between upstream and downstream pressure, $p_{upstream} - p_{downstream}$, and the kinetic energy per volume of the flow, ρu^2, are no longer necessary for the partial-similitude. However, effects of other non-dimensional groups may still affect the results and will be discussed later.

Yao *et al.* [97–99], Steckler *et al.* [105], and Rehm and Baum [118] argue that, as a saltwater plume with sufficiently weak source is a buoyancy-dominated flow with an inviscid thermally-non-conducting plume for which the Boussinesq approximation holds true, due to inherent differences between the fire and saltwater plumes at the source (neglecting the radiation effects), it is very difficult to practically match the remaining non-dimensional groups, namely Re, Gr, Pr and/or Sc. In this regard, Steckler *et al.* [105] discuss that if the diameter of the saltwater model is geometrically scaled with the (equivalent) diameter of the fire-induced plume, the model and prototype can be considered geometrically scaled, as fire is a heat source with a constantly changing spacial extent. In addition, the Boussinesq approximation ensures that the Grashof (Gr) number is finite and the pressure only deviates from the static pressure due to the fluid motion. Also, when $Gr \longrightarrow \infty$ the effect of pressure gradients vanishes as well [113]. The scalability of inertia and viscous forces can be shown using Re. In this regard, as the length scales of the saltwater model are reduced compared to the real fire plume, resulting in adjusted mass and momentum fluxes in the plume to ensure a buoyancy dominated flow (see section 3.2.4), it is difficult to match the Re number requirement for even partial-similitude. Steckler *et al.* [105] argue that, in saltwater models with Reynolds numbers of the order of 10^4 and larger, the molecular transport processes are negligible relative to turbulent transport. Nonetheless, adjacent to the wall surfaces, the temperature as well as velocity gradients become steep and the diffusive terms may not be negligible. Analogous to Re, in high Gr flows, i.e. $\mathcal{O}(Gr) \sim 10^9$, differences in Pr and Sc are negligible at far distances from the walls. As the focus of this study is on the

flow itself, the effects of boundary surfaces on similitude with a real fire scenario are not discussed. Detailed discussions on the effects of boundary conditions can be found in both Yao *et al.* [97–99] and Steckler *et al.* [105]. Therefore, as long as the reference velocities in both the model and prototype are well defined and the flow in both the model and prototype is maintained turbulent, i.e. Re and Gr are preserved, the inconsistencies between the Prandtl number (Pr) for air and the Schmidt number (Sc) for saltwater can be ignored and partial-similitude can be achieved. This means that the dimensionless quantities allow for easy comparison between various source strengths, spaces, and times, and behavior of the dimensionless conservation equations is the same.

3.2 Fire-Saltwater Analogy

The saltwater technique is a modeling tool used to investigate fire buoyant flows. In this technique a saltwater source is spread into fresh water to generate a buoyant-induced flow behaving similarly to that established in a fire. The fire-saltwater modeling analogy is established on the similarity of dimensionless conservation equations governing fire-induced flows and saltwater flows, respectively. Based on dimensionless groups obtained by normalizing fire-flows conservation equations, Quintiere [119] analyzed the fundamentals of fire scaling. Particularly, in regard to the fire plumes, Quintiere argues that fire induced effects (buoyancy) can be simulated by using a different fluid than air, such as water, where a solute (salt) simulates a heat fire source. Such a technique, known as analog modeling, has the main ad-

vantage of assuring a high Reynolds number (i.e. turbulence) for the reduced-scale saltwater system by means of the smaller kinematic viscosity of the water compared to air. Based on this analogy, the mass, momentum and species equations in the saltwater system correspond to the mass, momentum and energy equations of the fire system.

The analogy between the real fire-induced flow and the small scale saltwater flow is based on the comparison of mass, momentum, energy, and species equations when properly scaled by means of the flow characteristic numbers (e.g. Re, Pr, Gr).

3.2.1 Governing Equations for Fire-Induced Flow

Based on Boussinesq's assumptions, the governing equations for fire-induced flows are expressed as follows

Conservation of Mass

$$\rho = \rho_0 \tag{3.5}$$

In Eq. 3.5, ρ and ρ_0 represent the fire-induced flow density variable and the constant ambient density (air), respectively.

Conservation of Momentum

$$\rho_0(\frac{\partial u_j}{\partial t} + u_i\frac{\partial u_j}{\partial x_i}) = -\frac{\partial(p-p_0)}{\partial x_j} + \mu_T\frac{\partial^2 u_j}{\partial x_i \partial x_i} + (\rho-\rho_0)f_i \tag{3.6}$$

In Eq. 3.6, independent variables of time and space are t and x respectively, and subscripts i and j (where $i, j = 1, 2, 3$) refer to the cartesian coordinates in the reference frame, lying within the laser sheet plane as shown in Fig. 3.1. The

dependent variable u represents the velocity component either in the i- or j-direction, whereas the dependent variable p is the flow static pressure. Therefore, $(p - p_0)$ is the pressure difference between the fire-induced flow and the environment (air) at constant pressure p_0 as illustrated in Sec. 3.1. The body forces per unit volume (mainly gravity) are represented by the term f_i (force component in the i-direction). The dynamic viscosity of the flow is represented by μ_T, where subscript T (thermal) refers to the fire-induced flow environment.

Conservation of Energy

$$\rho_0 c_p \left(\frac{\partial T}{\partial t} + u_i \frac{\partial T}{\partial x_i}\right) = k_T \frac{\partial^2 T}{\partial x_i \partial x_i} + \dot{q}''' \tag{3.7}$$

Here, the dependent flow variable is represented by the temperature T. The dimensional group $\rho_0 c_p$ is the volumetric heat capacity of the flow, while k_T represents the thermal conductivity. The symbol $\dot{q}'''$ is the volumetric energy release rate.

Conservation of Species (Smoke)

$$\rho_0 \left(\frac{\partial Y_{smoke}}{\partial t} + u_i \frac{\partial Y_{smoke}}{\partial x_i}\right) = \rho_0 D_{smoke} \frac{\partial^2 Y_{smoke}}{\partial u_i \partial u_i} + \dot{w}'''_{smoke} \tag{3.8}$$

In Eq. 3.8, Y_{smoke} represents the smoke mass fraction and $\dot{w}'''_{smoke}$ represents the smoke mass release rate per unit volume in fresh air. The symbol D_{smoke} is the diffusivity of the smoke (gas).

Scaling parameters are therefore defined based on flow characteristic scales (subscript 0), in order to generate dimensionless equations. Particularly for the density and temperature scales, characteristic scales ρ_0 and T_0 for the buoyant flow equal those of the ambient flow, also characterized by subscript $()_0$. Other characteristic (or reference) scales such as U_0, t_0 and p_0 do not correspond to the scales

characterizing the ambient flow, but they are rather defined as characteristic scales based on their dependence upon the characteristic fire source strength, Q^*, and the characteristic length scale of the flow, L_T (as later shown in Eqs. 3.31, 3.32, 3.33). The dimensionless variables (superscript $(^*)$) can be defined as follows

Dimensionless Independent Variables

$$t^* = \frac{t}{t_0}; \overrightarrow{x^*} = \frac{\overrightarrow{x}}{L_T}; \tag{3.9}$$

where the characteristic length L_0=L_T, and the subscript T (thermal) refers to the fire-induced flow scenario and it is consistently used throughout the present study.

Dimensionless Dependent Variables

$$\overrightarrow{u^*} = \frac{\overrightarrow{u}}{U_0}; p^* = \frac{p - p_0}{p_0}; \theta_\rho^* = \frac{(\rho - \rho_0)/\rho_0}{(\rho_{source} - \rho_0)/\rho_0}; \theta_T^* = \frac{\beta_T(T - T_0)}{(Q^*)^{2/3}} \tag{3.10}$$

where ρ_{source} (in the definition of θ_ρ^*) represents the density of the buoyant flow of the fire source, and the dimensionless source strength, Q^*, is introduced in the definition of θ_T^*, and defined as follows

$$Q^* = \frac{\beta_T \dot{Q}}{\rho_0 c_p g^{1/2} L_T^{5/2}} \tag{3.11}$$

where $\dot{Q}$ represents the fire source heat release rate (HRR), and without special indication in this study, it is assumed $\dot{Q}$=$\dot{Q}_{convective}$.

Dimensionless Forcing and Source Terms

$$\overrightarrow{f^*} = \frac{\overrightarrow{f}}{g} \equiv (0, 0, -1); \dot{q}^* = \frac{\dot{q}''' L_T^3}{\dot{Q}}; \dot{w}_{smoke}^* = \frac{\dot{w}''' L_T^3}{\dot{m}_{smoke}} \tag{3.12}$$

where $\dot{m}_{smoke}$ is the smoke release rate.

Substitution of dimensionless parameters (Eqs. 3.9, 3.10, 3.12) into fire-induced

flow governing equations (Eqs. 3.5, 3.6, 3.7) results in a new set of dimensionless momentum, energy, and smoke species conservation equations (Eqs. 3.13, 3.14, 3.15), as follows

Fire Dimensionless Momentum

$$\frac{L_T}{t_0 U_0}\frac{\partial u_j^*}{\partial t^*} + u_i^*\frac{\partial u_j^*}{\partial x_i^*} = -\frac{p_0}{\rho_0 U_0^2}\frac{\partial (p^*)}{\partial x_j^*} + \frac{\mu_T}{\rho_0 U_0 L_T}\frac{\partial^2 u_j^*}{\partial x_i^* \partial x_i^*} + \frac{(\rho_{source} - \rho_0) g L_T}{\rho_0 U_0^2} f_i^* \quad (3.13)$$

Fire Dimensionless Energy

$$\frac{L_T}{t_0 U_0}\frac{\partial \theta_T^*}{\partial t^*} + u_i^*\frac{\partial \theta_T^*}{\partial x_i^*} = \frac{k_T}{\rho_0 c_p U_0 L_T}\frac{\partial^2 \theta_T^*}{\partial x_i^* \partial x_i^*} + \frac{\beta_T \dot{Q}}{\rho_0 c_p U_0 L_T^3 (Q^*)^{2/3}}\dot{q}^* \quad (3.14)$$

Fire Dimensionless Smoke Species

$$\frac{L_T}{t_0 U_0}\frac{\partial Y_{smoke}}{\partial t^*} + u_i^*\frac{\partial Y_{smoke}}{\partial x_i^*} = \frac{D_{smoke}}{U_0 L_T}\frac{\partial^2 Y_{smoke}}{\partial x_i^* \partial x_i^*} + \frac{\dot{m}_{smoke}}{\rho_0 U_0^2 L_T^2}\dot{w}_{smoke}^* \quad (3.15)$$

As suggested by Quintiere [119], by equating a π_T dimensionless group to 1 allows to determine a characteristic normalizing parameter in terms of other variables. Therefore, assume the characteristic development time or transient is based on flow time [119],

$$\pi_{1,T} = \frac{L_T}{t_0 U_0} = 1 \quad (3.16)$$

and the characteristic pressure is based on the flow pressure [119],

$$\pi_{2,T} = \frac{p_0}{\rho_0 U_0^2} = 1 \quad (3.17)$$

In addition,

$$\dot{m}_{smoke} = \dot{m}_{source}\left(Y_{smoke}\right)_{source} = \frac{\dot{Q}\left(Y_{smoke}\right)_{source}}{\Delta H_c} \quad (3.18)$$

where $\left(Y_{smoke}\right)_{source}$ is the smoke mass fraction generated from the fire source, and ΔH_c is the combustion enthalpy. Therefore, based on Eqs. 3.16, 3.17 and 3.18, Eqs.

3.13, 3.14 and 3.15 can be rewritten as follows

$$\frac{\partial u_j^*}{\partial t^*} + u_i^* \frac{\partial u_j^*}{\partial x_i^*} = -\frac{\partial (p^*)}{\partial x_j^*} + \frac{\nu_T}{U_0 L_T} \frac{\partial^2 u_j^*}{\partial x_i^* \partial x_i^*} + \frac{(\rho_{source} - \rho_0) g L_T}{\rho_0 U_0^2} \theta_\rho^* f_i^* \tag{3.19}$$

$$\frac{\partial \theta_T^*}{\partial t^*} + u_i^* \frac{\partial \theta_T^*}{\partial x_i^*} = \frac{\nu_T}{U_0 L_T} \frac{\alpha_T}{\nu_T} \frac{\partial^2 \theta_T^*}{\partial x_i^* \partial x_i^*} + \frac{\beta_T \dot{Q}}{\rho_0 c_p U_0 L_T^3 (Q^*)^{2/3}} \dot{q}^* \tag{3.20}$$

$$\frac{\partial Y_{smoke}}{\partial t^*} + u_i^* \frac{\partial Y_{smoke}}{\partial x_i^*} = \frac{D_{smoke}}{U_0 L_T} \frac{\partial^2 Y_{smoke}}{\partial x_i^* \partial x_i^*} + \frac{\dot{Q} \left(Y_{smoke}\right)_{source}}{\rho_0 U_0^2 L_T^2 \Delta H_c} \dot{w}_{smoke}^* \tag{3.21}$$

The characteristic velocity, U_0, can be expressed as $|\rho_{source} - \rho_0| / \rho_0$ as follows

$$U_0 \sim \left(\frac{|\rho_{source} - \rho_0|}{\rho_0} \right)^{1/2} (g L_T)^{1/2}. \tag{3.22}$$

Additionally, U_0 can be defined using the fire source strength, $\dot{Q}$

$$\dot{Q} = \dot{m}_{source} c_p \left(T_{source} - T_0\right) \tag{3.23}$$

where $\dot{m}_{source}$ represents the source characteristic mass flux, and T_{source} a characteristic source temperature. The characteristic flux $\dot{m}_{source}$ used in Eq. 3.23 can be also scales as follows:

$$\dot{m}_{source} \sim \rho_0 U_0 L_T^2 \tag{3.24}$$

Therefore, the characteristic velocity, U_0, can be expressed as a function of the source strength by replacing Eq. 3.24 into Eq. 3.23, thus obtaining Eq. 3.25

$$U_0 \sim \left(\frac{\dot{Q}}{\rho_0 c_p U_0 L_T^2} \right) \left(\frac{T_{source} - T_0}{T_0} \right)^{-1} \tag{3.25}$$

In the frame of the Boussinesq's approximation, the flow density variations are small, so that the density can be expressed using a Taylor's approximation,

$$\rho = \rho_0 + \left. \frac{\partial \rho}{\partial t} \right|_{p=p_0} (T - T_0) + \mathcal{O}(\Delta T^2) \tag{3.26}$$

In addition, the ideal gas assumption is applied so that $\frac{\partial \rho}{\partial t}\Big|_{p=p_0}$ results

$$\frac{\partial \rho}{\partial t}\Big|_{p=p_0} = -\rho_0 \beta_T = -\frac{p_0}{RT_0^2} = -\frac{\rho_0}{T_0} \tag{3.27}$$

where R represents the ideal gas constant. When Eq. 3.27 is replaced into Eq. 3.26, and assuming that the high order terms are negligible, we obtain

$$\rho = \rho_0 - \rho_0 \frac{T - T_0}{T_0} \rightarrow \frac{\rho - \rho_0}{\rho_0} = -\frac{T - T_0}{T_0} \tag{3.28}$$

By replacing Eq. 3.28 into Eq. 3.25, the characteristic velocity scale becomes

$$U_0 \sim \left(\frac{\dot{Q}}{\rho_0 c_p U_0 L_T^2} \right) \left(-\frac{\rho_{source} - \rho_0}{\rho_0} \right)^{-1} \tag{3.29}$$

Eventually, the $\frac{|\rho_{source} - \rho_0|}{\rho_0}$ can be expressed by combining Eq. 3.29 and Eq. 3.22

$$\frac{|\rho_{source} - \rho_0|}{\rho_0} \sim (Q^*)^{2/3} \tag{3.30}$$

with Q^* given by Eq. 3.11. Hence, the characteristic velocity, U_0, can be expressed in terms of Q^* by substituting Eq. 3.30 into Eq. 3.22

$$U_0 \sim (Q^*)^{1/3} (g L_T)^{1/2} \tag{3.31}$$

The combination of Eq. 3.31 with Eq. 3.16 and Eq. 3.17 provides the following characteristic time:

$$t_0 \sim (Q^*)^{-1/3} (g/L_T)^{-1/2} \tag{3.32}$$

and a source based characteristic pressure,

$$p_0 \sim \rho_0 g L_T (Q^*)^{2/3} \tag{3.33}$$

Once the characteristic scales (from Eq. 3.31 to Eq. 3.33) are defined as a function of the source strength and substituted into Eqs. 3.19, 3.20 and 3.21, the dimensionless

governing equations for fire-induced flows become

Fire-Induced Flow Dimensionless Governing Equations

$$\frac{\partial u_j^*}{\partial t^*} + u_i^* \frac{\partial u_j^*}{\partial x_i^*} = -\frac{\partial p^*}{\partial x_j^*} + \frac{1}{(Gr_T)^{1/3}} \frac{\partial^2 u_j^*}{\partial x_i^* \partial x_i^*} + \theta_T^* f_i^* \tag{3.34}$$

$$\frac{\partial \theta_T^*}{\partial t^*} + u_i^* \frac{\partial \theta_T^*}{\partial x_i^*} = \frac{1}{(Gr_T)^{1/3} Pr_T} \frac{\partial^2 \theta_T^*}{\partial x_i^* \partial x_i^*} + \dot{q}^* \tag{3.35}$$

$$\frac{\partial \theta_{smoke}^*}{\partial t^*} + u_i^* \frac{\partial \theta_{smoke}^*}{\partial x_i^*} = \frac{1}{(Gr_T)^{1/3} Sc_T} \frac{\partial^2 \theta_{smoke}^*}{\partial x_i^* \partial x_i^*} + \dot{w}_{smoke}^* \tag{3.36}$$

where Gr_T, Pr_T, Sc_T, are the source based Grashof, Prandtl and Schmidt numbers defined as

$$Gr_T = \frac{g L_T^2 \dot{Q}}{\rho_0 c_p T_0 \nu_T^3}; Pr_T = \frac{\nu_T}{\alpha_T}; Sc_T = \frac{\nu_T}{D_{smoke}}. \tag{3.37}$$

And dimensionless, source based (Q^*) variables are here reported as follows

Source Based Independent Variables

$$t^* = t(g/L_T)^{1/2}(Q^*)^{1/3} \tag{3.38}$$

Source Based Dependent Variables

$$\overrightarrow{u^*} = \frac{\overrightarrow{u}}{(gL_T)^{1/2}(Q^*)^{1/3}}; p^* = \frac{p}{\rho_0 g L_T (Q^*)^{2/3}}; \theta_\rho^* = \frac{\beta_T Y_{smoke} \Delta H_c}{c_p Y_{smoke,0} (Q^*)^{2/3}}; \theta_T^* = \frac{\beta_T (T - T_0)}{(Q^*)^{2/3}} \tag{3.39}$$

and the dimensionless independent variable $\overrightarrow{x^*}$ is defined by Eq. 3.9.

3.2.2 Governing Equations for Saltwater Flow

The following equations represent the conservation equations for saltwater flow based on Boussinesq's assumption

Conservation of Mass

$$\rho = \rho_0 \tag{3.40}$$

Similarly to the fire-induced flow conservation of mass (Eq. 3.5), in Eq. 3.40, ρ and ρ_0 represent the saltwater flow density variable and the constant ambient density (water), respectively.

Conservation of Momentum

$$\rho_0(\frac{\partial u_j}{\partial t} + u_i\frac{\partial u_j}{\partial x_i}) = -\frac{\partial(p-p_0)}{\partial x_j} + \mu_{sw}\frac{\partial^2 u_j}{\partial x_i \partial x_i} + (\rho-\rho_0)f_i \tag{3.41}$$

In Eq. 3.41, μ_{sw} represents the dynamic viscosity of saltwater flow, and subscript sw (saltwater) refers to the saltwater flow environment througout the present study.

Conservation of Salt Mass Species

$$\rho_0(\frac{\partial Y_{salt}}{\partial t} + u_i\frac{\partial Y_{salt}}{\partial x_i}) = \rho_0 D_{salt}\frac{\partial^2 Y_{salt}}{\partial u_i \partial u_i} + \dot{w}'''_{salt} \tag{3.42}$$

In Eq. 3.42, Y_{salt} represents the salt mass fraction and $\dot{w}'''_{salt}$ represents the salt mass release rate per unit volume in fresh water. Symbol D_{salt} is the salt diffusivity. Similarly to the approach employed for fire-induced flows, the dimensionless variables for saltwater flow are expressed as follows

Saltwater Dimensionless Independent Variables

$$t^* = \frac{t}{t_0}; \overrightarrow{x^*} = \frac{\overrightarrow{x}}{L_{sw}}; \tag{3.43}$$

where L_{sw} represents the characteristic length for the saltwater flow scaled model.

Saltwater Dimensionless Dependent Variables

$$\overrightarrow{u^*} = \frac{\overrightarrow{u}}{U_0}; p^* = \frac{p-p_0}{p_0}; \theta^*_{sw} = \frac{(\rho-\rho_0)/\rho_0}{(\rho_{source}-\rho_0)/\rho_0}, \tag{3.44}$$

where ρ_{source} (in the definition of θ^*_{sw}) represents the density of the buoyant flow of saltwater source, and θ^*_{sw} represents the equivalent of θ^*_ρ in saltwater flows.

Saltwater Dimensionless Forcing and Source Terms

$$\overrightarrow{f^*} = \frac{\overrightarrow{f}}{g} \equiv (0,0,-1); \dot{w}^*_{salt} = \frac{\dot{w}'''_{salt} L^3_{sw}}{\dot{m}_{salt}} \tag{3.45}$$

where $\dot{m}_{salt}$ is the salt release rate. Substitution of dimensionless parameters (Eqs. 3.43, 3.44, 3.45) into saltwater flow governing equations (Eqs. 3.40, 3.41, 3.42) results in a new set of dimensionless momentum and salt mass species conservation equations (Eqs. 3.46, 3.47), while mass conservation equation (Eq. 3.40) stays unaltered.

Saltwater Dimensionless Momentum

$$\frac{L_{sw}}{t_0 U_0}\frac{\partial u^*_j}{\partial t^*} + u^*_i \frac{\partial u^*_j}{\partial x^*_i} = -\frac{p_0}{\rho_0 U_0^2}\frac{\partial (p^*)}{\partial x^*_j} + \frac{\mu_{sw}}{\rho_0 U_0 L_{sw}}\frac{\partial^2 u^*_j}{\partial x^*_i \partial x^*_i} + \frac{(\rho_{source} - \rho_0) g L_{sw}}{\rho_0 U_0^2} f^*_i \tag{3.46}$$

Saltwater Dimensionless Salt Mass Species

$$\frac{L_{sw}}{t_0 U_0}\frac{\partial Y_{salt}}{\partial t^*} + u^*_i \frac{\partial Y_{salt}}{\partial x^*_i} = \frac{D_{salt}}{U_0 L_{sw}}\frac{\partial^2 Y_{salt}}{\partial x^*_i \partial x^*_i} + \frac{\dot{m}_{salt}}{\rho_0 U_0^2 L^2_{sw}} \dot{w}^*_{salt} \tag{3.47}$$

By equating π_{sw} dimensionless groups to 1 allows to determine characteristic parameters for saltwater flow for normalization. Therefore, assume the characteristic development time or transient is based on flow time [119],

$$\pi_{1,sw} = \frac{L_{sw}}{t_0 U_0} = 1 \tag{3.48}$$

and the characteristic pressure is based on the flow pressure [119],

$$\pi_{2,sw} = \frac{p_0}{\rho_0 U_0^2} = 1 \tag{3.49}$$

Therefore, based on Eqs. 3.48, 3.49, Eqs. 3.46 and 3.47 can be rewritten as follows

$$\frac{\partial u^*_j}{\partial t^*} + u^*_i \frac{\partial u^*_j}{\partial x^*_i} = -\frac{\partial (p^*)}{\partial x^*_j} + \frac{\nu_{sw}}{U_0 L_{sw}}\frac{\partial^2 u^*_j}{\partial x^*_i \partial x^*_i} + \frac{(\rho_{source} - \rho_0) g L_{sw}}{\rho_0 U_0^2} \theta^*_{sw} f^*_i \tag{3.50}$$

$$\frac{\partial Y_{salt}}{\partial t^*} + u_i^* \frac{\partial Y_{salt}}{\partial x_i^*} = \frac{D_{salt}}{U_0 L_{sw}} \frac{\partial^2 Y_{salt}}{\partial x_i^* \partial x_i^*} + \frac{\dot{m}_{salt}}{\rho_0 U_0 L_{sw}^2} \dot{w}_{salt}^* \tag{3.51}$$

Just as for fire-induced flows, all the characteristic scales, U_0, t_0 and p_0 can be expressed as a function of a saltwater source, $\dot{m}_{salt}$, here introduced as

$$\dot{m}_{salt} \sim \rho_0 \left(Y_{salt}\right)_{source} U_0 L_{sw}^2 \tag{3.52}$$

Equation 3.52 can be solved for U_0 as follows

$$U_0 \sim \frac{\dot{m}_{salt}}{\rho_0 L_{sw}^2} \frac{1}{\left(Y_{salt}\right)_{source}} \tag{3.53}$$

For saltwater flows, the Taylor series expansion shows a direct correlation between density and salt mass fraction changes. Thus, we have

$$\rho = \rho_0 + \frac{\partial \rho}{\partial Y}\Big|_0 \left(Y_{salt}\right) + \mathcal{O}(Y_{salt}^2) \tag{3.54}$$

Therefore, similarly to the fire flows, a volumetric expansion coefficient can be defined based on density gradients, as follows:

$$\beta_{sw} = \frac{1}{\rho_0} \frac{\partial \rho}{\partial Y}\Big|_0. \tag{3.55}$$

The use of β_{sw} (Eq. 3.55) in Eq. 3.54 leads to

$$\rho = \rho_0 + \rho_0 \beta_{sw} Y_{salt} \tag{3.56}$$

Thus, the salt mass fraction of the injected source, $\left(Y_{salt}\right)_{source}$, results

$$\left(Y_{salt}\right)_{source} = \frac{1}{\beta_{sw}} \frac{\rho_{source} - \rho_0}{\rho_0} \tag{3.57}$$

The correlation between saltwater density and salt mass fraction is empirically defined as [129]

$$\rho = \rho_0 + 0.76 \rho_0 Y_{salt} \tag{3.58}$$

with β_{sw}=0.76 [129] obtained by comparing Eq. 3.56 with Eq. 3.58. By replacing the salt mass fraction of Eq. 3.57 into the definition of U_0 of Eq. 3.53

$$U_0 \sim \frac{\dot{m}_{salt}}{\rho_0 L_{sw}^2} \left(\frac{1}{\beta_{sw}}\right)^{-1} \left(\frac{\rho_{source} - \rho_0}{\rho_0}\right)^{-1} \tag{3.59}$$

The term $\frac{\rho_{source}-\rho_0}{\rho_0}$ can be expressed as a function of the source strength using Eq. 3.59 and Eq. 3.22 (replacing L_T with L_{sw})

$$\frac{\rho_{source} - \rho_0}{\rho_0} \sim \left(\dot{m}_{sw}^*\right)^{2/3}, \tag{3.60}$$

where the saltwater source strength is

$$\dot{m}_{sw}^* = \frac{\beta_{sw}\dot{m}_{salt}}{\rho_0 g^{1/2} L_{sw}^{5/2}}. \tag{3.61}$$

Eventually, the characteristic velocity, U_0, is given as function of the saltwater source strength by substituting Eq.3.60 into saltwater modified Eq. 3.22

$$U_0 \sim \left(\dot{m}_{sw}^*\right)^{1/3} \left(g L_{sw}\right)^{1/2} \tag{3.62}$$

In full similarity with the definition given for fire-induced flows, the characteristic time, t_0, is defined based on the saltwater source strength as

$$t_0 \sim \left(\dot{m}_{sw}^*\right)^{-1/3} \left(g/L_{sw}\right)^{-1/2} \tag{3.63}$$

and a source based characteristic pressure is also defined as

$$p_0 \sim \rho_0 g L_{sw} \left(\dot{m}_{sw}^*\right)^{2/3} \tag{3.64}$$

Eventually, the source based definitions established for U_0, t_0 and p_0 (from Eq. 3.62 to Eq. 3.64) are used to define the dimensionless conservation equations for saltwater

flows, as reported below

Saltwater Flow Dimensionless Governing Equations

$$\frac{\partial u_j^*}{\partial t^*} + u_i^* \frac{\partial u_j^*}{\partial x_i^*} = -\frac{\partial p^*}{\partial x_j^*} + \frac{1}{(Gr_{sw})^{1/3}} \frac{\partial^2 u_j^*}{\partial x_i^* \partial x_i^*} + \theta_{sw}^* f_i^* \tag{3.65}$$

$$\frac{\partial \theta_{sw}^*}{\partial t^*} + u_i^* \frac{\partial \theta_{sw}^*}{\partial x_i^*} = \frac{1}{(Gr_{sw})^{1/3} Sc_{sw}} \frac{\partial^2 \theta_{sw}^*}{\partial x_i^* \partial x_i^*} + \dot{w}_{salt}^*, \tag{3.66}$$

where Gr_{sw}, and Sc_{sw}, are the saltwater source based Grashof and Schmidt numbers defined as

$$Gr_{sw} = \frac{\beta_{sw} g L_{sw}^2 \dot{m}_{salt}}{\rho_0 \nu_{sw}^3}; Sc_{sw} = \frac{\nu_{sw}}{D_{salt}}. \tag{3.67}$$

And dimensionless, source based ($\dot{m}_{sw}^*$) variables are here reported as follows

Saltwater Source Based Independent Variables

$$t^* = t(g/L_{sw})^{1/2} (\dot{m}_{sw}^*)^{1/3} \tag{3.68}$$

Saltwater Source Based Dependent Variables

$$\overrightarrow{u^*} = \frac{\overrightarrow{u}}{(gL_{sw})^{1/2} (\dot{m}_{sw}^*)^{1/3}}; p^* = \frac{p}{\rho_0 g L_{sw} (\dot{m}_{sw}^*)^{2/3}}; \theta_{sw}^* = \frac{\beta_{sw} Y_{salt}}{(\dot{m}_{sw}^*)^{2/3}} \tag{3.69}$$

and the dimensionless independent variable $\overrightarrow{x^*}$ is defined by Eq. 3.43.

3.2.3 Distortion: Limitations of Saltwater Modeling

A comparison between Eq. 3.34 and Eq. 3.65 shows that dynamic similarity is clearly demonstrated in both momentum equations for fire and saltwater configurations. However, the discrepancies between governing dimensionless groups Gr, Pr, Sc in the energy and mass species equations between fire and saltwater configurations may cause the flows to behave differently. Like all practical issues

of modeling through scaling, it is not always possible to preserve all dimensionless groups, but to achieve useful results with good approximations. Although Eqs. 3.35, 3.36 and 3.66 show a strong similarity in describing the behavior of fire and saltwater buoyant flows, Quintiere observed that the saltwater modeling technique shows some major limitations when comparing the diffusive terms of the energy (fire) and species (fire and saltwater) equations [119]. First, it is difficult to match the respective source-based Grashof numbers, $Gr_T = g\beta_T \dot{Q} L_T^2/(\rho_0 c_p \nu_T^3)$ for fire and $Gr_{sw} = g\beta_{sw} \dot{m}_{salt} L_{sw}^2/(\rho_0 \nu_{sw}^3)$ for saltwater, when running saltwater experiments at reasonable scales. Second, an inherent difference between the molecular properties of the two flows in comparison results in a gap between $Pr_T = \nu_T/\alpha_T$ (in Eq. 3.35), $Sc_{smoke} = \nu_T/D_{smoke}$ (in Eq. 3.36), and $Sc_{sw} = \nu_{sw}/D_{salt}$ (in Eq. 3.66) numerical values. These two factors cause a distortion in modeling fire-induced buoyant flows by means of saltwater modeling. Such distorsion can be easily neglected when assuming a turbulent flow (i.e. Grashof numbers exceeding 10^9), such that the molecular diffusion results relatively small when compared to turbulent mixing, and hence the associated dimensionless parameters (Gr, Pr, Sc) may be neglected. This enables one to neglect the diffusion terms from Eqs. 3.35, 3.36 and 3.66 for an optimal similarity between fire and saltwater flows. On the other hand, when close to a surface (e.g. a ceiling) or a wall, the molecular diffusion increases due to larger gradients at the wall so that differences between Pr and Sc should be included in the analysis. As later discussed in Chapter 5, the results obtained for the analysis on sloped ceilings are assumed for a $Gr_{sw} \approx 2 \cdot 10^{11}$ at the impingement point of the plume, in order to attenuate the distorsion effects along the slope. This high level

of turbulence ensured in the proximity to the ceiling is designed ad hoc to preserve the similarity between the saltwater and the fire-induced flow, enabling a turbulent rather than a diffusive transport and mixing.

3.2.4 Buoyancy Driven Design

To properly model the fire, the saltwater source must be carefully injected to ensure that the flow is buoyancy dominated, turbulent, and that the mixing dynamics is similar to that in a fire induced flow. In this section, some theoretical aspects of this technique are discussed. The source momentum makes the saltwater flow behave as a jet near the injection origin. This jet-like behavior differs from the initial source in an accidental fire. However, the initial momentum of the saltwater plume becomes negligible as buoyancy dominates further in stream-wise direction. In this regard, two source parameters are needed to establish the influence of the initial momentum on the flow behavior; these are respectively the source specific momentum flux,

$$M = 2\pi \int_0^{D/2} U_0^2 x_1 dx_1, \tag{3.70}$$

and, the source specific buoyancy flux,

$$B = 2\pi \left(\frac{\rho_{sw} - \rho_0}{\rho_{sw}} g \right) \int_0^{D/2} U_0 x_1 dx_1. \tag{3.71}$$

Where D is the outlet injector (nozzle) diameter, U_0 the source based or characteristic velocity, x_1 is the radial direction in cylindrical coordinate system as shown in Figure 3.1, and ρ_{sw} and ρ_0 are the source and fresh water densities, respectively. Utilizing these parameters an empirical momentum length scale is established by

Morton *et al.* [120] as,

$$L_M = \frac{M^{3/4}}{B^{1/2}}. \tag{3.72}$$

It is shown that for the vertically forced plumes the plume-like behavior, in which the mixing is dominated by buoyancy, develops at distances $x_3 \gtrapprox 5L_M$ from the injection point in the stream-wise direction [120, 121], while the transition from jet-like to plume-like occurs at $2 < x_3/L_M < 5$ [122]. In this study, the appropriate source strength is selected to ensure the initial momentum of the saltwater jet is dissipated quickly and the flow reaches unforced plume-like behavior.

3.2.5 Integral Solution

The unconfined point-source plume configuration has been used by previous researchers to establish plume theory. This theory provides solutions for the temperature profile, velocity profile and entrainment for thermal plumes at various elevations above the source [120]. Based on point source theory, the behavior of the fire plume is independent of the details of the heat source including the fuel source and source geometry. The turbulent flow induced by a heat point source is investigated estimating the total mass, momentum, and energy integrated over the plume cross-section. Additionally, the entrainment velocity is usually assumed proportional to the centerline velocity of the plume. Assuming the average temperature and velocity across the plume have Gaussian profiles, Zukoski *et al.* [104] provided a theoretical solution for the plume momentum and energy equations by using an

integral method. The solutions based on a Gaussian profile assumption are

$$\frac{\overline{\theta}}{\overline{\theta_c}} = e^{\frac{-\beta^2 x_1^2}{b^2}} \tag{3.73}$$

$$\frac{\overline{u_3}}{\overline{(u_3)_c}} = e^{\frac{x_1^2}{b^2}} \tag{3.74}$$

$$\frac{b}{x_3^+} = \frac{6}{5}\alpha \tag{3.75}$$

$$\overline{\theta_c} = C_T \left(Q^*\right)^{2/3} \tag{3.76}$$

$$\frac{\left(\overline{u_3}\right)_c}{\sqrt{g x_3^+}} = C_V \left(Q^*\right)^{1/3} \tag{3.77}$$

where both coefficients C_T and C_V in Eqs. 3.76 and 3.77 are constants expressed as functions of entrainment coefficient, α, and the ratio of the velocity half-width to the temperature half-width, β.

$$C_T = \frac{5}{6}\left[\frac{5}{9\pi^2}\right]^{1/3} \beta^{1/2} \left(1+\beta\right)^{2/3} \alpha^{-4/3} \tag{3.78}$$

$$C_V = \left[\frac{25}{24\pi}\right]^{1/3} \left(1+\frac{1}{\beta}\right)^{1/3} \alpha^{-2/3} \tag{3.79}$$

Symbol b represents the spanwise location (x_1) from the centerline where $\overline{u_3}/\overline{(u_3)}_c = 1/e$ and streamwise cartesian coordinate, x_3, is corrected by a factor, $(x_3)_0$, known as virtual origin (Fig.3.1). This constant is used to obtain the distance along the centerline corrected for the effects of initial injection momentum and finite injector geometry. Thus, the virtual origin defines a relative coordinate system,

$$x_3^+ = x_3 - (x_3)_0, \tag{3.80}$$

where a virtual source is located at $(x_3)_0$=0. Therefore, the down stream buoyancy dominated plume is considered as propagating from a point source at $(x_3)_0$=0. The

virtual origin (for concentration and for velocity) is obtained by displaying x_3^+ values (extrapolated from Eq. 3.76 and Eq. 3.77 using measured data of concentration and velocity, respectively) against x_3 and by finding the intercept x_3 of the (x_3, x_3^+) linear data fit when $x_3^+ = 0$ [123]. The virtual origin is used to correlate data in terms of point source theory. It depends on when the flow becomes buoyancy dominated and when the flow transitions to a turbulent state. Even with the same initial condition, the transition region from laminar flow to turbulent flow can still vary resulting in different virtual origins. Thus the virtual origin has to be estimated from each measurement.

The theoretical integral solution has been validated by many experiments [92, 93, 101, 123]. However, both constants of proportionality, C_T and C_V, determined from various experiments, have generated a wide ranges of values,

$$0.085 \leq \frac{6}{5}\alpha \leq 0.124 \tag{3.81}$$

$$0.86 \leq \beta \leq 1.4 \tag{3.82}$$

Large ranges of values found in literature [92, 93, 101, 123] for both C_T and C_V can be attributed to the systematic errors in measuring velocity and density difference scales. Particularly for this study, the integral solution has been used for measurements of velocity and density difference scales evaluated at the centerline of free plumes, in order to validate results obtained combining saltwater modeling with laser diagnostics.

3.3 Experimental Facility

Planar Laser Induced Fluorescence (PLIF) and Particle Image Velocimetry (PIV) are employed as diagnostics methods. Special attention has been paid to the initial flow conditions, light absorption effects in the PLIF measurements and the ability of the seeding particles to follow the flow in PIV measurements. The experimental setup is depicted in Fig. 3.2. As shown in Fig. 3.2, the experiments

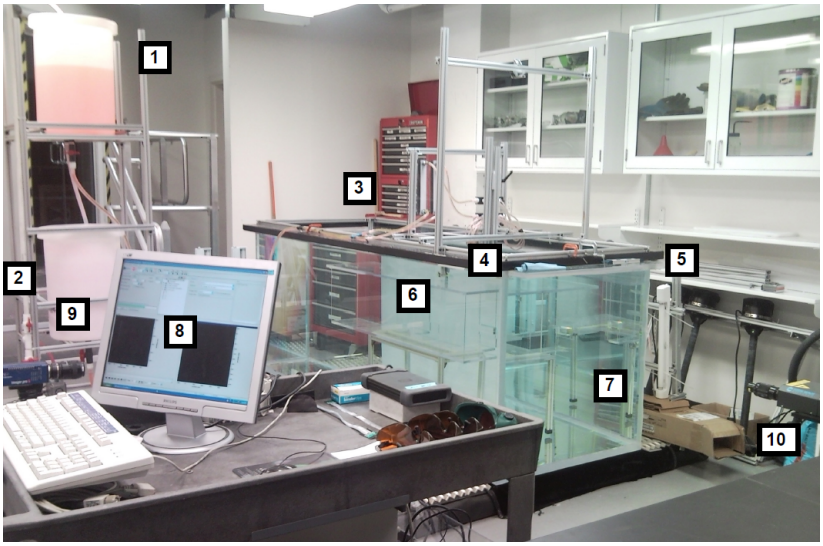

Figure 3.2: Saltwater Test Facility-(1) Saltwater tanks; (2) Circulating pump; (3) Flow meter; (4) Source Injector; (5) Back-lighting; (6) Acrylic building model (7) Fresh water tank; (8) PIV/PLIF Image acquisition System; (9) CCD Camera (with filter); and (10) 30 mJ double-pulsed green Nd:YAG laser with focusing lens system (Source: Layton's M.Sc. thesis, [100]).

were conducted in a large fresh water acrylic tank of 2.37 m length, 0.79 m width and 0.85 m depth. The plume source and surrounding equipment were coated with black paint to avoid noise in the form of back reflected light. Prior to each test,

fresh water was filtered using a 0.5 μm cotton filter cartridge. Since the plume was buoyancy-driven, experiments were started after at least 30 minutes had elapsed to suppress the natural flows due to filling and mixing. Also, saltwater injection was gravity-driven from the source tank. The plume source was generated using a 5.6 mm internal diameter (I.D.) aluminum tube. Saltwater flows from two 10-gallon high density polyethylene (HDPE) tanks set into a tower rack, one at the top and the other at the bottom [3]. A pump was utilized to flow the saltwater from the bottom tank to the top such that it is well-mixed. Also, the saltwater level kept constant, using a drain in the top tank, in order to provide constant pressure at the injector [3]. In addition to this, in each tank fans were used to keep the dye and seeding particles mixed for PLIF and PIV measurements, respectively [3].

Due to the sensitivity of Rhodamine 6G to light, each tank was surrounded by a blackout curtain by ThorLabs during PLIF tests [3]. To prevent the dye from breaking down because of chlorine into the water, a dechlorinator by Tetra was added to the saltwater source. Preliminary tests showed that the Rhodamine 6G concentration changed noticeably over time without the agent added [3]. Flow from the source tank was controlled using a 1 L/min maximum-flow meter by Gilmont (Model GF-6541-1230). Proper turbulence scaling was the first requirement in designing the experiments, while the second was to ensure the saltwater plume was buoyancy driven. Therefore, the saltwater injection velocity was set high enough to ensure a fully turbulent flow after $5L_M$ distance from the outlet, yet low enough such that the initial jet flow at the outlet would transition to a buoyant flow. The injector diameter was also designed to ensure that no back flow or recirculation could occur

at the injector outlet. The geometry of the injector was found to severely impact the structure of the flow exiting the injector. Generally, a small outlet diameter injector tends to rise to a turbulent jet, while a larger injector tends to produce a buoyant, laminar plume. Therefore, a balance between salt concentration, source flow rate and injector diameter must be reached, in order to achieve the desired flow characteristics. Taking this into account, the virtual origin values of M and B were adjusted to reach a plume-like behavior. Given these conditions, the flow in each meter was calibrated using saltwater and found to be the same as its initial fresh water calibration, despite the difference in viscosity between salt and fresh water. The initial flow conditions as well as the characteristic scales for the unconfined plume measurements are reported in Table 3.1.

Table 3.1: Initial Flow Conditions and Characteristic Scales.

Technique	PIV	PLIF
Outlet Diameter (D) [mm]	5.6	
Salt Mass Fraction (Y_{salt}) [-]	0.13	
$\dot{m}_{salt}$ [g/s]	0.45	
$\dot{m}^*_{sw}$ (Based on D) [-]	0.0456	
Volumetric Flow Rate ($\dot{V}$) [mL/min]	165	
Injection Velocity (U_{inj}) [mm/s]	≈112	
Virtual Origin (x_{3_0}) [mm]	-15.3 (Case 1); -16.2 (Case 2)	-12.3 (Case 1); -18.7 (Case 2)
Characteristic Length Scale (D^*) [mm]	1.5	
Re_D [-]	≈ 636	
Momentum Flux (M) [$\times 10^{-7}$ m^4/s^2]	4.12	
Buoyancy Flux (B) [$\times 10^{-6}$ m^4/s^3]	2.43	
Morton Length Scale (L_M) [mm]	13.44	

3.3.1 Laser Diagnostics

A 30 mJ double-pulse 532 nm Nd:YAG laser was employed as the excitation light source for the experiments. On top of the laser two cylindrical lenses of $f = -10$ mm and $f = -20$ mm focal length were attached; one to form the planar sheet out of the original 1.5 mm diameter laser beam, and one adjusting the thickness of the laser sheet at the probe volume in order to optimize the laser sheet intensity. The LaVision ProX 4M CCD camera with a resolution of 2048 $\times$ 2048 pixels (4 mega pixels) or an individual pixel size of 7.4 $\times$ 7.4 μm^2 space was employed for both PIV and single-frame PLIF measurements [3]. Both laser Solo II by New Wave Inc., consisting of laser head and power unit, and LaVision ProX 4M CCD camera are shown in Fig. 3.3 [7]. A Nikon 60 mm-$f/\# = 2.8$ lens was used to provide a 350

Figure 3.3: Optics. Left: New Wave Nd:YAG SOLO II- PIV/PLIF 532 nm wavelength, 15 Hz pulsed laser (source: New Wave Research [68]); right: LaVision ProX 4M pixel CCD camera (source: LaVision [67]).

mm field of view (F.O.V.) for characterization/validation of the unconfined plume,

while a Canon EF 200 mm-$f/\# = 2.8$ lens was used for a 50 mm F.O.V. to provide information up to 25μm single-pixel resolution in the plume images (resolution study, Sec. 4.3). Given the narrow field of view used for the resolution study, 8 sets of measurements were taken to cover the entire plume centerline. The lenses were chosen based on their manually adjustable aperture, which was set to wide open for better light input. For PIV, a 532 nm pass filter was set on top of the camera to collect only the light input elastically back scattered from the particles seeding the flow [4]. For the PLIF tests, a 532 nm-blocking filter by LaVison was utilized to filter out the excitation light wavelength and only collect the fluorescence exhibited by the Rhodamine 6G dye tracer [3,7]. The latter was chosen based on its resistance to photo-bleaching and low temperature sensitivity. Table 3.2 summarizes the specifics of PLIF and PIV diagnostics techniques. The combined use of the filters and wide-

Table 3.2: Specifics of the diagnostic techniques employed in experiments.

Technique	PIV		PLIF	
Tracer	50 μm PSL particles		Rhodamine 6G	
Camera	LaVision ProX 4M CCD			
Field of View (F.O.V) [mm]	350	50	350	50
Lens	60 mm-$f/\# = 2.8$	200 mm-$f/\# = 2.8$	60 mm-$f/\# = 2.8$	200 mm-$f/\# = 2.8$
Time Interval (dt) [ms]	50	5.5	[-]	

open aperture of the lens did not have impact on the image sharpness and depth of field for both PIV and PLIF techniques [3]. For all the tests, the camera was oriented perpendicular to the laser sheet, in order to optimize the collected light output from the particles or the dye tracer [3].

3.3.2 Calibration

A first step in the calibration process consisted of subtracting a background image from the PLIF images set, to account for the electric noise from the camera. Therefore, an average of approximately 45 photon counts (dark current), measured when the laser was off, were subtracted from all recorded images. Second, a "sheet image", out of an average of 500 images, was created illuminating the fresh water tank, where 0.01 mg/L of dye were dispersed to generate a multiplier for each pixel to apply to the measurement images set. This multiplier is intended to correct the output intensity on recorded images for the laser sheet intensity distribution and provide a uniform profile [3]. To generate the average "sheet image", it was ensured that the set of 500 images used was not affected by imperfections such as streaks, reflections or debris. Therefore, the number of water bubbles was minimized at the side walls of the tank by polishing the acrylic surfaces, and the laser sheet at the meniscus was masked off to minimize the meniscus of the water at the walls [100]. Lastly, the correlation between the dye concentration used for the measurements and the output light intensity was examined to complete the calibration process [3]. Rhodamine 6G dye fluorescence intensity in output linearly increased with increasing dye concentration, ranged from 0 to 0.12 mg/L for this test. Based on Layton's and Yao's [94, 100] saltwater experiments, the linearity between the dye concentration and the output fluorescence was verified using four concentrations, obtained by diluting the source by half at each step of these calibration tests [3]. The results for this part of the PLIF calibration confirmed the linearity between dye concentration

and excited fluorescence, as reported by Layton [100] and Yao [94].

Besides the regular steps for PIV calibration measurements [67], an additional analysis was conducted for an optimal setup, assuming the results from saltwater experiments by Layton [100]. Based on Layton's previous tests [100], PIV calibration was performed by taking into account the residual background flow motion in the tank. In particular, PIV time-series were run to quantitatively estimate the influence of these natural background motions on plume and ceiling jet velocity measurements. As later discussed in detail in Sec. 3.3.4, one major issue with PIV consists into the "peak-locking", a known bias error in this imaging-based technique [67]. Without going into details, it is important to assume that the image of the seeding particles (apparent size) must be not less than or equal to a pixel. A major factor in the estimate of the apparent size of the particles is the choice of the particle diameter ($50\,\mu m$ for this study), which also has to satisfy the Stokes's equation to be neutrally buoyant. In addition, as shown in Eqs. 3.96, 3.97, great care was taken of the aperture of the camera ($f/\#$), and its magnification, M, to avoid the "peak-locking". From a few calibration tests, the apparent size (or image size) of the particles was found to be about 4 pixels. This size, found using the laser power at 80% of its maximum capacity, consistently matched the one estimated using Eqs. 3.96, 3.97.

3.3.3 Planar Laser Induced Fluorescence

Planar Laser Induced Fluorescence (PLIF) is used in this study to measure the salt mass concentration in saltwater plumes [7]. Assuming the dye tracer and

salt dilute at the same rate, the salt mass concentration is directly proportional to the dye concentration. This non-intrusive technique provides researchers with a simple and convenient flow-marking scheme for measuring passive scalar quantities such as concentration [124–126]. Light from the incident light sheet is absorbed by the dye tracer present in the flow and re-emitted in all directions in a wavelength range characteristic of the specific dye tracer used. The intensity of the fluoresced light is proportional to the local dye concentration and the incident laser light intensity. Using a camera at a right angle to the laser sheet, two dimensional images of the fluorescent light distribution are obtained when the laser sheet passes through the flow. After careful calibration, the fluorescent light intensity distribution is converted to a dye concentration distribution. Detailed components of the PLIF system are provided in this section.

3.3.3.1 PLIF Theoretical Background

The estimate of the mass fraction, Y_{salt}, is extracted from PLIF images assuming the correlation between the laser light intensity, dye concentration and salt mass concentration [94]. The Beer-Lambert's equation establishes the relationship between dye concentration and fluorescent intensity [127, 128] as follows

$$I_e(b) = I_0 e^{-\epsilon \int_0^b C(x_1) dx_1} \tag{3.83}$$

In Eq. 3.83, terms $I_e(b)$ and I_0 represent the excited beam intensity (at a point b known as the absorption path length) and laser incident light intensity, respectively.

The ϵ and $C(x_1)$ terms are the characteristic extinction coefficient of the Rh-6G and its concentration estimated at x_1 (see Fig. 3.1) [94]. Studies conducted by Guilbault [127] established that only with less than 5% of I_0 absorbed, a linear correlation between the fluorescence output and the dye concentration is possible [94]. If no absorption is along the beam path, the mass concentration of the dye, C_{dye}, and the grey level (GL) of the normalized light intensity are linearly depending to each other, as follows

$$GL = a_0 C_{dye} \tag{3.84}$$

where a_0 represents a calibration coefficient. If the dye tracer has the same rate of dilution of the salt, the mass concentration of the salt and the one for the dye are assumed to be directly proportional as

$$C_{dye} = a_1 C_{salt} \tag{3.85}$$

where the coefficient a_1 is extrapolated using the initial conditions for dye and salt mass concentrations at the injection point [94]. Salt mass concentration is then expressed in terms of Y_{salt} as [94]

$$C_{salt} = \frac{m_{salt}}{V_{salt}} \frac{\rho_{sw}}{\rho_{sw}} = Y_{salt} \rho_{sw} \tag{3.86}$$

where ρ_{sw} is the density of saltwater, which according to Wolf [129], can be expressed as a function of Y_{salt} as follows,

$$\rho_{sw} = \rho_0 (1 + \beta_{sw} Y_{salt}) \tag{3.87}$$

where β_{sw}=0.76 and ρ_0 is the density of fresh water. By plugging Eq. 3.86 and Eq. 3.87 into Eq. 3.85 results in

$$C_{dye} = a_1 Y_{salt}(1 + \beta_{sw} Y_{salt})\rho_0 \tag{3.88}$$

Substituting Eq. 3.88 into Eq. 3.84 yields

$$GL = a_0 a_1 Y_{salt}(1 + \beta_{sw} \cdot Y_{salt})\rho_0 \tag{3.89}$$

and the salt mass fraction Y_{salt} is therefore

$$Y_{salt} = \frac{-a_0 a_1 \rho_0 + \sqrt{(a_0 a_1 \rho_0)^2 + 4 a_0 a_1 \beta_{sw} \rho_0 GL}}{2 a_0 a_1 \beta_{sw} \rho_0} \tag{3.90}$$

Eventually, based on the positive solution of Eq. 3.90, the temperature field for the real fire scenario can be determined by means of the saltwater analogy.

3.3.4 Particle Image Velocimetry

Particle Image Velocimetry (PIV) technique employs μ-particles to seed the flow under investigation. A double-pulsed laser light illuminates the particles, and the camera (equipped with a 532 nm pass filter) collects the back-reflected light (elastically scattered) from their surface across pairs of images to track their displacements. The short time interval in between the two consecutive frames (dt) is then used, along with the particle displacements, to reconstruct the velocity field. The basic PIV setup, comprehensive of the laser, the laser sheet, and the seeded flow is shown in Fig. 3.4. Compared to traditional methods (probes), PIV represents a non-intrusive and therefore more accurate system for quantitative measurements of velocity for several flows [110].

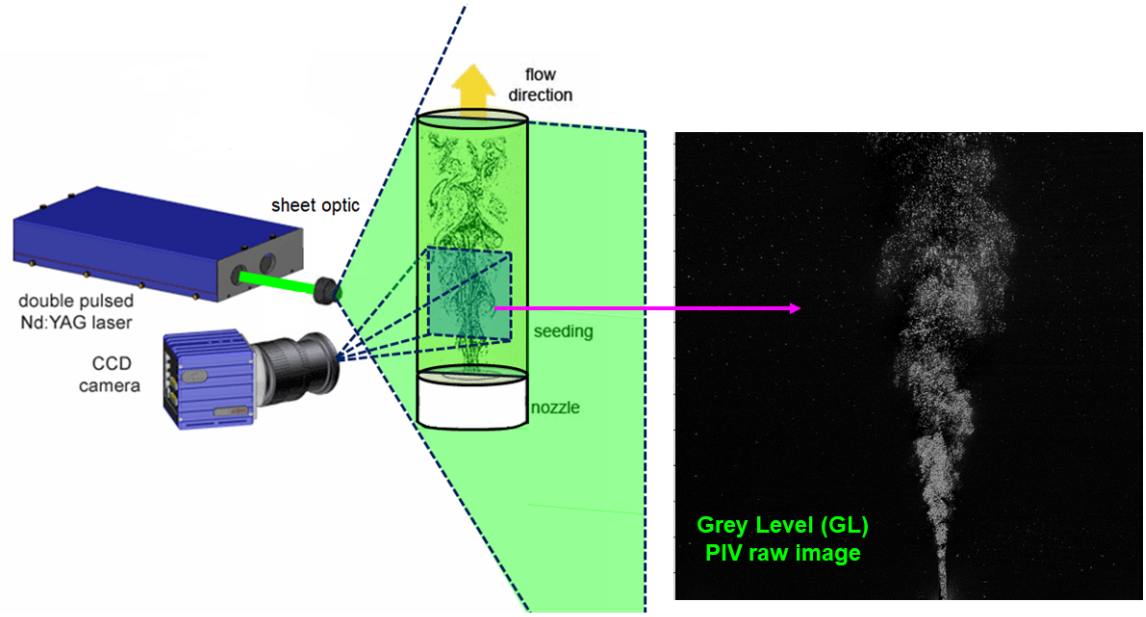

Figure 3.4: PIV laser technique. Setup schematic (left); instantaneous GL (Grey-Level) image of the inversed saltwater buoyant plume (right).

LaVision DaVis software (7.2 edition) provides a number of parameters used to estimate the particle velocity field. After calibration of the system, the software normalizes the intesity of the seeding particles and subtracts a sliding background image (averaged over a number of 50 images for these tests) to improve the contrast. The results of such a process are shown by a sample of high particle density (50μm diameter) flow, framed within a 100×100 pixels (2.5 mm×2.5 mm) window (Fig. 3.5), used in the resolution study, presented in Sec. 4.3. In detail, a high particle concentration is required to drastically improve the Signal-to-Noise Ratio (SNR). Once an optimal setup (particle size, particle density) is obtained, the cross-correlation method is used to track particle displacements across the pairs of images. Interrogation windows of 32×32 pixels are initially overlaid on each of the

Figure 3.5: PIV digital particle image captured and corrected by subtracting a sliding background image for contrast improvement. The image sample shows a sample of 100×100 px (2.5 mm×2.5 mm) for high particle concentration flow.

paired-frame to determine an average velocity to use as guidance for refined, highly-spatially measurements. The latter can be obtained by balancing higher particle concentration and smaller particle diameter with increasingly smaller interrogation windows (e.g. from 32×32 pixels to 8×8 pixels). In order to obtain an accurate velocity field at any point, it is important to keep low the number of particle image pair outliers, while increasing the resolution of the interrogation window. Figure 3.6 shows this process for double-frame cross-correlation using a decreasing window size. Other options are available that use a constant size interrogation window or only a single frame with double exposure, but these provide less accuracy for the flow field.

Keane and Adrian [110] first established design rules for the PIV technique by running Monte Carlo simulations. The objective of these rules (reported below) was

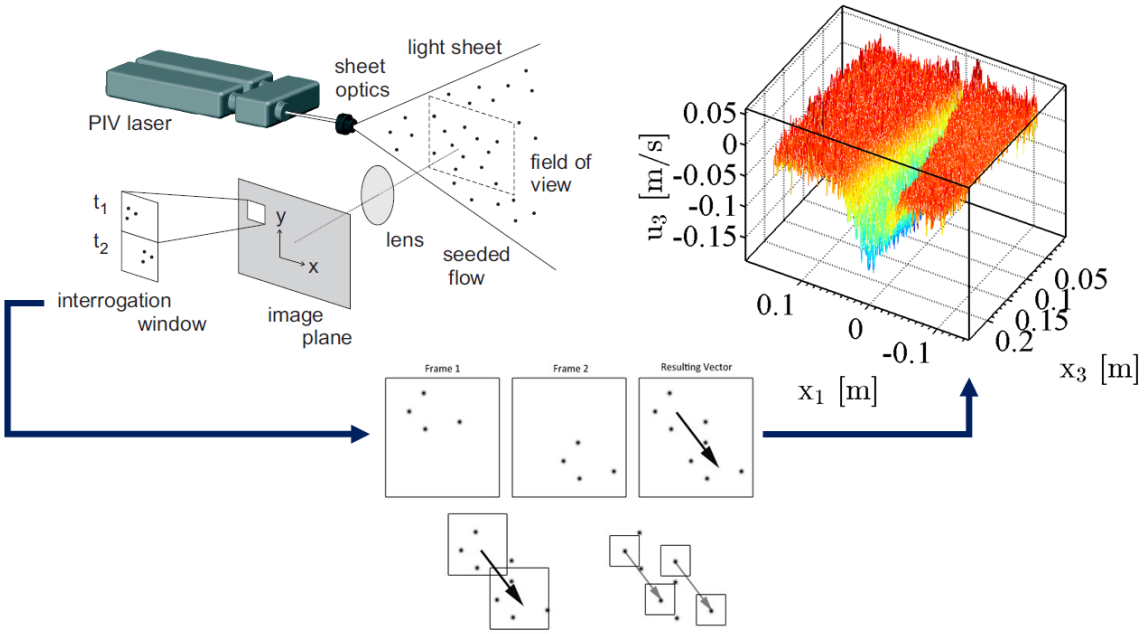

Figure 3.6: PIV laser technique. Acquisition, particle tracking, interrogation window refinement and velocity processing (from left to right)

to provide useful guidelines to produce optimal measurements in the post-processing phase. In detail, these rules are as follows:

First, the number of particles, N_I, in the interrogation region shall be greater than ten:

$$N_I > 10 \tag{3.91}$$

The particle image displacement, Δx, shall be less than $1/4^{\text{th}}$ of the width of the interrogation window, d_I:

$$\mid \Delta x \mid < \frac{1}{4} d_I \tag{3.92}$$

The out-of-plane displacement, Δz, shall be less than $1/4^{\text{th}}$ the thickness of the light sheet, Δz_0:

$$| \Delta z | < \frac{1}{4} \Delta z_0 \tag{3.93}$$

Local variation of displacements shall be less than $1/20^{\text{th}}$ the size of the interrogation region:

$$M | \Delta u | \cdot \Delta t < \frac{1}{20} d_I \tag{3.94}$$

where M represent the magnification parameter given as the size of the camera chip, L_{chip}, to the size of the field of view $L_{F.O.V.}$ ratio:

$$M = \frac{L_{chip}}{L_{F.O.V.}} \tag{3.95}$$

Based on Eqs. 3.3.4 to 3.3.4, preliminary tests were performed in intervals. An initial interrogation window of 32×32 pixels was picked with the intent to provide enough spatial resolution and less variation in displacements within each region. However, these large windows showed to be inaccurate in determining velocity in turbulent regions (e.g. fully-buoyant region) since the region's resultant vector is given by the average velocity within the same region.

A second step consisted in determining the particle size and the seeding concentration. Polystyrene Latex Spheres (PSL) seeding particles were selected based on successful use in previous saltwater modeling experiments by Siang [109], and due to neutral buoyancy, good reflectivity, and a short velocity response time. Particles with an average diameter of 50 μm were used for the unconfined plume and tests for the sloped fires (Chapter 5). An important condition required for the seeding density is that of a large number of particles in the interrogation region for

a higher SNR. However, an exceeding particle concentration causes the so-called speckle regime. At this point, the interference between elastic light constructive and destructive reflected waves produces the appearance of unreal particles. The speckle regime is similar to a saturation point—as one reaches this stage, the increase of particle density becomes unnoticeable, and the particle locations are no longer detectable. Therefore, additional testing was performed to determine the optimum particle concentration—gradually increasing the concentration (mg/L), images were taken and analyzed, until it was found that beyond 60 mg/L diminishing effects occurred. Eventually, for 50μm particles, a concentration of 60 mg/L was selected, and in order to minimize the attenuation of light (given the high seeding density), a 20 mg/L concentration was set in the fresh water tank.

An additional requirement to avoid the "peak-locking" effect, which consists into the lack of peak intensity interpolation when the particle image (d_τ) is less than 1, is that to obtain an apparent size of the particles, d_τ, of about 2 pixels at least. Olsen and Adrian [58] provide an estimate of the apparent size as:

$$d_\tau = \sqrt{(M \cdot d_p)^2 + (d_{diff})^2} \tag{3.96}$$

where d_p represents the seeding particle diameter, and, the diffraction term, d_{diff}, is given as

$$d_{diff} = 2.44(f/\#) \cdot (1 + M) \cdot \lambda \tag{3.97}$$

where $f/\#$ is the camera focal ratio, or equivalently, the focal length to the entrance pupil diameter ratio, while λ represents the incident light wavelength. Calculations gave an estimate for the particle size of about 15 μm ($\approx$2 pixels).

Once the parameters above were defined, the time interval, dt, between the two frames was set such that the maximum particle displacement (Eq. 3.3.4) was about a $1/4^{\text{th}}$ of d_I, that is 8 pixels (for d_I=32×32 px) and able to provide the order of magnitude of the expected maximum velocity. Therefore, in a refinement loop process, dt was progressively reduced until the maximum velocity did not exhibit any change. As found in the past, tracking buoyant flows using PIV showed to be a difficult task because of the large range of velocities in the field of view. Depending on the specific goal to achieve, different dt can be used to describe the same flow at different level of investigation. Particularly, for the unconfined plume two field of view (see Table 3.2) were related to two different time interval—the larger (F.O.V=350 mm) required a time frame of 50 ms, in order to produce the same order of magnitude of the centerline velocities found for a F.O.V of 50 mm with dt=5.5 ms. The major difference between the two scenarios was the level of accuracy achieved for the velocity range—the cross-correlation processing can still provide vectors with enough accuracy for slow moving flow with a short dt, but it cannot produce any realistic vectors with a long dt.

Chapter 4: Highly-Resolved Measurements of Turbulent Transport in an Unconfined Plume

4.1 Introduction

4.1.1 Saltwater Plume Dynamics

The study of turbulent buoyant plumes is a common denominator for research associated with different branches of science and engineering, ranging from natural phenomena such as volcano eruptions and deep-sea "black smokers", to engineering applications such as cooling towers and fire protection systems [48]. The fundamental mechanics of of such flows is mostly known and already applied, but it still under investigation for several reasons. First, transition of the flow, from laminar to fully turbulent, is encountered at the base of the plume, usually within a few inlet diameters from the source. Once turbulent, plumes are characterized by large-scale vorticity created as a result of buoyancy and shear forces arising from the interaction of the jet with the ambient fluid [49]. The transition from a jet-like to a fully buoyant plume starts concurrently with flow instabilities at the interface between

the saltwater source and the fresh water due to their density difference (see Fig. 4.1).

Currently, the nature of these instabilities is still under investigation by many researchers [18, 20, 21] and a detailed description of their physics goes beyond the scope of this study. Nontheless, some general observations about the dynamics of the plume can still be drawn based on the analysis of the highly-resolved PLIF instantaneous images shown below (Figs. 4.1, 4.2, 4.3).

Supported by the observations of Cetegen [20] and Maragkos [49], the characteristic large scale, puffing motion of the saltwater plume (Fig. 4.1) is believed to originate from disturbances forming upstream, where the laminar flow is seen to breakdown (Fig. 4.1). The wavy motion (vorticity) downstream the injector (Fig. 4.1), caused by the shear at the interface between fresh water and saltwater flow, further grows downstream boosted by increasing velocity and density fluctuations. Periodically, these fluctuations develop at the smallest scales first, then grow in magnitude and eventually interact with developed large vortical structures moving downstream (Fig. 4.2). This staged process ends with the formation of larger ubiquitous mushroom-shaped spikes dominating the flow downstream, as shown in Figs. 4.2 and 4.3.

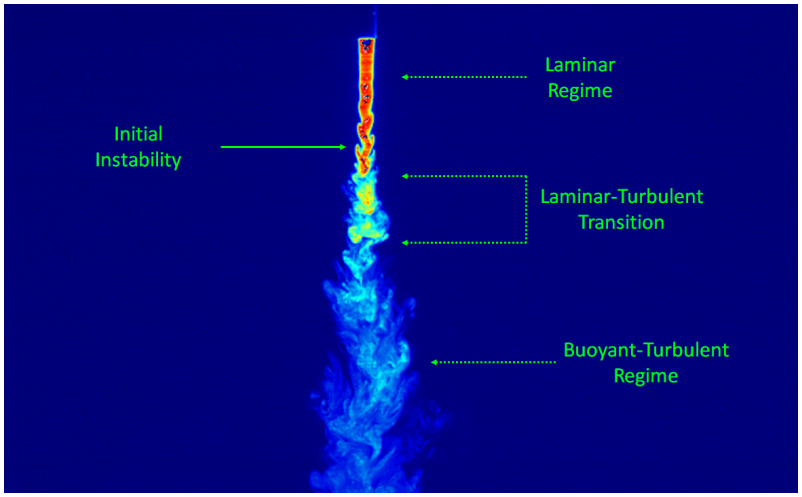

Figure 4.1: Initial instability generated at the interface between saltwater source and fresh water captured by a PLIF instantaneous image.

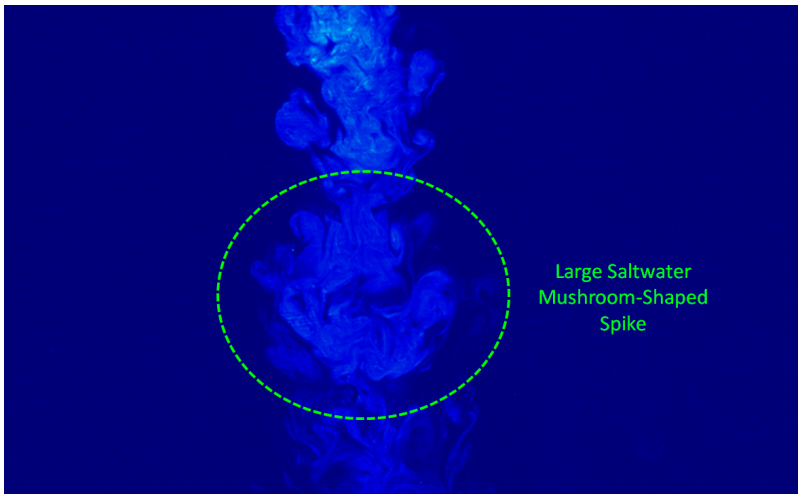

Figure 4.2: PLIF instantaneous image of a large-scale mushroom-shaped spike forming in the far-field of the plume. This is generated by the interaction of buoyancy forces with vorticity originated at the base of the plume.

Additionally, it is argued that secondary instabilities (Fig. 4.3) can arise from velocity shear at the interfaces of the injected flow [49]. The occurrence of these

secondary mechanisms leads to growing kinetic and scalar energies ("inverse" cascade) which fuel the large-scale vortices as the plume develops. The onset of these instabilities along with the presence of the buoyancy force generates the typical "puffing" motion of the plume [49], as shown in Figs. 4.2 and 4.3. Because of this motion, the characteristic vortex rings observed in Fig. 4.3 are caused by a mass of denser saltwater flow pushing upward through the overlying freshwater [19, 20]. In a highly turbulent environment, the primary instabilities causing the laminar to the turbulent transition of the plume are often seen to occur along with additional toroidal vortices that augment the entrainment of fresh fluid and make the puffing motion more irregular [20, 49]. Such a periodic motion is typical of buoyant plumes, and it results from a complex interaction between small and large-scale turbulent structures.

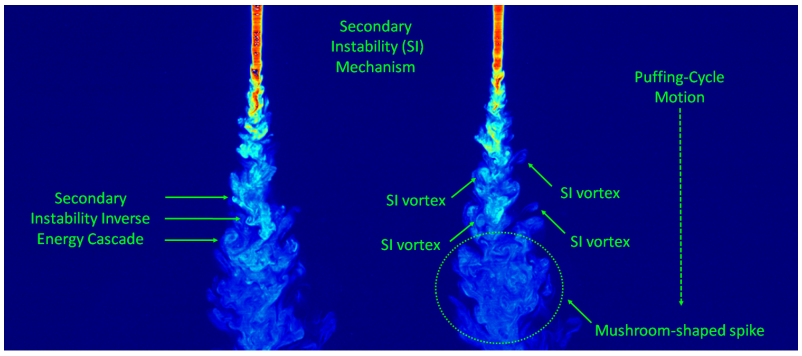

Figure 4.3: Secondary instability captured in two consecutive PLIF instantaneous frames: (left) the inverse energy cascade of kinetic and scalar energies characterizing the instability shown by means of three consecutive vortices of increasing sizes and increased energy as the plume moves downstream; (right) vortices appear on both interfaces of the plume, while the interaction of buoyancy and vorticity generates a characteristic "puffing" motion to the flow in the stream-wise direction.

The investigation of the mechanisms originating turbulence (primary and secondary instabilities) in fire-induced plumes is a complex matter and still the objective of a number of studies. Nonetheless, it is well established that scalar (species) and momentum (velocity) fields are coupled through the density [75], which depends on the mixture composition (mixture molecular weight) [49]. The buoyancy term in the momentum equations for a low-Mach flow is determined by the product of gravity and density. Given the mixing occurring because of the buoyant forcing, temperature difference (and density difference) couples the two sets of equations [49]. Such a coupling mechanism produces the so-called "buoyancy-generated turbulence" [21]. According to Tieszen *et al.* [22] experiments on helium plumes (simulating smoke plumes), the turbulent field of these flows originates from the aforementioned buoyancy-generated vorticity and the vorticity transport mechanisms which lead to entanglement of the vorticity itself [49].

4.1.2 Objective of the Investigation

In this study, we use the canonical free buoyant plume as a benchmark case to resolve transport characteristics at different spatial resolutions and provide useful guidelines for computational analysis of similar fire-induced flows. The harsh environment and large scale of real fires limits our ability to apply sensitive diagnostics in order to characterize flow features such as entrainment and turbulent mixing. The saltwater modeling technique provides an efficient representation of larger buoyant flows by injecting saltwater (denser) into fresh water (lighter), simulating turbu-

lent mixing some distance from the fire plume when appropriate Reynolds (Re) and Froude (Fr) numbers are reached [97]. The accuracy of this technique relies on the similarity between the dispersion mechanism of a saltwater source into fresh water and that of turbulent mixing of the hot gases generated by fire and fresh air. At these smaller scales, in a fresh water tank, we used Planar Laser Induced Fluorescence (PLIF) to determine the salt concentration as a scalar property of the buoyant plume. The concentration simulates the temperature of the hot gases, both being flow properties dominated by turbulent convective transport. Scaling of the saltwater plume, using non-dimensional analysis of the governing conservation equations, allows preservation of groups between the scale-model and full-scale plumes. We also use Particle Image Velocimetry (PIV) to determine velocities and turbulence statistics of the resulting flow. By maintaining turbulent flow in both full- and reduced-scale models, Re is preserved without having to be scaled as long as a reference velocity is defined. Dimensionless quantities therefore allow for easy comparison between various source strengths, spaces, and times. The use of different resolutions applied to a single or a set of images collected over time was intentionally designed to establish a method to experimentally probe the sub-grid resolution scales which are usually modeled for Computational Fluid Dynamics (CFD) simulations.

Figure 4.4 shows two instantaneous quantitative images (PLIF on the left, and PIV on the right) with a superimposed virtual grid consisting of pixelated windows of size L. Here, a visual comparison is made between a coarsened image resolution, obtained by averaging the single pixels binned within L, and the highest resolution

obtainable, represented by the single pixel within the same window. The information resulting from both the single-pixel and the pixel-averaged window represents a different level of accuracy attained for the statistics to estimate. In detail, Fig. 4.4 (left), shows an instantaneous PLIF analysis image of the density difference (θ_{sw}) under two different perspectives. The half plume on the left represents the superimposition of a grid with a 18×18 pixel resolution on top of the instantaneous image on the right which is averaged over the 324 pixels within the cell. The magnified contour image of the 18×18 single grid cell shows the actual density difference for a single pixel. The comparison between the single spatially-averaged cell and the corresponding close up showing resolution at a single pixel level demonstrates the depth and sensitivity of the resolved information with respect to the level of resolution. The same approach is applied to an instantaneous image of the PIV analysis, shown on Fig. 4.4 (right). The left half represents the raw PIV image, while the right half is the 6×6 pixel-averaged contour of the normalized stream-wise velocity, i.e. $|u_3|/U_0$. Here, U_0 represents the source-based characteristic velocity. A magnification of the 6×6 pixels interrogation window is also depicted on the bottom right.

Figure 4.4 shows how an adequate resolution can help to capture flow details that would otherwise be missed by simply averaging the information over the grid super-imposed on the interrogation window. Analogously, in the context of LES, an adequate mathematical model (e.g. Smagorinsky) can help to resolve those unclosed quantities associated with the very small scales (i.e. sub-grid scales, SGS) filtered out by the low-pass filter of LES. These modeled scales are then reintroduced to

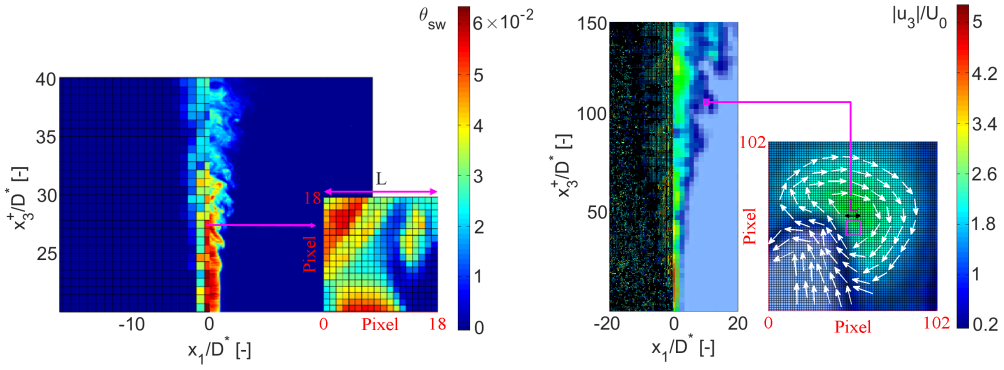

Figure 4.4: Sub-grid resolution of instantaneous PLIF- (left) and PIV-based (right) images with and without an overlaid virtual grid for spatial averaging. For both sets of measurements, the close up on the bottom right-hand side shows the resolution that can be obtained by single pixel resolution within the cell. The comparison between the pixel-averaged half image and the close up window of size L highlights a different level of accuracy attained for the estimated statistics.

close the system, and represent the influence of the SGS on the resolved field.

In this study, we aim to establish a cut-off length for the resolution, L, in order to obtain converged statistics within (i.e. at the subfilter resolution) and on (i.e. at the grid-resolved resolution) the interrogation window. A convenient way to express the size of the window (or resolution), L, is to use an integral length scale for the saltwater experiments as a common scaling factor (or reference length scale).

A characteristic length scale, D_T^*,

$$D_T^* = \left(\frac{\beta_T \dot{Q}}{\rho_0 c_p g^{1/2}} \right)^{2/5} \tag{4.1}$$

was originally introduced in fire research by Ma *et al.* [50] for grid sensitivity analysis assuming the burner diameter, D, is a fire characteristic length, L_T, for the definition of Q^* (see Eq. 3.11). In Eq. 4.1, ρ_0 is the density of the ambient fluid (i.e. air),

c_p its specific heat capacity, g is the gravitational acceleration, $\dot{Q}$ is the fire source strength and β_T is the volumetric thermal expansion coefficient of the air.

Based on the fire-saltwater analogy, the equivalent of D_T^* in the saltwater frame (denoted by subscripts $()_{sw}$) is:

$$D_{sw}^* = \left(\frac{\beta_{sw} \dot{m}_{salt}}{\rho_0 g^{1/2}} \right)^{2/5}, \tag{4.2}$$

with ρ_0 representing the water density, $\dot{m}_{salt}$ the salt release rate, and β_{sw} the density modification coefficient of saltwater, respectively. Here, the length scales in Eq. 4.2 use the virtual origin-corrected domain, i.e. (x_1, x_2, x_3^+).

The choice of the grid size to resolve the flow should reflect not only the impact of fire source dimension, but also the fire size. Indeed, D_T^* (Eq. 4.1) combines the impact from both burner diameter, D, and the fire size, Q^*, $D_T^* = D\,(Q^*)^{2/5}$. Hence, D_{sw}^* should be resolved for a proper scaling of the fire with saltwater modeling. Our measurements mostly focus on transport and mixing occurring in the fully-developed state of the buoyancy-dominated turbulent plume, occurring at $x_3 > 5L_M$ in the stream-wise direction [121]. Experiments using PIV and PLIF were performed separately on the free-plume scale model based on the use of one camera only, and the flow was characterized in terms of the stream-wise velocity u_3 and dispersion variable $\theta_{sw} = \beta_{sw} Y_{salt}$. Table 3.1 summarizes experimental configurations, initial flow conditions and characteristic length scales for the saltwater measurements. Based on previous work performed by Yao [94], the density modification coefficient (β_{sw}) was assumed to be 0.76 [94,97], and the salt mass fraction (Y_{salt}) was set to 0.13 for both PIV and PLIF measurements.

4.2 Results

4.2.1 Saltwater Modeling Technique Validation

The first set of analyses examined time-averaged quantities at the plume centerline and compared then with previous fire plume data [101] and a point-source model by Zukoski [31] (see Sec. 3.2.5). This showed that the measurements performed by means of saltwater modeling are in line with those obtained in real fire scenarios. Saltwater experiments are conducted in a canonical unconfined plume geometry. This is selected as the validation configuration for the quantitative saltwater modeling technique because it is a well-studied problem in fire research. Previous investigators have presented theoretical solutions of the plume characteristics in this fire configuration as well as extensive experimental data from actual fires for comparison. These previous studies provide a large body of data to validate the saltwater modeling measurements and the associated scaling theory [34, 101, 133, 135]. Flow visualization images of saltwater plumes are valuable for understanding the dispersion dynamics and mixing patterns in real fire plumes. Examples of quantitative instantaneous images from PLIF measurements are provided in Fig. 4.5. The dimensionless density difference, θ_{sw}, represents $\beta_{sw} Y_{salt}$ for the saltwater plume (the equivalent of $\beta_T \Delta T$ for the fire plume). The PLIF saltwater images in Fig. 4.5 are inverted for easy comparison with real fire plumes. If there is no specific indication, the PLIF saltwater images presented in this study are inverted (e.g. body force,

$f_3 = g$).

The plume dynamics where the plume transitions from laminar flow to turbulent flow are clearly observed in Fig. 4.5 (left). Although these plumes are turbulent, the initial state of the plumes is laminar. For example, the Reynolds number based on the injector diameter is only $Re_D \sim 600$ (Table 3.1). The buckling of the plume and associated vortex structure responsible for entrainment and dispersion is also apparent in the instantaneous images, which are consistent with expectations from a real fire [120, 121]. The visualization of the instantaneous images also shows how fresh water is entrained into the plume and mixed with the saltwater. The ambient fresh water penetrates into the saltwater plume by entrainment and dilutes the saltwater concentration along the flow path. The turbulent vortex structure is larger in the far-field area than that in the region near the injector. The vortices continue to grow as the flow convects from the source. In the following section, quantitative measurements of stream-wise velocity u_3 from PIV data and θ_{sw} from PLIF saltwater images are compared with actual fire data, theory, and thermal plume data to validate the quantitative saltwater modeling technique. The two cases (i.e., Case 1 and 2) presented here refer to the coarse field of view (F.O.V.) of 350 mm (see Table 3.2) which frames the whole plume, whereas the more refined F.O.V. = 50 mm is used for Sec. 4.3. This is in order to only evaluate the centerline mean values for both characteristic scales. In fact, compared to the F.O.V. = 50 mm used for the resolution study (Sec. 4.3), a coarser F.O.V. still provided accurate estimates of velocity and density difference for the mean flow at the centerline, but at expense of the details for the turbulence statistics (later investigated in Sec. 4.3).

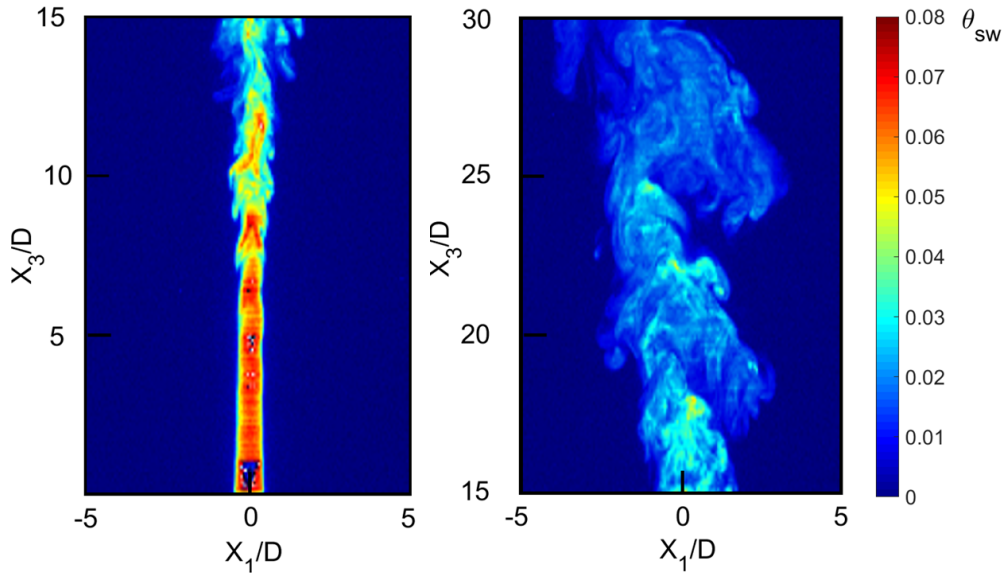

Figure 4.5: Visualization of the density difference, θ_{sw}, for the unconfined saltwater plume captured by an instantaneous PLIF frame; near-field (left); far-field (right). Dimensionless stream-wise (x_3/D) and spanwise (x_1/D) coordinates are not corrected by the virtual origin, $(x_3)_0$, and normalized using the injector diameter, D, instead of the characteristic length, D^*.

For convenience, in this section the subscript $()_{sw}$ was dropped to indicate the characteristic length, D^*_{sw}, and both plume characteristic scales used for the comparison were time-averaged over a set of 500 images, unless otherwise noted. Expression of scaling laws are made possible by normalizing both independent variables and stream-wise coordinate values with the source length scale, D^* (e.g. $u_3^* = u_3/\left[(gD^*)^{1/2}(m^*_{sw})^{1/3}\right]$). Thereby, x_3^+/D^* is used throughout the remaining parts of this chapter (except for the analysis of the kinetic energy).

PIV *Measurements Validation*

In this study, PIV saltwater results are used to characterize the plume velocity at the centerline for validation and comparison. In this regard, the plume conditions

assumed for the all sets of measurements demonstrate consistency with the theoretical model proposed by Zukoski [31] when compared with his $(-1/3)$ velocity power-law model (or point-source theory).

Two different buoyancy sources (see Tables 3.1 and 3.2) are employed in the PIV validation/characterization experiments to both validate the scaling theory, and show consistency of different sets of measurements with the Zukoski's model [31]. Figure 4.6 shows clear agreement between the data resulting from the PIV measurements and the point-source plume theory (dotted line). Similarly, McCaffrey's

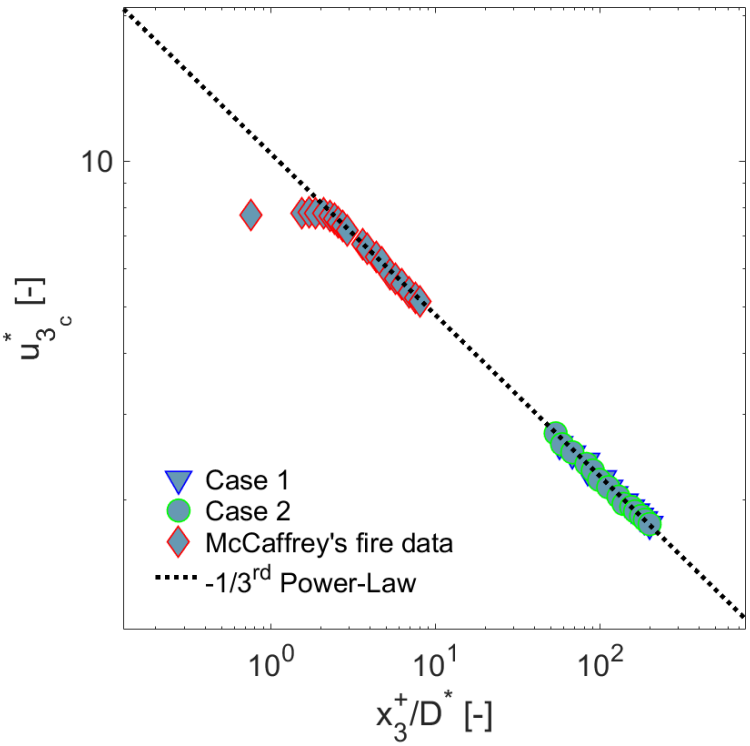

Figure 4.6: Dimensionless stream-wise velocity, $u^*_{3_c}$, distribution along the dimensionless plume centerline, x_3^+/D^*; (▽) saltwater $u^*_{3_c}$ measurements for Case 1; (●) saltwater $u^*_{3_c}$ measurements for Case 2; (◆) McCaffrey's $u^*_{3_c}$ fire data [101]; (·····) $(-1/3^{rd})$ power-law.

plume velocity measurements [101] are plotted in Fig. 4.6 to show the difference between the strength of saltwater plumes compared to fire plumes. As displayed in Fig. 4.6, the dimensionless velocity, $u^*_{3_c}$, in a saltwater plume is much smaller than that in a real fire plume. The virtual origins of the saltwater plumes based on the centerline velocity measurements are $(x_3)_0 = -15.3$ mm for Case 1, and $(x_3)_0 = -16.2$ mm for Case 2, while the velocity-based virtual origin of McCaffrey's experiments is $(x_3)_0 = 298$ mm. Note that virtual origins based on velocity measurements are different from values based on the dimensionless density difference. The virtual origin is used to correlate data in terms of point-source plume theory and will depend on the flow quantity measured. Similar values for the virtual origin for two different run of experiments were found and a general agreement of the measurements was seen. Eventually, the agreement of velocity measurements, fire data and point-source theory shows the ability of using saltwater modeling to study fire-induced flows.

PLIF *Measurements Validation*

Measurements in the unconfined saltwater plumes are compared with point-source plume theory from Zukoski [31] and fire data from McCaffrey [101] to validate the implementation of the PLIF saltwater results. Measurements correspond to the unconfined plume Case 1 and Case 2 (see Table 3.1).

From PLIF measurements it is found the scalar field, that is the average density difference at the centerline $\theta^*_{sw_c}$, follow the $(-5/3)$ power-law of the turbulent point-source plume theory (Fig. 4.7). In addition, McCaffrey's plume measurements for pool fires [101] are displayed to show the relative strength of the saltwater

plume compared to fire plumes. The dimensionless density difference for saltwater was much smaller than $\theta^*_{T_c}$ measured for fires, indicating the saltwater plumes investigated were relatively weak compared to fire plumes. The virtual origins

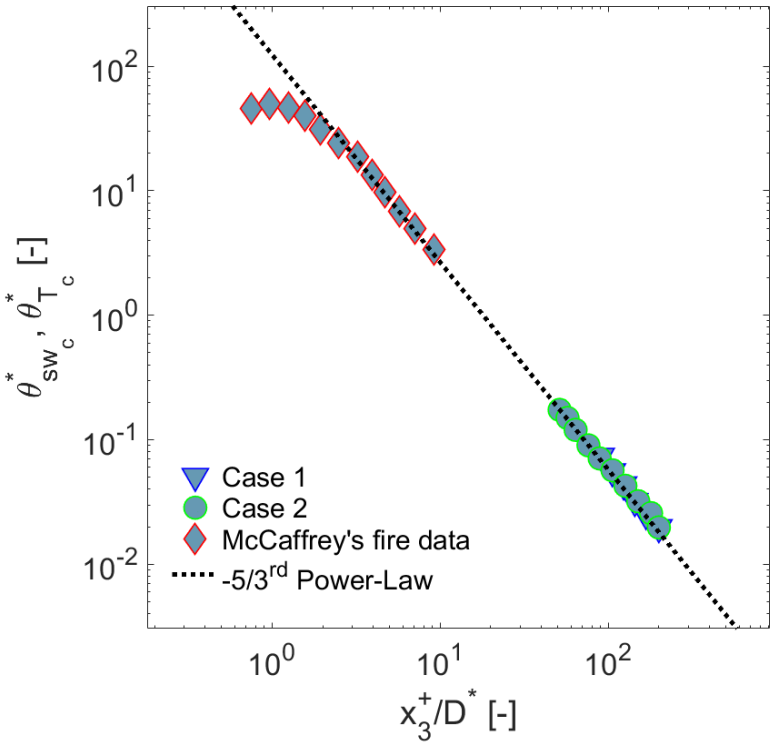

Figure 4.7: Dimensionless density difference, $\theta^*_{sw_c}$, distribution along the dimensionless plume centerline, x_3^+/D^*; (▽) θ^*_{sw} measurements for Case 1; (●) θ^*_{sw} measurements for Case 2; (◆) θ^*_T fire data from McCaffrey [101]; (·····) $(-5/3^{rd})$ power-law.

of the saltwater plumes based on the scalar measurements are $(x_3)_0 = -12.3$ mm and $(x_3)_0 = -18.7$ mm for Case 1 and Case 2, respectively. Note that a negative value represents a point below the injector outlet point at $x_3 = 0$. The virtual origin of McCaffrey's experiments is $(x_3)_0 = -89.7$ mm. The virtual origin, $(x_3)_0$, is calculated by the method of Heskestad [123]. Despite the lower density difference

of the saltwater plumes relative to actual fire plumes, the decay of the dimensionless density difference obeys the familiar $(-5/3)$ power law obtained from turbulent point-source plume theory.

4.2.2 Characterization of the Plume Region

4.2.2.1 Cross-Stream Distribution of Velocity and Density Difference

Evaluation of cross-stream distributions of dimensionless density difference, θ^*_{sw}, and the dimensionless velocity components, u^*_3 (stream-wise) and u^*_1 (span-wise), for Case 1 (see Table 3.1) yields more information about unconfined plume dynamics in the fully buoyant region (i.e., $x_3/L_M > 5$). The results for this analysis are reported in Figs. 4.8, 4.9 and 4.10. First, the cross-stream profiles of θ^*_{sw} are shown in Fig. 4.8 for locations at $x^+_3/D^* = 56, 75, 93$, in order to illustrate the flow dynamics in the far-field. Then, for the same locations, the two components of the velocity field are analyzed (Figs. 4.9, 4.10).

In Fig. 4.8, two instantaneous profiles for θ^*_{sw} (green and magenta lines) are extracted from two instantaneous frames respectively and, for each x^+_3/D^* assumed, compared with those obtained by averaging all frames (blue line). The density difference-based plume half-width, b_θ, is also determined by means of the cross-stream profiles and displayed in the same figure (blue dotted line in Fig. 4.8): by definition, b_θ (see Section 3.2.5) represents the cross-stream location from the centerline where $\theta^*_{sw} = \theta^*_{sw_c}/e$. Similarly, based on the stream-wise velocity u^*_3 distribution, a velocity-based plume half-width b_u (originally introduced as b in Section

3.2.5) can be estimated at the distance from the centerline where $u_3^* = u_{3_c}^*/e$. The ratio between b_u and b_θ is β (see Section 3.2.5), and its value, usually slightly below unity [31, 48], indicates a faster spread rate (i.e. $db/d(x_3^+)$) of θ_{sw}^* than u_3^*.

Figure 4.8 illustrates a symmetrical spatial distribution of the mean θ_{sw}^* profiles. These show a typical Gaussian behavior; however, the instantaneous realizations appear as denticulate top-hats with associated large gradients at the edges. Such a result is consistent with Zukoski's postulate that the mean Gaussian profile is realized from the instantaneous turbulent top-hat behavior [31, 97]. The instantaneous radial profiles clearly show that the instantaneous θ_{sw}^* can be much higher than the mean value. In addition, the left-hand side of Fig. 4.8 illustrates that b_θ (blue dotted line in Fig. 4.8) increases linearly along the distance from the plume source, as expected [31].

As discussed in Chapter 3, a linear relationship exists between the plume half-width, b_u, and the entrainment constant, α, as shown in Eq. 3.75. For this analysis, the entrainment coefficient α, measured from the saltwater experiments, was estimated to be $\sim$0.13, and $\beta = b_u/b_\theta = 0.956$, in good agreement with Zukoski's results [31]. The value found for α matches that estimated by Alpert [133] and agrees well with both Zukoski's $\alpha = 0.11$ [31], and Papanicolaou and List's $\alpha = 0.12$ [48]. Eventually, both velocity- and density difference-based plume half-widths are compared in the stream-wise direction x_3^+/D^*, as shown in Fig. 4.11.

In the past, several experimental and numerical studies on free-shear flows (buoyant jets, plumes) [31, 48, 133] showed that [31, 48, 133] the Gaussian distribution well represents the cross-stream behavior of both u_3 velocity and temperature. Saltwater

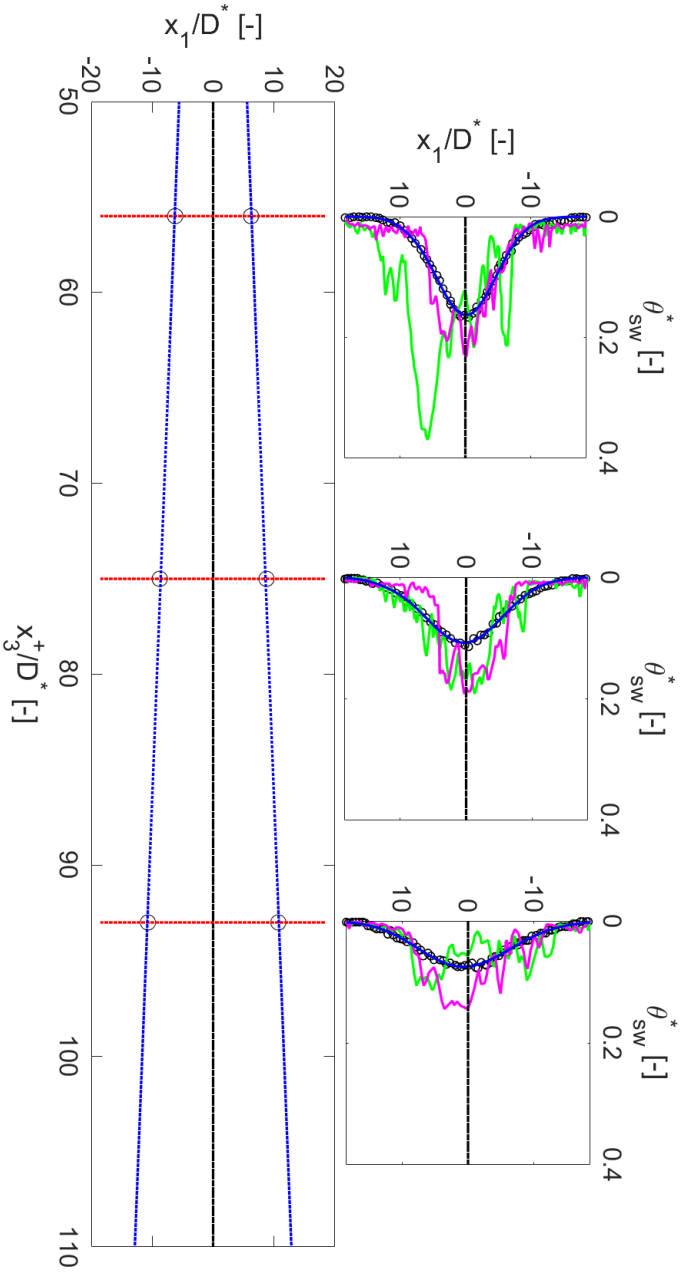

Figure 4.8: Visualization of the time-averaged dimensionless density difference of an unconfined saltwater plume in the fully buoyant region. Image time-averaged θ^*_{sw} saltwater data (O) for locations at $x_3^+/D^* = 56$, 75 and 93 (·····, left) show a Gaussian behavior (——, right), while instantaneous profiles (—— and ——, right) for θ^*_{sw}, extracted from two PLIF single frames, exhibit a turbulent top-hat behavior as observed by Zukoski [31] (right). The plume half-width b_θ (·····) is obtained by a linear fit to the data (O) corresponding to the $\theta^*_{sw} = \theta^*_{sw_c}/e$ condition on the Gaussian curves.

measurements of the unconfined plume also clearly reveal that the Gaussian profile is a superior fit to the data, as shown in Fig. 4.9. From the analysis of the u_3^* profiles taken in the stream-wise direction, it can be observed that increasing the elevation from $x_3^+/D^* = 56$ to $x_3^+/D^* = 93$, the Gaussian distribution decreases due to the entrainment and mixing that the front of the plume experiences as it moves forward in the fresh water. This is also consistent with the results discussed in Fig. 4.6, where the velocity at the centerline decreases as $(x_3^+/D^*)^{-1/3}$.

Generally, accurate results for the cross-stream velocities are important for unconfined turbulent plumes because entrainment controls mixing, a very important parameter for pool fires where combustion processes are mixing-controlled. Therefore, an analysis of the spanwise dimensionless velocity component, u_1^*, is also performed. In Fig. 4.10, saltwater measurement cross-stream profiles for u_1^* are displayed for $x_3^+/D^* = 56$, 75 and 93, respectively. First, as a consequence of mass conservation, a decrease in the stream-wise velocity u_3^* (Fig. 4.9) corresponds to a decrease in the cross-stream velocity, u_1^*, as we move downstream from $x_3^+/D^* = 56$ to $x_3^+/D^* = 93$.

A more detailed analysis of the cross-stream velocity profiles as a function of x_1/D^* shows that the plume experiences a small outflow near the centerline and a large inflow far away from it. The decay in the centerline velocity with downstream distance, x_3^+/D^*, is associated with a decrease in the axial volume flux for a small control volume (CV) centered at the centerline axis. The excess volume exits the lateral sides of the CV resulting in a lateral outflow near the plume centerline. However, for a CV extending to large x_1/D^* and therefore encompassing almost the

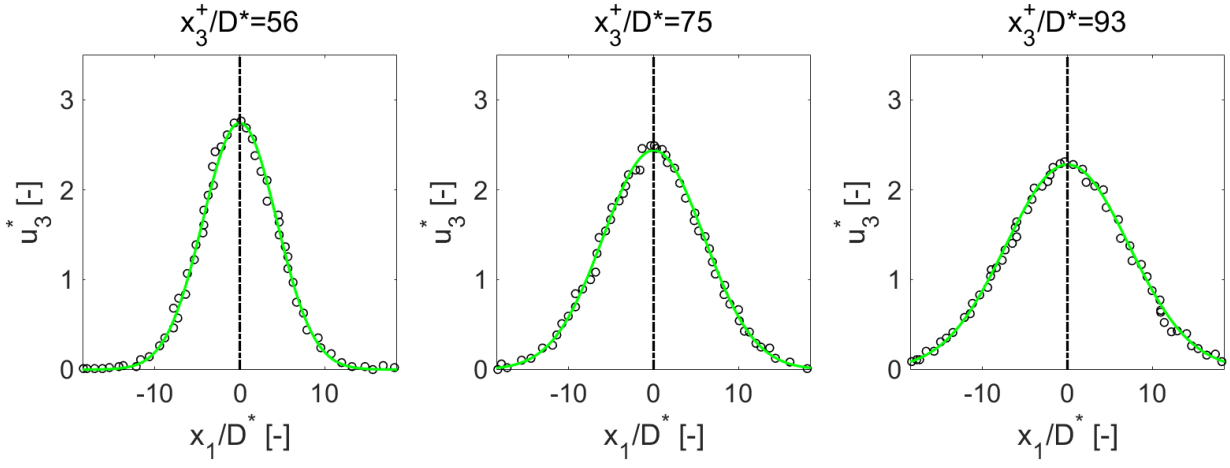

Figure 4.9: Cross-stream distribution of stream-wise velocity component, u_3^*, at $x_3^+/D^* = 56$, 75 and 93 above the source; saltwater measurement points (O); Gaussian fit to data (——); centerline (- · - · -).

entire plume (as displayed in Fig. 4.10), a net increase in the axial volume flux is associated with a lateral volume flux pointing inward. This larger inflow is responsible for greater mixing in the plume.

More insight into the flow dynamics is gleaned by analyzing the time-based probability density function of the dimensionless density difference, $\mathrm{PDF}_t(\theta_{sw}^*)$. The PDFs of θ_{sw}^* at selected stream-wise and spanwise locations are provided in Fig. 4.12. The stream-wise positions assumed are the same as those previously discussed in Figs. 4.8, 4.9, and 4.10 (i.e. $x_3^+/D^* = 56, 75, 93$). At each elevation, the center of the plume ($x_1/b_\theta \sim 0$), and positions near the middle of the plume ($x_1/b_\theta \sim 0.5$) and edge of the plume ($x_1/b_\theta \sim 1$) are selected. Information can be obtained from these PDFs for understanding the flow mixing characteristics at these locations. A few

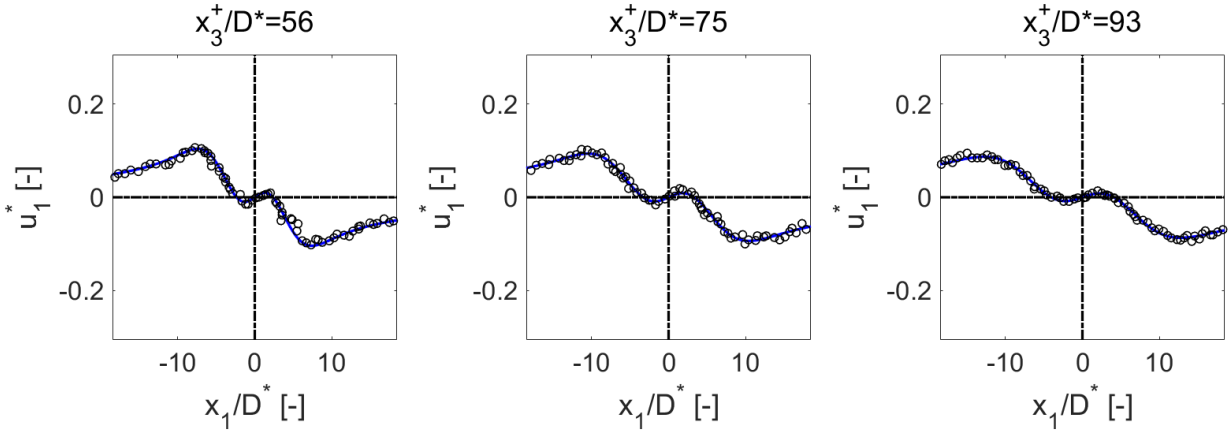

Figure 4.10: Cross-stream distribution of spanwise velocity component, u_1^*, at $x_3^+/D^* = 56$, 75 and 93 above the source; saltwater measurement points (O); fit to data (——); centerline (-·-·-).

general observations can be made from this set of PDFs. The information inferred from Fig. 4.12 represents a qualitative analysis of the mixing and the entrainment occurring along the dimensionless cross-stream axis of the plume, x_1/b_θ. The centerline PDFs show the fresh water penetration (i.e. $\theta_{sw}^* \sim 0$) to the centerline at all of the elevations, x_3^+/D^*, providing quantitative data consistent with the significant unmixedness and large scale turbulence observed in the instantaneous PLIF images (Fig. 4.5 (right)). In detail, as we move downstream from $x_3^+/D^* = 56$ to $x_3^+/D^* = 93$ along the centerline (i.e., x_1/b_θ =0), one may observe that the amount of fresh water penetrating in the inner plume increases. At the same time, this behavior is reflected in the PDFs near the plume edge (i.e., $x_1/b_\theta \sim 1$), which, not infrequently, have occurrences of mass concentrations near the peak centerline value.

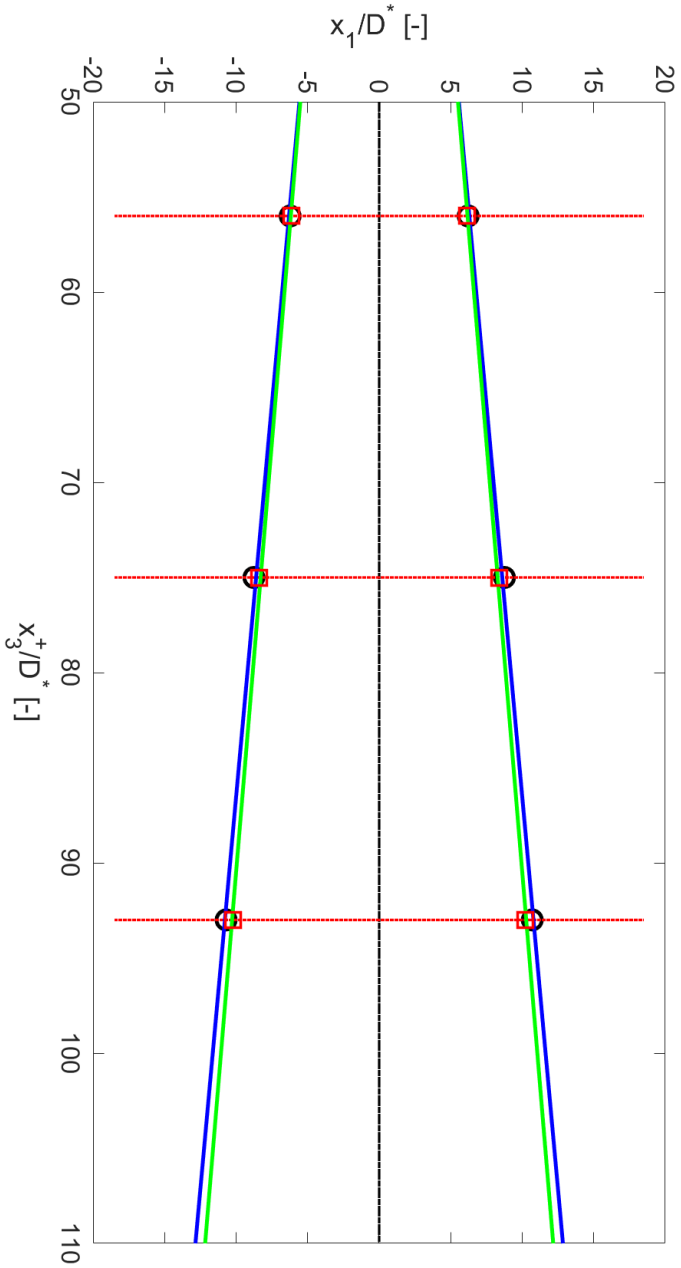

Figure 4.11: Comparison between velocity-based, b_u, and density difference-based, b_θ, half-plume width in the fully buoyant region of the plume; linear fit for b_u (—); linear fit for b_θ (—); saltwater measured point at $u_3^*/u_{3_c}^* = 1/e$ (□); saltwater measured point at $\theta_{sw}^*/\theta_{sw_c}^* = 1/e$ (○); centerline (- · - · -).

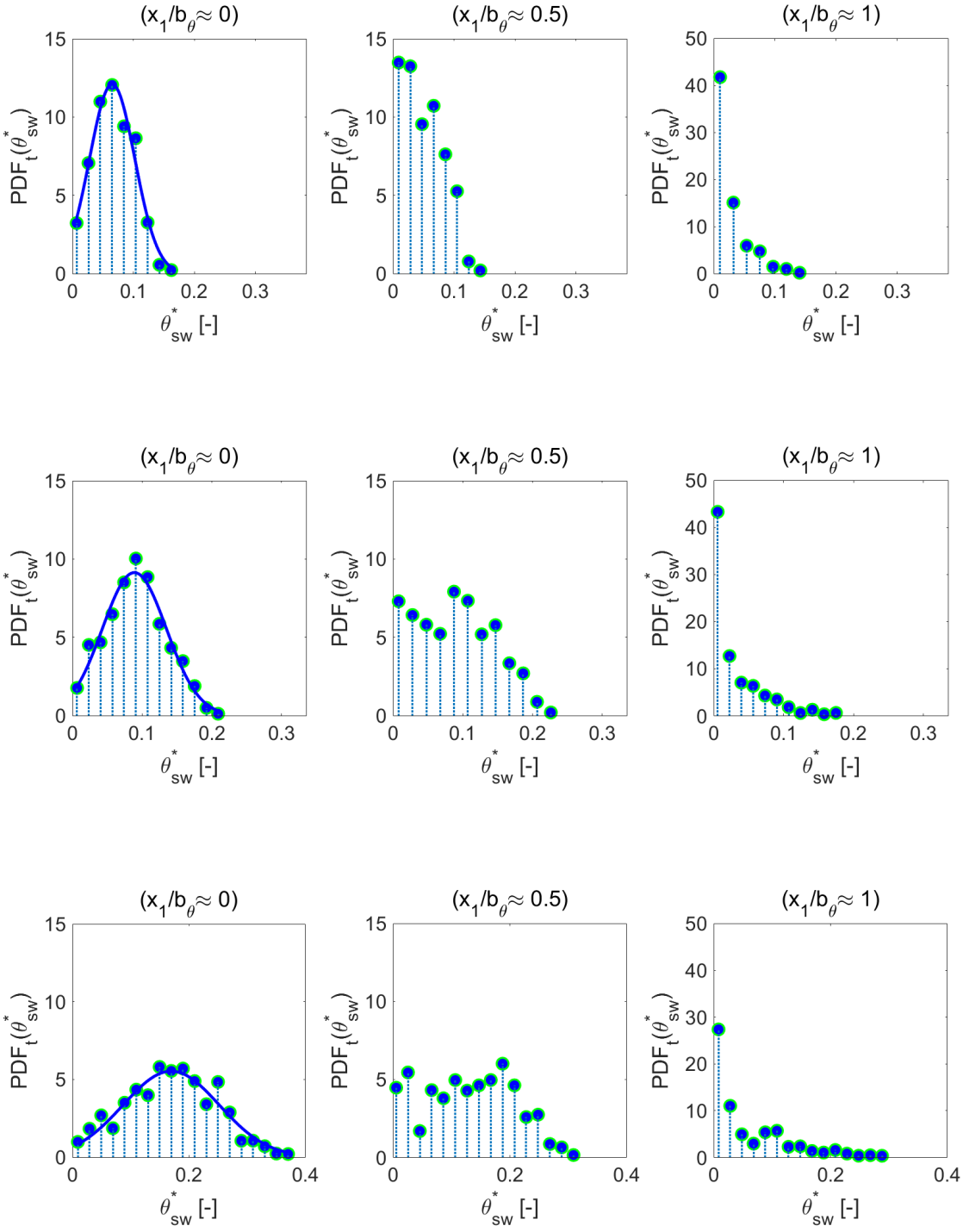

Figure 4.12: $\mathrm{PDF}_t(\theta^*_{sw})$, for x_1/b_θ =0, 0.5, 1 cross-stream locations, at $x_3^+/D^* = 56$, 75 and 93 above the source.

These two observations are complementary and consistent with the physics of the plume: moving downstream in the flow, the increasing size of the vortical structures embrace a larger portion of the plume along x_1/b_θ, thus transporting a larger amount of fresh water inside, while moving denser fluid from the centerline towards the edge of the plume. On the other hand, a double peak behavior is observed in the mid-plume region suggesting strong fluctuations as we move upstream the flow, and weak mixing between the saltwater plume and the entrained fresh water.

4.3 Resolution Study

The idea of a "resolution study" for highly-resolved PIV and PLIF images was inspired by the mean filtering concept used by both LES simulations and image processing. Figure 4.4, earlier discussed, illustrates the concept of image filtering for a given resolution using a virtual pixelated grid. However, note that, compared to a computational grid-refinement process, the filtering used for this study works inversely, as a coarsening process applied to a highly-resolved set of images. This approach is due to both time-consuming experimental setup and time-consuming design phase of the experiments for a single set of PIV or PLIF measurements. If on one side the time spent on the setup/design can be compared to the computational cost of a very refined computational mesh run, on the other, PIV and PLIF measurements have the advantage to provide real information from physical phenomena. Apart from the intrinsic differences, one of the common goals between experimental and computational environments is the investigation of the spatial and temporal

resolutions at which the flow fully resolves.

In LES, the low-pass filtering operation can be applied to a spatial and temporal field, for instance $\phi(\boldsymbol{x}, t)$, such that the LES filter operation may be spatial, temporal, or both. The resolved part $\bar{\phi}(\boldsymbol{x}, t)$ of the space-time variable $\phi(\boldsymbol{x}, t)$ is defined formally by the relation [55]

$$\bar{\phi}(\boldsymbol{x}, t) = \frac{1}{\Delta} \int_{-\infty}^{\infty} \int_{-\infty}^{\infty} \phi(\boldsymbol{\xi}, \tau) \cdot \mathbf{G}(\frac{\boldsymbol{x} - \boldsymbol{\xi}}{\Delta}, t - \tau) d\boldsymbol{\xi} d\tau, \tag{4.3}$$

where $\boldsymbol{\xi}$ and τ are dummy variables in Eq. 4.3, while $\mathbf{G}$ represents a convolution kernel which is characteristic of the filter used (spatial or temporal), and associated with the cut-off scale in space and/or time, (Δ) and (τ_c), respectively.

The resolved field (Eq. 4.3) can be written as a convolution operation:

$$\bar{\phi} = \mathbf{G} \cdot \phi \tag{4.4}$$

Based on Eqs. 4.3 and 4.4, scales smaller than Δ and τ_c are filtered out from $\bar{\phi}$. Using this definition, any field ϕ may be split up into a filtered and sub-filtered (Eq. 4.6) portion, as

$$\phi = \bar{\phi} + \phi^{'}, \tag{4.5}$$

where

$$\phi^{'} = (1 - \mathbf{G}) \cdot \phi \tag{4.6}$$

Similarly, in PIV and PLIF image processing, the mean filtering process (assumed as spatial) acts as a low-pass frequency filter by reducing the spatial intensity derivatives present in the image. Usually, such a process is indispensable to drastically reduce the noise (consisting in a number of high-frequency phenomena) caused

by the equipment (e.g. camera) or by the specific fixtures interacting with measurement tools (e.g. laser light illuminating the saltwater injector).

For instance, the mean filtering (referred to as "mask") used by the software DaVis by LaVision during saltwater measurements works by simply replacing each pixel value in the image with the mean ("average") value of its neighbors, including itself. This has the effect of eliminating pixel values which are unrepresentative of their surroundings (noise), such as those due to non-uniformities in the tracked flow (e.g. particle clusters for PIV, or non-uniformly dispersed dye for PLIF), or laser back-reflected light from surfaces in the experimental setup (e.g. a metal injector). Mean filtering is usually thought of as a convolution filter. Like other convolutions, it is based around a kernel (or interrogation window), which represents the shape and size of the neighborhood to be sampled when calculating the desired mean. The size of a kernel can vary from small (such as a 3×3 pixel square kernel) to larger kernels for more severe smoothing, depending on the level of noise (mostly related to the accuracy of the experimental setup).

The results presented in the following sections were obtained assuming the similarity about the mean filtering (here assumed as a spatial low-pass filter), which is common for both computational and experimental environments. Quantification of the ability of the measurement resolution to capture both grid-resolved (or filtered) and the subfilter (single-pixel related) characteristics (velocity and density difference) was approached in the following manner. A virtual interrogation window of varying size L (or dimensionless resolution L/D^*) was centered at various heights along the plume centerline. Then, statistical moments (mean, variance)

were computed for both time-averaged and instantaneous PIV and PLIF images, in order to analyze the response of the scales of interest (mean, turbulence intensities, kinetic energy) to a change of the spatial filter, L/D^*.

By varying the resolution, first and second order statistical moments based on the binned data points (pixels within the window) were used to quantify the flow characteristic mean and fluctuations resulting from the grid-resolved and subfilter scales, respectively, as shown in detail in Secs. 4.3.1, 4.3.2 and 4.3.3. In this analysis, steps of $0.1D^* \sim 150\mu$m for the resolution L were assumed until converged statistics were obtained. The results were then displayed in such a way that the threshold resolution for converged statistics could be clearly identified and substantial differences with coarser resolutions could be highlighetd.

4.3.1 First Order Statistics

Investigation of the effect of image resolution first started with the analysis of dimensionless values $\widetilde{\overline{\theta^*_{sw_c}}}$ and $\widetilde{\overline{u^*_{3_c}}}$. Both these scales represent the spatial average ($\widetilde{\ }$) over the interrogation window (L/D^*) of the mean flow (i.e. time-averaged over the image ensemble, ($\overline{\ }$)) characteristics of the plume, θ^*_{sw} and u^*_3 (Eqs. 4.7).

$$\widetilde{\overline{\theta^*_{sw_c}}} = \frac{1}{V_\Omega}\int_\Omega \overline{\theta^*_{sw_i}}(\boldsymbol{x})d\boldsymbol{x} \quad ; \quad \widetilde{\overline{u^*_{3_c}}} = \frac{1}{V_\Omega}\int_\Omega \overline{u^*_{3_i}}(\boldsymbol{x})d\boldsymbol{x} \tag{4.7}$$

Here, Ω (with $\Omega \subset \mathbb{R}^2$, and $\mathbb{R}^2$ representing the laser sheet plane) is assumed as the spatial domain of area V_Ω, which varies in size with respect to the resolution L/D^*. In Eq. 4.7, the single-pixel area (constant) is represented by vector $\mathbf{x}$ and the mean flow value measured at the single-pixel is denoted by subscript ($_i$). Note

that the ($\tilde{}$) notation was used to denote the spatial average (or spatial filter), as it is usually done in the context of turbulence analyses associated with LES. Also note that the spatial filter, L/D^*, was applied to time-averaged images resulting from the ensemble of 500 instantaneous frames. The operations of spatial filtering (L/D^*) and time-averaging (or ensemble averaging) were found to commute with negligible impact on the results. This, similar to the computational environment [66], was found to be consistent with the fact that the filter used, either spatial or temporal, was linear (i.e. mean or average). Last, even if the whole resolution study focused on values estimated at the centerline, the subscript ($_c$) used for the scales in Eqs. 4.7 was kept for clarity in illustrating the results of the second order statistics (Sec. 4.3.2).

The results are shown along the virtual origin corrected and normalized streamwise direction, i.e. x_3^+/D^*, in Figs. 4.13 and 4.14. As shown in Fig. 4.13, by increasing the imaging resolution, $\widetilde{\overline{\theta^*_{sw_c}}}$ at the centerline converges to higher values. Nevertheless, two distinct regions of the plume were identified where the effects of the spatial filtering are different—the laminar-to-turbulent transition region (near-field) and the fully buoyant region (far-field).

In Fig. 4.13, the results are displayed on both regular (above) and logarithmic (below) scale for convenience. As one may observe from Fig. 4.13 (above), the fully buoyant region of the plume ($x_3^+/D^* > 53$) barely shows the difference of $\widetilde{\overline{\theta^*_{sw_c}}}$ at increasing L/D^*, when compared to that of the near-field (grey-shaded region), where the effects of the resolution are more pronounced. On the contrary, the logarithmic scale (below) highlights a clearer trend for the curves with respect to the resolution

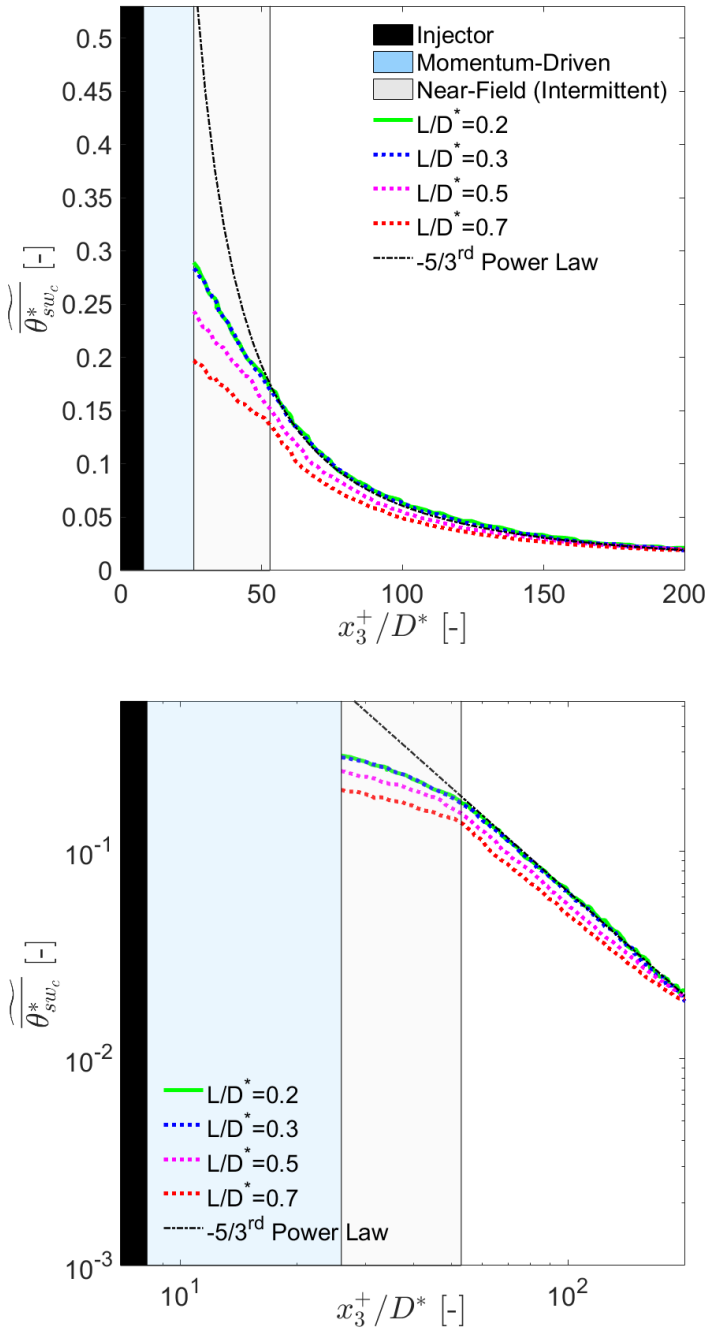

Figure 4.13: Dimensionless mean flow density difference, $\widetilde{\overline{\theta^*_{sw_c}}}$, spatially averaged for different interrogation window size resolutions, L/D^*. The increasing resolution causes the centerline values to converge beyond $L/D^* = 0.3$.

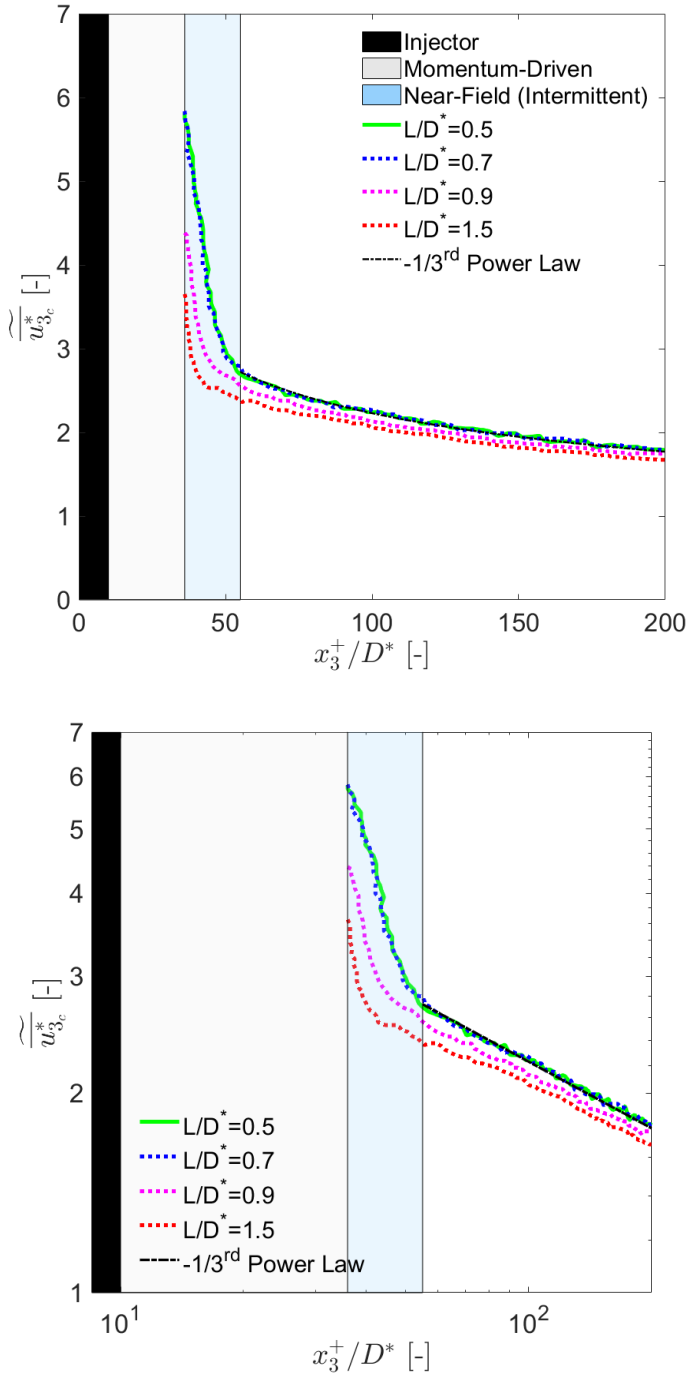

Figure 4.14: Dimensionless mean flow stream-wise velocity, $\widetilde{\overline{u_{3_c}^*}}$, spatially averaged for different interrogation window size resolutions, L/D^*. The increasing resolution causes the centerline values to converge beyond $L/D^* = 0.7$.

L/D^*—the far-field shows little, but still visible variation between the curves with respect to the spatial filter until a resolution of $L/D^* = 0.3$, where data starts to collapse. On the other hand, the near-field shows a marked difference between low and high resolutions, which eventually reduces to less than 2% between $L/D^* = 0.3$ and $L/D^* = 0.2$.

The analysis reveals that beyond a 0.45 mm ($0.3D^*$) resolution window size, data converge in both near- and far-field regions. This observation is important in that it identifies a threshold for the mean density difference which can be used as a probe and possibly refining the current LES scales being used for modeling fire plumes.

The evaluation of these results requires an analysis accounting for both the effects of the resolution technique employed and the physical interpretation of the information resulting from the pixel sample binned within the interrogation window (depending on its location along the plume centerline). Before convergence, larger differences were observed in $\widetilde{\overline{\theta^*_{sw_c}}}$ by increasing L/D^* from 0.7 to 0.3 in the near-field, while negligible differences were found in the fully buoyant region of the plume.

The reason for higher values of $\widetilde{\overline{\theta^*_{sw_c}}}$ at higher resolutions could be found in the number of pixels included in the interrogation window and used for the averaging of the scale. In fact, a higher resolution (low L/D^*) corresponds to a reduced number of pixels binned within the interrogation window. Given the high level of unmixedness (increasing fluctuations) in the transitional region of the plume, single pixels are characterized by a very heterogeneous distribution of $\overline{\theta^*_{sw_i}}$ (see Eq. 4.7). On the other hand, in the far-field, this distribution appears more homogeneous due to the

enhanced mixing (stable fluctuations) between saltwater and ambient fresh water.

Two sample distributions of the single pixels binned within a given interrogation window, $\overline{\theta^*_{sw_i}}(\boldsymbol{x})$ (see Eqs. 4.7), are shown in Fig. 4.15. One sample of 30×30 pixels ($L/D^* = 0.5$) was extracted from the near-field (i.e. intermittent region, Fig. 4.15, left) at $x_3^+/D^* = 40$, and one of equal size from the far-field (i.e. fully-buoyant region, Fig. 4.15, right) at $x_3^+/D^* = 100$ for comparison. In the near-field, by increasing the resolution from 30 pixels (0.75 mm, magenta square) to 12 pixels (0.3 mm, blue square), the standard deviation of $\overline{\theta^*_{sw_i}}$ tends to decrease and their spatial average over the window narrows down to the highest value characteristic of the centerline. In other words, as the resolution is increased the window filters out the effects of the turbulent mixing off of the centerline, and provides a converging value for the spatial mean. This should explain the higher $\widetilde{\overline{\theta^*_{sw_c}}}$ found at higher resolutions and the pronounced difference between $L/D^* = 0.7$ and $L/D^* = 0.3$ found in the near-field. On the other hand, in the far-field, the enhanced mixing in the buoyant region generates a more homogeneous distribution of $\overline{\theta^*_{sw_i}}$ (Fig. 4.15, right), thus having a lower standard deviation and a lower mean in the window compared to the near-field (Fig. 4.15, left). Therefore, as we increase the resolution from $L/D^* = 0.5$ to 0.2 at $x_3^+/D^* = 100$, the impact on the spatial average (Eqs. 4.7) is minimal. As we move further downstream, this filtering process yields similar values for all resolutions given the well-mixed flow. All of this should provide a reasonable explanation for the small differences found at increasing resolutions L/D^* in the fully-buoyant region.

The same approach was used for the dimensionless stream-wise velocity, $\widetilde{\overline{u^*_{3_c}}}$,

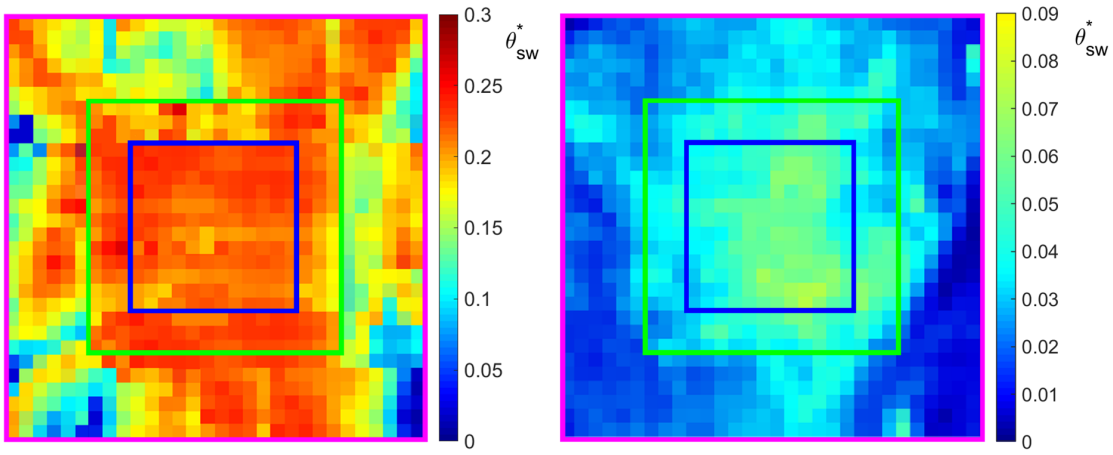

Figure 4.15: Highly resolved, time-averaged PLIF image. On the left, virtual interrogation windows of $L/D^* = 0.2$ (blue square), $L/D^* = 0.3$ (green square) and $L/D^* = 0.5$ (magenta square) are centered at $x_3^+/D^* = 40$ (intermittent region). The spatial mean computed over the pixeled grid of $L/D^* = 0.2$ equals (with a confidence interval less than 1%) the mean at $L/D^* = 0.3$, whereas at resolution $L/D^* = 0.5$ the spatial mean lowers because of the contribution of parcels of fluid at lower concentration framed by the larger interrogation window. On the right, the same virtual windows are centered at $x_3^+/D^* = 100$ (buoyant region), but the well-mixed flow generates similar spatial averages for each resolution.

analyzed along the centerline, x_3^+/D^*, at different resolutions, L/D^* (Fig. 4.14). A similar behavior to that of the $\widetilde{\overline{\theta^*_{sw_c}}}$ curves was observed for the velocity profiles at increasing resolutions, and a distinctive effect of the interrogation window was found between the intermittent and the fully-buoyant region. Larger variations between the spatial averages computed over incresing window resolutions were found in the intermittent region, while negligible differences were noticed in the self-similar region. This is primarily due to the high level of unmixedness resulting from the laminar-to-turbulent transition and the increasingly enhanced mixing in the fully-buoyant region as similarly discussed for the density variable. The explanation in

the next paragraph is in support of this observation.

Figure 4.16 shows the time-averaged PIV velocity field for the $\overline{u_{3_c}}$ component, displayed in the $x_1/D - x_3/D$ plane. This contour results from a field of view (F.O.V.) of 350 mm for the camera setup (Table 3.2), coarser than the F.O.V. of 50 mm used for this resolution study. Recall that the spatial resolution for a given F.O.V. equals the magnification of the camera ($M = \frac{L_{F.O.V.}}{L_{chip}}$, see Eq. 3.3.4) times the size of one pixel of the camera sensor, that is 7.4 μm. Given the camera sensor size, $L_{chip} = 15.15$ mm, the resolution for F.O.V. = 350 mm is about 170 μm, whereas it goes up to 25 μm for F.O.V. = 50 mm. Therefore, the F.O.V.=350 mm is still able to accurately capture the centerline velocity, but not all the details resulting from a F.O.V. = 50 mm, as previously shown in Fig. 4.15 for $\overline{\widetilde{\theta^*_{sw_c}}}$. Nonetheless, even if at a coarser resolution, the contour still provides evidence of how the spatial filter works at varying resolutions. As shown in Fig. 4.16, a window of $L/D^* = 1$ (1.5 mm) and one of $L/D^* = 0.7$ (~ 1 mm) within it are centered at the same locations assumed for the $\overline{\widetilde{\theta^*_{sw_c}}}$ analysis. As one may see, by shifting from a resolution of $L/D^* = 1$ to $L/D^* = 0.7$ in the intermittent region, the window filters out part of the range of velocities framed by $L/D^* = 1$, thus providing a different spatial average at that point. On the other hand, the same shift in resolution at $x_3/D \sim 30$ (i.e. $x_3^+/D^* = 100$) shows no evident change. A smaller effect is observed for the spatial average that reduces moving further downstream. Using a F.O.V. = 50 mm (higher resolution setup), the effects discussed so far are more accurately estimated, but the baseline conclusions stay the same. Eventually, when the resolution exceeds $L/D^* = 0.7$ (~ 1 mm), the spatial average locally converges in both the intermit-

tent and far-field. This provides a limit for the size of the interrogation window that is needed for a correct interpretation of the velocity data, and that could be potentially used to provide guidelines or probe LES simulations.

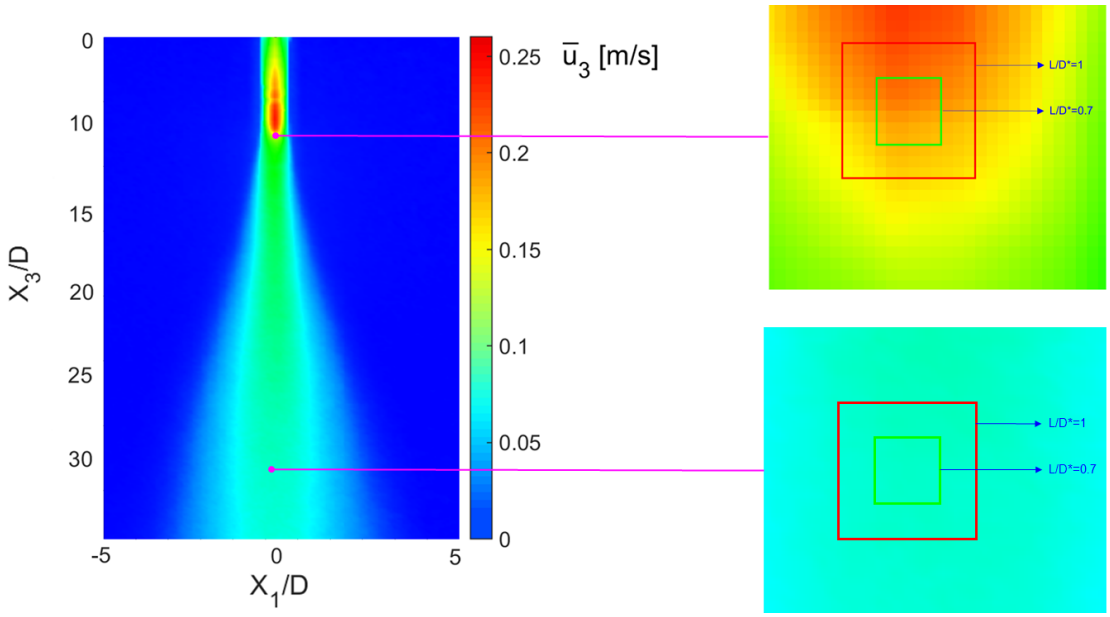

Figure 4.16: Time-averaged velocity field for the entire plume at 350 mm field of view (F.O.V.). On the right hand side two close ups at $x_3/D \sim 11$ (i.e. $x_3^+/D^* = 40$; above) and $x_3/D \sim 30$ (i.e. $x_3^+/D^* = 100$; below) are analyzed: resolution windows of $L/D^* = 1$ (red square) and $L/D^* = 0.7$ (green square) are centered at these two locations. The two windows/resolutions centered at $x_3/D \sim 11$ shows a sensitive change in the pixel contour binned within each one, while no change is found at $x_3/D \sim 30$.

As one may observe from Fig. 4.14, the higher the resolution, the higher the velocity value which is resolved at a given stream-wise location. This is caused by the filter (i.e. window) which cuts out the effects of the smaller scales and produces a converged mean value, representative of the window scale. This is particularly evident in the intermittent region and it reduces as the mixing increases in the far-

field.

The discussion so far shows the function of a virtual interrogation window and how it can be reasonably compared to that of a computational grid. A numerical mesh grid is usually refined until results converge, similar to the resolution window, with the advantage of physical information provided from real measurements. However, it must be noted that in order to provide reliable results, enough resolution of the camera should be considered in the setup phase. Major considerations on the flow behavior can still be drawn using coarser resolutions as long as they are designed ahead to obtain estimates in the region of interest, but highly-resolved images are important when dealing with turbulent statistics.

Depending on the interest in validating/resolving computational analysis targeting the plume centerline velocity, or the temperature or both, the minimum size of the interrogation window (resolution) should be $L = 0.7D^*$, $L = 0.3D^*$, or the smallest between the two resolutions able to resolve both fields, respectively.

An additional note must be spent here regarding the difference between the resolution for converged velocity and the one for converged density difference. The highest resolution ($L = 0.3D^*$) found for the scalar can be easily explained based on the scale at which the turbulent mixing occurs, that is the molecular scale. In fact, because of the chemical bonds established between the Rh-6G dye tracer and the salt dissolved into the source, the fluorescence exhibited by the plume when illuminated by the laser allows tracing the salt concentration down to the molecular level. This explains the presence of sharper concentration gradients observed in Fig. 4.15 even at sufficiently high resolutions for which velocity already converged,

and thereby the need to filter them out by decreasing L/D^* (increasing resolution).

For PIV measurements, particles size of 50μm (d_p), chosen based on the Stokes'law ($Re_{d_p} \lessapprox 1$) to track the flow motion with no particle buoyant or inertial effects, only enables to characterize velocities at larger scales (bulk motion, advection) than molecular scales (diffusion).

In addition to all this, the use of nonlinear filters in image pre-processing, which provided local velocity by averaging near values in locations where no particle displacement could be tracked, likely caused the smoother velocity gradients observed in PIV and the consequent coarser resolution ($L = 0.7D^*$) for converged statistics.

4.3.2 Second Order Statistics

This section focuses on the estimate of turbulence intensities for dimensionless density difference, θ^*_{sw}, and streamwise velocity, u^*_3, scales of the plume at varying resolutions, L/D^*. Spatial (interrogation window) and temporal (image ensemble) filters were both applied to PIV and PLIF single-frames to determine a measure of the turbulence intensity along the centerline axis, x^+_3/D^*. In the literature, this turbulence property is conventionally defined as the fluctuation of a particular scale (dimensionless θ^*_{sw} and u^*_3 in this study) with respect to the mean flow (time-averaged) at the centerline [14, 37, 47, 48, 94, 95]. As shown in the following sections, the turbulence was found to scale with the mean flow as predicted by dimensional analysis and self-similarity [48] for any L/D^* examined in this study. However,

the investigation conducted for the resolution revealed that only beyond a given resolution L/D^* (threshold resolution), the interrogation window spatially filtered the measurements provided resolved centerline fluctuations (turbulence intensity) for axial velocity and concentration.

4.3.2.1 Turbulent Intensities

The goal for this analysis was to determine the largest interrogation window L/D^* to span over, in order to resolve the turbulence intensity for dimensionless velocity and concentration, respectively. By progressively scaling up the spatial resolution of the images, the turbulence intensity was computed using the window-based statistics and the results obtained in Sec. 4.3.1 for the first order statistics analysis. This coarsening process was applied to each set of spatially, highly-resolved images (velocity and concentration) until determining the size of the interrogation window enabling convergency of the turbulence intensity of the flow. The details for this investigation are described in the following paragraphs.

For each single-frame of the images set, the spatial average for both dimensionless scales (Eqs. 4.8) was computed using the single-pixel values (subscript $_i$) framed by the window. At a given resolution L/D^*, the same equations used for the first order statistics (Eqs. 4.7) were employed for the spatial average, by replacing the time-averaged values, $\overline{\theta^*_{sw_i}}(\boldsymbol{x})$ and $\overline{u^*_{3_i}}(\boldsymbol{x})$ in Eqs. 4.7, with instantaneous single-pixel values, $\theta^*_{sw_i}(\boldsymbol{x},t)$ and $u^*_{3_i}(\boldsymbol{x},t)$.

$$\widetilde{\theta^*_{sw}}(t) = \frac{1}{V_\Omega}\int_\Omega \theta^*_{sw_i}(\boldsymbol{x},t)d\boldsymbol{x} \quad ; \quad \widetilde{u^*_3}(t) = \frac{1}{V_\Omega}\int_\Omega u^*_{3_i}(\boldsymbol{x},t)d\boldsymbol{x} \tag{4.8}$$

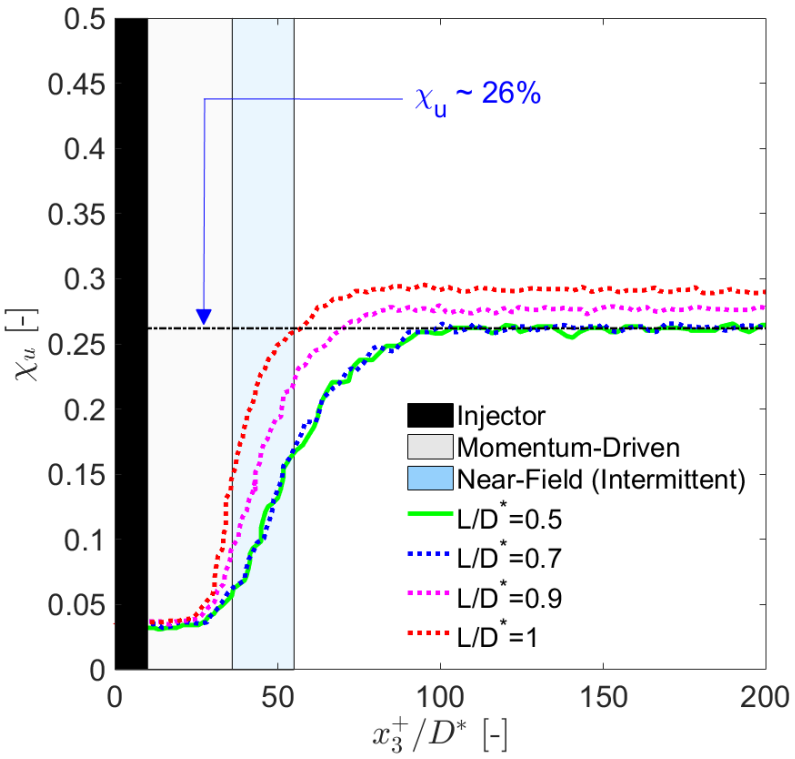

Figure 4.17: Dimensionless streamwise velocity turbulence intensity, χ_u, along the centerline axis, x_3^+/D^*, at different spatial resolutions, L/D^*. At $L/D^* = 0.7$ the turbulence intensities are fully resolved and attain a plateau corresponding to $\sim 26\%$ at ~ 25 diameters from the injection point.

In Eqs. 4.8, both $\theta^*_{sw_i}(\boldsymbol{x}, t)$ and $u^*_{3_i}(\boldsymbol{x}, t)$ were extracted from a single-pixel $(\boldsymbol{x})$, binned within the virtual window, L/D^*, locally overlaid on top of the instantaneous frame (t).

In order to quantify the magnitude of the fluctuation (turbulence intensity) at a given resolution, the ensemble average of the spatially-averaged scales (Eqs. 4.8) was first estimated as in Eqs. 4.9, and the standard deviation was then computed

according to Eqs. 4.10 and 4.11.

$$\overline{\widetilde{\theta^*_{sw}}} = \frac{1}{N_{frames}} \sum_{n=1}^{N_{frames}} \widetilde{\theta^*_{sw_n}}(t) \quad ; \quad \overline{\widetilde{u^*_3}} = \frac{1}{N_{frames}} \sum_{n=1}^{N_{frames}} \widetilde{u^*_{3_n}}(t) \tag{4.9}$$

In Eqs. 4.9, 4.10 and 4.11, the symbol ($^-$) represents the ensemble average over the set of 500 instantaneous images ($n = 1, ..., N_{frames}$). Also, as one may note, $\overline{\widetilde{\theta^*_{sw}}}$ and $\overline{\widetilde{u^*_3}}$ in Eqs. 4.9 are approximately equivalent to $\overline{\widetilde{\theta^*_{sw_c}}}$ and $\overline{\widetilde{u^*_{3_c}}}$ in Eqs. 4.7, given the linearity of the spatial and temporal filters applied (see comments regarding Eqs. 4.7 in Sec. 4.3.1). In Eqs. 4.10 and 4.11, the Bessel's correction (i.e., $N_{frames} - 1$) was used to correct possible bias in the fluctuations, but no large difference was found using N_{frames} instead of $N_{frames} - 1$.

$$\sigma_\theta = \sqrt{\frac{1}{N_{frames}} \sum_{n=1}^{N_{frames}} \left(\widetilde{\theta^*_{sw_n}}(t) - \overline{\widetilde{\theta^*_{sw}}} \right)^2} \tag{4.10}$$

$$\sigma_u = \sqrt{\frac{1}{N_{frames}} \sum_{n=1}^{N_{frames}} \left(\widetilde{u^*_{3_n}}(t) - \overline{\widetilde{u^*_3}} \right)^2} \tag{4.11}$$

Eventually, the turbulence intensities for the dimensionless scales, θ^*_{sw} and u^*_3, were estimated dividing the standard deviations σ_θ and σ_u (Eqs. 4.10 and 4.11) by their respective time-independent first statistical moments, $\overline{\widetilde{\theta^*_{sw_c}}}$ and $\overline{\widetilde{u^*_{3_c}}}$ (Eqs. 4.7), as shown in Eqs. 4.12:

$$\chi_\theta = \frac{\sigma_\theta}{\overline{\widetilde{\theta^*_{sw_c}}}} \quad ; \quad \chi_u = \frac{\sigma_u}{\overline{\widetilde{u^*_{3_c}}}} \tag{4.12}$$

The results for this investigation are displayed in Figs. 4.18 and 4.17, where the statistics given above (from Eqs. 4.8 to Eqs. 4.12) were evaluated at different heights along the centerline, x_3^+/D^*.

From a preliminary analysis (Figs. 4.18, 4.17), the evolution along the central

axis of both the velocity (axial component) and the density difference turbulent intensities was found to be consistent with the results reported in a number of studies (experimental and numerical) [48, 59–63, 94, 122]. Figures 4.18 and 4.17 showed indeed the distributions comprised of two distinct regions for the turbulence intensity. The initial region, transitional from laminar to turbulent (or near-field), where the turbulence intensity increases, and a second, the fully-buoyant region (far-field), where the intensity values keep increasing and gradually attain a plateau.

Regarding this last aspect, it is well established that, in the far-field, the standard deviation of either the concentration (density difference) or the streamwise velocity for the mean (time-averaged) flow follow the same decay laws as their mean values along the centerline [48, 122]. This implies that the turbulent intensities, i.e. standard deviation normalized by the corresponding mean value, are constant along the axis.

The analysis to evaluate the effects of the resolution, L/D^*, was thereafter performed for both intensities, χ_u and χ_θ. Figure 4.17 shows the results obtained by measuring axial velocity turbulence intensity χ_u at the centerline locations by varying the filter resolution, L/D^*. At increasing resolutions, the intensity values progressively decreased, and $L = 0.7D^*$ ($\sim$ 1 mm) was observed to be the size of the window at which the flow resolved. Based on this, $L = 0.7D^*$ (Fig. 4.17) was considered as a threshold for the spatial resolution needed to obtain reliable estimates of velocity turbulence intensity, whereas the interval $L > 0.7D^*$ was assumed as compromising this reliability.

At $L = 0.7D^*$, where the flow is resolved, χ_u starts to increase from the

injection point, where its value is low, and reaches a plateau close to $\sim$ 26% at $\sim$ 25 diameters ($x_3^+/D^* \sim 100$). These numbers were in good agreement with Laser Doppler Velocimetry (LDV) tests performed by Papanicolaou *et al.* [48, 122] with turbulence intensity at the centerline of 25% at ~30 diameters from the injection point and the saltwater LDV measurements from Yao [94, 97] with a fluctuation of 21% at $x_3^+/D^* \sim 100$.

From Fig. 4.17, the development of the velocity turbulence intensity showed also a different sensitivity with respect to L/D^*, depending on the specific region of the plume (near-field or far-field). Turbulence intensity statistics were observed to converge for a resolution greater than $L/D^* = 0.7$ (see the results for $L/D^* = 0.5$ in Fig. 4.17), whereas the values found for coarser resolutions ($L/D^* = 0.9$ and $L/D^* = 1.5$ in Fig. 4.17) identified two regions when compared to those estimated at higher resolutions ($L/D^* \leq 0.7$)—one, corresponding to the near-field (transitional region), where larger differences were noted, and the other, the far-field, where those differences reduced. The likely reasons for this result were therefore investigated as follows.

Given the definition of χ_u (Eq. 4.12, right), the analysis started by looking separately at the effects of the resolution, L/D^*, on both σ_u and $\widetilde{\overline{u_{3_c}^*}}$, respectively the numerator and denominator of χ_u. The filtered (i.e. spatially-averaged) velocity fluctuation over time, $\left(\widetilde{u_{3_n}^*}(t) - \widetilde{\overline{u_3^*}}\right)$, embedded in the standard deviation of Eq. 4.11, and the filtered mean velocity, $\widetilde{\overline{u_{3_c}^*}}$ (Eq. 4.7, right), resulting from the first order statistics were the objective of this analysis. The observations inferred for

$\left(\widetilde{u^*_{3_n}}(t) - \overline{\widetilde{u^*_3}}\right)$ resulted from the resolution study of the spatially-filtered turbulent kinetic energy, $k_{t,filter}$, presented in the next section (Sec. 4.3.2.2). As later discussed and shown in Fig. 4.19 (left), the spatially-filtered turbulent kinetic energy, $k_{t,filter}$ (Eq. 4.17), was computed using the same fluctuation of the turbulence intensity (see $\left(\widetilde{u_{3_n}}(t) - \overline{\widetilde{u_3}}\right)$ in Eq. 4.17), with the exception of an additional energy component related to the spanwise velocity, u_1. However, assuming negligible contribution of the spanwise velocity compared to that of the streamwise component in the estimate of $k_{t,filter}$ at the centerline, the response of $k_{t,filter}$ to different resolutions L/D^* (Fig. 4.19, left) was thought to depend upon the $\left(\widetilde{u_{3_n}}(t) - \overline{\widetilde{u_3}}\right)$ fluctuation only.

As one may note from Fig. 4.19 (left), no relevant change of $k_{t,filter}$ (and therefore of the $\left(\widetilde{u_{3_n}}(t) - \overline{\widetilde{u_3}}\right)$ fluctuation) resulted by varying the resolution L/D^*. In addition, it should be noted that the $\left(\widetilde{u}_{3_n}(t) - \overline{\widetilde{u_3}}\right)$ fluctuation was generally small (i.e. <1), therefore the squared value, $\left(\widetilde{u}_{3_n}(t) - \overline{\widetilde{u_3}}\right)^2$, and the subsequent ensemble average, $\overline{\left(\widetilde{u_{3_n}}(t) - \overline{\widetilde{u_3}}\right)^2}$, assumed for $k_{t,filter}$ (Eq. 4.17) tended to flat the differences between the $\left(\widetilde{u}_{3_n}(t) - \overline{\widetilde{u_3}}\right)$ fluctuations estimated at each L/D^* (Figs. 4.19, left), whereas the square root in σ_u (Eqs. 4.11) tended to restore these original differences (Fig. 4.17). In light of this, we concluded that the different resolution sensitivity of the turbulence intensities observed in the near- and the far-field respectively (Fig. 4.17), was mostly linked to the response of $\overline{\widetilde{u^*_{3_c}}}$ (Eq. 4.7, right) to a change of resolution L/D^*. As shown in Fig. 4.14, higher resolutions corresponded to lower $\overline{\widetilde{u^*_{3_c}}}$ mean values, with larger differences between the curves in the near-field than those exhibited in the fully-buoyant region. This eventually explained the higher

turbulence intensities at lower resolutions and the different resolution sensitivity of the curves in the two distinct flow regions (see Fig. 4.17).

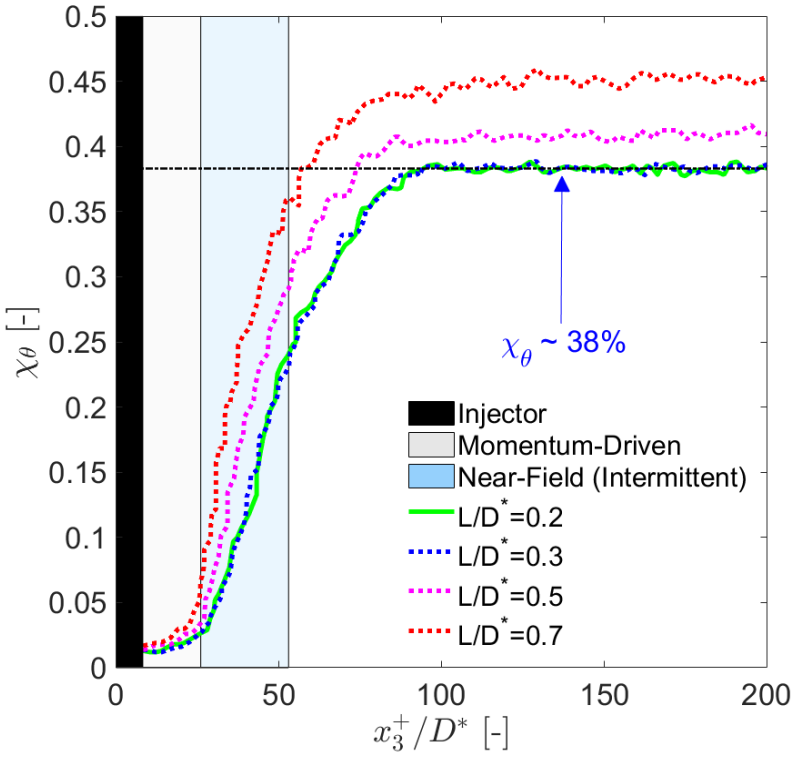

Figure 4.18: Dimensionless density difference turbulence intensity, χ_θ, along the centerline axis, x_3^+/D^*, at different spatial resolutions, L/D^*. At $L/D^* = 0.3$ the turbulence intensities are fully resolved and attain a plateau corresponding to $\sim 38\%$ at ~ 25 diameters from the injection point.

A similar analysis was conducted for the scalar turbulence intensities χ_θ and the results are shown in Fig. 4.18. The curves exhibited lower intensities at increasing resolutions as for the velocity field (Fig. 4.17) and collapsed at $L/D^* = 0.3$ (0.45 mm). At this resolution, the resolved turbulence intensity in the far-field attained a value of $\sim 38\%$ at the centerline. This value was found consistent with previous

results from PLIF saltwater experiments by Yao [94] ($\chi_\theta \sim 41\%$), matching with Shabbire and George's fire correlation prediction of 38% [95] and slightly lower than the results from Kostovinos [52] and Nakagome and Hirata [51], both in the range 43-44%. These preliminary considerations showed once again the ability of the salt-water modeling to closely simulate fire characteristics of interest.

As for the velocity intensities χ_u, the trend for χ_θ was thought to depend upon the influence of L/D^* on both σ_θ (Eq. 4.10) and $\overline{\widetilde{\theta^*_{sw_c}}}$ (Eqs. 4.7, left), respectively numerator and denominator of χ_θ. First, as earlier shown in Fig. 4.13, lower resolutions corresponded to lower mean values $\overline{\widetilde{\theta^*_{sw_c}}}$ caused by a larger number of pixels framed by larger windows L/D^* (see Fig. 4.15). As thoroughly discussed in Sec. 4.3.1, the higher unmixedness of the near-field produced lower $\overline{\widetilde{\theta^*_{sw_c}}}$ compared to those of the far-field due to the inhomogeneity of the $\overline{\theta^*_{sw_i}}$ single-pixel contour used for the statistics (refer to Sec. 4.3.1 for further details). Therefore, since $\chi_\theta \propto 1/\overline{\widetilde{\theta^*_{sw_c}}}$, lower $\overline{\widetilde{\theta^*_{sw_c}}}$, corresponding to coarser resolutions L/D^* (Fig. 4.13), were expected to give higher χ_θ intensities in a first approximation.

In order to complete the analysis for the influence of the resolution, additional information was extrapolated by investigating the effects of L/D^* on σ_θ (numerator of χ_θ in Eq. 4.12, left). As one may note, according to Eq. 4.10, σ_θ is based on the time fluctuation of the spatially-averaged concentration, $\left(\widetilde{\theta^*_{sw_n}}(t) - \overline{\widetilde{\theta^*_{sw}}}\right)$, which is directly affected by the resolution. Therefore, similarly to the approach adopted for χ_u, the effects of L/D^* on σ_θ were studied via the effects of L/D^* on $\left(\widetilde{\theta^*_{sw_n}}(t) - \overline{\widetilde{\theta^*_{sw}}}\right)$.

As later presented in Sec. 4.3.3, the spatially-averaged concentration estimated for each single-frame $\widetilde{\theta^*_{sw_n}}(t)$ was analyzed over time (t^*), in the far-field (Fig. 4.21,

left). The temporal PDFs of istantaneous $\widetilde{\theta^*_{sw_n}}(t)$ were collected at different resolutions and found to have larger standard deviations with respect of their mean at increasing L/D^* (Fig. 4.21, right). In summary, the larger the resolution of L/D^*, the larger the fluctuation of $\widetilde{\theta^*_{sw_n}}(t)$ with respect to the time-averaged mean (Fig. 4.21, left), i.e. larger $\left(\widetilde{\theta^*_{sw_n}}(t) - \overline{\widetilde{\theta^*_{sw}}}\right)$. This provides a full understanding of the net differences between the curves in Fig. 4.18 at increasing L/D^*, due to the effects of the resolution on both numerator, σ_θ, and denominator, $\overline{\widetilde{\theta^*_{sw_c}}}$, of the concentration turbulence intensity, χ_θ.

In this investigation, axial turbulence intensities for velocity and density difference were found to behave similarly over the abscissa x_3^+/D^* with an initial increase of the fluctuations χ_u and χ_θ, and the subsequent attainment of a plateau which identifies the turbulence intensity in the plume region [48]. Also, with respect to the interrogation window size, L/D^*, as the the resolution increased, both χ_u and χ_θ decreased until obtaining convergent values at $L/D^* = 0.3$ (~ 0.45 mm) for χ_θ and $L/D^* = 0.7$ (~ 1 mm) for χ_u, respectively (Figs. 4.17 and 4.18). Nonetheless, the influence of the resolution L/D^* on the curves highlighted some differences between χ_u and χ_θ, particularly in the plateau region, which deserved some more comments. The maximum difference measured between the curves (at the plateau) of χ_θ at the coarsest and the finest resolution was of $\sim 20\%$ (Fig. 4.18), whereas such difference reduced to $\sim 10\%$ when comparing the plateau of χ_u at $L/D^* = 0.7$ (finest) and that at $L/D^* = 1$ (coarsest) (Fig. 4.17). Given the slight differences observed for both $\overline{\widetilde{\theta^*_{sw_c}}}$ and $\overline{\widetilde{u^*_{3_c}}}$ curves when estimated at different L/D^* in the far-field (Figs. 4.13 and 4.14), the aformentioned differences of $\sim 20\%$ (for $\chi_\theta = \sigma_\theta/\overline{\widetilde{\theta^*_{sw_c}}}$) and $\sim 10\%$

(for $\chi_u = \sigma_u/\widetilde{\overline{u^*_{3_c}}}$) were thought to be more likely the result of the influence of L/D^* on their respective time fluctuations, $\left(\widetilde{\theta^*_{sw_n}}(t) - \widetilde{\overline{\theta^*_{sw}}}\right)$ and $\left(\widetilde{u^*_{3_n}}(t) - \widetilde{\overline{u^*_3}}\right)$, via σ_θ and σ_u respectively (see Eqs. 4.10 and 4.11).

On one hand, the analysis for $\widetilde{\theta^*_{sw}}(t)$ (single-frame, spatially-filtered concentration) over dimensionless time, t^*, later presented in Sec. 4.3.3 (where the subscript n for the single frame was dropped from $\widetilde{\theta^*_{sw_n}}(t)$ because unneeded for the temporal analysis), showed a clear trend for the time fluctuations, $\left(\widetilde{\theta^*_{sw_n}}(t) - \widetilde{\overline{\theta^*_{sw}}}\right)$, which increased at increasing L/D^*. On the other hand, the behavior for the velocity time fluctuations, $\left(\widetilde{u^*_{3_n}}(t) - \widetilde{\overline{u^*_3}}\right)$, was directly inferred from the response of $k_{t,filter} \propto \overline{\left(\widetilde{u_{3_n}}(t) - \widetilde{\overline{u_3}}\right)^2}$ (see Eq. 4.17) when varying the resolution, L/D^* (Figs. 4.19, left). As earlier discussed, it is assumed that by taking the square of $\left(\widetilde{u_{3_n}}(t) - \widetilde{\overline{u_3}}\right)$ (lower than unity) and applying the ensemble average (over 500 images) for the estimate of $k_{t,filter}$, the differences between the $\left(\widetilde{u_{3_n}}(t) - \widetilde{\overline{u_3}}\right)$ at each L/D^* were further reduced, thus producing convergent results in the far-field of $k_{t,filter}$ as shown in Figs. 4.19 (left). On the contrary, when assuming the fluctuation $\left(\widetilde{u^*_{3_n}}(t) - \widetilde{\overline{u^*_3}}\right)$ (here dimensionless) to compute the standard deviation σ_u (Eq. 4.11) for χ_u, the influence of different L/D^* affecting σ_u via $\left(\widetilde{u^*_{3_n}}(t) - \widetilde{\overline{u^*_3}}\right)$ showed up as in Fig. 4.17. Given the small difference of $\sim 10\%$ between the plateau at $L/D^* = 0.7$ and $L/D^* = 1$ (Fig. 4.17), and the fact that such a difference is also the result of a decreasing $\widetilde{u^*_3}$ with increasing L/D^* ($\chi_u \propto 1/\widetilde{\overline{u^*_{3_c}}}$), it is reasonable to conclude that the time fluctuations for the velocity, $\left(\widetilde{u^*_{3_n}}(t) - \widetilde{\overline{u^*_3}}\right)$, are very similar at varying resolutions, L/D^*.

A likely explanation for a higher sensitivity to L/D^* of the density difference time fluctuation, $\left(\widetilde{\theta^*_{sw_n}}(t) - \widetilde{\overline{\theta^*_{sw}}}\right)$, compared to a nearly constant $\left(\widetilde{u^*_{3_n}}(t) - \widetilde{\overline{u^*_3}}\right)$ time fluctuation at varying L/D^*, was found in the different frequency used for the acquisition of the PIV and PLIF images, respectively. The maximum imaging frequency set for the camera was $\sim$ 14 Hz for both setups, but the double-frame mode for the PIV measurements allowed the PIV images to be taken at a maximum rate of $\sim$ 5 Hz (assuming data transfer rates on the hardware). Therefore, even if the flow cannot be considered fully temporally-resolved in either case (PIV and PLIF), the higher frequency for the single-frame PLIF experiments still ensures the ability to capture more details and estimate statistics frame-to-frame (i.e. puffing magnitude) with a faster rate than the double-frame PIV measurements. Given the above, it is believed that the decreased PIV acquisition frequency (approximately half of that of the PLIF tests) reduced the number of points (i.e. $\widetilde{u^*_{3_n}}(t)$ over a shorter time), needed to properly evaluate the fluctuations for different interrogation window sizes, L/D^*. By means of high-speed cameras with frequencies in the range of 100-200 fps (frames per second, or Hz) [64], this aspect of the research could be further investigated and the results easily improved.

4.3.2.2 Estimates of Spatially- and Temporally-Resolved Kinetic Energy

Estimates of kinetic energy using the concept of a low-pass filtering resolution window, L/D^*, are inspired by the LES computational approach; nevertheless, the

analogy between the computational and experimental frameworks call for general clarification. First of all, care must be taken in the terminology used. In LES, the resolved-scale motions are referred to grid-resolved, while the smaller scales, the effects of which are parameterized by the sub-grid model, are called sub-grid "unresolved" scales. For the image filtering process, the "grid-resolved" definition still holds because the interrogation window, L/D^*, is used as spatial filter, but the term "sub-grid" should be more appropriately replaced by "subfilter", as there is no link with the numerical definition of it. A subfilter value (velocity or density difference) is defined here as resulting from a single pixel (25 μm) framed by the virtual interrogation window, and the single pixel is indeed the smallest image possible. Therefore, claiming that the single-pixel represents the sub-grid scales could result in a vague and misleading statement, because the entire field is also the result of phenomena occurring at smaller scales. Given the above, and referring to the interrogation window as a local, pixeled grid, the term subfilter (or residual) was used for the statistics concerning the single-pixel resolution and "grid-resolved" (or filtered) for that estimated over the pixels binned within a window L/D^*.

In light of this, estimates of the filtered, $k_{t,filter}$, and sub-filtered, ($k_{t,subfilter}$) turbulent kinetic energy were computed at different resolutions, L/D^*. Highly-resolved measurements helped establish the relative contribution to the energy budget of both resolved and "unresolved" turbulent kinetic energy by means of the statistics at a given resolution. The relative proportions of these two kinetic energy contributions were quantitatively assessed through a dimensionless kinetic energy

factor, M [56], depending on the resolution L/D^* and given as

$$M(L/D^*) = \frac{k_{t,filter}}{k_{t,filter} + k_{t,subfilter}}. \tag{4.13}$$

In a LES simulation, Eq. 4.13 represents the percentage of the mean (i.e. time-averaged) turbulent kinetic energy that is resolved by the numerical grid, attaining a value equal to one when $k_{t,subfilter}$ is negligible and decreasing toward zero as $k_{t,subfilter}$ begins to dominate over $k_{t,filter}$. It should be noted that in simulations the mean sub-grid kinetic energy, k_{sgs}, results from the use of a specific model [42,46]; on the contrary, in this investigation, $k_{t,subfilter}$, is based on real information coming from the residual flow at the single-pixel scale (~ 25 μm). In the computational environment, the M criterion is purely associated with the degree of influence that the sub-grid turbulence model has on the flow field, but here, through the dependence on the interrogation window (L/D^*) and the statistics associated with it, it becomes a tool enabling the estimate of the filtered-to-residual kinetic energy ratio from real measurements. Such information could provide useful grid resolution guidelines for modeling fire buoyant plumes, which typically require $M > 0.8$ to be considered well-resolved anywhere in the flow.

In this study, PIV measurements provided a temporally- and spatially-resolved vector field from which the grid-resolved (filtered), sub-grid (residual) and the total turbulent kinetic energy ($k_{t,filter} + k_{t,subfilter}$) estimates were assessed using the fluctuating velocity field, given as [56]

$$\boldsymbol{u}'(\boldsymbol{x},t) = \boldsymbol{U}(\boldsymbol{x},t) - <\boldsymbol{U}(\boldsymbol{x},t)>, \tag{4.14}$$

where the residual field $\boldsymbol{u}'(\boldsymbol{x},t)$ equals the difference between the velocity field, $\boldsymbol{U}(\boldsymbol{x},t) = (u_1, u_3)$, and its filtered field, $< \boldsymbol{U}(\boldsymbol{x},t) >$. In turbulent-flow experiments and simulations, several kinds of averaging are used to define means that can be related to $< \boldsymbol{U}(\boldsymbol{x},t) >$ [66], such as spatial, temporal (usually) and ensemble averaging. Therefore, the $<>$ symbol can either represent a temporal or a spatial average. As emphasized by Pope [66], Eq. 4.14 appears analogous to the Reynolds decomposition, but (in general) $< \boldsymbol{U}(\boldsymbol{x},t) >$ (filtered field) is a random field and the filtered residual field is not zero:

$$< \boldsymbol{u}'(\boldsymbol{x},t) > \neq 0 \tag{4.15}$$

For the estimates of $k_{t,filter}$ and $k_{t,subfilter}$, both spatial and temporal (i.e. images ensemble) filters were applied.

For a free-shear flow (e.g. jet and plume), the turbulent kinetic energy $k(\boldsymbol{x},t)$ (per unit mass) is defined as follows:

$$k(\boldsymbol{x},t) = \frac{1}{2} < \boldsymbol{u}' \cdot \boldsymbol{u}' > = \frac{1}{2} < u_i' u_i' > ;\ i = 1,3 \tag{4.16}$$

Equation 4.16 is valid under the assumption of isentropic flow, given only two of the three velocity components (planar PIV). Based on Eq. 4.16, the grid-resolved kinetic energy, $k_{t,filter}$, was evaluated assuming the interrogation window spatial-averaged velocity $\widetilde{\boldsymbol{U}}(t) = (\widetilde{u_1}, \widetilde{u_3})$ (see Eq. 4.7, right), replacing $\boldsymbol{U}(\boldsymbol{x},t) = (u_1, u_3)$ in Eq. 4.14. The fluctuating velocity field $\boldsymbol{U}(\boldsymbol{x},t) - < \boldsymbol{U}(\boldsymbol{x},t) >$ (Eq. 4.14) was therefore intrepreted as the difference between $\widetilde{\boldsymbol{U}}(t)$ for the instantaneous frame and its time-averaged (or ensemble-averaged) value, $\overline{\widetilde{\boldsymbol{U}}}$, over the set of 500 images. Here, the overline symbol represented the time average filter, which replaced the

comprehensive (i.e. time or space) symbol $<>$ used in Eq. 4.14. Eventually, the fluctuating velocity field, $\widetilde{\boldsymbol{U}}(t) - \overline{\widetilde{\boldsymbol{U}}}$, was squared and temporally averaged over the ensemble of 500 images, as shown in Eq. 4.17

$$k_{t,filter} = \frac{1}{2}\overline{(\widetilde{\boldsymbol{U}}(t) - \overline{\widetilde{\boldsymbol{U}}})^2} \tag{4.17}$$

Equation 4.17 was then estimated at each centerline location x_3/D, where the L/D^* window was centered.

Following a similar procedure to that described above, the residual flow kinetic energy, $k_{t,subfilter}$, was extracted using the local information from the single pixels framed by the interrogation window. Specifically, the fluctuating velocity field (Eq. 4.14) for the residual flow was estimated for each pixel using the single-pixel instantaneous velocity, $\boldsymbol{U}(\boldsymbol{x},t)$ and the spatial average of the instantaneous velocity $\boldsymbol{U}(\boldsymbol{x},t)$ (extracted from the left pixels of the window) over the window area, $\widetilde{\boldsymbol{U}}(t)$ (replacing $< \boldsymbol{U}(\boldsymbol{x},t) >$ in Eq. 4.14). The fluctuating velocity for each individual pixel of the grid, $\boldsymbol{U}(\boldsymbol{x},t)$-$\widetilde{\boldsymbol{U}}(t)$, was then elevated to the second power to generate the kinetic energy contribution from the single pixel, and the spatial average over the whole pixeled grid was taken to provide the total subfilter contribution. In order to obtain a single value of the residual kinetic energy in the average sense, the time-average over the ensemble of images was eventually estimated, as shown in Eq. 4.18.

$$k_{t,subfilter} = \frac{1}{2}\overline{\widetilde{(\boldsymbol{U}(\boldsymbol{x},t) - \widetilde{\boldsymbol{U}}(t))^2}} \tag{4.18}$$

The results for this study are presented in Figs. 4.19 and 4.20. Both kinetic energy, $k_{t,filter}$ and $k_{t,subfilter}$ profiles were normalized by gD^* and displayed along the

centerline x_3/D, thus obtaining dimensionless values, $k^*_{t,filter}$ and $k^*_{t,subfilter}$, related to the source through D^*. The contribution in the kinetic energy budget resulting from the flow largest and smallest scales (at a given L/D^*) was assessed using the factor M, given in Eq. 4.13 (Fig. 4.20).

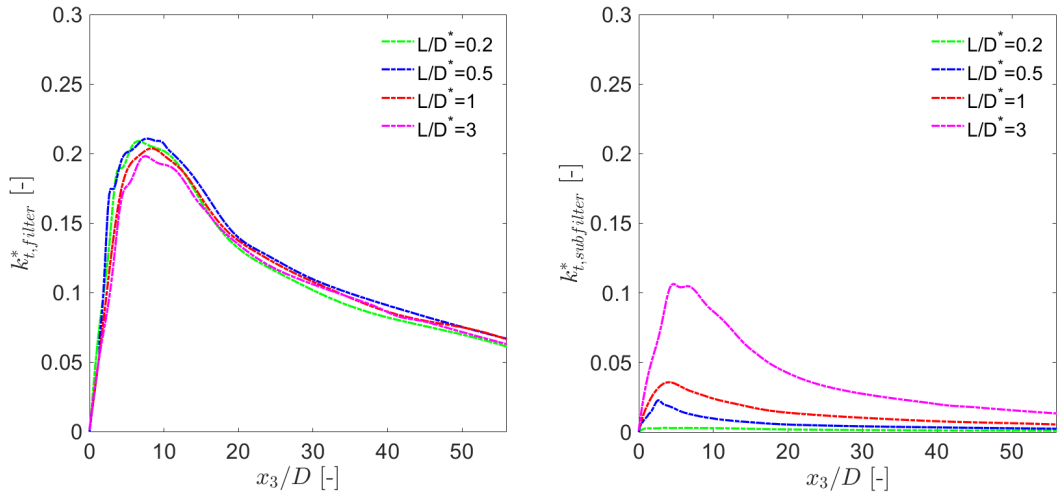

Figure 4.19: Dimensionless turbulent kinetic energy along the plume centerline, x_3/D, for the resolved grid scale, $k^*_{t,filter}$ (left), and residual flow length scale, $k^*_{t,subfilter}$ (right), estimated at different resolutions, L/D^*.

As shown in Fig. 4.19 (left), $k_{t,filter}$ profiles match the behavior expected for a buoyant plume—the turbulent kinetic energy starts to increase as the laminar-to-turbulent transition occurs ($0 \lesssim x_3/D \lesssim 15$, Fig. 4.5) and shear layers are supposed to develop (i.e. $u_i u_i \neq 0$, Eq. 4.16); once these reach the centerline moving from the interface with the fresh water to the core of the plume along x_1, the turbulent production grows in the established buoyancy region ($x_3/D \gtrsim 15$) and then it starts

to decay for $x_3/D \gtrsim 25$ (or $x_3^+/D^* > 100$, see Fig. 4.17). Similar patterns are observed for the $k_{t,subfilter}$ profiles (Fig. 4.19, right), but with shapes depending on the window resolution, L/D^*—the higher the resolution, the smoother the curve becomes.

With regard to the window resolution, values for $k_{t,filter}$ (Fig. 4.19, left) are well-converged amongst all considered L/D^*, while values for $k_{t,subfilter}$ (Fig. 4.19, right) decrease steadily with increasing L/D^*. In both cases, the resolution window seems to operate as a filter for the unrelated effects to the flow scale of interest, i.e. residual effects for the filtered flow and vice-versa. This is particularly evident looking at the curves for $k_{t,subfilter}$ (Fig. 4.19, right), where, at a coarse resolution of $L/D^* = 3$, the profile is still resembling one for $k_{t,filter}$, whereas at $L/D^* = 0.2$, the curve assumes a plateau-like behavior. The concept of the interrogation window as a filter is reinforced by the collapsed profiles observed for $k_{t,filter}$. These suggest that the spatial-filtering over the pixelated-grid ($\widetilde{\boldsymbol{U}}(t)$ in Eq. 4.17) smooths out the subfilter (i.e. pixel-to-pixel) velocity fluctuations, when estimating the grid fluctuations, $\widetilde{\boldsymbol{U}}(t) - \overline{\widetilde{\boldsymbol{U}}}$.

Figure 4.20 shows the results for M obtained by combining the information resulting from the estimate of the grid scale resolved ($k^*_{t,filter}$) and the total turbulent kinetic energy ($k^*_{t,filter} + k^*_{t,subfilter}$). The resolution factor, M, clearly exhibits a resolution dependent behavior as we move from $L/D^* = 3$ (coarse resolution) up to 0.2 (fine resolution). As one may observe, by increasing the resolution the amount of turbulent kinetic energy resolved by the grid increases. With an interrogation window of $L/D^* = 0.2$, the resolution factor attains an average value of 0.98 in

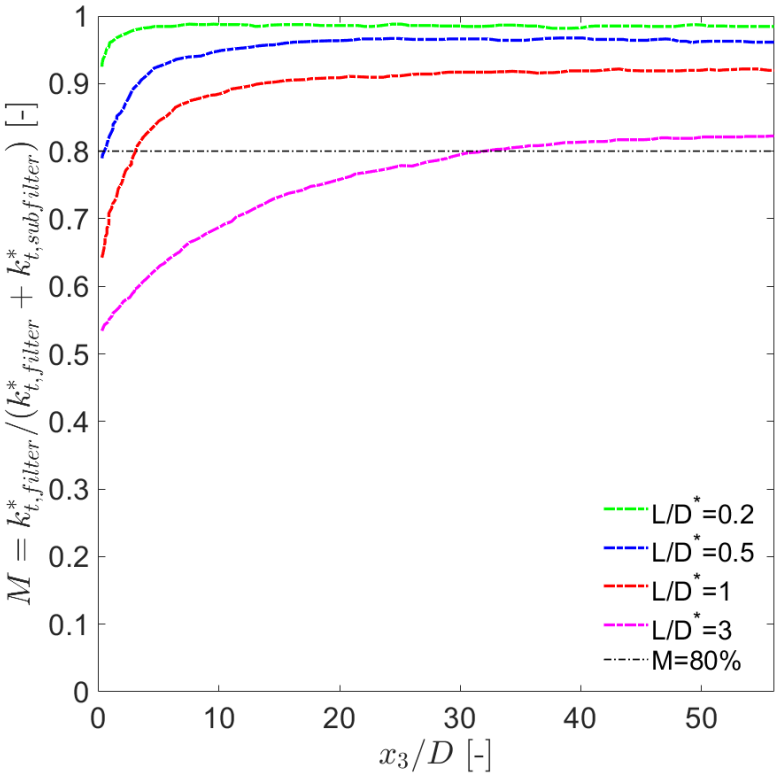

Figure 4.20: Resolution factor, M, evaluated at the plume centerline, x_3/D, for different interrogation window resolutions, L/D^*. Note that, even for a coarse resolution of $L/D^* = 3$ ($L = 4.5$ mm), the plume exhibits resolved turbulence in the buoyancy dominated region ranging from 75 to 83%. The higher the resolution of the virtual grid applied to the images, the lower the turbulence at sub-grid scales.

the far-field (fully-buoyant) and even in the transition region, the level of resolved turbulence is still high. This implies that 98% of the turbulence is resolved along the centerline of the plume by means of the grid-resolved information within the interrogation window. However, even when decreasing the resolution L/D^* by a factor 15 (from $L/D^* = 0.2$ to 3), the resolution factor M is still larger than 0.8 in the fully-buoyant region of the plume, and a residual amount of turbulence ($\sim$ 17-

25%) comes from sub-grid scale. On the other hand, the intermittent region for the coarse resolution of 3 resolves less than 80% of the turbulent kinetic energy.

This analysis shows how the local resolution (virtual window, locally applied) can impact estimates of the grid-resolved, $k^*_{t,filter}$, and residual $k^*_{t,subfilter}$ kinetic energy. In detail, the use of the kinetic energy factor, M, allows for an understanding of the balance between the contribution of the large scales and the local small scales to the energy budget and it shows that, even at a coarse spatial resolution of $L = 4.5$ mm, greater than 80% of the total kinetic energy can be estimated in the far-field using grid-resolved statistics. The residual $\sim 20\%$ can still be estimated by $k^*_{t,subfilter}$ which leverages real information resulting from spatially, highly-resolved images. In consideration of this result and the preceding grid-convergence analysis, a range from $L = 0.45$ mm to $L = 1$ mm resolution range is deemed adequate to obtain resolved converged first and second order statistics, and therefore suiting the aims of the present study.

4.3.3 Higher-Order Statistics for Dimensionless Density Difference

Figures 4.21 and 4.22 show the results found by investigating the grid-resolved dimensionless mean and the "unresolved" sub-grid fluctuation of the density difference over dimensionless time, t^* (Eq. 3.68). The statistical moments estimated here were computed based on the pixel-level information, extracted from the interrogation window of size L (or resolution L/D^*) for each instantaneous image collected. The time between two consecutive frames with a single-pulse laser mode (PLIF)

was 0.07 s, given the 14 fps frame rate of the CCD camera (synchronized with the laser). Therefore, the full set of 500 images was collected within 36 s after attaining a steady-state. The interrogation window was set along the centerline at a height of $x_3^+/D^* = 75$, in the fully-buoyant region of the plume.

The results displayed in Figs. 4.21 and 4.22 represent the first and the second statistical moments (mean and standard deviation) of saltwater density difference, respectively. Using a similar approach to that employed for the time-averaged flow (Secs. 4.3.1, 4.3.2) but on an instantaneous PLIF frame, the first moment was calculated based on the spatial averaging of the single-pixel information ($\theta^*_{sw_i}$) over the spatial domain, Ω, enclosed within the interrogation window of area V_Ω, as shown in Eq. 4.19

$$\widetilde{\theta^*_{sw}}(t) = \frac{1}{V_\Omega}\int_\Omega \theta^*_{sw_i}(\mathbf{x},t)d\mathbf{x}. \tag{4.19}$$

The second statistical moment (standard deviation), representing a measure of the fluctuation of θ^*_{sw} at the sub-grid scale, was also computed for each of the 500 instantaneous PLIF frames, based on Eq. 4.20:

$$\widetilde{\sigma_{\theta^*_{sw}}}(t) = \sqrt{\frac{1}{N_{pixels}}\sum_{i=1}^{N_{pixels}}\left[\theta^*_{sw_i}(\mathbf{x},t) - \widetilde{\theta^*_{sw}}(t)\right]^2} \tag{4.20}$$

where $\widetilde{\sigma_{\theta^*_{sw}}}(t)$ represents a time-dependent (or "frame-dependent") function built upon N-pixel-contributions from the window. These are given as the difference between dimensionless density difference at a single-pixel level, $\theta^*_{sw_i}(\mathbf{x},t)$, and the grid-spatial average value, $\widetilde{\theta^*_{sw}}(t)$.

Both Figs. 4.21 and 4.22 display the results in a way that the time ensemble for the larger scales ($\widetilde{\theta^*_{sw}}$) can be compared with that of the smaller scales ($\widetilde{\sigma_{\theta^*_{sw}}}$).

The analysis is carried out by first studying the response of the time ensemble of both scales to the variation of the resolution L/D^* (Figs. 4.21, left and 4.22, left) and then representing the temporal PDF_t over the same resolution range (Figs. 4.21, right and 4.22, right).

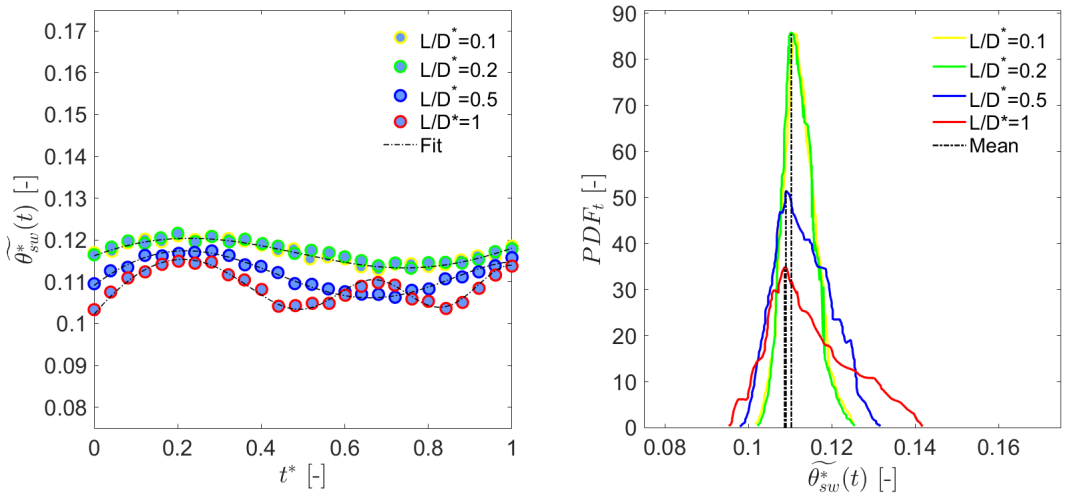

Figure 4.21: Higher-order statistics for window-resolved dimensionless density difference, $\widetilde{\theta^*_{sw}}(t)$: variation of the time ensemble over the dimensionless time scale for resolution, L/D^*, ranging from 0.2 to 1 (left); temporal PDF_t estimated for the same window size resolution range (right).

As one may observe by comparing Fig. 4.21 (left) and Fig. 4.22 (left), the time ensemble for $\widetilde{\theta^*_{sw}}$ and $\widetilde{\sigma_{\theta^*_{sw}}}$ both exhibit a periodic-like behavior in the dimensionless time range t^* from 0 to 1 (where only 25 frames are captured). This periodic oscillation is believed to be caused by the puffing motion of the plume. However, it appears that the mixing at grid-scale resolution, $\widetilde{\theta^*_{sw}}$, and the level of unmixedness represented by $\widetilde{\sigma_{\theta^*_{sw}}}$, occur at different frequencies. By comparing one-to-one $\widetilde{\theta^*_{sw}}$

and $\widetilde{\sigma_{\theta^*_{sw}}}$ at each window resolution, the turbulent mixing at the small scales occurs faster than that of the corresponding filtered flow. This is also consistent with the fact that the small eddies (down to the Kolmogorov scale) tend to dissipate faster than to those at the larger scales. As shown in Fig. 4.21 (left), at a "coarse" reso-

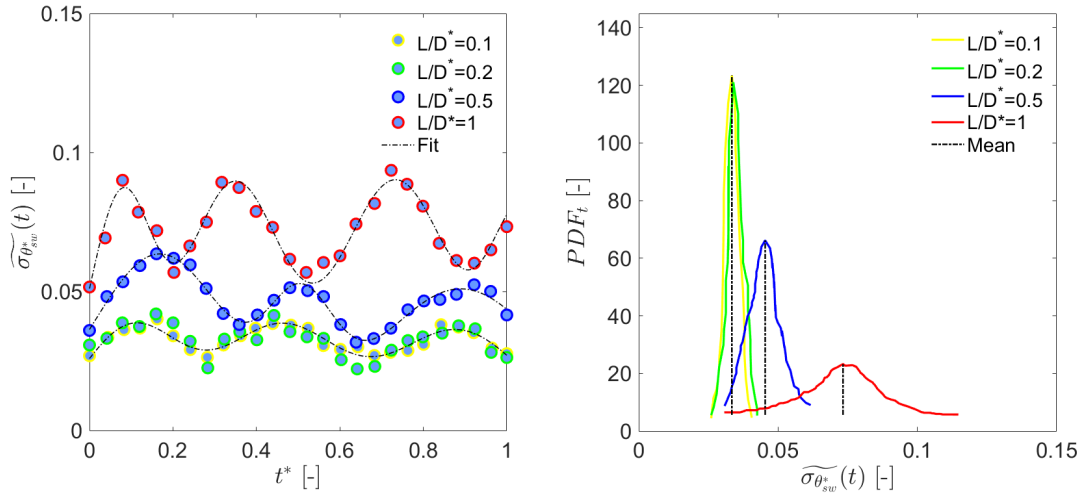

Figure 4.22: Higher-order statistics for subfilter dimensionless density difference fluctuations, $\widetilde{\sigma_{\theta^*_{sw}}}$: variation of the time ensemble over the dimensionless time scale for interrogation window size, L/D^*, ranging from 0.2 to 1 (left); temporal PDF$_t$ estimated for the same window size resolution range (right).

lution ($L/D^* = 1$), the resolved scales, $\widetilde{\theta^*_{sw}}$, vary over time at a frequency double of that required for higher resolutions ($L/D^* = 0.1$, 0.2, 0.5), where the time scale is approximately t^* (i.e. time-resolved integral behavior). This faster time-oscillation of $\widetilde{\theta^*_{sw}}$ at a coarser resolution likely originates from larger portions of the flow captured at each frame by a larger interrogation window and used for the statistics. These larger windows incorporate those regions around the centerline where the

entrainment is more effective and cyclically (e.g. by a puffing motion) dilutes the source, thus affecting the estimates of $\widetilde{\theta^*_{sw}}$ frame by frame, as shown in Fig. 4.23. On the other hand, by further increasing the resolution up to 0.2 (where $\widetilde{\theta^*_{sw}}$ starts to collapse), the narrower window focuses closer to the centerline, where the higher saltwater concentration oscillates more slowly due to less penetration of the fresh water. Consistently, as shown in Fig. 4.22 (left), as we increase the resolution, the standard deviation decreases and vice-versa (see Fig. 4.15 and related discussion). Interestingly, for a given resolution, the time scale for the mixing at the small scales (Fig. 4.22, left) reduces approximately to a half if compared to that occurring at the grid-scale (Fig. 4.21, left). This is in agreement with the isotropic interpretation of the turbulence [54], where the small eddies in charge of the mixing at the small scales quickly dissipate due to the viscous effects—the short duration of small vortices within the grid (and their cyclic replacement due to the puffing motion) has a smaller but faster effect on the small-scale density difference ($\widetilde{\sigma_{\theta^*_{sw}}}$).

In addition, if we separately analyze $\widetilde{\theta^*_{sw}}$ and $\widetilde{\sigma_{\theta^*_{sw}}}$ across the resolution range L/D^*, we can also observe that the frequency of the oscillations (due to the puffing motion) almost doubles increasing the resolution by 5 times (i.e. reducing L/D^* from 1 to 0.2) for both $\widetilde{\theta^*_{sw}}$ and $\widetilde{\sigma_{\theta^*_{sw}}}$ (Fig. 4.21 (left) and Fig. 4.22 (left)).

Overall, these results could have a potential impact on the LES low-pass filtering process, where the experimentally-based resolution for converged statistics could inform appropriate cutoff length scales, usually denoted as Δ, to split up the density difference field into a filtered and sub-filtered field. Ideally, this conceptual approach could be applied to any field of interest (e.g. mixture fraction, vorticity)

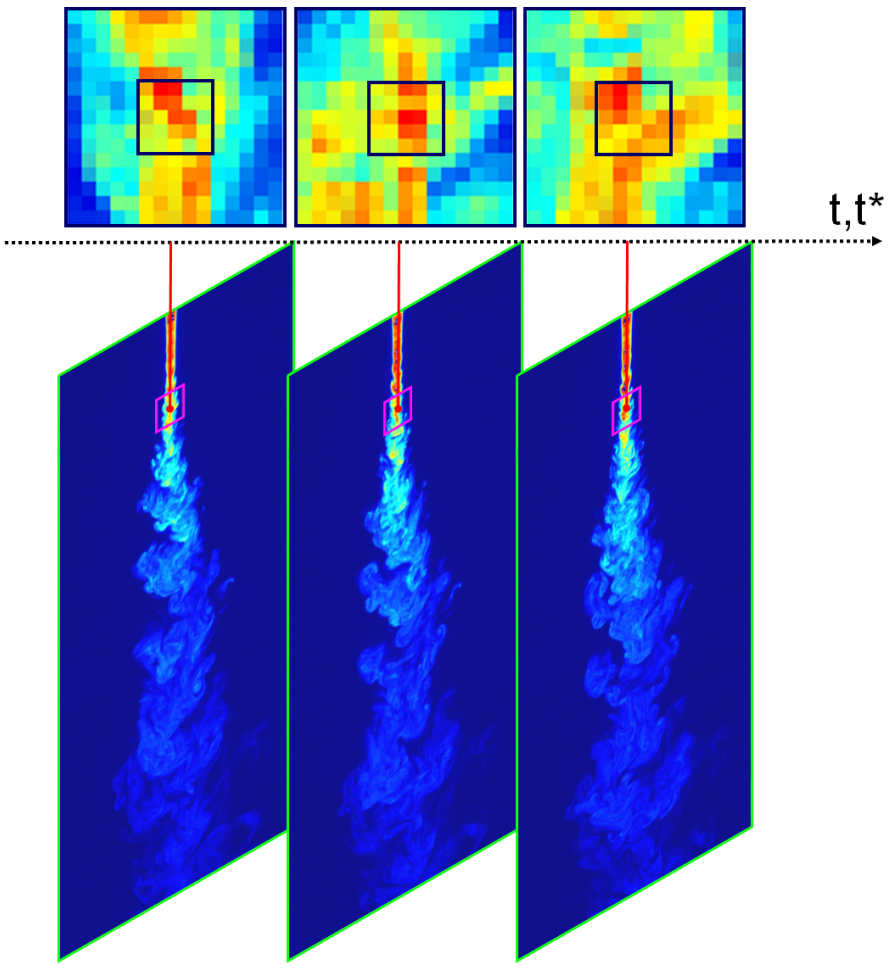

Figure 4.23: High and coarse resolution window effects for higher order statistics, based on the comparison between three instantaneous, consecutive PLIF images at $x_3^+/D^* = 75$. Note the inner interrogation window (higher resolution) compared to the outer interrogation window (9 times larger) over time: the high-resolution window shows a smoother change in time for the density difference, while it gets faster at a coarser resolution (outer window) because of the entrainment captured in the window and due to the puffy motion of the plume.

that can be investigated by means of image processing.

The analysis for the time ensembles of $\widetilde{\theta^*_{sw}}$ and $\widetilde{\sigma_{\theta^*_{sw}}}$ was integrated by temporal probability density functions (PDF_t) for both scales, as shown in Figs. 4.21 (right) and 4.22 (right). Both the instantaneous, dimensionless $\widetilde{\theta^*_{sw}}(t)$ and $\widetilde{\sigma_{\theta^*_{sw}}}(t)$ resulting

from the application of the spatial filter (Eqs. 4.19 and 4.20) on each frame were collected over the entire dimensionless time period, t^*, corresponding to the acquisition of 500 PLIF images (t ~36 s). The PDF$_t$ curves shown in Figs. 4.21 (right) and 4.22 (right) were built upon this information and displayed for each L/D^* resolution assumed for the preceding time ensembles analysis.

The PDF$_t$ curves for $\widetilde{\theta^*_{sw}}$ illustrated in Fig. 4.21 (right) clearly show the effect of an increasing resolution L/D^* —higher the resolution and lower is the variance around the constant mean of the temporal distribution ($\sim$ 2.5% difference between the mean of the two PDF_t at $L/D^* = 0.2$ and $L/D^* = 1$). As one may observe, this result consistently agrees with that anticipated by the time series, where at higher resolutions ($L/D^* = 0.1$, 0.2) the instantaneous values of $\widetilde{\theta^*_{sw}}$ fluctuate over time less than those at $L/D^* = 0.5$ and 1. Most importantly, when at $L/D^* = 0.2$ (Fig. 4.21, right), the statistics converge showing a resolved flow for scales of about 0.3 mm ($L/D^* = 0.2$). This reduction of the PDF$_t$ standard deviation with respect to the resolution translates into an effective capacity of the virtual interrogation window to filter out the independent effects of the sub-grid scale mixing, thus only representing the progress over time of the grid-resolved statistics.

On the other hand, the PDF$_t$ for $\widetilde{\sigma_{\theta^*_{sw}}}$ exhibits a different behavior with respect to L/D^* (Fig. 4.21, right), although the window still exerts a similar function to that observed for the PDF$_t$($\widetilde{\theta^*_{sw}}$). In fact, at increasing resolution L/D^*, both the mean and the variance of the PDF$_t$($\widetilde{\sigma_{\theta^*_{sw}}}$) reduce in the range $0.2 < L/D^* \leq 1$, until the flow at the small scales is resolved for $L = 0.3$ mm (converged statistics at $L/D^* = 0.2$). This can be interpreted as the effect of the grid that gradually filters

out the information related to the larger scales (grid-resolved) by narrowing down the variance and providing a stable value (i.e. constant mean of the $\mathrm{PDF}_t(\widetilde{\sigma_{\theta^*_{sw}}})$) for the fluctuation occurring at the smallest scales (subfilter). This demonstrates how the concept of the resolution window of variable size (L/D^*) is a viable tool to analyze experimental data within the interrogation windows (i.e. statistics at the subfilter scale) and on interrogation windows (i.e. statistics at the grid-resolved scale), if virtually applied to highly temporally and spatially resolved images.

Future investigations could focus on similar analysis exploring both other heights along the centerline and the boundary regions, thus mapping the cyclic evolution of the plume.

In this study, we investigated how the spatial filter resolution, L/D^*, affects the statistics of interest for an unconfined plume, performing calculations at its centerline and using spatially-averaged values of neighbouring pixels (framed by the interrogation window L/D^*) instead of the axis-centered, single-pixel value. This coarsening procedure applied to highly-resolved images approximately simulated the response of a probe with a decreased spatial resolution, or equivalently, a coarser mesh-grid for computational sensitivity analyses purposes. Based on the same concept of the low-pass filter used in CFD, but applying the aforementioned "inverse" mechanism of image coarsening, we pursued the same goal of obtaining length scales for converged statistics of the flow field. Table 4.1 summarizes the L/D^* resolutions found for the first, the second and the higher statistical moments investigated in this study. From the analysis of the first order statistics (mean flow), a threshold

Table 4.1: Resolution L/D^* for Resolved Statistical Moments.

Flow Scale	u_3^*	θ_{sw}^*
First Order Statistics	$L/D^* = 0.7$	$L/D^* = 0.3$
Second Order Statistics	$L/D^* = 0.7$	$L/D^* = 0.3$
Higher Order Statistics	[-]	$L/D^* = 0.2$

of $L \sim 0.5$ mm ($L = 0.3D^*$) for the concentration, and $L \sim 1$ mm ($L = 0.7D^*$) for the streamwise velocity were found, so that a resolution of $L \sim 0.5$ mm was considered sufficient to resolve both transport characteristics. Also, $L \sim 0.5$ mm corresponded to ~ 5 times the Kolmogorov lengthscale (η), which was estimated based on the saltwater characteristic lengthscale (also assumed as turbulent integral length scale) $D^* = 1.5$ mm, and the characteristic velocity U_0 (Eq. 3.53), according to $\eta \sim (\nu_{sw}^3/\epsilon)^{1/4} = (\nu_{sw}^3/(U_0^3/D^*))^{1/4} \sim 100\mu$m [66]. Therefore, for the mean flow, the resolution L/D^* providing converged density difference and converged velocity resulted among the larger scales in both scale analysis. In fact, since the ensemble averaging (temporal filter) of the images scrambled up the contribution of the smaller scales (instantaneous flow), the spatial filter, L/D^*, mostly provided the contribution from the largest scales. Physically, by increasing the resolution, the high number of different pixel-to-pixel gradients (or interfaces) initially framed by the largest windows ($L/D^* = 0.7$ for density difference and $L/D^* = 1$ for velocity) were progressively smoothed out (see Fig. 4.15 and related discussion) until obtaining a more homogeneous contour at the highest resolutions ($L/D^* = 0.3$ for density difference and $L/D^* = 0.7$ for velocity). Assuming that larger gradients (velocity

and concentration) correspond to larger eddies, the smoothing of these pixel-to-pixel interfaces at increasing resolutions was interpreted as the attainment of resolved flow conditions (converged $\widetilde{\overline{\theta^*_{sw_c}}}$ and $\widetilde{\overline{u^*_{3_c}}}$).

The results for the second order statistics showed that the turbulence intensities for density difference, χ_θ, and velocity, χ_u, also converged for the same resolutions of $L \sim 0.5$ mm ($L/D^* = 0.3$) and $L \sim 1$ mm ($L/D^* = 0.7$) of their respective first statistical moments. At these resolutions, the region of the plume, where the turbulent fluctuations attain a constant value [48], was characterized by a plateau of $\chi_\theta \sim 38\%$, for the density difference, and $\chi_u \sim 26\%$ for the velocity, both in good agreement with the literature [48]. For this investigation, given the definition of χ_θ and χ_u (Eqs. 4.12), the influence of L/D^* was evaluated by separately analyzing the effects of the interrogation window on the time fluctuations of both scales (via σ_θ and σ_u in Eqs. 4.12), and $\widetilde{\overline{\theta^*_{sw_c}}}$ and $\widetilde{\overline{u^*_{3_c}}}$ (Eqs. 4.7). Absolute differences of about 20% for χ_θ were found by reducing the size of the window L/D^* by ~ 3 times in the plateau region, whereas 10% was the maximum difference in magnitude exhibited by χ_u in the same region. Given the little sensitivity of $\widetilde{\overline{\theta^*_{sw_c}}}$ and $\widetilde{\overline{u^*_{3_c}}}$ to the resolution L/D^* (see Eqs. 4.12), the aformentioned differences between concentration and velocity turbulence intensities were adduced to larger time fluctuations of the scalar at larger L/D^* (coarser resolution) compared to those of the velocity field. The causes for a reduced sensitivity of the velocity time fluctuations were not fully investigated, but a reduced acquisition frequency of the camera imposed by the PIV technique limited the information (time series data points) for a correct evaluation.

An additional comment should be supplemented to the above discussion on

time-averaged flow resolutions (Table 4.1) in order to provide handy guidelines for computational analysis of similar large-scale flows. The numbers reported in Table 4.1 indicate the resolution to obtain converged statistics in both intermittent (transitional) and fully-buoyant regions of the flow. However, it should be noted that the saltwater similarity with fire-induced flows rigorously applies to the plume region only. This narrows down the resolutions for converged statistics (first and second order) of both scales in the region of interest to one range. In light of this, by reviewing the results reported in Figs. 4.13, 4.14, 4.17 and 4.18, time-averaged flow and turbulent intensities should be resolved for $L/D^* \leq 0.5$.

Given the velocity field (instantaneous and ensemble-averaged), estimates of turbulent kinetic energy for the larger and smaller scales were obtained using fluctuating velocities. The use of the spatial filter, L/D^*, for this analysis showed that the kinetic energy based on the time fluctuations of the window spatially-averaged velocity ($k_{t,filter}$) converged over a large resolution range (from $L = 4.5$ mm up to $L = 0.3$ mm). On the other hand, based on the analysis of the contribution from the smaller scales ($k_{t,subfilter}$) to the total kinetic energy, it appeared that the higher the resolution, the lower was this contribution. Given the intrinsic difficulties in modeling the smallest scales in CFD codes, this result informs on an adequate resolution to sufficiently resolve the turbulence by mostly relying on the contribution from the larger scales. In such regard, to quantify the percentage of the turbulent kinetic energy that is resolved by the spatial filter (larger scales) with respect to the total kinetic energy (larger and smaller scales) the resolution factor, M, was used [66]. By increasing the resolution up to $L = 0.3$ mm, it was shown that $\sim 90\%$

of the turbulence was resolved by the larger scales all along the centerline (intermittent+plume region).

The investigation of the time trace for the density difference (Sec. 4.3.3) reinforced the idea of the virtual window as a spatial filter for the evaluation of the contribution from either the larger and the smaller scales in the plume dynamics. By first gathering the spatially-filtered mean, $\widetilde{\theta^*_{sw}}(t)$, for each of the 500 instantaneous images of a measurement set, we derived temporal probability density functions, PDF_t, for different resolutions, L/D^*. Ranging from $L = 1.5$ mm ($L/D^* = 1$) up to $L = 0.3$ mm ($L/D^* = 0.2$), the observed PDF_t Gaussian distributions gradually reduced their variance, while maintaining a constant mean over time, and eventually converge for $L = 0.3$ mm ($L/D^* = 0.2$). Given the fact that instantaneous images include information resulting from both the larger and the smaller scales, the behavior just described is associated with the ability of the virtual window to filter out effects of the residual flow when calculating the mean over the pixels binned within it. Also, as one may note, the resolution of $L = 0.3$ mm ($L/D^* = 0.2$) was very close to that of $L = 0.45$ mm ($L/D^* = 0.3$) found for $\overline{\widetilde{\theta^*_{sw}}}$, where the same analysis was assessed based on the ensemble-averaged flow. This is consistent with the fact that, the instantaneous PLIF frames were always sharper than those resulting from the ensemble averaging of 500 frames, where the single-pixel corresponded to a time average of 500 values. This translated into pixel-to pixel higher concentration gradients instantaneously framed by $L/D^* = 0.3$, when compared to the gradients smoothed out in the ensemble-averaged image and framed by the same window ($L/D^* = 0.3$). Therefore, in order to filter out these gradients and find

converged statistics (as described above for the first order statistics), a resolution of $L/D^* = 0.2$ was required for the instantaneous image.

The PDF$_t$ profiles of $\widetilde{\sigma_{\theta^*_{sw}}}(t)$, which provide a reasonable measure of the contribution from the smallest scales filtered by the window, were seen to shift their mean to lower values while simultaneously narrowing down their variance. At $L = 0.3$ mm ($L/D^* = 0.2$), the distributions at higher resolutions ($L/D^* = 0.1$) converged, thus providing a resolved value for the fluctuation $\widetilde{\sigma_{\theta^*_{sw}}}(t)$, represented by the mean of the PDF$_t$ distribution. This phenomenon was seen as the result of a filtering process operated by the interrogation window to progressively eliminate the contribution of the larger scales as increasing the resolution, and estimate the one originated from the smaller scales (previously filtered out to obtain converged $\widetilde{\theta^*_{sw}}(t)$).

Given the overall analysis of the statistics above, the results obtained showed that the virtual interrogation filter was a valid tool to determine a range of resolution scales at which the unconfined plume resolves at the centerline. In light of the numbers resulting from each individual statistical analysis, the resolved time-average mean flow (density difference and velocity) and turbulence intensities (dealing with the largest scales) can be both resolved by a spatial resolution of $L \sim 0.5$ mm ($L/D^* = 0.3$), approximately 5 times the average Kolmogorov scale, $\eta \sim 100$ μm, based on the characteristic, intergral length scale of the flow, D^*. For the same resolution length scale $L \sim 0.5$ mm ($L/D^* = 0.3$), more than 90% of the total turbulent kinetic energy is resolved by the largest scales (resolved by the filter). To resolve the contribution of the smallest scales (supposed filtered by the interrogation window), which dissipate faster than the time for the acquisition of 500 images ensemble ($\sim$

30-40 s), the resolution required shifts to $L \sim 0.3$ mm ($L/D^* = 0.2$). This filter size also enables to instantaneously resolve the larger scales framed by the window. Summarizing, a comprehensive spatial resolution of $L \sim 0.3$ mm ($L/D^* = 0.2$) should be able to resolve the flow transport characteristics at the centerline and obtain more than 90% of the total turbulent kinetic energy from the larger turbulent scales.

Chapter 5: Sloped Ceiling Jet Flows

5.1 Background

The study presented here focuses on ceiling jet flows developing on inclined surfaces and their close correlation with the activation of suppression devices (sprinklers). When a buoyant plume impinges onto a ceiling, the gases transported originate a characteristic flow (turbulent and relatively thin) running beneath the ceiling. In the early stage of fires within buildings, this hot jet is bounded by an upper and a lower interface, as it develops along the slope: the upper interface is represented by the ceiling, while on the lower side, the ceiling jet flow interacts with the fresh ambient air.

Understanding the characteristics of ceiling jet flow is important because most fire detectors and suppression devices are designed to operate within the ceiling jet during the early phase of fire growth. Characteristics such as the temperature, velocity and smoke concentration within the ceiling jet flow must be known to model the early-phase activation. Prediction of the activation time required for ceiling mounted heat-sensitive sprinkler heads and smoke detectors responding to

a growing fire is a critical step in the design process of these devices. Although the activation time for sprinklers and smoke detectors is based on the knowledge of the ceiling jet characteristics for both cases, the two devices perform different fire safety functions. In fact, temperature rise (for sprinklers) and smoke concentration (for detectors) are flow properties both depending on fire source characteristics (e.g. rate of growth): smoke detectors are designed to provide early warning of fires, while sprinklers are intended to control the development of a fire. Smoke detectors are usually designed to alert the occupants of a building in a timely manner. This allows the occupants to egress the building when the fire is still at its early-stage and manual suppression still might be a viable option [70, 111]. Despite the differences between the two types of devices, in both cases the knowledge of the ceiling jet flow resulting from the impingement of the plume is pivotal to make such devices fully functional.

In most buildings, detection and fire suppression systems are mounted below ceiling surfaces. In the event of a fire, combustion products originate from the burning fuel and form a rising plume above the fire source. When the plume impinges into the ceiling, the surface causes the buoyant flow to change its original path, first turning around the impingement point first, and then radially moving under the ceiling. The response of smoke detectors, heat detectors, and sprinklers—designed to be operative within the layer of hot gases—provides the basis for detectors and suppression systems in fire protection engineering. Studies characterizing the flow of hot gases under a ceiling resulting from the impingement of a fire plume have been conducted since the 1950's [144]. Research has been conducted in such regard,

and most of the studies sought to characterize velocities and temperatures within the hot ceiling flow produced by steady fires below smooth, unconfined horizontal ceilings [144].

The present study provides (1) a detailed analysis of density difference (temperature) and velocity characteristics for a ceiling jet flow developing on a sloped surface (slope range 0° to 40°), and (2) investigates the correlation between front arrival, t_{FA}, delay, t_{lag}, and activation times, t_{act} of virtual sprinklers in a 3D environment by means of saltwater modeling (later presented in Chapter 6).

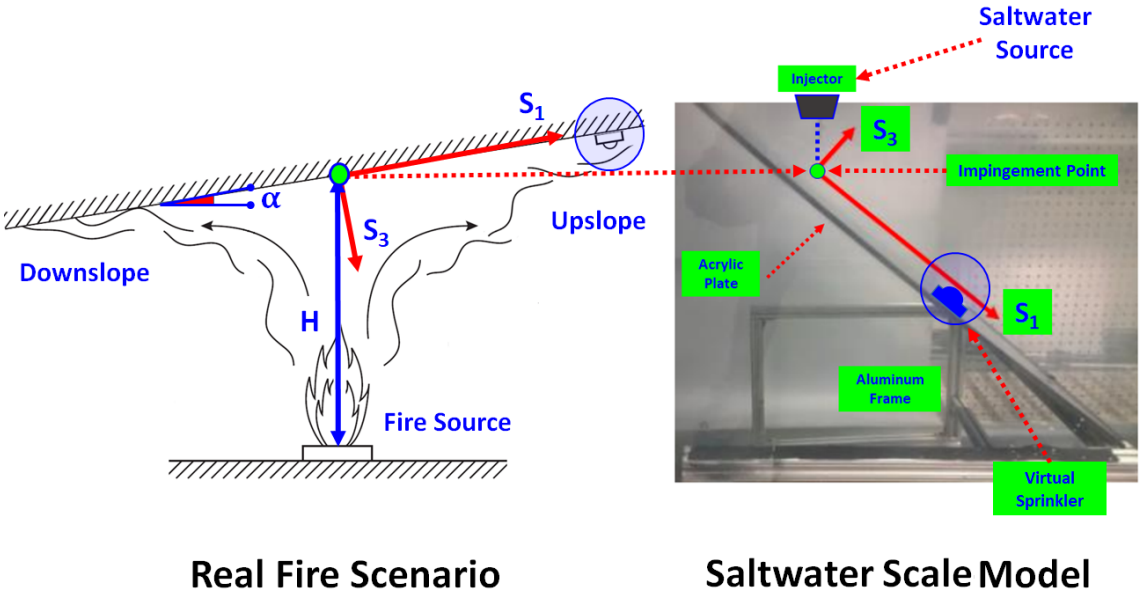

Figure 5.1: Ceiling jet flow beneath a sloped, unconfined ceiling. On the left-hand side a schematic illustrates a real fire scenario of a sloped ceiling; on the right-hand side, the upside-down "inverse" configuration, consisting of an angled acrylic plate residing in a large freshwater tank, depicts the approach used to simulate such scenarios with the saltwater modeling technique.

Figure 5.1 shows how the problem of activation on sloped ceilings in a real

fire scenario which has been studied by means of saltwater modeling. In Fig. 5.1 (left), a schematic represents the actual fire, where the hot, moving gas develops in both upslope (S_1 positive) and downslope (S_1 negative) directions. The ceiling jet flow starts to develop from the impingement point and, as it radially spreads, it entrains fresh air from the layer lower interface and it gets thicker. The entrainment causes the gases to cool and reduce the velocity; at the same time, the heat transfer cools the flow at the interface with the ceiling surface. The suppression system (e.g. sprinklers) operate in such an environment, and its activation delay depends on the flow velocity and temperature profiles established at the surface.

On the right-hand side of Fig. 5.1, the sloped ceiling scenario is recreated by means an upside-down "inverse" configuration consisting of an angled acrylic plate residing in a large freshwater tank and mounted on top of an aluminum frame set in the tank, fully submerged. The inverse configuration is used due to the impracticality of injecting the source from the bottom side of the tank, and it does not affect the measurements because of the reduced gravity effects in the water. The saltwater source (simulating the buoyant-driven flow) is injected at a distance H above the impingement point of the plume on the plate. From the impingement point a local reference frame, S_1, S_3 in the laser sheet plane is assumed for measurements of local velocity, u_1 (parallel to the ceiling surface), and density difference θ_{sw}.

5.1.1 Flow Design and Diagnostics for Inclined Experiments

Experiments assessed for the unconfined plume presented in Chapter 4.3 did not require any description of the boundary conditions for obvious reasons. However, as discussed in Chapter 3, the presence of a ceiling/wall in the flow domain imposes boundary conditions that need to be interpreted in light of the analogy between the two buoyant flows. The sloped plate designed for the experimental setup of inclined fires measurements represents an impermeable wall for the flow of interest. At the surface, there are zero mass fraction gradients which reproduce the adiabatic boundary conditions of a real fire scenario. As discussed in Chapter 3, equations and boundary conditions for θ^*_{sw} and θ^*_T scalar variables in the saltwater and fire configuration behave similarly. This similarity is established only if the dimensionless parameters are matched in the equations of both scenarios (see Eqs. 3.66, 3.36). However, the different nature of the diffusion processes (Sc, Pr) of the fire-induced flow and the saltwater flow can cause the two flows to behave differently at the wall. A good strategy to preserve the similarity is to establish a highly turbulent regime at the impingement point—this ensures that the transport along the ceiling is governed by turbulence rather than diffusion. Therefore, if the $Re{=}Gr^{1/3}$ is sufficiently high at the impingement point (and along the slope) molecular diffusion will be small and differences in molecular properties and their associated dimensionless parameters can be neglected (see Eqs. 3.66, 3.36). These considerations were the baseline to design the experiments along the sloped ceilings here presented.

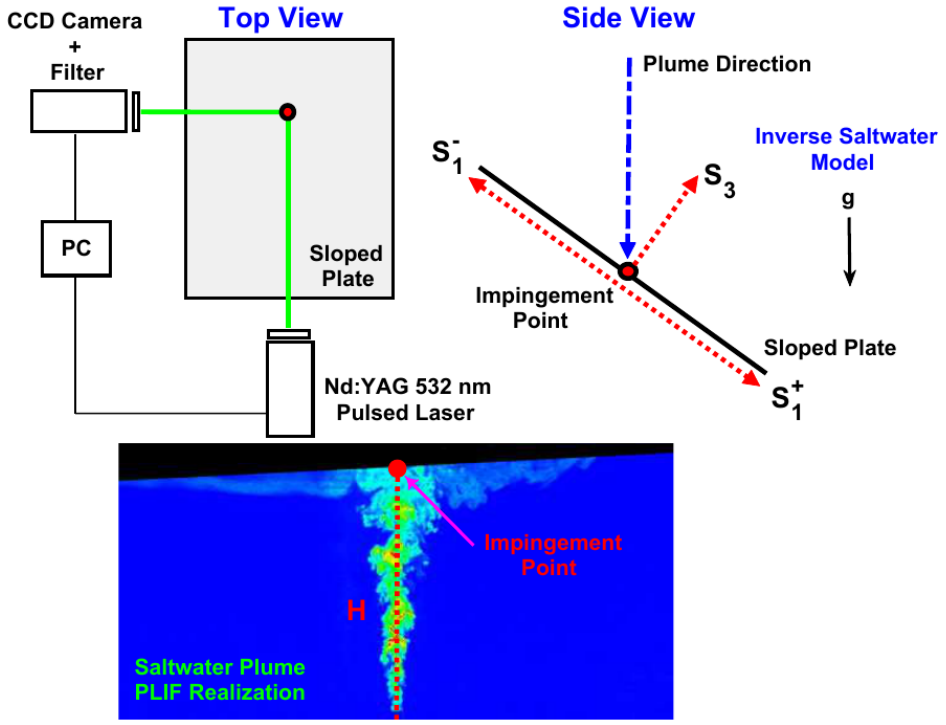

Figure 5.2: Schematic illustration of the experimental setup (above): coordinated axes are centered at the impingement point and chosen such that S_1 represents streamwise locations along the plate (S_1^+ upslope and S_1^- downslope), S_2 the spanwise axis, and S_3 the axis perpendicular to the plate. An instantaneous PLIF realization captured by a CCD camera and resulting from the fluorescence of an impinging plume excited by a 532 nm Nd:YAG pulsed laser is shown below [7].

A high level of turbulence (i.e., $Gr_H \approx 2 \cdot 10^{11}$) at the impingement point (i.e. H=0.34 m from the injector outlet) was reached by increasing the salinity of the saltwater source up to Y_{salt}=0.3 (and therefore the density based on Eq. 3.56), while using the same flow conditions of Table 3.1 regarding volumetric flow rate and injection velocity. The salt concentration Y_{salt} influenced the salt release rate, $\dot{m}_{salt}$, and eventually the saltwater source strength, $\dot{m}^*_{sw}$ as reported in Table 5.1. Based on Eqs. 3.67, the Gr_H was estimated around $1.57 \cdot 10^{11}$ and the

$Re_H = {Gr_H}^{1/3} = 5.36 \cdot 10^3$ at the impingement point, H, above the injector. It should be mentioned that source strength effects were evaluated in a preliminary series of experiments involving different salt concentrations ranging from $Y_{salt} = 0.1$ to $Y_{salt} = 0.5$. The purpose of this analysis was to establish saltwater flow conditions providing scalable concentration and velocity measurements respecting the analogy between fire and saltwater frameworks. In light of this, rather than simulating a given fire strength, $(\dot{Q})$ by saltwater modeling, the target was to meet the limitations imposed by the technique by picking a concentration to obtain a high level of turbulence and minimize the near wall diffusion effects. Over the range of Y_{salt} reported above, Y_{salt}=0.3 was eventually chosen 1. because able to provide highly turbulent flow along the slopes, starting at the impingement point with $Gr_H \approx 10^{11}$ (or equivalently $Re_H \approx 5 \cdot 10^3$) and 2. because for $Y_{salt} > 0.3$ the amount of Rh-6G dissolved into the source and proportional to salt concentration causes phenomena of light absorption affecting scalar measurements.

The experimental apparatus consisted of a sloped black opaque acrylic 0.91 m long, 0.61 m wide, and 0.006 m thick plate placed in the large fresh water tank (Fig. 5.2). The inclination angles (from 0^0 to 40^0) were accurately measured by a Bosch GAM 220 MF-digital angle finder and the plate adjusted in the tank for each measurement set. The injector, the laser/optics apparatus combined with the image acquisition system (PC and CCD Camera) were the same used for the unconfined plume (Fig. 5.2, upper portion). The same gravity head delivery system was used to supply saltwater to the injection system at a fixed flow rate (see Table 5.1). The saline plume rising from the injector outlet impinged the midpoint of the plate at

Table 5.1: Initial Flow Conditions and Characteristic Scales.

Technique	PIV	PLIF
Outlet Diameter (D) [mm]	5.6	
Salt Mass Fraction (Y_{salt}) [-]	0.3	
$\dot{m}_{salt}$ [g/s]	1.05	
$\dot{m}^*_{sw}$ (Based on H) $\times 10^{-6}$[-]	3.95	
Volume Flow Rate ($\dot{V}$) [mL/min]	165	
Injection Velocity (U_{inj}) [mm/s]	≈112	
Re_H $\times 10^3$[-]	≈5.36	
Gr_H $\times 10^{11}$[-]	≈ 1.57	

a vertical distance H, where the ceiling jet starts to develop stream-wise (up-, S_1^+, and downslope, S_1^-) (Fig. 5.2, side view) and span-wise, S_2 (inward and outward the plane of Fig. 5.2, side view).

Given the expected range of velocity around the impingement point (5-6 cm/s) similar to that of the far-field of the unconfined plume, PIV measurements were designed with an F.O.V. of 500 mm and a dt of 40 ms (see Sec. **??**) enough to capture the velocity field around the range of 5-6 cm/s. The same field of view of 500 mm was also used for PLIF measurements, whereas the other setup conditions to those employed for the unconfined plume (see Sec. **??**). Both PIV and PLIF sets of measurements were assessed using the Nikon EF 60 mm focal length, $f/\#$=2.8 lens (Table 3.2). For PIV, the camera mounted the high-pass 532 nm filter for the particle scattered light, while for PLIF, a 540 nm cut-off filter captured the higher

wavelengths exhibited by the Rh-6G fluorescence spectrum [7].

5.2 Characterization of Sloped Ceiling Jet Flows

Saltwater measurements of plume impingement onto an inclined ceiling using laser diagnostics are presented below. First, in order to validate the saltwater methodology and compare results with those found in literature [94], a description of the flow behaviour of a ceiling jet generated along a horizontal ceiling is provided; then sloped ceiling jet characteristics are analysed for an unconfined sloped surface with angles ranging from α=0° to α=40°. Both the time-averaged velocity component ($\overline{u}_1$) and density difference ($\overline{\theta}_{sw}$) are displayed for comparison with experimental data [83, 98, 130–134] and numerical simulations [82] from the available literature. In addition, all values presented here are time-averaged, unless otherwise specified. Particularly for this section, the analysis was limited to an estimate of the velocity component u_1 along the slope direction, S_1 (Fig. 5.1), due to a specific interest in evaluating velocity similarity and boundary layer profiles along the slope based on the velocity component parallel to the wall surface. The analysis presented involves data resulting from PIV and PLIF imaging along the centreline of a single plane. A comprehensive analysis of the ceiling jet transport is eventually assessed through the radial distribution of the velocity and thermal boundary layers and the similarity profiles along the slope. The inverse saltwater modelling approach is then used to determine the dimensionless front arrival time, t^*_{FA} , using the same data sets extracted from the centerline. The investigation is later extended to a multi-planar

imaging grid to locally estimate both arrival and lag times for a virtual detector.

Ceiling Jet Flow Measurements

The following paragraph is intended to provide a qualitative overview of a few aspects characterizing the ceiling jet flow, later analyzed in detail through a quantitative analysis. First, based on raw images, the effects of the buoyant driving force on both ceiling jet velocity and concentration fields are evaluated in light of the influence of an increasing slope, α. Second, the "laminarization" (turbulent to laminar regime transition) occurring for flat ceiling scenarios, also experienced by Yao [94] in his saltwater experiments, is examined by comparing the flow structure at upstream and downstream S_1/H locations. Lastly, a physical interpretation of the penetration distance, namely the maximum distance covered by the downslope jet flow after the impingement of the plume, is presented.

Raw measurements for velocity (PIV) and density difference (PLIF) are shown in Figs. 5.3 and 5.4 to qualitatively illustrate how the slope α influences the velocity and the concentration of the front of the ceiling jet. The objective of these images

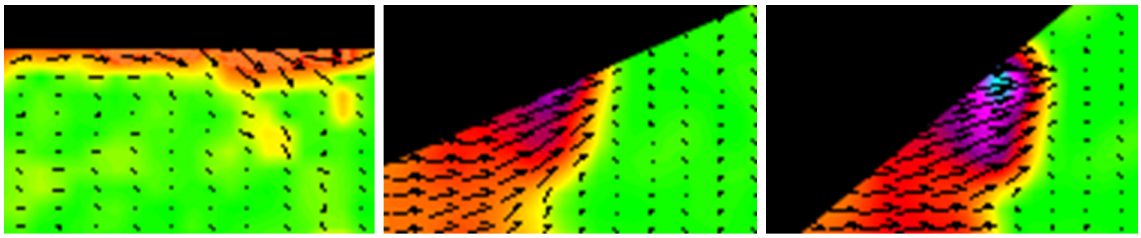

Figure 5.3: PIV raw image close ups for α=0°, α=24° and α=40° (from th left to the right). The PIV raw image close ups qualitatively show increased velocity (vector field+contour) of the ceiling jet front as the slope angle increases. This is due to an increased buoyancy force component along the upslope direction which accelerates the flow.

was to preliminary describe the difference in the ceiling flow conditions at increasing slopes, based on the correlation between the buoyancy force (developed during the rising of the plume and) and the inclination angle. Later in this chapter, velocity and density difference raw profiles below sloped ceilings were quantified to confirm the observations drawn here for increasing angles. As reported by Kung *et al.* [77] in an early work on sloped ceiling jets, the buoyancy force (depending on the gravity force) exerts increasing or decreasing effects on velocity and concentration (entrainment) depending on the slope α. In fact, a simple projection of the buoyancy force vector along S_1 and S_3 (perpendicular to the ceiling wall) produces gravity vector components $\propto g \cdot \sin\alpha$ and $\propto g \cdot \cos\alpha$, respectively. From the analysis of these $g \cdot \sin\alpha$ and $g \cdot \cos\alpha$ components, it appears that at increasing α the component $\propto g \cdot \sin\alpha$ acts favorably along S_1^+ (upward) by accelerating the flow upward, causing faster flows for higher angles at each given location in the upslope. Similarly, the magnitude of the buoyancy component along S_3 (positive downward) decreases at increasing α because of the $g \cdot \cos\alpha$ gravity force component. This reduced force component inhibited the entrainment of freshwater into denser fluid at the lower jet interface as α gets larger. These considerations agreed consistently with the raw measurements reported in Figs. 5.3 (velocity contour) and 5.4 (exhibited fluorescence) for α=0°, α=24°, α=30° and α=40°. The qualitative comparison of the raw images (at S_1 ≈16 cm) for these 4 cases exhibited an increasingly denser and increasingly faster jet flow when ranging from α=0° up to α=40°slope.

For the horizontal ceiling plate (i.e., α=0°), the ceiling jet flow was found to be drastically less turbulent for locations $S_1/H \geq 0.65$. In order to illustrate this

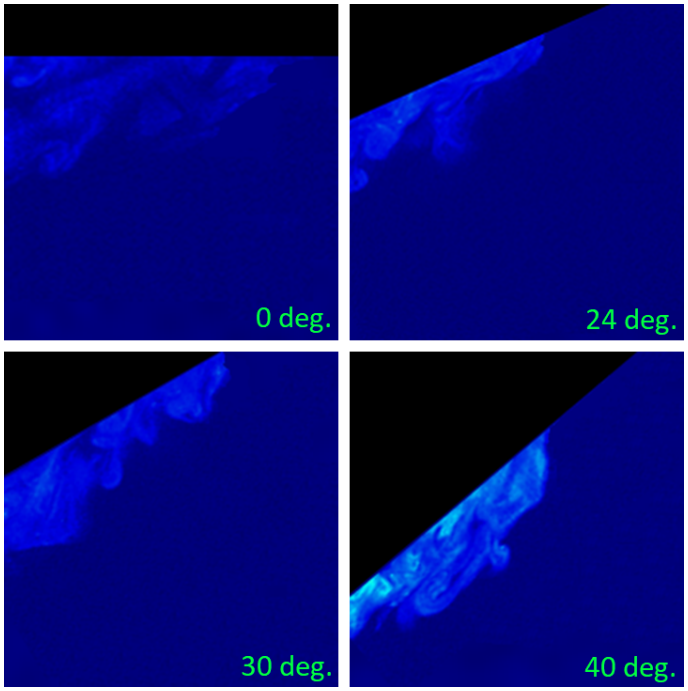

Figure 5.4: PLIF raw image close ups for α=0°, α=24°, α=30° and α=40° (from the top left to the bottom right). The raw images qualitatively show an increasingly denser ceiling jet developing along the plate as the slope angle increases. This is due to a reduced buoyancy force component perpendicular to the plate which inhibits entrainment of fresh water into the saltwater flow.

phenomenon, two representative instantaneous PLIF images, at two different locations along the ceiling are shown in Fig. 5.5. Such images reveal a clear trend in the evolution of turbulent structures that govern flow and thermal transport in the ceiling jet. Downstream of the impingement region, $0.2 \leq S_1/H \leq 0.45$, fresh fluid is entrained deep within the plume creating large-scale unmixed vertical structures characterized by sharp density gradients (Fig. 5.5, above). However, very near the ceiling, the sharp interfaces between the freshly entrained flow and the plume flow start to decrease because of the presence of the plate. This occurs because of the

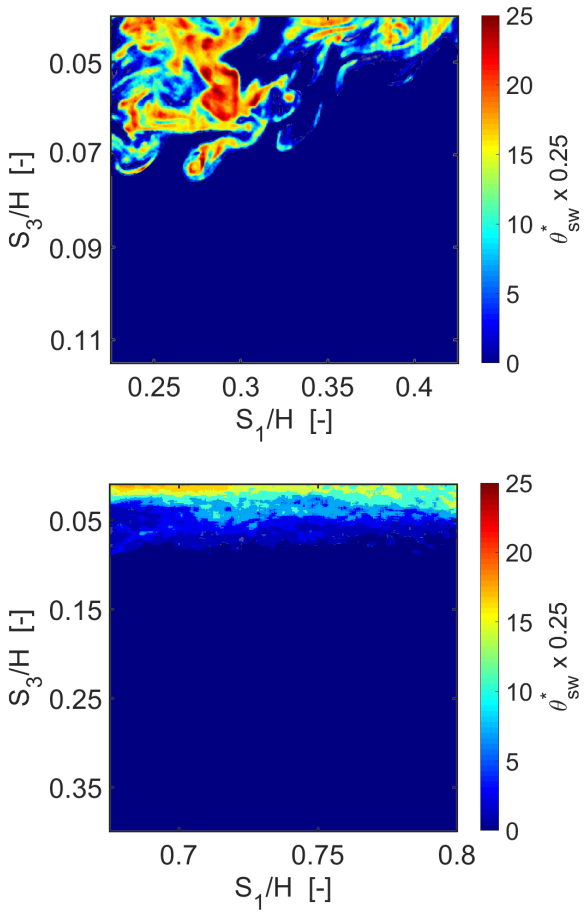

Figure 5.5: Ceiling jet flow evolution for α=0°: close up of the turbulent ceiling jet structure instantaneously captured in the region $0.2 \leq S_1/H \leq 0.45$ (above); laminarization effect in the region $0.65 \leq S_1/H \leq 0.8$ (below).

steep gradients introduced by the wall. Such gradients result in smaller length scales and associated smaller turbulent length scales (dissipation of kinetic energy), which act to remove these sharp interfaces. By zooming into Fig. 5.5 (above), two parcels of saltwater flow can be identified close to the wall: one at $0.25 \leq S_1/H \leq 0.3$, and the other further downstream at $0.35 \leq S_1/H \leq 0.4$. By comparing the two parcels very near to the surface, it can be noticed that the gradients of θ^*_{sw} become smoother

as we move from $0.25 \leq S_1/H \leq 0.3$ to $0.35 \leq S_1/H \leq 0.4$.

Large-scale turbulent motions are observed along the ceiling jet in Fig. 5.5, occasionally penetrating to the wall, indicating that entrainment is important. It is expected that the entrainment will be reduced along the ceiling layer as the Richardson number, $Ri = Gr/Re^2$, increases. This is also in agreement with Alpert's observation regarding the entrainment, E, as function of the Richardson number ($E \propto e^{-3.9Ri}$) [133]. The Ri describes the ratio of potential energy associated with density differences (which inhibits mixing and entrainment) and kinetic flow energy (which promotes mixing and entrainment). In such regard, the Ri number along the sloped plate (S_1/H) at increasing slope α, was not estimated given (1) the difficulty in defining a proper characteristic length for the ceiling jet flow (e.g. boundary layer or ceiling jet layer; momentum or thermal layer), and (2) the limited amount of sources found in the literature [94, 133]. Further away from the impingement region, at $0.65 \leq S_1/H \leq 0.8$, turbulence almost disappears and the flow tends to "laminarize" (or stratify), as shown in Fig. 5.5 (below). Occasional turbulent structures are observed on the surface of the layer, but never penetrate to the wall. In this region, based on previous observations by Yao [94] on flat ceilings, the Ri is expected to increase to the extent that entrainment is almost completely inhibited.

Another phenomenon investigated (later discussed in detail in Sec. 5.2) was the downslope flow reversal and the associated "penetration distance". As observed by Kung *et al.* [77], after the impingement of the fire plume on a sloped ceiling, the jet flow developing in the downward direction has different characteristics from the

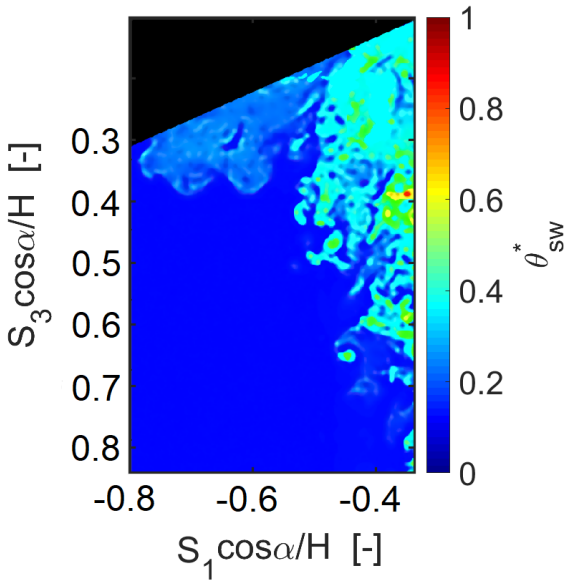

Figure 5.6: Close up of an instantaneous PLIF realization showing the downslope ceiling jet flow reversal and the penetration distance at 24° slope.

one upward. For $S_1/H<0$ (downward direction), the buoyancy component along the ceiling acts against the downslope flow direction causing it to decelerate. At a certain distance from the impingement point, the penetration distance, the gas velocity decreases to zero, the flow turns up and again approaches zero. The larger the slope angle, the smaller the penetration distance. According to Chatterjee *et al.* [76, 82], the penetration distance also corresponds to the point where the gas temperature approaches the ambient quite fast. Chatterjee *et al.* [82] also reports that smaller eddies compared to those moving upward dominate the downslope region. The instantaneous concentration image (PLIF) of the downward ceiling jet for α=24° (Fig. 5.6) captures the moment when the flow front starts to reverse. Note that Fig. 5.6 was brightened to enhance the contrast of the flow reversal region which

corresponds to a weak concentration region. In fact, as one may see, very low saltwater concentration (compared to that of the plume rising on the right) is transported by weak, slow rotating vortices with curved edges (far left of Fig. 5.6) suggesting a counterclockwise, upward motion. These features seem to agree with Chatterjee's observations (mentioned above). The interest in the penetration distance is mostly dictated by the fact that sprinklers are not able to activate beyond this distance, where no threshold conditions for activation can be found. Therefore, an accurate estimate of this parameter can contribute to sprinkler spacing strategy on a larger sloped ceiling (well approximated by unconfined ceilings here investigated) and the activation in the early stage of an incipient fire, before the accumulation of smoke layers significantly changes the scenario (better described by a confined fire).

Upslope and Downslope Jet Flow Characteristics

In this section, results are reported for the non-dimensional density difference, $\theta_{sw}/(\theta_{sw})_c$, and dimensionless velocity in the direction of the ceiling slope, $u_1/(U_c)$, both extracted at a parallel plane located ≈6 mm below the ceiling plate. The purpose is to evaluate the behavior of the ceiling jet flow upward and downward the slope after the impingement of the unconfined saltwater plume. Here, $(\theta_{sw})_c$ is the density difference at the centerline and (θ_{sw}) is the density difference between the local value in the ceiling jet flow at ≈6 mm beneath the ceiling and the ambient (fresh water) density. Similarly, U_c represents the centerline absolute velocity of the plume, while u_1 is the velocity component parallel to the ceiling slope at ≈6 mm distance from the plate. Values of $(\theta_{sw})_c$ and U_c ($\approx |(u_3)_c|$) are extracted from the plume centerline at the same height in the ≈6 mm parallel plane to the plate,

based on tests performed without the presence of the plate. Measurements of U_c and $(\theta_{sw})_c$, with and without the plate, were found to be approximately the same (2-3% variation range for both scales) for every inclination at the given ≈6 mm distance. The small variations of U_c and $(\theta_{sw})_c$ at ≈6 mm were thought to depend on the relatively minor effect of the downward flow reversal at increasing angles, causing (1) a slight increase of u_1 velocity component upward, and (2) a small dilution of the source due to the reversed transport and the turbulent mixing. Because of these negligible variations, U_c and $(\theta_{sw})_c$ formed valid reference scales for all cases (α from 0° to 40°).

Both velocity and density difference are displayed in Figs. 5.7 and 5.8 for each slope, α, in the range 0° to 40°. Data are extracted from the symmetry plane of the ceiling jet, i.e. the mid-plane of the impinging plume illuminated by the laser sheet, and plotted against non-dimensional radial distance, S_1/H, where H, the ceiling height to the impingement point, is assumed as characteristic length. Positive locations ($S_1/H>0$) are along the upward side of the ceiling plate, whereas negative locations ($S_1/H<0$) are along the downward side. Positive velocities along the downslope direction indicate flow reversal. In the downward direction, the buoyancy component along the plate acts on the ceiling jet to decelerate the flow. Therefore, at a certain distance from the impingement point, when density difference decreases to zero and a flow reversal occurs (i.e., the negative downward velocity approaches to zero, becomes positive, and again approaches zero with an inflection point in the velocity distribution over S_1/H) the front of the ceiling jet flow is at a location also known as the penetration distance [77]. The larger the ceiling slope, α, the smaller

the penetration distance. The results for ceiling jet characteristics plotted in Figs. 5.7 to 5.8 generally show a similar behavior of the flow over the radial distance from the impingement point both upslope ($S_1/H>0$) and downslope ($S_1/H<0$), but at increasing slope angles relevant changes in velocity and density difference distribution are observed.

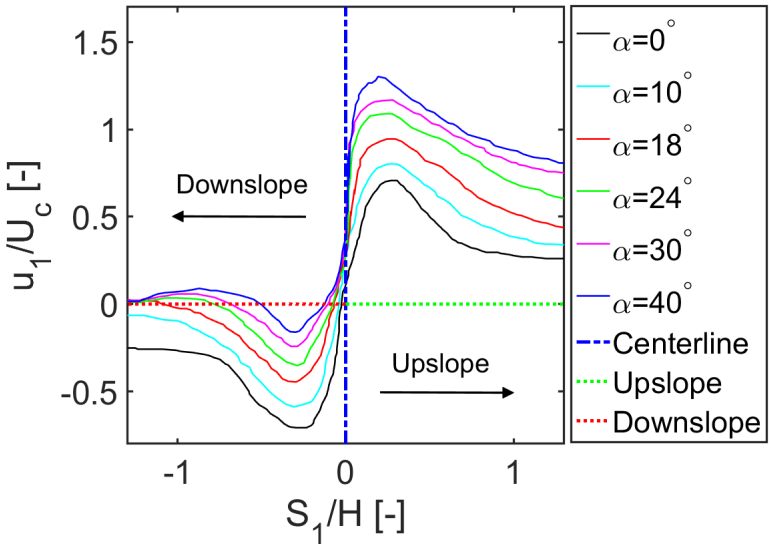

Figure 5.7: Dimensionless velocity, u_1/U_c, upslope ($S_1/H>0$) and downslope ($S_1/H<0$) the impingement point of the plume for α=0° to α=40° ceiling inclination; (—) α=0°; (—) α=10°;(—) α=18°; (—) α=24°; (—) α=30°; (—) α=40°; (-·-) S_1/H =0; (- - -) S_1/H >0; (- - -) S_1/H <0.

The results obtained for a horizontal ceiling (α=0°, black line) are shown in Figs. 5.7 and 5.8. Both u_1 and θ_{sw} extracted from saltwater measurements both exhibit symmetry around the impingement point, as expected for a flow beneath a horizontal ceiling. The predicted values for $\theta_{sw}/(\theta_{sw})_c$ are higher than unity near the central region. Flow stagnation caused by the presence of the ceiling plate results

in an increase of θ_{sw} (i.e., temperature in real fire scenarios) close to the middle as compared to when no ceiling is present ($\theta_{sw} = (\theta_{sw})_c$). In Fig. 5.7, normalized velocity, u_1/U_c, symmetrically accelerates in both directions because the initial buoyancy-generated momentum of the flow, reaching a peak, from which it gradually decreases, and eventually reaches a plateau in the far region where turbulence and flow stratification is observed. Concurrently, the density difference shown in Fig. 5.8 decreases monotonically as the saltwater source entrains freshwater, reducing the buoyancy force along the ceiling jet layer. Similar to velocity, the laminarization of the flow described above causes $\theta_{sw}/(\theta_{sw})_c$ to reach a plateau in the far region both upward and downard from the mid-point.

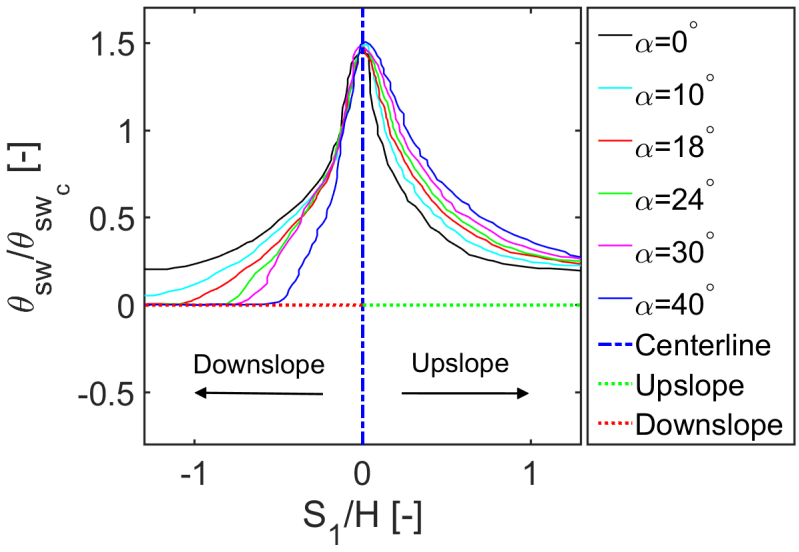

Figure 5.8: Dimensionless density difference, $\theta_{sw}/(\theta_{sw})_c$, upslope ($S_1/H>0$) and downslope ($S_1/H<0$) the impingement point of the plume for α=0° to α=40° ceiling inclination; (——) α=0°; (——) α=10°;(——) α=18°; (——) α=24°; (——) α=30°; (——) α=40°; (-·-·-) S_1/H =0; (- - -) S_1/H >0; (- - -) S_1/H <0.

When the ceiling inclination is increased to α=10°, both flow profiles (cyan line in Figs. 5.7 and 5.8) still maintain relative symmetry with respect to the mid-point. However, the density difference, $\theta_{sw}/(\theta_{sw})_c$, on the elevated side of the ceiling plate does not increase much, as seen in Fig. 5.8, along with a marginal increase in the velocities (Fig. 5.7), whereas the converse is noted on the lower side. Particularly, at S_1/H=-1.3, the non-dimensional velocity magnitude noticeably reduces by a ∼70% as the component of the gravity vector along the ceiling slope decelerates the flow. Gradually increasing the ceiling slope from 18° up to 40°, and by comparing the inclination cases shown in Figs. 5.7 and 5.8, it can be observed that the symmetry originally exhibited by the flow characteristics at 0° and 10° is interrupted by different conditions occurring in the downslope and upslope region of the plate at increasing angles. As shown in Fig. 5.7, velocities on the elevated side of the slope show increasing magnitudes with ceiling plate slope rise. However, differences are noticed on the downslope direction.

Three common regions for u_1/U_c at α=18° (red line), α=24° (green line), α=30° (magenta line), and α=40° (blue line) can be identified along the downslope direction (S_1/H<0): (1) a turning region over a short distance along S_1/H, where u_1/U_c>0 because the flow is initially deflected upward by the lower side of the plate while turning, (2) a subsequent region where u_1/U_c<0 because of the flow moving downward along the plate driven by buoyancy, and (3) a flow-reversal region where both u_1/U_c and $\theta_{sw}/(\theta_{sw})_c$ first approach zero due to an adverse buoyancy component. The ceiling jet moves upslope until it stops ($u_1/U_c \approx$0). As we increase the slope of the plate, u_1/U_c marginally increases in the first region due to a marginal

effect of the upward deflection of the flow. In the second region, the ceiling jet first speeds up and thereafter starts to slow down due to the adverse buoyancy effect. The whole phenomenon is further slowed down by increasing the inclination of the plume which leads to an increase of the adverse buoyancy component which causes the ceiling jet to reverse [77]. Finally, in the third region, the higher the angle and earlier the flow starts to reverse upward ($u_1/U_c>0$) to then slow down.

When comparing u_1/U_c for α=18° up to α=40° (red, green, magenta, blue lines in Fig. 5.7) to those at lower angles (i.e., α=0° (black line) and α=10° (cyan line)) in Fig. 5.7, a major difference in the downslope region can be observed: no flow-reversal seems to occur within the boundaries of the plate. The likely reason is the reduced adverse buoyancy component for α=10°, and a zero adverse buoyancy component for α=0°. Both conditions extend the point where the front of the flow separates from the ceiling and turns upward beyond the plate.

An asymmetric trend for $\theta_{sw}/(\theta_{sw})_c$ with respect to the impingement point of the plume (S_1/H=0) is also found at increasing inclination angles. Raising the slope from α=18° up to α=40° as shown in Fig. 5.8, on the upslope of the ceiling plate, we observe that the density difference values are consistently higher than those measured for α=0° (black line) to α=10° (cyan line). The component of the buoyancy force of the ceiling jet flow along the surface is in the same direction as the upward ceiling front and increases with ceiling slope. This component acts on the saltwater ceiling jet to accelerate the flow. But the component of the buoyancy force perpendicular to the ceiling decreases as the ceiling slope increases, which inhibits entrainment of freshwater into the saltwater ceiling flow. Entrainment of ambient

flow (water) is the major mechanism in decreasing the ceiling jet flow density difference.

Conversely, on the lower side of the ceiling plate ($S_1/H<0$), we can observe that the density difference, $\theta_{sw}/(\theta_{sw})_c$, increases slightly as the inclined angle decreases, which is exactly the opposite of the upward direction. This is because the influence of the buoyancy component force has an opposite impact for upward flow and downward flow. As shown in Fig. 5.8, $\theta_{sw}/(\theta_{sw})_c$ first decreases with a faster decay rate. Then, a sudden switch occurs and the density difference approaches zero. As mentioned earlier, in downward direction, the buoyancy component of the ceiling jet flow is in the opposite direction to the flow motion, which causes the flow stagnate at certain distance. The density difference drops drastically where the downward flow cannot reach, and causes an abrupt decay ($\theta_{sw}/(\theta_{sw})_c \approx 0$). This transition has been more recently investigated by Oka *et al.* [79] for pool fires and the travelling distance along the inclined ceiling to the transition point was called the back-layering, or penetration distance.

Focusing on the downward region of the ceiling jet, the saltwater density approaches the fresh water density with an increase in the distance from the impingement point of the plume. The point where the density difference becomes zero should also correspond to the location where the saltwater flow separates from the sloped surface and starts to turn up and reverse. The distance from the point where either the density difference is zero, or the velocity on the lower side of the slope shows an inflection point, is called penetration distance. The analysis of both ceiling jet characteristics on the downward and upward direction displayed in Figs. 5.7 and

5.8 therefore enables to estimate the penetration distance for each slope inclination, α. Figure 5.9 shows all measured distances extracted from Figs. 5.7 and 5.8 and displayed over the range of slopes assumed in this study.

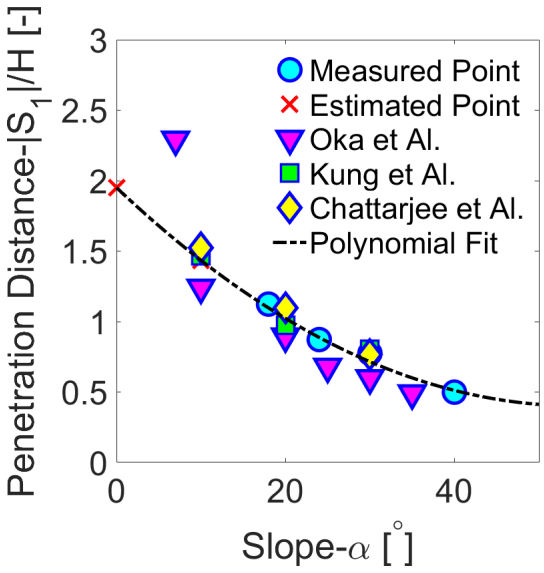

Figure 5.9: Dimensionless penetration distance, $|S_1|/H$, measured on the downward direction of the slope ($S_1/H<0$) from the impingement point of the plume. Data are extracted from both PIV (velocity) and PLIF (density difference) measurements for α ranging from 0° to 40°. For α=0° and α=10°, the penetration distance (red cross) is estimated to be off of the unconfined plate, based on a quadratic polynomial fit of the measured data for higher slopes. Saltwater measurements are compared with fire data sets resulting from Kung *et al.*'s predicting model [77], Oka and Imazeki's measurements [79] and Chatterjee *et al.*'s CFD simulations [82].

The predicted penetration distances are then compared in Fig. 5.9 with fire experimental data of Oka *et al.* [79], fire experimental correlations from Kung *et al.* [77], and FireFOAM simulations from Chatterjee *et al.* [82]. For all data sets, a general trend of penetration distance decreasing with increasing inclination is observed, and good agreement between saltwater measurements, Kung *et al.*'s predic-

tions and Chatterjee *et al.*'s computational analysis is found. The lower penetration depth estimates of Oka *et al.* [79], compared to the other fire data sets and saltwater results differ somewhat, however. A likely explanation lies in the approach used. In Oka *et al.*'s [79], where only velocity measurements were used to estimate the penetration distance biasing results obtained using temperature measurements. In fact, according to Oka *et al.*, thermal diffusion, which dominates the flow, would cause the temperature to remain above T_0 (ambient temperature) for a greater distance than where the velocity becomes zero, therefore explaining the differences with Kung *et al.* and Chatterjee *et al.* On the other hand, diffusion effects are accounted analyses by both Kung *et al.* and Chatterjee *et al.* such that the estimated penetration distances from velocity measurements match those found by means of temperature measurements. Saltwater measurements are characterized by a reasonable level of turbulence (i.e., $Gr \approx 10^{11}$ at the impingement point) such that the molecular diffusion based on concentration gradients is overtaken by faster turbulent diffusion. Velocity is also regulated by turbulent mixing, therefore, both velocity and density difference are governed by the same mechanism which leads to a similar penetration distance, where both characteristics become zero and the flow reverses.

A different scenario is represented in the case of the α=0° and α=10° angled plate. Here, the penetration distance is extrapolated from a quadratic polynomial fit of the measured data for higher slope angles (from α=18° to α=40°), as shown in Fig. 5.9 (red cross ticks). As previously discussed, the lack of an adverse buoyancy force component for α=0° and a very low adverse component for α=10° along the lower side of the ceiling plate enables both flows to move downward and reach the

penetration distance point at a further down (i.e., out of the plate boundaries).

Upslope Ceiling Jet Momentum (δ_u, L_u) and Thermal (δ_θ, L_θ) Layers

The analysis presented above, conducted on the upslope and downslope ceiling jet, allows the following observations to be drawn: (1) ceiling inclination causes biased flow towards the elevated side of the ceiling due to buoyancy and (2) the downslope ceiling jet flow tends to reverse earlier and slowing down faster at increasing ceiling slopes.

Therefore, at increasing inclinations, two different scenarios emerge in the downslope and upslope directions. On one hand, the downslope flow is approximately resolved with knowledge of the penetration distance (Fig. 5.9), and the time after the impingement needed to reverse and slow down the front of the plume: this information, in terms of time (t_{FA}) and space, is quite relevant in the investigation of the activation time (t_{act}) and the sprinkler spacing, as later discussed in Chapter 6. On the other hand, according to Chatterjee [76], the biased ceiling flow developing upward rises major concerns regarding (1) possible sprinkler delays and (2) sprinklers further away from the fire source activating first (with delayed activation times), causing the need for high sprinkler densities resulting from larger fire size [76]. These concerns motivate the current interest in studying the ceiling jet flow characteristics (particularly in the upslope direction) because of their correlation with the activation in inclined fire scenarios (Chapter 6). In light of the aformentioned correlation, the physics of the ceiling jet thermal, L_T, and momentum, L_u, layers becomes a priority when studying the upslope ceiling jet at increasing slope angles.

These represent the environment in which suppression systems operate, and as such, they are affected by increasing slopes.

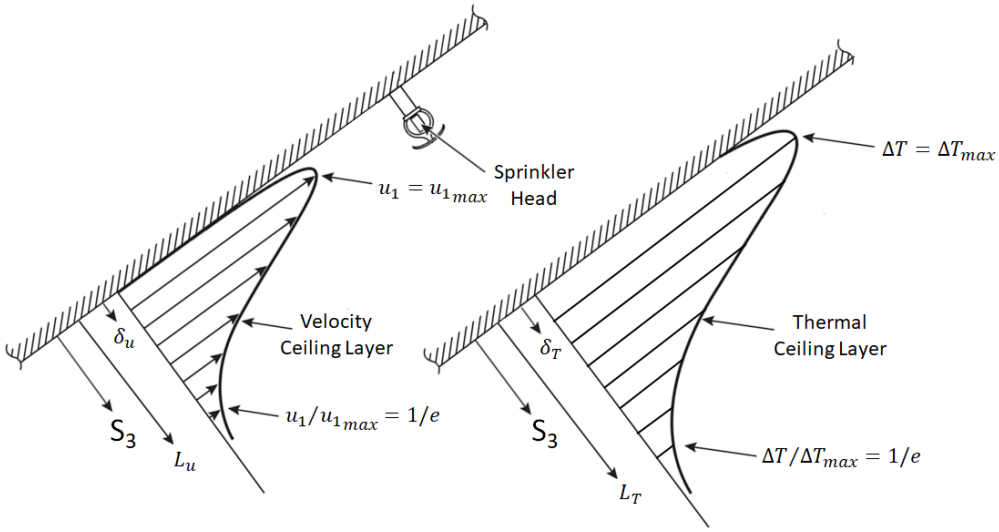

Figure 5.10: Schematic of the ceiling jet layers (momentum and thermal) and their characteristic parameters.

Figure 5.17 shows a schematic of the key parameters that define both momentum (L_u) and thermal (L_T) ceiling jet layers of a ceiling jet flow developing on a sloped surface. L_u and L_T are regions where the effects of the viscous and the thermal interactions between ceiling jet and solid surface are bounded. Hence, as shown in Fig. 5.17, each layer (momentum and thermal) is given as the sum of two sub-layers: the boundary layer and the half-Gaussian layer, as reported in Eqs. 5.1

$$L_u = \delta_u + l_{u_{1/e}}, \qquad L_T = \delta_T + l_{T_{1/e}} \tag{5.1}$$

The momentum and thermal boundary layer thickness are denoted as δ_u and δ_T, respectively. These two quantities identify a region of the jet where flow velocity and temperature vary from the wall no-slip conditions to maximum values, u_{1max}

and ΔT_{max}, with higher intensity of both viscous and thermal (e.g. heat transfer) effects [94, 133]. At distances beyond the boundary layer (δ_u and δ_T), the ceiling jet flow behaves like a free jet and an additional layer, called half-Gaussian layer ($l_{u_{1/e}}$ and $l_{T_{1/e}}$), extends the ceiling jet region growth until the point where $\Delta T/\Delta T_{max} = 1/e$ for the thermal layer and $u_1/u_{1max} = 1/e$ for the momentum layer, respectively. It is important to note that values of u_1 and ΔT discussed here, as well as their respective maxima, u_{1max} and ΔT_{max}, are assumed as time-averaged values. This also implies that corresponding values in the saltwater analogy frame are assumed likewise.

According to Alpert's results [144], fire detectors and sprinklers can be placed at distances from the ceiling that are either outside or inside the boundary layer (δ_u and δ_T) and therefore experience a range of temperatures and velocities depending on where the standoff distance of a sprinkler, ξ, lays (δ_u, δ_T or $l_{u_{1/e}}$, $l_{T_{1/e}}$). In facilities with very high ceilings, the suppression sytems (or detectors) can be closer to the ceiling than 1-2% of the fire source-to-ceiling separation and will fall in the ceiling jet thermal and momentum boundary layers. Beyond this range, the sprinkler operates in the half-Gaussian layer, and past this region, both temperatures and velocities drastically drop. Alpert [145] locates this low temperature/velocity outer region of the ceiling jet is at about 12-13% of the ceiling height at the impingement point, H. In case suppression or detection systems are submerged at a distance greater than 12-13% of H, their response time increases.

Given the synopsis of the literature review (Chapter 2), it appears that slope-dependent correlations were only found for δ_v and δ_T because of the focus on earlier

activation of suppression systems based on maximum ceiling jet characteristics (best case scenario) [83]. To the best knowledge of the author, studies in the literature [83] only proposed correlations between slope and boundary layers (within the ceiling jet), given the interest in determining the conditions (maximum temperature and velocity) for quick activation of the suppression systems. On the contrary, a lack of similar correlations for the ceiling jet layers, L_u, L_T, was found for sloped ceiling fire scenarios [145]. Given the fact that suppression systems could operate in the half-Gaussian layer (beyond the boundary layer) [144], where lower temperatures and velocities than those of the boundary layer correspond larger delay times, a dedicated analysis is here presented. The objective of this study is that to determine correlations able to predict the local extent of both momentum and thermal layers, in response to a given ceiling angle, α, falling in the range 0° to 40°. This would provide a quite powerful predictive tool to quickly determine the operative environment (velocity and temperature) for sprinkler sensitive element design.

The idea of building empirical correlations for both L_u, L_T as functions of slope, α, involved several steps, which included: (1) an estimate of the velocity and density difference profiles along the perpendicular to the plate, S_3; (2) the evaluation of both momentum, δ_u, and "thermal", δ_θ, boundary layers; (3) the use of a regression least-squared method (see Appendix A.1) to generate an empirical correlation able to predict $L_u(\alpha, S_1/H)$ and $L_T(\alpha, S_1/H)$ for each slope, α. For this last step, only cases at 0°, 10°, 18°, 24° and 40° were employed in the method, while data points for 30° slope were used to validate the correlation. The results for this analysis (Figs. 5.11 to 5.17) were obtained as following described.

For each slope, saltwater measurements of u_1 and θ_{sw} were collected along S_1 (upward) for about a hundred points in the interval from ≈0 to ≈32 cm from the impingement point. Four probe locations total were picked to be displayed in Fig. 5.17 at S_1 ≈8 cm, S_1 ≈16 cm, S_1 ≈24 cm and S_1 ≈32 cm respectively, but all points were employed for the curves obtained by means of the regression method and shown in Fig. 5.17. For all locations considered along S_1, u_1 and θ_{sw} in the perpendicular direction to the ceiling plate, S_3, were evaluated spanning from ≈0 to ≈6 cm below the surface. These data points were also used to determine the boundary layers (δ_u and δ_θ in Figs. 5.12 and 5.15) and therefore L_u and L_T in Fig. 5.17.

Figure 5.11 shows both dimensionless u_1^* and θ_{sw}^* centerline profiles along the S_3 direction in the range of slopes assumed in this study. Both dimensionless u_1^* and θ_{sw}^* displayed in Fig. 5.11 are extracted from saltwater measurements at S_1=16 cm from the impingement point. From Fig. 5.11(a) and (b), the flow appears well resolved, revealing both the boundary layer close to the surface (corresponding to the peak), followed by a Gaussian-decaying jet region along S_3. As shown in Fig. 5.11(a), the velocity increases with an increase in the slope angle of the ceiling and similarly does the density difference, θ_{sw}^*, as shown in Fig. 5.11(b). The distribution profiles are thought to depend on the increase in buoyancy of the ceiling jet with the slope along the S_1 upward direction which is proportional to $g \cdot sin\alpha$. On the other hand, the component of the buoyancy perpendicular to the sloped plate (proportional to $g \cdot \cos\alpha$) should decrease as the slope increases. This inhibits the entrainment of fresh water into the saltwater ceiling jet flow while moving upward, as also confirmed by a denser flow of the jet front captured through PLIF raw im-

ages. Entrainment of fresh water is a major mechanism in decreasing the ceiling jet density difference.

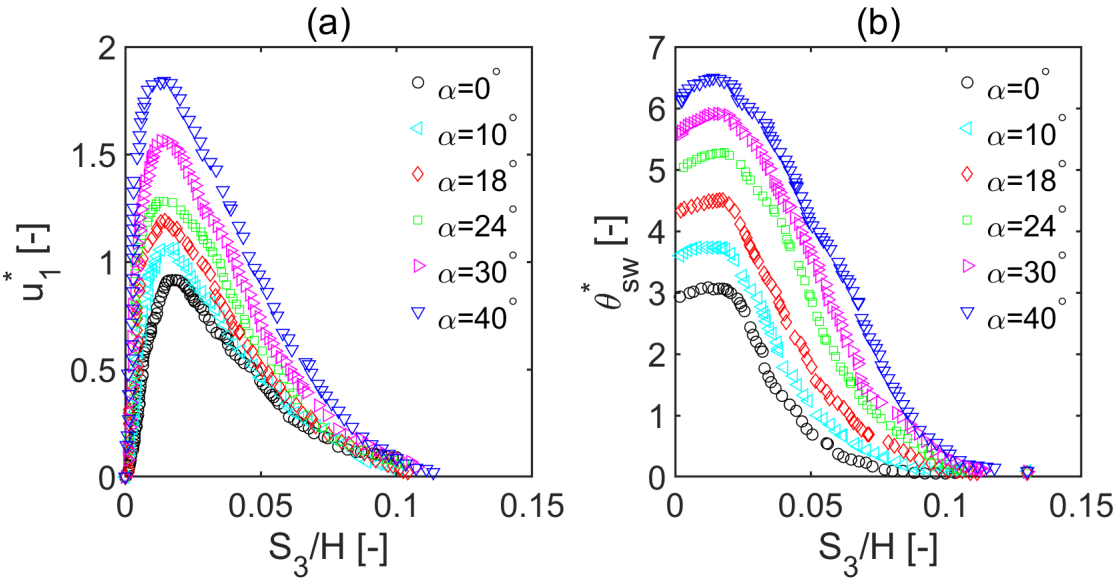

Figure 5.11: Sloped ceiling jet raw dimensionless profiles of u_1^* (a), and θ_{sw}^* (b) below the ceiling plate at S_1 located 16 cm from the impingement point.

Positions for $u_{1_{max}}^*$ and $\theta_{sw_{max}}^*$ which define δ_u and δ_θ along S_3 were estimated at each point, based on a Gaussian fit to data from points in proximity of the measured maxima. Note that the difference between the measured maxima and maxima based on the Gaussian fitting has never exceeded 3%. Subsequently, the locations where $u_{1_{max}}^*$ and $\theta_{sw_{max}}^*$ both decrease by a factor $1/e$ were identified, thus obtaining the half-Gaussian layers for velocity, $l_{u_{1/e}}$, and the density difference, $l_{\theta_{1/e}}$, respectively. Based on Eqs. 5.1, saltwater ceiling jet Gaussian layers for u_1, L_u, and θ_{sw}, L_θ, were eventually determined. Results for the ceiling jet boundary layers (δ_u and δ_θ) and Gaussian layers (L_u and L_θ) are displayed in Figs. 5.12, 5.15 and 5.17. It

should be noted that the curves displayed in Fig. 5.17 are the result of the non-linear least-squares method employing the L_u and L_θ data points extracted from the measurements, and not the straight L_u and L_θ calculated at each S_1/H location using Eqs. 5.1. This is because the objective was to generate a α-dependent correlation able to predict the extent of L_u and L_θ for any angle in the range 0° to 40° along S_1/H.

Therefore, an analysis of both dimensionless δ_u/H and δ_θ/H against S_1/H is shown first, along with a comparison to fire tests on both horizontal and inclined ceilings. The results displayed in Figs. 5.12 and 5.15 are represented by measurement data points estimated at nine locations and overlaid on top of the fitting curves (dotted lines) obtained by means of all measured points. Second, the empirical correlations developed to predict dimensionless L_u/H and L_θ/H in the upslope direction S_1/H at increasing α inclination angles are described.

The momentum boundary layer thickness, δ_u, was extracted from PIV saltwater measurements (Fig. 5.12(a)) and compared with previous work for fire horizontal ceilings from Alpert [133], Cooper [134], Motevalli *et al.* [135], saltwater measurements from Yao [94], and fire experiments for a similar slope range from Oka and Ando [83] (Fig. 5.12(b)). Our data set for horizontal ceiling (black circles) showed to be consistent with Yao's data which in turn were closer to Motevalli's model and similar to Oka and Ando's PIV-based experimental correlation [83]. From the comparison, saltwater results for horizontal ceilings (black dotted line) appeared to: (1) converge and predict Oka *et al.*'s δ_u growth for $S_1/H \leq 0.4$ (range not investigated by Oka *et al.*), while over-predicting their estimates for $S_1/H \geq 0.4$, (2) consistently

fit Yao's saltwater results [94] and (3) well approximate the rate of growth for δ_u based on Motevalli's correlation.

First, large differences with Oka *et al.* in the range $S_1/H \leq 0.4$ (Fig. 5.12) are mostly due to a very large amount of PIV data (based on experiments conducted with several fire sources $\dot{Q}$) used by the author to fit the curves. Although based on quality data and large number of images for data processing, the results presented here are limited to the use of one $\dot{m}^*_{sw}$ only. Multiple source strengths, $\dot{Q}$, should be explored in the future to evaluate the exclusive dependency of δ_u from the inclination angle, α, and the radial distance from the impingement point, S_1/H, when the source is on the order of several tens of kilowatts , as reported by Alpert [92,133]. On the other hand, based on saltwater analogy, Motevalli's similar dimensionless flow conditions, but lower Grashof estimated at the impingement point ($Gr_H \approx 10^9$) should explain the slightly thicker δ_u with a similar rate of growth. Lastly, a matrix of saltwater initial conditions close to that used by Yao [94] for the horizontal ceiling cause his data to fit our curve, also reflecting the change in the rate of growth of δ_u observed starting from S_1/H ≈0.65. Indeed, as previously found by Yao [94], the momentum boundary layer thickness for horizontal ceilings starts to transition from $\delta_u \approx (S_1/H)^{4/5}$ (δ_u=0.0311$(S_1/H)^{0.8}$) to $\delta_u \approx (S_1/H)^{1/2}$ (δ_u=0.0263$(S_1/H)^{0.47}$) at S_1/H ≈0.65 where the laminarization occurs (Fig. 5.12). However, a different scenario occurred for slopes from 10° to 40°: the boundary layer thickness, δ_u, was observed to get marginally thinner at increasing slopes (faster ceiling jet), and increase along S_1/H at a constant rate of growth. The trend for these cases was found

to follow a specific power law fit, as the one reported in Eq. 5.2

$$\delta_u \approx a\,(S_1/H)^n \tag{5.2}$$

where a (depending on local velocity) and n are coefficients estimated for each slope by fitting the saltwater measured points. Values for n were found to be in the range 0.8-0.87. These values indicate a typical turbulent regime in the boundary layer region, as also reported in Cooper's work [134], where $\delta_u \approx (S_1/H)^{0.9}$ power law was found for horizontal ceilings.

In support of the turbulent regime of the boundary layer observed through the measurements, a qualitative analysis based on time probability density function for the density difference, $PDF_t(\theta^*_{sw})$, was assessed using PLIF instantaneous images. Two probe locations, one at S_3 ≈2 mm (within the boundary layer) and one in the peripheral region of the ceiling layer at S_3 ≈3.5 cm (out of the boundary layer) were chosen, and the results are shown in Figs. 5.13 and Figs. 5.14 for α=0° and α=40°, respectively. This investigation, presented for the two cases at different heights and two different slopes, was not intended to discuss the turbulence in detail (e.g. turbulent scales), but rather provide a qualitative picture of the turbulent mixing behavior at these locations to better interpret and substantiate the results shown in Figs. 5.12 and 5.15.

By first comparing the $PDF_t(\theta^*_{sw})$ obtained for the horizontal ceiling at two different locations (Figs. 5.13(a), (b)) in the perpendicular direction to the plate, S_3, the appearence of the two distributions revealed two different scenarios. In the inner part (i.e. S_3 ≈2 mm within the boundary layer), a double peak distribution of θ^*_{sw}

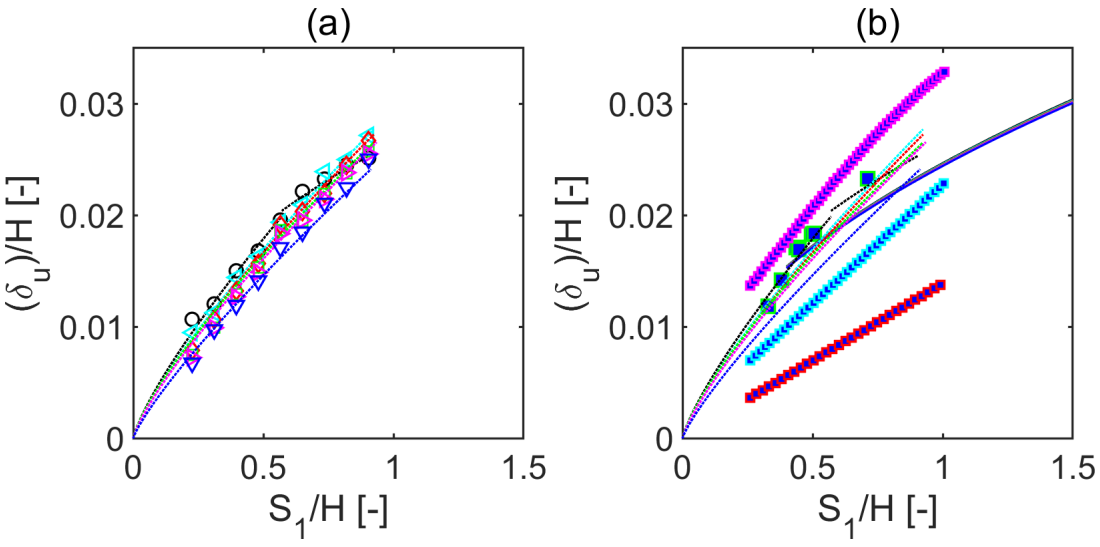

Figure 5.12: Momentum boundary layer δ_u; (a) saltwater measurements at α=0° (○); α=10° (◁); α=18° (◇); α=24° (□); α=30° (▷); α=40° (▽); (b) comparison between measurement fit curves and Motevalli and Mark [135], Cooper [134], Alpert [133], Oka *et al.* [83] and Yao [94]; δ_u=0.0311$(S_1/H)^{0.8}$ and δ_u=0.0263$(S_1/H)^{0.47}$ (·····) for α=0°; δ_u=0.0295$(S_1/H)^{0.8}$ for α=10° (·····); δ_u=0.0292$(S_1/H)^{0.8}$ for α=18° (·····); δ_u=0.0282$(S_1/H)^{0.8}$ for α=24° (·····); δ_u=0.028$(S_1/H)^{0.8}$ for α=30° (·····); δ_u=0.026$(S_1/H)^{0.87}$ for α=40° (·····); Motevalli and Mark's correlation for α=0° (■); Cooper's correlation for α=0° (■); Alpert's model for α=0° (■); Yao's saltwater data for α=0° (■); Oka *et. al* measurements at α=0° (—), α=10° (—), α=18° (—), α=24° (—), α=30° (—) and α=40° (—).

at low θ^*_{sw} values occurred. The double peak suggests fluctuations and unmixedness (intense mixing) between two predominant values, but both peaks appear near the well-mixed flow condition ($\theta^*_{sw} \approx 0$), as shown in Fig. 5.13(a). On one hand, the intense mixing shows to be consistent with the large entrainment found for horizontal ceilings [77, 94] promoted by a favorable buoyancy component along the perpendicular to the ceiling, while the two close peaks of the $PDF_t(\theta^*_{sw})$ (small concentration

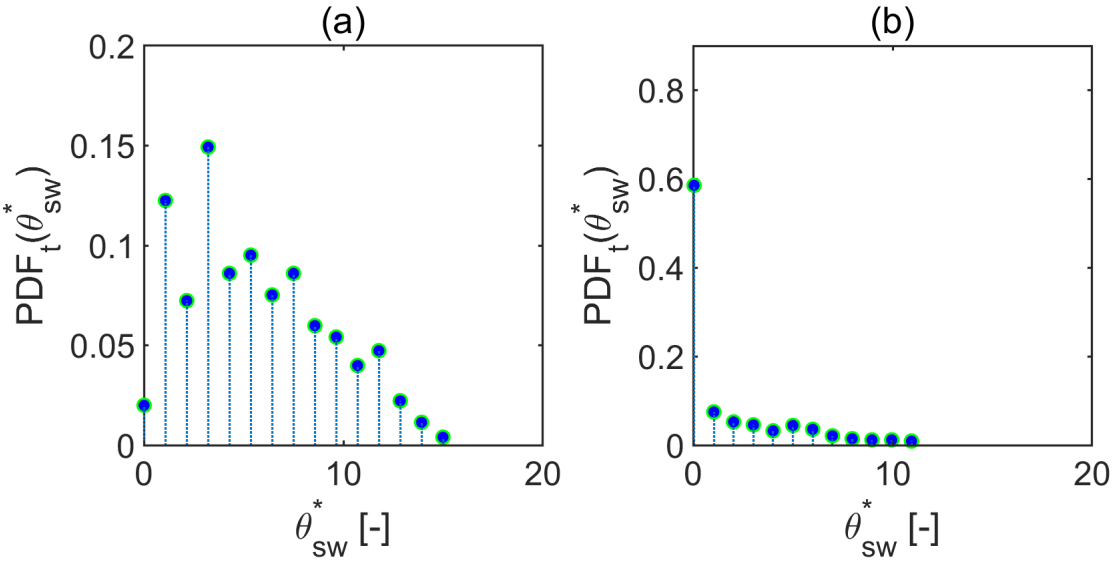

Figure 5.13: Horizontal ceiling temporal probability density function for density difference, $PDF_t(\theta^*_{sw})$, for S_1/H=0.4 estimated at (a) S_3/H ≈0.006 and (b) S_3/H ≈0.1.

gradients) indicate that mixing and transport are dominated by smaller vortices. The size of these eddies is suggested by lack of higher θ^*_{sw} values that would otherwise generate stronger gradients (indicative of large eddies) and a by lower eddy kinetic energy level (compared to the case at α=40°), $\epsilon = u_l^3/l$, being u_l the velocity gradient (within δ_u) across the size of an eddy, l. This observation was inferred from previous results illustrated in Fig. 5.7, where flat ceilings show lower velocities (and lower velocity gradients given the results in Fig. 5.12) compared to those at higher slopes.

Further proof of the turbulence and intense mixing within the boundary layer (Eq. 5.2) comes from the presence of fresh water ($\theta^*_{sw} = 0$ in Fig. 5.13(a)) that penetrates to the ceiling surface by means of larger entraining vortices located in

the outer layer (S_3/H ≈0.1), as already observed in the raw images (Fig. 5.5). At the same time, these larger vortices, which extend their influence to both inner and outer region of the ceiling layer, transport from the inner (S_3/H ≈0.006) to the outer (S_3/H ≈0.1) region parcels of high concentration fluid ($\theta^*_{sw} > 0$), as shown in Fig. 5.13(b).

By plotting the results for α=40° for the same S_3/H locations (Fig. 5.14), further comparison between the two slopes at 0° and 40° was possible. The distribution of θ^*_{sw} found within the boundary layer shows less intense turbulent mixing occurring (single peak Gaussian distribution in Fig. 5.14(a)), compared to that of 0° slope (bi-modal distribution in Fig. 5.13(a)). This appears to be consistent with the small entrainment of fresh water at α=40° (Fig. 5.4) depending on the reduced buoyancy component along the perpendicular to the ceiling. In addition to this, the higher average velocity (or higher local Re) compared to that of the horizontal ceiling (Fig. 5.7) yields a scenario where larger unstable vortices are in charge of transporting mass and energy. These large eddies are because of the higher vortical energy content of the flow (according to Kolmogorov's energy cascade [54]), i.e. eddy kinetic energy, $\epsilon = u_l^3/l$, being u_l the velocity gradient (within δ_u) across the size of the eddy, l).

Lastly, for α=40°, no fresh water is seen to penetrate to the wall as shown in (Fig. 5.14); this aspect seems to confirm the lower entrainment at higher slopes due to a lower buoyancy component perpendicular to the surface. Substantial confirmation of this observation comes also from Alpert's work on ceiling jet layers [133], where the entrainment, E, is a function of both local buoyancy and kinetic energy

through $Ri = Gr/Re^2$ as $E \propto e^{-3.9Ri}$.

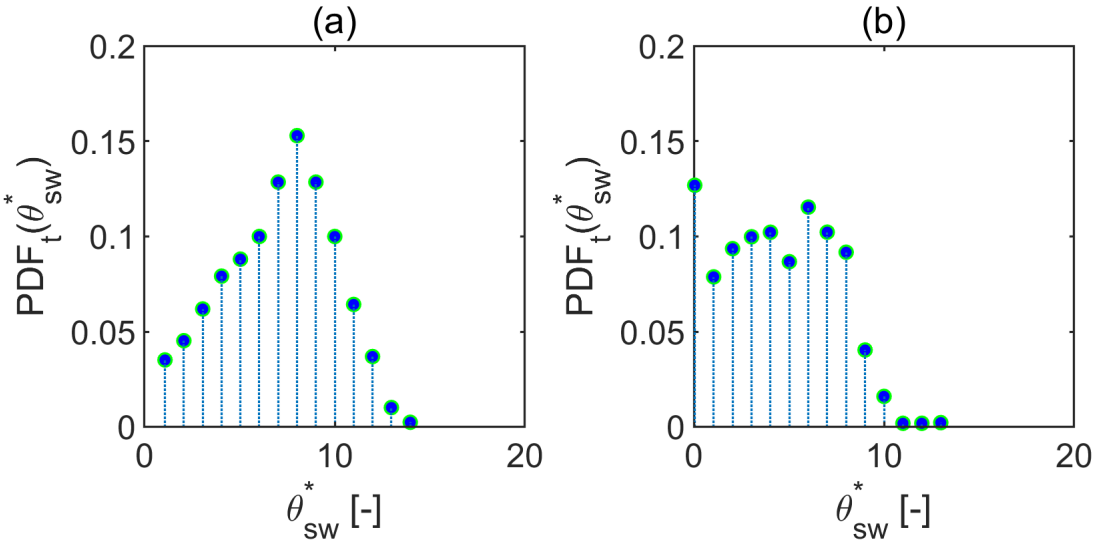

Figure 5.14: Temporal probability density function for density difference, $PDF_t(\theta^*_{sw})$, at α=40° for S_1/H=0.4, estimated at (a) S_3/H ≈0.006 and (b) S_3/H ≈0.1.

From Fig. 5.12, higher slopes do not show the turbulent-to-laminar transition (laminarization) experienced by the horizontal ceiling (black circles in Fig. 5.12). For the latter (α=0°), it is reasonable to assume that the momentum boundary layer growth is retarded, as the initial momentum of the ceiling jet diminishes due to increasing viscous losses. On the other hand, as we increase the inclination angle, the momentum boundary layer increases indefinitely (according to the general Eq. 5.2) due to an increasing buoyancy content (higher velocity) which opposes to viscous forces along the upslope. It was well established by Cooper [133,134] that for small to moderate values of radial distance from the impingement point ($0.2 < S_1/H < 1.3$), inertial forces are generally large compared to buoyancy forces in the momentum

boundary layer of a plume-driven ceiling jet. Based on an extensive study, Cooper concluded that flow characteristics of δ_u over a plate are very similar to those of free turbulent wall jets (unheated or weakly heated), when next to the ceiling plate. Thus, for the similar range investigated in this study ($0.2 \leq S_1/H \leq 0.95$), the ceiling jet driven by the saltwater plume was presumedly charcterized by identical flow properties describing an equivalent momentum-driven free jet over a plate. The criteria of equivalence, originally proposed by Alpert [133], assumed identical mass and momentum for both types of flows (plume and free jet) at their respective impingement points. In light of this, the power law for δ_u reported in Eq. 5.2, typically representing a crude approximation for free jet turbulent boundary layers, found validation in the saltwater measurements framework.

Using a similar method to that used for the velocity field, the "thermal" (concentration) boundary layer thickness, δ_θ, was determined using density difference images from PLIF tests. As shown in Fig. 5.15(a), the δ_θ boundary layer thickness values appeared to be very close to those evaluated for the momentum layer, δ_u (Fig. 5.12(a)), in the range α=0° to α=40° ($\delta_u \approx 97\%$ of δ_θ). This result was expected given the high Grashof number at the impingement point ($Gr_H \approx 10^{11}$) which ensured momentum transport (in δ_u) and mass transport (in δ_θ) to be governed by turbulence along the plate, rather than diffusion. In fact, in a turbulent environment, the ratio of δ_u to δ_θ is no longer provided by the $\delta_u/\delta_\theta \approx Sc^{1/3}$ relationship (typical of laminar flows), but rather by $\delta_u \approx \delta_\theta$ [75], which consistently matches with $\delta_u \approx 97\%$ of δ_θ. Additionally, as earlier discussed in Sec. 3.2.3, a highly turbulent flow near the ceiling wall allows to overcome the distortion of the saltwater

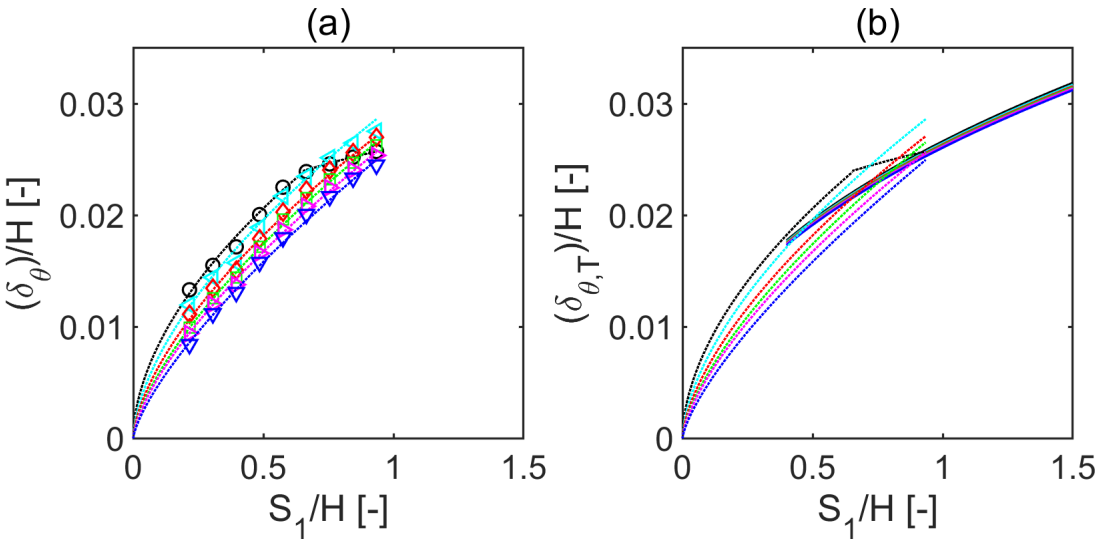

Figure 5.15: "Thermal" boundary layer for saltwater, δ_θ, and fire, δ_T, measurements; (a) saltwater measurements (δ_θ) at α=0° (○); α=10° (◁); α=18° (◇); α=24° (□); α=30° (▷); α=40° (▽); (b) comparison between measurement fit curves (dotted lines) and fire experiments (solid lines) from Oka *et al.* [83]; δ_θ=0.03017$(S_1/H)^{0.55}$ and δ_θ=0.02606$(S_1/H)^{0.2}$ (·····) for α=0°; δ_θ=0.0298$(S_1/H)^{0.6}$ for α=10° (·····); δ_θ=0.02828$(S_1/H)^{0.63}$ for α=18° (·····); δ_θ=0.02777$(S_1/H)^{0.67}$ for α=24° (·····); δ_θ=0.02687$(S_1/H)^{0.68}$ for α=30° (·····); δ_θ=0.02622$(S_1/H)^{0.72}$ for α=40° (·····); Oka *et. al*'s δ_T at α=0° (——), α=10° (——), α=18° (——), α=24° (——), α=30° (——) and α=40° (——).

modeling and provide a good analogy with real turbulent fire scenarios (where usually, for $Pr \approx 1$, $\delta_T \approx \delta_u$). From the plot in Fig. 5.15(a), the comparison between different slope cases reveals a similar behavior of that observed for the momentum layer: at increasing inclination angles the thickness appears slightly thinner, and for horizontal ceilings, δ_θ changes its rate of growth after $S_1/H \approx 0.65$ due to laminarization effects. This similitude found between δ_θ and δ_u suggests a similar explanation to that provided for the momentum layer and consistent with the results displayed

in Figs. 5.13 and 5.14. Further comparison with real fire experiments on sloped ceilings up to 40° by Oka *et al.* is provided in Fig. 5.15(b). The curves displayed for saltwater measurements (dotted lines) and for Oka *et al.* small-fire experiments (solid lines) both represent power fit to data curves depending on the inclination angle, α. First, as observed earlier for δ_u, a specific pattern as the one shown in Eq. 5.2 is exhibited by δ_θ for the saltwater fit curves, where the n coefficient is found in the range 0.6-0.7.

To develop an empirical correlation able to describe L_u and L_θ at any inclination angle included in the range 0° to 40°, L_u and L_θ data points, obtained feeding Eqs. 5.1 with measurements of δ_u, δ_θ, $l_{u_{1/e}}$ and $l_{\theta_{1/e}}$, were employed along with a modified function of slope α formulated by Alpert [133] for horizontal ceiling. Based on Alpert's observations, both L_u and L_T for horizontal ceiling fire experiments should behave according to the following functions:

$$\frac{L_u}{H} = A_u \left[1 - e^{B_u\left(\frac{S_1}{H}\right)}\right] \tag{5.3}$$

$$\frac{L_T}{H} = A_T \left[1 - e^{B_T\left(\frac{S_1}{H}\right)}\right] \tag{5.4}$$

Both Eqs. 5.3 and 5.4 are exponential functions depending on the dimensionless upslope distance from the impingement point, S_1/H, and coefficients A_u, B_u, A_T, B_T, depending on the ceiling angle, α. The same non-dimensional equations were extended to the saltwater frame, as follows:

$$\frac{L_u}{H} = A_u \left[1 - e^{B_u\left(\frac{S_1}{H}\right)}\right] \tag{5.5}$$

$$\frac{L_\theta}{H} = A_\theta \left[1 - e^{B_\theta\left(\frac{S_1}{H}\right)}\right] \tag{5.6}$$

Given Eqs. 5.5 and 5.6, the objective was to find a function for coefficients A_u, B_u, A_θ, B_θ explicitly depending on α, such that Eqs. 5.5 and 5.6 could be turned into a predictive tool for L_u and L_θ at any slope between 0° and 40°.

Hence, based on the relationship between the ceiling jet layers, L_u and L_θ, and the upslope distance, S_1/H, for each inclination angle, the two sets of coefficients, (A_u, B_u), for u_1, and (A_θ, B_θ), for θ_{sw}, were determined using nonlinear regression analysis (least squared method) by fitting Eqs. 5.5 and 5.6 to the saltwater measured data of L_u and L_θ from the experiments. The values estimated for the coefficients (A_u, B_u), and (A_θ, B_θ) are displayed in Fig. 5.16.

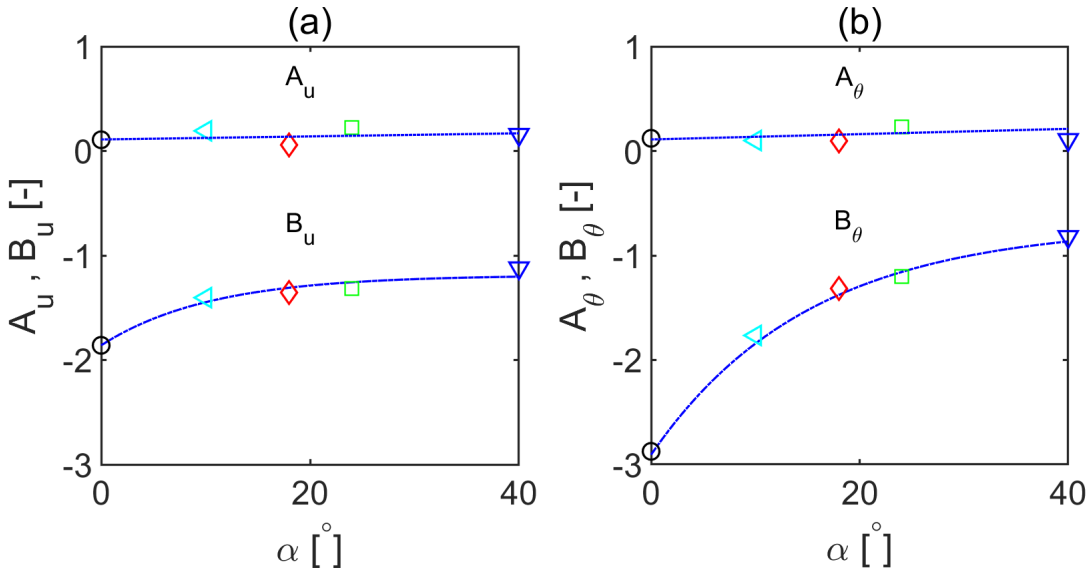

Figure 5.16: Variation of momentum (A_u, B_u) and density difference (A_θ, B_θ) ceiling jet layer coefficients with the inclination angle; (O) α=0°; (◁) α=10°; (◇) α=18°; (□) α=24°; (▽) α=40°; (- - -) A_u and A_θ coefficients; (-·-·-) B_u and B_θ coefficients.

Details of the calculation method using the least-squares technique are de-

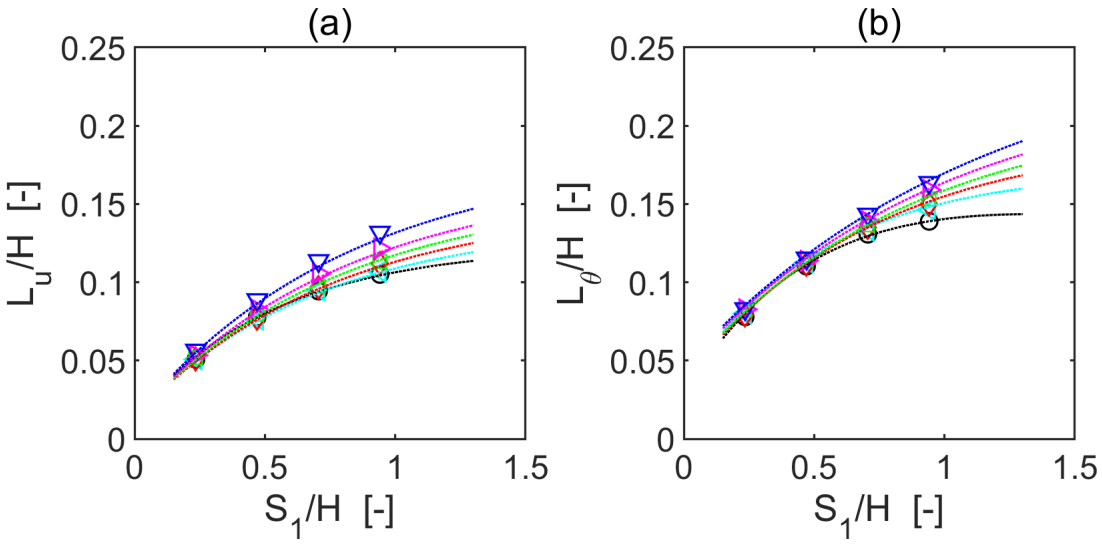

Figure 5.17: Ceiling jet layers, L_u and L_θ, for slope inclinations 0° to 40°. The correlations were developed based on data resulting from 0° to 24° slope cases, whereas measurements of L_u and L_θ at 30° (▷) were used to test the predictibility of the empirical correlations on higher slopes; empirical correlations: (·····) α=0°; (·····) α=10°;(·····) α=18°; (·····) α=24°; (·····) α=30°; (·····) α=40°; saltwater measurements: (○) α=0°; (◁) α=10°; (◇) α=18°; (□) α=24°; (▷) α=30°; (▽) α=40°.

scribed in detail in Appendix A.1. To be able to test the empirical correlation tool, both L_u and L_θ thicknesses (dotted lines in Fig. 5.17) were determined by employing data from α=0° to α=24° and α=40° in the regression analysis, whereas measurements extracted from tests at α=30° were only used to validate the predicting correlations.

Based on the results for A_u, B_u and A_θ, B_θ, the following empirical correlations for L_u and L_θ were found as function of the slope α (Fig. 5.17).

$$\frac{L_u}{H} = (0.0015\alpha + 0.12)\left[1 - e^{\left[-1.87+0.68\left(1-e^{-0.09\alpha}\right)\right]\frac{S_1}{H}}\right] \tag{5.7}$$

$$\frac{L_\theta}{H} = (0.0025\alpha + 0.15)\left[1 - e^{\left[-2.92+2.21\left(1-e^{-0.06\alpha}\right)\right]\frac{S_1}{H}}\right] \tag{5.8}$$

Figure 5.17 shows that profiles for L_u and L_θ (dotted lines) agrees well with values extracted from measurements (ticks in Fig. 5.17) at $S_1/H \approx 0.2$ (S_1=8 cm), $S_1/H \approx 0.5$ (S_1=16 cm), $S_1/H \approx 0.7$ (S_1=24 cm) and $S_1/H \approx 0.95$ (S_1=32 cm). In particular, this can be seen for the case at α=30° used to test the effectiveness of Eqs. 5.7 and 5.8 in predicting the layers thickness. At each location, the "thermal" (concentration) ceiling layer appears to be greater than the corresponding velocity layer at the same slope, as expected [133, 135]. For both L_u and L_θ, it is observed that thicknesses gradually increase with the increase of the inclination angle of the ceiling. For the horizontal ceiling (black dotted line and circles), the growth of L_u and L_θ is retarded as S_1/H increases and they approach a constant thickness. This asymptotic behavior is particularly evident for L_θ profile at locations $S_1/H \geq 0.65$ and thought to be due to the effect of an increasing Richardson number (laminarization).

Therefore, Eqs. 5.7 and 5.8 provide handy empirical correlations able to quickly trace back both the temperature and velocity conditions at which a given sprinkler head should operate. Indeed, as shown in Figs. 5.17, the observation data points for the case at α=30° (not involved in the least-squares method but only used to test the fit of L_u and L_θ with the observations) well agreed with the predicted model function resulting from Eqs. 5.7 (for velocity) and 5.8 (for density difference). This, although limited to one case (α=30°), indicates that L_u and L_θ can be easily determined for any ceiling inclination of interest in the range 0° to 40° for $0.2 < S_1/H < 1.3$. Future studies should extend to other α-angles (within the range 0° to 40° proposed) to provide a larger database to validate the model described in Eqs. 5.7 and 5.8

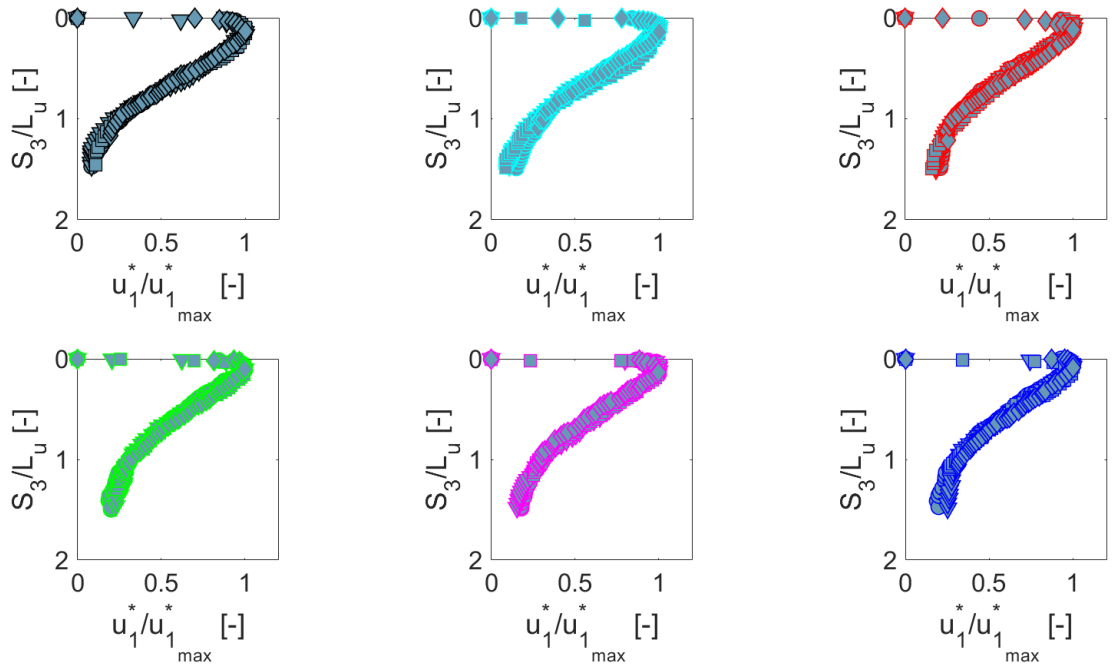

Figure 5.18: Sloped ceiling jet dimensionless velocity similarity profiles at S_1 located at 8 cm (α=0° ●; α=10° ●; α=18° ●; α=24° ●; α=30° ●; α=40° ●), 16 cm (α=0° ▼; α=10° ▼; α=18° ▼; α=24° ▼; α=30° ▼; α=40° ▼), 24 cm (α=0° ■; α=10° ■; α=18° ■; α=24° ■; α=30° ■; α=40° ■) and 32 cm (α=0° ◆; α=10° ◆; α=18° ◆; α=24° ◆; α=30° ◆; α=40° ◆) from the impingement point.

To complete the characterization of the ceiling jet transport, normalized ceiling layer velocity and density difference profiles were compared at various S_1/H along the ceiling, for all the slopes under investigation, as shown in Figs. 5.18 and 5.19. The dependency from the radial distance from the impingement point of the plume was easily removed for both ceiling jet characteristic distributions by normalizing by their respective maxima, while the coordinate perpendicular to the ceiling plate, S_3, was normalized with respect to the ceiling jet layer thickness (L_u for u_1^* and L_θ for θ_{sw}^*) measured at each radial distance (i.e., S_1=8, 16, 24 and 32 cm from

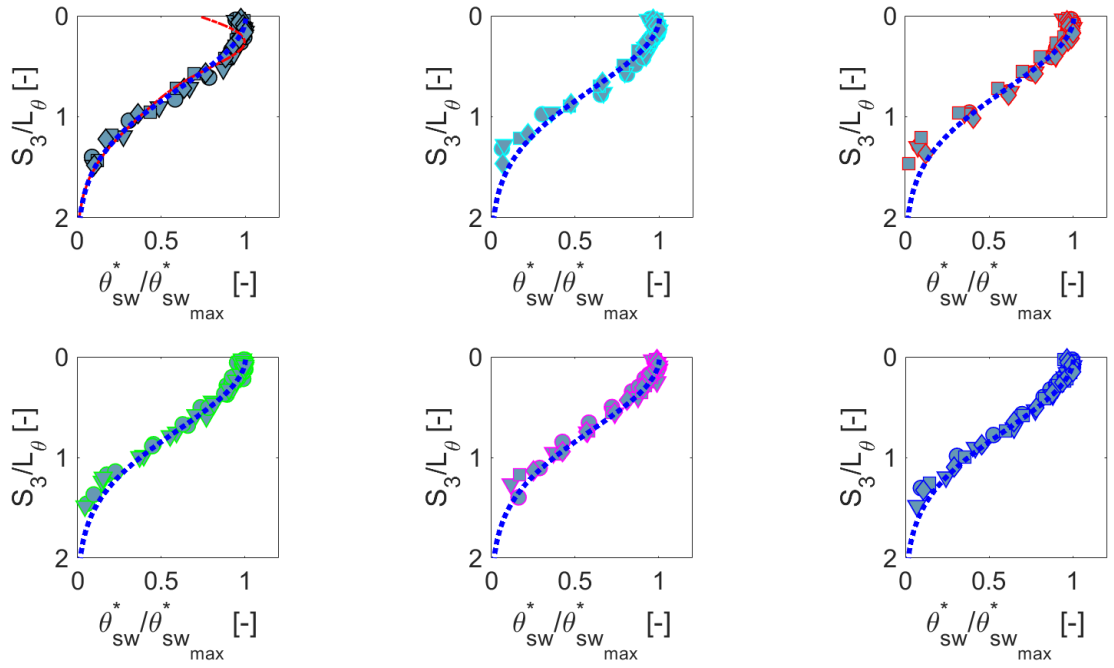

Figure 5.19: Sloped ceiling jet dimensionless density difference similarity profiles at S_1 located at 8 cm (α=0° ●; α=10° ●; α=18° ●; α=24° ●; α=30° ●; α=40° ●), 16 cm (α=0° ▼; α=10° ▼; α=18° ▼; α=24° ▼; α=30° ▼; α=40° ▼), 24 cm (α=0° ■; α=10° ■; α=18° ■; α=24° ■; α=30° ■; α=40° ■) and 32 cm (α=0° ◆; α=10° ◆; α=18° ◆; α=24° ◆; α=30° ◆; α=40° ◆) from the impingement point. Motevalli's correlation for α=0° (-·-·-); half-Gaussian fit (·····)

the impingement point in Fig. 5.17). For 2D wall-bounded flows like that depicted in Fig. 5.17, temperature and velocity similarity is defined as the case where two temperature and velocity profiles from different locations along the slope in the flow direction differ only by a scaling parameter in S_3 and a scaling parameter of the temperature and velocity profile, respectively. The results displayed in Figs. 5.18 and 5.19 show that it is possible to extend the use of L_u and L_θ as scaling parameters from flat ceiling jet flows [133] to sloped ceiling jet flows. This aspect adds

insight into the knowledge of such flows on inclined surfaces (and therefore into the understanting/prediction of detection/activation devices) because it enables to easily describe the flow (temperature and velocity) at any location by assuming that the downstream profiles of the ceiling jet are a stretched version of those upstream.

The choice of L_u and L_θ as reference scales for the distance from the ceiling was based on two main considerations. First, the boundary layer region is driven by the initial momentum of the plume, and the flow velocity and temperature are forced to zero and to ceiling temperature, respectively, from the centerline plume velocity temperature. The buoyancy-dominated outer region (i.e., $l_{u_{1/e}}$ and $l_{\theta_{1/e}}$) of the ceiling jet does not go through the same drastic transformation. Therefore, δ (momentum and thermal) does not have an analogous parameter in the plume whereas L (momentum and thermal) is similar in definition to the plume width, b (see Sec. 3.2.5), the spanwise location (originally defined for the velocity scale) where the maxima at the centerline decrease by $1/e$. Second, the transition $\approx \delta_u^{4/5}$ to $\approx \delta_u^{1/2}$ along S_1/H, experienced just by the horizontal ceiling, does not provide a common baseline for the normalization for all other cases, which follow a $\approx \delta_u^{4/5}$ pattern all along the assumed range of S_1/H (Fig. 5.12).

The dimensionless saltwater profiles of $u_1^*/u_{1_{max}}^*$ and $\theta_{sw}^*/\theta_{sw_{max}}^*$ are well described by a half-Gaussian distribution as expected, based on Alpert's recommendation [93, 133] on horizontal ceilings. By increasing the slope up to 40°, all profiles collapse on top of each other along S_3/L_u for velocity (Fig. 5.18), and along S_3/L_θ for density difference (Fig. 5.19), respectively. The similarity between the characteristic profiles of $u_1^*/u_{1_{max}}^*$ (Fig. 5.18) and $\theta_{sw}^*/\theta_{sw_{max}}^*$ are proved to be indipendent

of the radial distance from the impingement point of the plume and to persist regardless the inclination angle. Particularly for $\theta^*_{sw}/\theta^*_{sw_{max}}$, the zero θ^*_{sw} gradient achieved in proximity to the surface for all slopes consistently follows the adiabatic wall analogy represented by saltwater modeling, as shown in Fig. 5.19. Our data sets also favorably compare with the Motevalli's correlation [135] in the region beyond δ_θ, where the flow behaves governed by buoyancy [136]. The discrepancies with Motevalli's correlation within the thermal boundary layer, and in particular in the no-slip region ($S_3 \approx 0$), are due to Motevalli's correlation inaccuracy in resolving this flow region. In fact, the heat losses at the surface accounted in Motevalli's experiments cause the steep wall gradients and off-ceiling peak temperatures shown by the red dash-dotted line in Fig. 5.19.

In this chapter, transport characteristics and mixing dynamics of inclined ceiling jet flows were analyzed using quantitative measurements of a scaled saltwater flow. Preliminary observations of a faster and denser flow in the upslope, due to a favorable gravity component along S_1/H, were confirmed by PIV and PLIF measurements, respectively. On the other hand, because of an adverse gravity component acting in the lower side of the plate, the flow was found to reverse at a location closer to the impingement point (and over an increasing time) as the slope was increased. This location, also know as penetration distance, was located within the boundaries of the plate for all slopes, except for α=0° and α=10°, where a decreased effect of the gravity component along S_1/H caused the saltawater jet to flow further downslope (S_1/H <0) with no visible flow reversal within the ceiling plate boundaries. As

later discussed in detail in Chapter 6, the knowledge of the penetration distance, along with velocity, temperature and front arrival time in this region, is essential in the selection of the sprinkler type (e.g. standard or quick) and for the sprinkler spacing strategy, given the increasing delay in the activation in between symmetrical locations up- and downslope at increasing angles. Therefore, similar results for α=0° and α=10°, in addition to a similar upslope and downslope behavior for the velocity and the concentration (temperature), are indicative of similar operative conditions for the sprinklers. For $\alpha \geq$24°, the symmetry observed for these flow operative conditions (velocity and concentration) at low angles no longer exists. This suggests that, as the slope increases, fire suppression on inclined ceilings should be approached with a different design for the upward and the downward side of the ceiling, respectively. Particularly, at increasing slopes, the increasingly fast and hot flow developing upslope requires a faster activation response and a larger number of devices to prevent structural damages caused by higher temperatures and higher heat transfer rates.

This investigation also provided scaled engineering tools to determine the regions of interest for suppression and detection devices based on velocity and concentration distributions below the ceiling plate, namely boundary, and ceiling jet layers (momentum and thermal). Consistent results for boundary layers with those obtained in the literature for small fire experiments [94,134,135,137] suggested that the saltwater modeling technique can be employed to characterize this ceiling jet region where temperature and velocity are the highest, and the activation of suppression systems occurs faster (activation best case scenario). An accurate estimate

of the boundary layer growth along the upslope provides valuable guidelines on the sprinklers layout (sprinkler height) to use based on the ceiling slope.

The results obtained showed that, for any slope, the momentum boundary layer grown along the upslope as $(S_1/H)^{4/5}$ according to a typical flat plate in turbulent parallel flow, where transport is dominated by turbulence rather than diffusion. This observation consolidated by the results obtained for the concentration boundary layer, δ_θ, which was found to be $\approx \delta_u$, as expected for a fully turbulent layer [75]. These two points provided evidence of the minimized effects of the diffusion near the wall (δ_u from 4 mm up to 9 mm below the plate) obtained by increasing the Gr_H (or Re_H) up to $\approx 10^{11}$ (or $\approx 10^5$).

In addition, as previously discussed in 4.3.1, the choice of 50μm diameter (d_p) particles for PIV measurements was motivated by the limits imposed by the Stokes'law ($Re_{d_p} \lessapprox 1$) regarding optimal tracking capability of the suspended particles (no buoyant or inertial effects). So, it could be argued that smaller particles (within the limits of the Stokes'law) could have better described the wall-bounded diffusion effects, but the higher particle density required by PIV to characterize both the near and the far wall field would have affected the velocity measurements with an exceeding amount of elastically scattered light from the surface of the particles (noise) and the risk of peak-locking [110]. Upon all the above observations, it can be inferred that our results can be scaled up to describe similar real fire scenarios, but both comparisons with large scale tests and numerical simulations are required for validation.

Eventually, the analysis of the region of influence of the ceiling jet flow along

the wall, S_1/H, was completed with relationships able to directly predict the edge of such region (L_u for velocity and L_θ for concentration) for upslope locations in the range $0 \leq S_1/H \leq 1.3$ and slope angles from 0° to 40°. The correlations $L_u = L_u(\alpha, S_1/H)$ and $L_\theta = L_\theta(\alpha, S_1/H)$ were determined using measurements from all slopes, except one used as test case to show convergence between direct measurements and predicting correlations. Based on these results, both sets $L_u = L_u(\alpha, S_1/H)$ and $L_\theta = L_\theta(\alpha, S_1/H)$ could be potentially applied to full-scale scenarios to design activation systems sensing lower temperatures and lower flow velocities (early fire activation/detection).

Chapter 6: Activation on Sloped Ceilings

6.1 Sprinkler Activation Background

In fire protection, it is well known that the response time in activation systems, such as sprinklers, is a direct result of the time required for the convective transport of the ceiling jet flow to reach the detector (front arrival time, t_{FA}), and the lag or delay time (t_{lag}) required to sense the threshold values of the flow jet characteristics (velocity and temperature) to activate the device. Equation 6.1 shows the relation between t_{act}, t_{FA}, and t_{lag}:

$$t_{act} = t_{FA} + t_{lag} \tag{6.1}$$

Testing results for sloped ceiling fire scenarios are not widely available in the literature [76], especially in regards to relevant applications such as sprinkler activation. Leveraging scaled saltwater measurements, the primary aim of the present work was to evaluate the dimensionless sprinkler activation times, t^*_{act}, based on the ceiling jet characteristics under an inclined surface (0^0 to 40^0 slope), and investigate the streamwise-to-spanwise spatial correlation between sprinkler delay times, t^*_{lag}, for sprinkler spacing purposes. This goal was achieved using saltwater measurements

of θ_{sw} and u, obtained using a "multi-planar" laser technique, and plugged into an experimental model for real sprinkler activation [91], modified to embed saltwater measurements. Such an approach allowed for representation of the activation time as a two-dimensional spatial distribution below the ceiling surface and analysis the behavior of the lag time at increasing slopes.

This study was limited by a lack of knowledge on heat transfer characteristics at the surface of the sensitive element of a sprinkler, instead opting for a previously-developed empirical correlation. This is an aspect of this research that could be improved in the future, however results from this saltwater technique may still be applicable in improved calculations. The heat transfer coefficient (h) for a sprinkler sensitive element was therefore embedded into a constant factor, namely the response time index, or RTI. This constant describes a specific sprinkler type based on a number of constructive characteristics, such as lumped mass, exposed surface area, and material heat capacity.

Therefore, even if the unknown heat transfer coefficient (h) represents a limiting factor in the estimate of the actual activation time, our results in the form of t^*_{act} represent a comprehensive model still able to provide useful information on the activation characteristics, once a relevant RTI is used. For this study, $RTI = 30$ $\mathrm{m}^{1/2}\mathrm{s}^{1/2}$ was chosen, as later discussed in detail.

Conveniently presented in the form of isocontour lines (t^*_{act}=const.) in the S_1S_2 ceiling plane (Fig. 6.3), the results allowed: (1) to spatially visualize the impact of the slope on the activation patterns and (2) to interpret the spatial correlation between lag and activation times along streamwise S_1 and spanwise S_2 directions at

a given distance from the surface. This information, given the knowledge of the specific RTI for the sprinkler in use, could potentially be used in real fire scenarios for sprinkler spacing strategies below sloped ceilings.

The optimization of both detector response time and detector spacing is mostly dependant on the fire plume dynamics (early stage of a fire), and the subsequent interaction between the ceiling wall and the jet flow developing on it [7]. Sprinkler response (or activation) time, t_{act}, is fundamental when it comes to evaluating the performance of the sprinkler system [73]. Too short of an activation time results in a false response of the sprinkler, whereas the opposite corresponds to a failure of the suppression system [73]. The progress achieved in the development of fast response sprinklers relies on accurate prediction of the response time and on all of those factors involved in its evaluation [73]. This whole process aims for prompt fire hazard suppression to maintain a survivable environment and reduce losses [73]. In regard to sloped ceilings, major concerns result from (1) possible delays in sprinkler activation due to the biased, upslope flow of hot gases under the sloped surface, and (2) sprinklers further away from the fire source activating first (with delayed activation times), causing the need of higher sprinkler densities in response of a larger fire [82]. This emphasizes the pivotal relationship between an accurate estimate of the sloped ceiling jet characteristics and the activation/spacing strategy for sprinklers.

The response time of a sprinkler installed below a ceiling is essentially determined by its operative temperature and heat balance on its heat sensing element. In case of a fire, the heat transfer balance for the sensing element of the sprinkler includes the convective heating by hot gases in a ceiling jet, radiative heating from

the fire source and losses by conduction through the hardware (pipes, valves) of the sprinkler [73]. Figure 6.1 describes the heat transfer taking place between a heat detector and its environment.

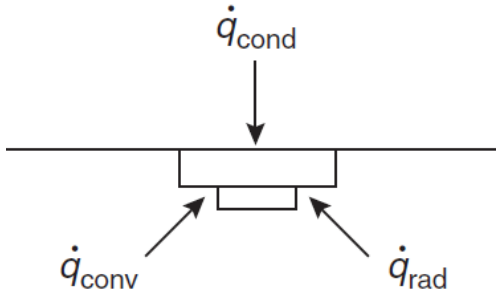

Figure 6.1: Sprinkler sensing element schematic: the total heat transfer to the ceiling-mounted sensing element is given by the contribution of convective and radiative heat transfer, whereas major lossess are from the conductive heat transfer to the sprinkler hardware.

The total heat transfer rate to a sprinkler unit, $\dot{q}_{total}$, can be expressed by the following relationship

$$\dot{q}_{total} = \dot{q}_{convective} + \dot{q}_{radiative} + \dot{q}_{conductive}. \tag{6.2}$$

At the early stage of a fire, $\dot{q}_{radiative}$ is usually negligible. To date, available heat detectors are designed to minimize conductive heat losses with the sprinkler hardware [72]. Therefore, the total losses of the sprinkler heat-sensitive element by conduction are relatively small compared to the convective heat transfer contribution [72]. This exclusion leaves a net rate of heat transfer to the detector equal to $\dot{q}_{convective}$. These assumptions, which reduce $\dot{q}_{total}$ to the contribution of the $\dot{q}_{convective}$

only, fit with the ability of saltwater modeling to simulate a steady-state fire characterized by heat transfer at the surface mainly by convection. Thus, the convective heat transfer rate to the detector is described by

$$\dot{q}_{total} \approx \dot{q}_{convective} = hA(T_{gas} - T_{det}), \tag{6.3}$$

where h is the convective heat transfer coefficient, A represents the sensing element surface exposed to the ceiling jet flow at temperature T_{gas}, while the sensing element is initially at temperature T_{det}. Assuming the sensitive element as a lumped mass, m, its temperature change is given as [72]

$$\frac{dT_{det}}{dt} = \frac{\dot{q}_{total}}{mc} \tag{6.4}$$

where c represents the specific heat of the sensitive mass. This equation leads to the following relationship for the change in temperature of the detector with respect to time,

$$\frac{dT_{det}}{dt} = \frac{hA(T_{gas} - T_{det})}{mc}. \tag{6.5}$$

Heskestad and Smith [140] have proposed use of a time constant, τ, to describe the convective heat transfer to a particular detector element given by

$$\tau = \frac{mc}{hA}. \tag{6.6}$$

thus giving

$$\frac{dT_{det}}{dt} = \frac{(T_{gas} - T_{det})}{\tau}. \tag{6.7}$$

The time constant, τ, is a function of the mass, area, and specific heat of the particular detector element under investigation. For a given fire-gas temperature

and velocity and a particular detector design, an increase in mass results in an increase in the time constant. A larger τ results in slower heating of the element.

In addition, the convective heat transfer coefficient, h, is a function of the velocity of the gases flowing past the detector element and the shape of the detector element. For a given detector, if the gas velocity is constant, h is constant. Past research [141] has shown that the convective heat transfer coefficient for simple shapes (e.g. spheres, cylinders) is $\approx \sqrt{Re}$.

Given the proportionality between Re and the local velocity u of a ceiling jet flow passing a given detector, the h coefficient and, hence, $\tau \approx \sqrt{u_{gas}}$, where u_{gas} is the velocity of hot gases. This relationship can be expressed as a characteristic response time index, RTI, for a given detector

$$RTI = \tau u^{1/2} = \tau_0 u_0^{1/2} \approx const. \tag{6.8}$$

where τ_0 referes to a reference value (generally measured in laboratory) and estimated based on some reference gas velocity, u_0. In light of this, Eq. 6.8 is used to determine τ at any other gas velocity, u, for that detector. The RTI is a convenient function to describe convective heat transfer to the sensitive element of the sprinkler, which is usually identified based on its type (fast response sprinkler, standard sprinkler, etc.). Estimates of the RTI parameter often involves several plunge tests in a characteristic heated flow for a given sprinkler. This empirical approach is often favored rather than direct determination of the heat transfer coefficient, h [72],. However, all tests start from the assumption that τ (and therefore h) [72] is approximately equivalent to the square root of the gas velocity, regardless of the

magnitude of the velocity [72]. For instance Schifiliti *et al.* [72] and Hollman [141] concluded that h (therefore τ) can be approximated as $\approx Re^n$, with n depending on the Re range [72].

Heskestad and Bill [91] proposed a model for sprinkler activation (later described in Sec. 6.1.1) where the activation time, t_{act}, is directly correlated to gas velocities and temperatures for a given sensing element characterized by a specific RTI. Heskestad and Bill [91] indicate that the RTI, which condenses in one parameter the sprinkler sensitive-element thermal and design requirements, completes the required set of information to estimate sprinkler response time, beyond sprinkler site velocity and temperature [91].

In this study, Heskestad and Bill's simple model was employed because of the simplifications already assumed for the original fire model (i.e., $\dot{q}_{total} \approx \dot{q}_{convective}$), which is in line with the limitations imposed by saltwater modeling, i.e. the inability to describe radiative heat transfer and conductive losses. An RTI of 30 $\mathrm{m}^{1/2}\mathrm{s}^{1/2}$ was also chosen to perform a comparison with fire simulations from Chatterjee *et al.* More accurate models proposed by Ruffino and diMarzo [69] provide similar values to those of Chatterjee *et al.* with a RTI of 42 $\mathrm{m}^{1/2}\mathrm{s}^{1/2}$ for both dry or wet conditions. Nonetheless, according to the same authors [69], lower values such as those proposed by Chatterjee *et al.* are accurate only for estimating the activation of sprinklers closest to the impingement point, but not for those set further away from it. A lower value is due to the lack of assuming water droplets deposit on the activation element of distant sprinklers following activation of the first set of sprinklers—water droplets evaporation delays the activation because of the heat

absorption at the surface of the sprinkler link [69]. Therefore, although Ruffino and diMarzo's RTI [69] is more comprehensive (activation + spray phenomena), Chatterjee's value, based on the separation of the activation from spray suppression phenomena, allows for obtaining first-order effects of ceiling slope on the activation time. Ultimately, this goal better aligns with our objective and the saltwater technique limitations, unable to account for the sprinkler spray phenomena.

6.1.1 Sloped Ceiling Activation Results

Results from saltwater measurements of a ceiling jet developing along an inclined plate (with $0 \leq \alpha \leq 40°$) and their correlation with sprinkler activation are presented in this section. In this study, PIV and PLIF laser diagnostics were implemented to investigate the activation based on the flow characteristics already used for the analysis of the ceiling jet (see Sec. 5.1.1); first by means of a "single planar" imaging technique, and then by means of a "multi-planar" technique. The first approach, already implemented to preliminary describe the sloped ceiling jet flow behavior in Sec. 5.2, was used here to show how to determine the front arrival time, t_{FA}, along the centerline. The same concept has been later applied to the "multi-planar" approach for the same purpose. The term "multi-planar" refers to a grid of laser sheets generated by placing the laser (and the camera perpendicular to the laser) at equidistant locations from the impingement point, along the streamwise and the spanwise axis of the plate, respectively.

Given the ceiling jet flow asymmetry with the respect of the flow spanwise axis,

S_2 (Fig. 6.3), the saltwater "multi-planar" grid approach was therefore thought to be suitable to properly study the activation of sprinklers virtually mounted below the sloped ceiling plate. In detail, the ability of saltwatwer modeling to provide a two-dimensional, scaled representation of the activation time under a sloped ceiling was investigated using local, dimensionless saltwater measurements of θ^*_{sw} and u^* (with u^* as the absolute value of the velocity in the laser plane) as inputs for a model originally formulated for fire suppression systems (sprinklers) [91].

Based on a sprinkler activation model by Heskestad and Bill [91] for real fire scenarios, the "multi-planar" laser sheet grid was created to capture saltwater velocity, density difference, and front arrival time of the ceiling flow. By integrating saltwater measurements into the activation model, conveniently modified for dimensionless saltwater flow field, two-dimensional activation time contours were plotted for each slope. This provided valuable information as to the effect of slope that may be reduced to simplified models useable as a critical design tool.

In addition to the aforementioned observations, some considerations should be made in order to frame the following saltwater results in comparison to a specific real fire scenario. In most real fires the heat-release rate, $\dot{Q}$ is assumed to follow a polynomial (t^2 fire) or exponential growth function [145]. Saltwater modeling, however, only allows for simulation of steady fires. An intrinsic assumption is therefore taken, i.e. simulation with a steady-fire (i.e. $\dot{Q}$=const.) rather than a time-dependent fire (i.e. $\dot{Q(t)}$). When full effects of a change in heat release rate occurring at the fire

source are immediately felt everywhere in the flow field, or equivalently:

$$\frac{\dot{Q}}{d\dot{Q}/dt} > (t_f - t_i) \tag{6.9}$$

where t_f is the average time for gases to reach the suppression device, and t_i represents the ignition time (or initial time for the fire growth). Equation 6.9 represents the "quasi-steady" condition. This equation is the idealization of an early-stage fire scenario, where the combustion products (smoke) are supposed to be faster in reaching a detector submerged in the ceiling jet starting from the source [145], than the rate of change of the fire source, $\dot{Q}$. In literature, Kung *et al.* [77] found correlations for ceiling jet velocity and ceiling jet temperature, induced by rack-storage fires using a quasi-steady assumption [145]. Although gas travel times for large-scale experiments may amount to many seconds, Eq. 6.9 shows that a sufficiently small fire-growth rate (e.g. first-stage of a fire or small fires) allows a quasi-steady analysis to be used [145].

Another fundamental aspect discussed in this analysis is the ceiling standoff distance, ξ, assumed for sprinklers. It is unlikely that commercially available sprinklers or fire detectors could match any operative condition dictated by the ceiling geometry and the ceiling jet development over it. Therefore, it is possible that both suppression and detection devices are outside of the ceiling flow, where lower temperatures and velocities are sensed. Based on Alpert's research [92,93,133,143,145], in case of very high ceilings, standard detectors (or sensitive elements of suppression systems) operate at about 1-2% of the ceiling height, H, from the ceiling surface. This distance falls in the range of influence of either the thermal or the momen-

tum boundary layers (sub-layers of the ceiling jet). According to Alpert [145], for low-ceiling facilities, the maximum extension of the ceiling jet below the surface is ≈12% of the fire source-to-ceiling height [145]. Therefore, in some cases, it is likely for suppression or detection devices to operate out of the influence region of the ceiling jet, thus increasing the response time. In this section, both cases of a standoff distance outside and inside the boundary layer will be discussed by scaling down a real sprinkler standoff distance (ξ=33 cm) [82] based on three different ceiling height scenarios (i.e., H ≈30 m, H ≈6 m and H ≈3 m).

"Single Planar" Front Arrival Time

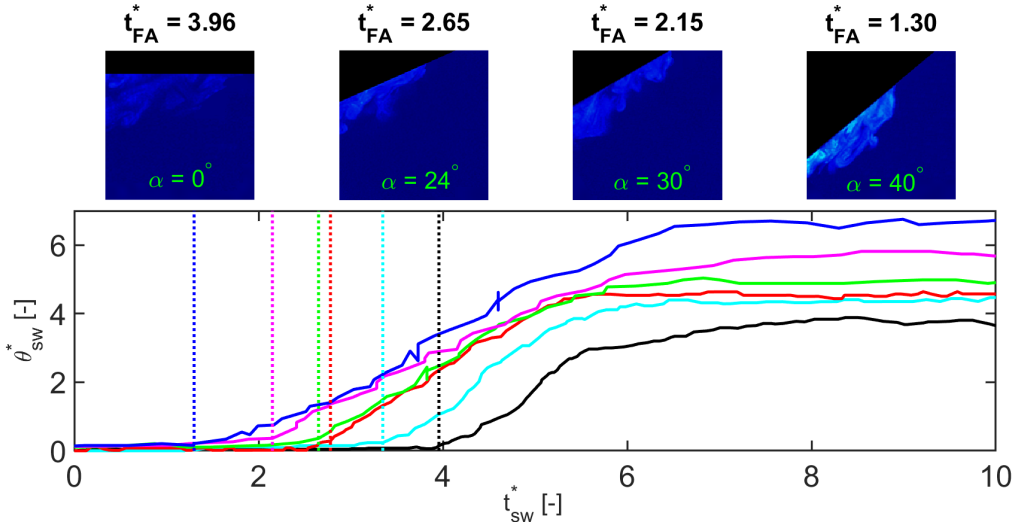

Figure 6.2: Dimensionless front arrival time, t^*_{FA}, for a virtual sprinkler head located 16 cm upslope from the impingement point of the saltwater plume along the centerline; (-·-·-) t^*_{FA}=3.96 for (—) α=0°; (-·-·-) t^*_{FA}=3.34 for (—) α=10°; (-·-·-) t^*_{FA}=2.78 for (—) α=18°; (-·-·-) t^*_{FA}=2.65 for (—) α=24°; (-·-·-) t^*_{FA}=2.15 for (—) α=30°; (-·-·-) t^*_{FA}=1.30 for (—) α=40°.

Figure 6.2 shows the results for the dimensionless front arrival time, t^*_{FA} (Eq. 6.1),

of the ceiling jet moving upslope along the centerline. This figure illustrates the approach used here to determine the front arrival time for a single laser plane and is later extended to the "multi-planar" activation study. For Fig. 6.2 the same set of PLIF images collected for the analysis of the ceiling jet flow (Sec.5.2) were used and the dimensionless arrival time for the front of the flow, t^*_{FA}, was determined by monitoring the level of θ^*_{sw} at a given location (S_1^+=16 cm) over time. All slope inclinations in the range 0° to 40° were investigated and the results were displayed in a non-dimensional form [94, 109], using Eq. 3.68 for t^*_{FA} (Chapter 3).

The upper portion of gure g. 6.2 displays instantaneous PLIF realizations captured 16 cm upslope the impingement point of the plume for α=0°, α=24°, α=30° and α=40°, where the images show clearly the difference in denser flows at increasing slopes. On the other hand, no appreciable difference between cases at α=10° and α=18° was found, as confirmed by their respective t^*_{FA} curves (cyan and red lines), displayed in the lower part of Fig. 6.2.

The images provide insight on the evolution of the ceiling jet flow at different angles. As the slope is increased, the density at the front of the jet increases, due to both poor mixing with fresh water as well as reduced entrainment. By increasing the slope from the horizontal, a gravity component (and therefore a buoyancy force component) along the upslope aligns with the flow thus for the ceiling jet to adhere closer to the surface [7]. Because of the favorable upward buoyancy component, at higher inclination angles correspond higher velocities of the front, and therefore shorter t^*_{FA} (as observed in Fig. 6.2).

The lower part of Fig. 6.2 shows the dimensionless front arrival time t^*_{FA} based

on the scalar θ^*_{sw} along $t^*_{sw} = t(g/H)^{1/2}(\dot{m}^*_{sw})^{1/3}$ for the virtual sprinkler located at S_1^+=16 cm. The exact arrival time was picked at the instant when the density difference was seen to rise with the steepest slope before the flow attained a steady state at that location over time, t^*_{sw}.

Based on the similarity between a saltwater source and a fire induced ceiling jet flow, this preliminary result approximates the hazards in a real fire scenario, and thus provides useful information for the prevention of such. A higher density difference for steeper slopes translates into higher temperatures and higher heat fluxes near the ceiling, thereby introducing potential structural integrity problems and faster activation of sprinklers.

"Multi-Planar" Activation

Increasing the slope α from 0° to 40°, the ceiling jet exhibits a non-symmetric behavior with respect of the spanwise axis S_2 (Fig. 6.3) due to a reduced content in buoyancy for the downslope ceiling jet (along S_1^-), compared to that of the upslope flow (along S_1^+). Given these flow conditions, measurements were taken radially both spanwise and streamwise from the center. As shown in Fig. 6.3, a grid of 81 intersecting measurement points was obtained crossing streamwise and spanwise laser sheets at the same locations. Therefore, a 4 cm × 10 cm cell formed between intersecting points (red rectangle in Fig. 6.3). Within the unit cell, a grid of interpolated values originated from the measured points laying on each side of the cell (full green line in Fig. 6.3, representing a section of the single laser sheet), including the intersections at the corners (blue dots in Fig. 6.3). The general procedure approached to obtain the interpolated data (velocity, density difference and front

arrival time) within the cells is following described.

As shown in Fig. 6.3, the measured time-averaged velocity, time-averaged density difference and front arrival time resulting from the PLIF time series were only available along the spanwise and the streamwise lines (full green lines) forming the "multi-planar" grid. In order to generate a denser grid of 1 mm resolution (256,000 points total, see Fig. 6.3) that included the unit cell inner points (to be interpolated), the measured values of density difference, velocity (u_1, u_2 and u_3 components) and front arrival time were assumed at 1 mm step along the laser sheets (full green lines in Fig. 6.3). When simultaneously available from both a set of spanwise images and streamwise images, all measured values were averaged at the points of intersection (blue dots) between the laser sheets (e.g. u_3 velocity component along the perpendicular to the ceiling plate, S_3, resulting from both PIV over the $S_1 - S_3$ plane and $S_2 - S_3$ plane).

Before interpolating the inner points, the dimensionless front arrival time, t^*_{FA}, was estimated following the "single-planar" approach (described earlier) and applied to each laser sheet (streamwise and spanwise) of the "multi-planar grid", thus providing values for each side of the 4 cm$\times$10 cm unit cell. Due to the acquisition frequency of the camera (time interval between two consecutive frames) and given the resolution step of 1 mm chosen to interpolate the inner points, t^*_{FA} was not always available straight out of a single PLIF frame. In such an event, a linear interpolation between the time related to two consecutive frames and the locations of the flow front around (before and after) the point where to interpolate t^*_{FA} was performed. As expected, front arrival times were found to vary with distance from

the impingement point. Similarly, measured scalar θ^*_{sw} and components of u^* (u_1 along S_1, u_2 along S_2 and u_3 along S_3) were also extracted at 1 mm resolution step from the time-averaged PLIF and PIV images (mean flow), respectively. Particularly for the velocity, note that spanwise measurements (laser sheets cutting along S_2, Fig. 6.3) provided u_2 (along S_2) and u_3 along S_3) components, while streamwise measurements (laser sheets cutting along S_1, Fig. 6.3) only provided u_1 (along S_1, up- and downslope) and u_3 (along S_3). The latter was found negligible compared to u_1 and u_2 at $\xi \approx$4 mm, but nonetheless considered in this analysis.

Once extracted, the data points were measured at 1 mm resolution along the S_1 and S_2 grid lines and the *meshgrid* Matlab function was used to generate a uniform grid of 256,000 points total (4,000 points each unit cell). The time-averaged measurements available were used to feed the *scatteredInterpolant* Matlab function [65] to obtain local values at each point. Such a function was used to perform interpolation on a 3-D data set of scattered data (S_1 and S_2 coordinates of a point, plus the scale to interpolate measured at $\xi \approx$4 mm). A total of 256,000 data points maximum (4,000 each cell) laying on a plane parallel to the inclined plate and distant $\xi \approx$4 mm from the surface was eventually generated, and each of the 256,000 points was characterized by local values of t^*_{FA}, θ^*_{sw} and u^*, respectively. Note that, as we increased the inclination of the plate, the flow (at steady-state) progressively skewed upward and shrunk spanwise (see Fig. 6.4), thus reducing the area of the plate covered by the flow; this reduced the number of measured points and hence the number of interpolated points (approximately by a half from α=0° to α=40°).

The activation times, t^*_{act}, were determined based upon local θ^*_{sw} and u^*, both

calculated over the virtual grid shown in Fig. 6.3 at a given distance, ξ, perpendicular to the ceiling. Such estimates were obtained implementing θ^*_{sw} and u^* information resulting from streamwise and spanwise measurements into Heskestad and Bill's activation model, described below. In this study, we referred to the plane at standoff

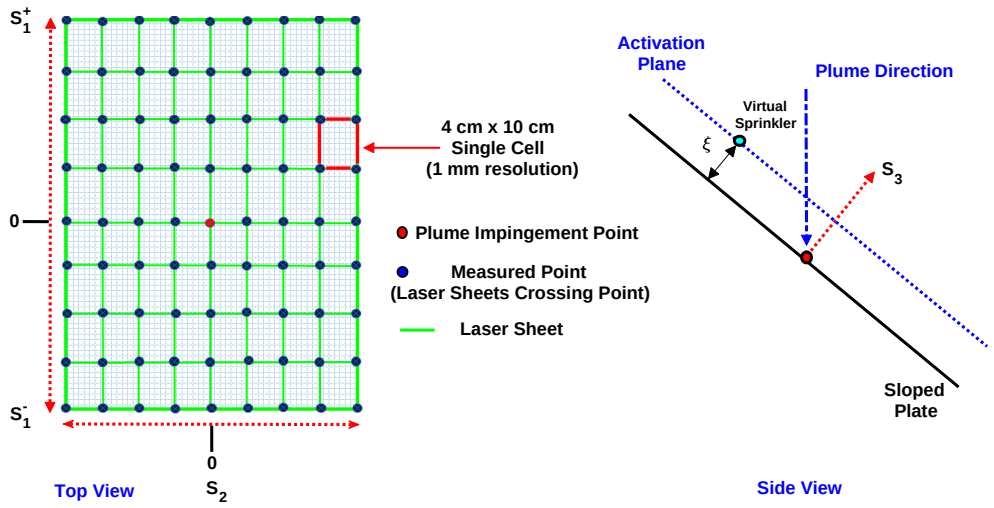

Figure 6.3: Measurement point grid over the plate at a distance ξ (activation plane) from the ceiling surface. The top view (left) shows the 1 mm resolution single cell delimited by four measurement points, while the side view (right) shows the activation plane assumed at distance ξ, where sprinkler heads are virtually set.

distance (or sprinkler height), ξ, as the "activation plane", where sprinkler heads virtually activate. As already discussed above, the standoff distance for sprinkler heads was suggested by the current practice in fire protection engineering, where a distance of 33 cm perpendicular to the ceiling is assumed [76]. Therefore, a $\xi \approx$4 mm (3.7 mm) distance over a ceiling plate height at the impingement point of H=34 cm was obtained by scaling ξ_T=33 cm (real sprinkler standoff distance, subscript $_T$) on a scale $\approx 1/100$, in order to simulate a real high ceiling of $H \approx$30 m. The

value of $\xi \approx 4$ mm for the saltwater experiments was chosen because characteristic of a location within/at the boundary layer, based on the ceiling jet flow characterization results discussed in Sec. 5.2. This choice was also substantiated by Alpert's research [92, 93, 133] reporting a standoff distance for the sprinklers in the range of ≈1-2% of H for high ceilings.

Figure 6.4 shows the results for non-dimensional density difference, θ^*_{sw}, obtained employing the gridded "multi-planar" approach described above. Data were extracted for a standoff distance $\xi \approx 4$ mm (3.7 mm) from the plate at each slope angle in the range 0° to 40°. The density difference distribution of radial (0° to 18°) or of elliptical shape (24° and 30°) was observed for low angle slopes, while the distribution changed and expanded to a round egg-like shape for a steeper ceiling slope (40°) as shown. In detail, for all cases, the highest density difference occurs at the central location on the plane, with concentric contours indicating the reduction in θ^*_{sw} with increasing radial distance. For the horizontal, the contours of θ^*_{sw} exhibit symmetry with respect to the impingement point, which gradually disappears at increasing slopes. At higher angles, these contours roughly maintain the symmetry with respect to the S_1 axis, but they elongate in the upward direction and shorten in the downward, disrupting the symmetry with respect to the S_2 axis. This, as recently observed in Chatterjee *et al.* [76, 82], results into a progressive distortion of the original symmetry of the θ^*_{sw} patterns, that show bias towards the elevated side of the ceiling for higher slopes [82]. At the lowest point of the ceiling, values of θ^*_{sw} are closer to zero, indicating that flow reversal is about to occur. Further increase of the inclination to α=24° and α=30° causes the ceiling jet to concentrate

on the elevated ceiling side as can be observed in Fig. 6.4. The central high density difference region shows elongation towards the upward direction. Flow reversal now is closer to the ceiling plane center. Finally, at α=40° ceiling inclination, the ceiling jet narrows. Compared with lower angles, the density difference contours at higher angles shift from a rounded shape to an egg-like shape, stretching their region of action further upward as the inclination increases. Additionally, on the downslope, the buoyancy component along the ceiling slope slows down the front of the ceiling jet causing the penetration distance to shorten, closer to the plume impingement point [82].

The mean values for density difference, θ^*_{sw}, and velocity, u^*, over 256,000 points of the activation plane (see Fig. 6.3) were therefore employed to determine the activation time, t^*_{act}, by plugging these values into a real model for sprinkler activation proposed by Heskestad and Bill [91] (Eq. 6.14). Such model starts assuming the law of conservation of energy

$$m_{det} c_{p,det} \Delta T_{det} = \left(\dot{Q}_{in} - \dot{Q}_{out} \right) \Delta t \tag{6.10}$$

which characterizes the thermal response, ΔT_{det}, of an automatic sprinkler exposed to a hot gas environment. In Eq. 6.10, m_{det}, $c_{p,det}$, and ΔT_{det} are respectively the mass of the heat sensitive element (subscript $_{det}$), its heat capacity and the temperature difference reached by the lumped element (i.e. the element temperature is uniform throughout) with the respect to the ambient temperature at time t. The net heat transfer of the sensitive element over Δt is represented by the term $(\dot{Q}_{in} - \dot{Q}_{out})$.

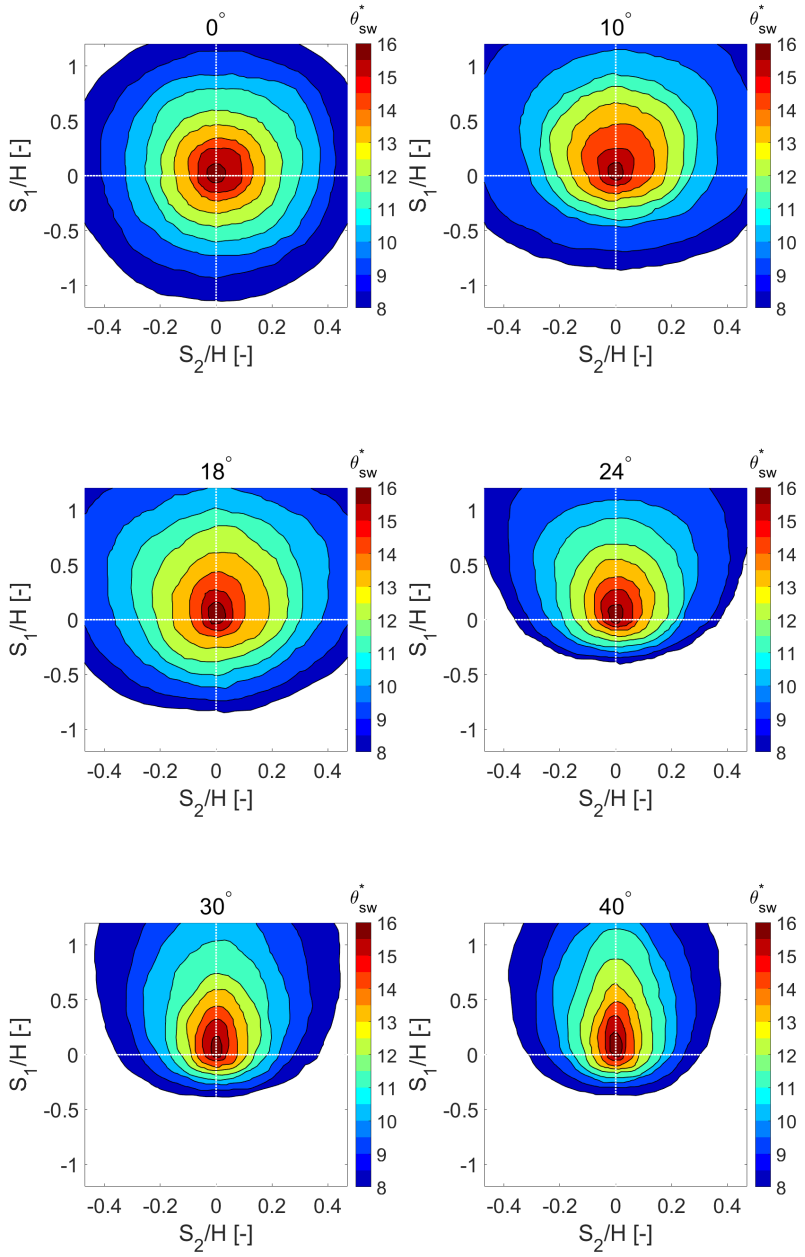

Figure 6.4: Dimensionless density difference θ^*_{sw} distribution map: contours for α=0°, α=10°, α=18°, α=24°, α=30° and α=40° slope.

Heskestad and Bill's model given as

$$\frac{d\Delta T_{det}}{dt} = \frac{\sqrt{u}}{RTI}\left[\Delta T_{gas} - \left(1 + \frac{C}{\sqrt{u}}\right)\Delta T_{det}\right] \tag{6.11}$$

rearranges Eq. 6.10 such that the convective heat transfer from the hot ceiling jet to the sensitive element, and the conductive losses through the sprinkler fixture (e.g. sprinkler pipe) can be accounted through the response time index of the sensitive element, RTI, and the loss factor C, respectively. As discussed earlier, the RTI is a constant characterizing the sprinkler heat sensitive element which includes its convective coefficient, h, and other constructive specifications such as mass, heat capacity, and the heat sensitive element surface exposed to the hot environment [71, 91]. Equation 6.11 also depends on u, representing the ceiling jet velocity in proximity of the sensitive element, and ΔT_{gas}, the temperature excess of the sensitive element with respect to the hot ceiling jet flow. When the sprinkler sensitive element is plunged into a hot ceiling jet flow with constant velocity and temperature, Eq. 6.11 can be rearranged as follows:

$$\Delta T_{det} = \frac{\Delta T_{gas}}{1 + \frac{C}{\sqrt{u}}} \left[1 - e^{\frac{-t\sqrt{u}\left(1+\frac{C}{\sqrt{u}}\right)}{RTI}} \right] \tag{6.12}$$

where the temperature of the sprinkler element appears as a function of time [71]. This equation can be eventually solved for t when the sprinkler activates (subscript $_{act}$), thus having:

$$t_{act} = \frac{RTI \cdot \ln \left[\left(1 - \frac{\Delta T_{det,act}}{\Delta T_{gas,act}\left(1+\frac{C}{\sqrt{u}}\right)^{-1}} \right)^{-1} \right]}{\sqrt{u}\left(1 + \frac{C}{\sqrt{u}}\right)} \tag{6.13}$$

In Eq. 6.13, $\Delta T_{det,act}$ corresponds to a fixed threshold for the activation. The most commonly accepted value in engineering practice for a quick-response sprinkler is of about 347 K [71, 82, 142].

Based on saltwater analogy (Sec. 3.2) and neglecting the C-factor given the

inability of saltwater modeling to describe losses due to conduction, Eq. 6.13 can be re-written in terms of dimensionless saltwater density difference and dimensionless velocity solving for the activation time as follows:

$$t^*_{act} = RTI \cdot A \cdot \frac{\ln\left(\frac{1}{1-\frac{\theta^*_{det,act}}{\theta^*_{sw,act}}}\right)}{\sqrt{u^*}} \tag{6.14}$$

where $A = \sqrt{(g/H^3)^{1/2}\,(\dot{m}^*_{sw})^{1/3}}$ is a constant (in $\mathrm{m}^{-1/2}\mathrm{s}^{-1/2}$) obtained expressing the scales in the fire framework as function of their respective dimensionless terms, and depending on the fire characterstic height, H, and the dimensionless source, $\dot{m}^*_{sw} = Q^*$.

Equation 6.14 represents the dimensionless activation time, t^*_{act}, where the constant $RTI = 30\ \mathrm{m}^{1/2}\mathrm{s}^{1/2}$ is characteristic of real quick sprinklers [76]. The saltwater ratio, $\frac{\theta^*_{det,act}}{\theta^*_{sw,act}}$, in Eq. 6.14 is the equivalent of the $\frac{\Delta T_{det,act}}{\Delta T_{gas,act}}$ ratio in the real fire scenario. In fact, as one might note, the ratio $\frac{\Delta T_{det,act}}{\Delta T_{gas,act}}$ in Eq. 6.13 equals the dimensionless $\frac{(\theta^*_{det,act})_T}{(\theta^*_{gas,act})_T}$ (with subscript $_T$ used here to indicate fire-induced flows), since the ratio cancels out the common terms of the normalization, that is β_T and $(Q^*)^{2/3}$ in the general expression $\theta^*_T = \frac{\beta_T \Delta T}{(Q^*)^{2/3}}$ (and equivalently, β_{sw} and $\dot{m}^*_{sw}$ for saltwater θ^*_{sw}). Symbol $\Delta T_{det,act}$=347 K in Eq. 6.13 [76, 82] was converted into the dimensionless equivalent $\theta^*_{det,act}$ (based on Table 5.1 and the assumption of $H = 30$m for the real fire scenario) in saltwater experiments, while $\theta^*_{sw,act}$, the dimensionless equivalent of $\Delta T_{gas,act}$ in Eq. 6.13, represented the measured local density difference for each virtual sprinkler location in the grid at the time of the activation (subscript $_{act}$). In addition, for the same locations, u^* (Eq. 6.14) represented the dimensionless magnitude of the velocity, based on the three grid-interpolated components along

S_1, S_2 and S_3 (see Fig. 6.3).

The results obtained employing Eq. 6.14 over the gridded activation plane are presented in Fig. 6.5 and displayed as isocontour lines for α ranging from 0° to 40° angle. The time isocontours show the dimensionless time needed for activation starting from the moment the plume impinges the plate [7]. The time needed for the plume to reach the impingement point from the outlet of the injector was a constant for each case and estimated to be 5 s. The plume rapidly propagates over the ceiling in both S_1/H and S_2/H, with relatively good symmetry with respect to the S_2/H dimensionless axis [7]. By increasing the slope, the activation times progressively tended to skew to the upslope direction and a delay in the activation time was found for the downslope locations of the plate, mainly due to a decrease in the front arrival time in that region [7]. In other terms, the delay in activations between virtual sprinklers located below the elevated and lower sides of the ceiling plate was found to increase at increasing slopes, α. This result agreed with simulations for different ceiling heights reported by Chatterjee and Meredith [76]. Similar patterns were found in the 0° to 18° and for 30° to 40° slope range, while a large difference was observed in the transition from 18° to 24° scenarios. As earlier discussed, the activation times are shown here for a specific class of sprinklers, that is quick sprinklers with a $RTI = 30$ m$^{1/2}$s$^{1/2}$. However, dimensionless times, t^*_{act}, can be theoretically calculated for sprinklers with different RTI (e.g. standard with $RTI = 100$ m$^{1/2}$s$^{1/2}$ [76]), in order to estimate the activation at larger scales for sloped ceilings at various angles. Using the real fire scenario height, H=30 m, and the fire source strength based on H, i.e. $\dot{Q}$=100 kW, reasonable activation times

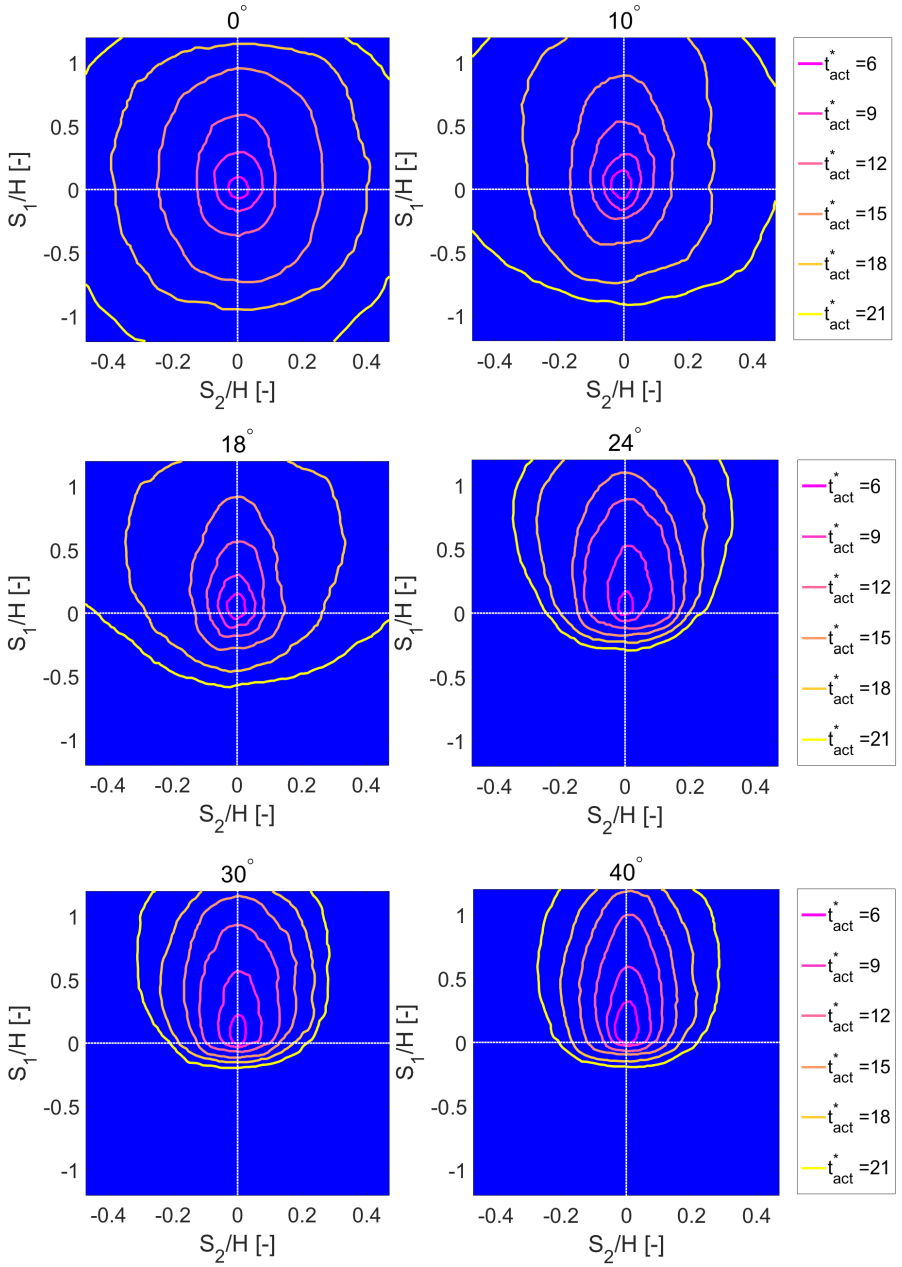

Figure 6.5: Dimensionless activation time distribution map: t^*_{act} contour lines for virtual sprinkler heads located at a distance ξ=4 mm from the ceiling surface for α=0°, α=10°, α=18°, α=24°, α=30° and α=40° slope.

for a real fire scenario ranging from t_{act} ≈25 s (for t^*_{act}=6, Fig. 6.5) up to t_{act} ≈80 s (for t^*_{act}=21, Fig. 6.5) from the impingement of the plume were found. As shown in

Fig. 6.5, the range from t_{act} ≈25 s to t_{act} ≈80 s is the same for all the slopes considered (i.e. same isocontour lines for α=0^0 to α=40^0), but the spatial distribution of the isocontour lines tends to skew increasingly upwards at increasing angles.

Given the increasing level of skewness observed for the spatial distribution of the activation time contours, it was inferred that, at increasing α, sprinklers symmetrically located around the impingement point of the plume activate with an increasing delay streamwise along S_1 (faster activation upslope, slower downslope), and between the upslope sprinkler (faster activation) and those located spanwise along S_2 (slower activation). This phenomenon was particularly evident for $\alpha > 18°$, as later shown in Fig. 6.7.

Chatterjee *et al.* [76] came to similar conclusions by simulating the activation of quick response sprinklers ($\xi_T = 33$ cm, $RTI = 30$ m$^{1/2}$s$^{1/2}$) below a 24 m × 24 m ceiling located 3.05 m above a time growing fire source (convective HRR from 0 to 15 MW in 150 s) for $0 \leq \alpha \leq 33.7°$. Figure 6.6 shows the comparison between the activation delay, $\Delta t_{act} = t_{act_{downslope}} - t_{act_{upslope}}$, extracted from Chatterjee's activation contours (see Figs. 3.7, 3.9 and 3.11 in [82]) for 0°, 18.4° and 33.7° and saltwater results for similar ceiling slopes of 0°, 18° and 30°. Both fire simulations from Chatterjee and saltwater results (Fig. 6.6) were displayed over the same dimensionless distances $\Delta S_1/H = S_1^+/H - S_1^-/H$ of 0.25, 0.5, 0.75, 1 and 1.25, being $S_1^+/H > 0$ the upslope sprinkler location and $S_1^-/H < 0$ the symmetrical downslope.

Both saltwater and fire data sets show a similar trend for each slope investigated—the higher level of skewness for steeper slopes causes larger delays, and $\alpha = 18°$ exhibits values of Δt_{act} closer to those of the flat ceiling, whereas $\alpha = 30°$

produces much larger Δt_{act} for the same sprinkler locations. By comparing the results from fire simulations with those from saltwater measurements, the latter largely overestimate the Δt_{act} of the correspondent fire scenario for the same slope.

The likely reason for this might depend on how different source conditions

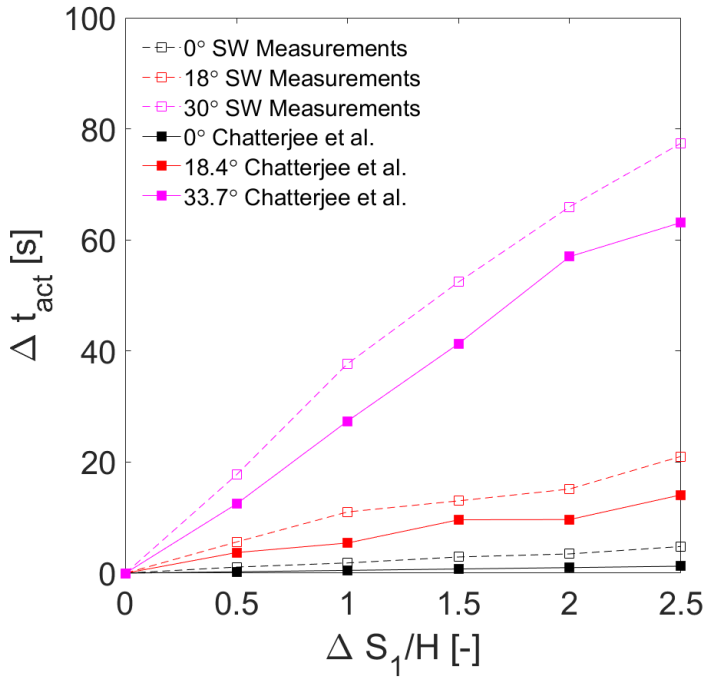

Figure 6.6: Upslope to downslope activation delay, Δt_{act}, versus dimensionless sprinkler distance, $\Delta S_1/H$, for saltwater measurements (dotted lines) at $\alpha = 0°$, $\alpha = 18°$ and $\alpha = 30°$, and for fire simulations at $\alpha = 0°$, $\alpha = 18.4°$ and $\alpha = 33.7°$ from Chatterjee *et al.* (full lines) [76].

(time-varying for fire simulations and steady for saltwater experiments) affected both arrival time and lag time for the two different scenarios. From saltwater measurements, t_{FA} (measurable from PLIF) accounted for 20-30% of t_{act} (Eq. 6.14), whereas the remaining 70-80% represented the delay time, t_{lag} (not directly measurable). These numbers stay constant for a steady $\dot{m}^*_{sw}$, and thus the Δt_{act} estimated in

Fig. 6.6. On the other hand, even if not directly reported by Chatterjee's study [76], it is reasonable to assume that, for an increasing convective HRR over time, higher velocities and higher temperatures are responsible for shorter t_{FA} (convective time) and t_{lag} (thermal responsiveness) and consequent lower activation time, t_{act} (upslope and downslope).

These results suggested that in spite of a constant saltwater source strength, our measurements were able to qualitatively capture the slope influence on sprinkler activation as well as shown by time-varying fire source ($\dot{Q}(t)$) simulations, characterized by the same trend. However, compared to the fire results [76], the saltwater $\dot{m}^*_{sw}$ =const. provided an overestimate of Δt_{act} which showed that the saltwater technique has a major limitation in quantitatively estimating time-varying scenarios, where increasing velocities lower t_{FA}, and increasing temperatures lower sprinkler lag times, t_{lag}, respectively.

In addition, because no information regarding the ratio between t_{FA} and t_{lag} in the balance of t_{act} was available from Chatterjee *et al.* [76], and no model was used directly to estimate t_{lag} in saltwater experiments (given the lack of information about the heat transfer), no comparison for t_{FA} and t_{lag} from the two scenarios was possible. Nonetheless, given a smaller contribution of the t_{FA} (20-30% of t_{act}) compared to t_{lag} in saltwater measurements and the small fire source strength represented by the experiments ($\dot{Q}$ = 100 kW, i.e. early stage of a fire), we inferred that our results could be reasonably used to describe a quasi-steady fire scenario, where the time required for a change in the source in the early stage of a fire (about 20 s, see Fig. 2.9 in [76]) are greater than the convective t_{FA} (Eq. 6.9).

The effect of increasing slopes on the activation time spatial distribution (i.e. S_1/H-S_2/H plane) was further analyzed based on a length ratio L_2/L_1, as shown in Fig. 6.7 (left). The L_2/L_1 parameter, referred as the "activation time spread ratio" for convenience, is given as the L_1 to L_2 length ratio. Both segments L_1 (along S_1/H) and L_2 (along S_2/H) are displayed in Fig. 6.7 (left) and overlayed on one of the activation contour lines as example. Each length is given as the distance between the points where their respective mid-axes for the impingement point, i.e. S_1/H for L_1 and S_2/H for L_2, cross a single contour line. Estimates of L_2/L_1 for each contour line, i.e. t^*_{act} from 6 up to 15, were made for each slope angle from α=0^0 to α=40^0 and shown in Fig. 6.7 (left). Calculations for the L_2/L_1 ratio were limited to t^*_{act} up to 15 since t^*_{act}=18 and t^*_{act}=21 showed to be open patterns in the measurement field (Fig. 6.5), thus no assessment of L_1 or L_2 was possible. The L_2/L_1 ratio, which defines a measure of how a given activation time contour line spatially spreads (spanwise to streamwise), behaves similarly for each activation pattern (t^*_{act} from 6 up to 15) as we increase α from 0° to 40° (Fig. 6.7, left). As observed in Fig. 6.5, as the activation patterns tend to skew to the upslope and pile up to the downslope at increasing angles, the spread L_2/L_1 tends to decrease. However, this occurs at two different rates $d(L_2/L_1)/d\alpha$, corresponding to two α intervals. As shown in Fig. 6.7 (left), for $0° \leq \alpha \leq 18°$, L_2/L_1 is approximately constant with a zero rate, whereas for $24° \leq \alpha \leq 40°$, L_2/L_1 is found quadratically decreasing at increasing α. The slope range $18° < \alpha < 24°$ is where a transition occurs.

This information is particularly useful in evaluating sprinkler spacing at increasing slopes: given these results, it appears that devices located streamwise up-

slope activate faster than those placed downslope and spanwise. In other words, as the inclination of the plate increases, the delay between the activation of sprinklers virtually located on the upslope (streamwise) increases with respect to those located both downslope (streamwise) and spanwise. However, this happens with $L_2/L_1 \approx$ const. for lower inclinations (0° to 18°), whereas at higher slopes, the speed at which the activation streamwise occurs faster than the activation spanwise increases quadratically, as we go from 24° to 40° slope. Future investigations should focus on the transition of L_2/L_1 occurring in the slope range $18° < \alpha < 24°$; this could be useful to determine a "critical" ceiling inclination angle where the $d(L_2/L_1)/d\alpha$ rate changes. Even if a "critical" angle is not defined here, one might still reasonably refer to a "critical" range, since this interval of slopes is quite small. Given this slope range distribution based on the skewness of the activation patterns, it is clear that angles $\alpha \geq 24°$, characterized by greatly skewed activation patterns towards the elevated side of the plate, will exhibit an increasing disparity between the number of activated sprinklers on the upslope (higher number at increasing α) and the downslope (lower number at increasing α) when compared to $0° \leq \alpha \leq 18°$.

Other two virtual "activation planes", at two different sprinkler heights from the plate, ξ, were evaluated in this study—ξ=1.5 cm (off of the boundary layer) and ξ=3.7 cm (in the "tail" of the Gaussian ceiling jet) from the plate were investigated. However, the analysis concerning these two values of ξ lent itself to a double interpretation, as following described. One interpretation focused on the understanding of how the sprinkler could operate right outside the boundary layer (i.e. at lower temperatures and velocities) assuming the same corresponding real

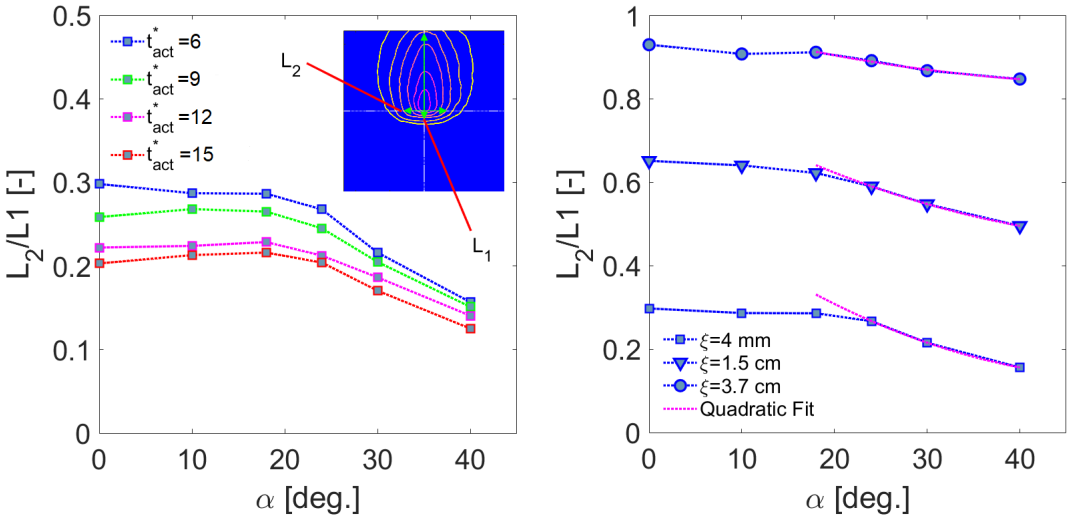

Figure 6.7: Activation time spread ratio, L_2/L_1, for sprinkler heads virtually located at ξ=4 mm from the ceiling surface for 0° to 40° slope angles (left); comparison of the activation time spread ratio, L_2/L_1, for t^*_{act}=6 at ξ=4 mm, ξ=1.5 cm and ξ=3.7 cm (right)

fire scenario with H ≈30 m but with a sprinkler height larger than ξ_T=33 cm. The second, where the standard sprinkler height ξ_T=33 cm was rescaled assuming two different ceiling heights of H ≈6 m and H ≈3 m [76,82], respectively. However, note that the assumption of two different ceiling heights (H ≈6 m and H ≈3 m) would have also imposed the rescaling of the corresponding fire strengths, Q^*, function of H (see Eq. 3.11). In other words, based on this second interpretation, one would have seen the same sprinkler (ξ_T=33 cm) to operate in three different fire scenarios with different Q^*. Given the interest in evaluating the results for different operative conditions of the sprinkler based on a common scenario, the first interpretation appeared more reasonable.

The results for this study, shown in Fig. 6.7 (right), were obtained only for the activation contour line t^*_{act}=6 at ξ=1.5 cm and ξ=3.7 cm and compared with previous results for ξ=4 mm. Two general comments emerged from the curves in Fig. 6.7 (right) from a preliminary observation. First, at increasing distance ξ, the activation time spread ratio, L_2/L_1, increases over the whole slope range, and for ξ=3.7 cm reaches higher values, close to unity. Second, as observed earlier, in the range $0° \leq \alpha \leq 18°$, the spread ratio $L_2/L_1 \approx$ const., whereas at higher slopes ($24° \leq \alpha \leq 40°$), the ratio quadratically decreases with respect to α (Fig. 6.7, right). In addition, as we increase ξ, the concavity of L_2/L_1 for $24° \leq \alpha \leq 40°$ reduces, as shown in Fig. 6.7 (right). Stemming from these observations, we first started investigating the lower values of skewness found at ξ=1.5 cm and 3.7 cm when compared to those at ξ=4 mm.

By extending the sprinkler vertical distance from the ceiling (along S_3), the virtual sensing element is found to operate in a flow environment that behaves differently to that of the boundary layer at ξ=4 mm. As we increase ξ from 4 mm to 3.7 cm, the sprinkler head progressively moves out of the boundary layer and responds to a change in local velocity and density difference. When at ξ=3.7 cm, the activation time spread ratio is very close to unity for all slopes considered. This translates into an activation pattern t^*_{act} less-skewed along S_1 and more uniformly shaped into a circle. Particularly for the case of ξ=3.7 cm, which corresponds to a sprinkler height in the "tail" of the ceiling jet (momentum and thermal), the flow conditions to trigger the sprinkler are almost the same everywhere around the impingement point of the plume. Therefore, it is reasonable to imagine a circular

activation pattern, t^*_{act}, and hence a uniformly distributed activation around the impingement point. On the other hand, this observation does not apply as the distance is reduced (i.e. ξ=1.5 cm and ξ=4 mm). As one gets closer to the ceiling, and more the ceiling jet flow conditions differentiate based on the distance from the impingement point and the ceiling slope; this generates a more likely pattern skewed to the upward.

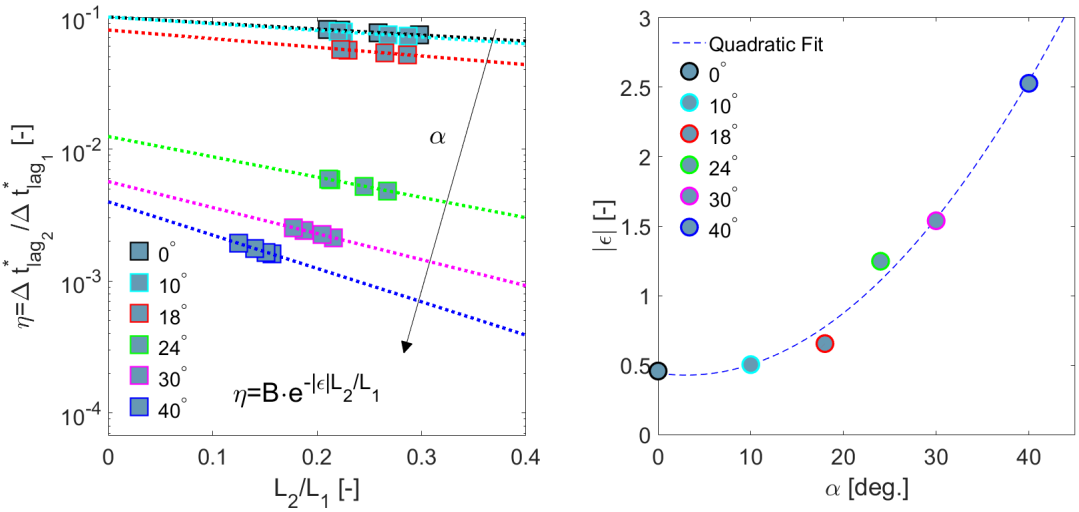

Figure 6.8: Analysis of virtual sprinkler lag time spread at ξ=4 mm from the ceiling surface: lag time spread, η, vs. activation time spread, L_2/L_1 (left); lag time spread rate, ϵ, vs. slope angle, α (right).

In light of the observations stemming from the activation time contours t^*_{act} shown in Fig. 6.5, an analysis for sprinkler lag (or delay) times was performed based on the information provided by each activation contour line (t^*_{act}=const.) for a given slope, α. Dimensionless quantities $\Delta t^*_{lag_{L_1}}$ and $\Delta t^*_{lag_{L_2}}$, representing the difference (Δ) between lag times at the endpoints of the L_1 and L_2 segments of a single ac-

tivation pattern (previously discussed), were investigated assuming the relationship between activation, delay and front arrival time (Eq. 6.1) at each endpoint. Given the rising level of skewness of the activation patterns at increasing ceiling slopes, the focus of this study was to find a spanwise-to-streamwise lag time correlation able to predict the response of the sprinklers to a change of scenario over a wide range of angles (0° to 40°).

Because of the symmetry of the activation patterns in the spanwise direction (Fig. 6.5), a similar delay time was expected for the two endpoints of L_2 ($\Delta t^*_{lag_{L_2}} \rightarrow 0$); on the contrary, due to the different flow transport dynamics between the downslope (adverse buoyancy) and the upslope (favorable buoyancy), particularly pronounced at higher angles ($24° \leq \alpha \leq 40°$) as shown in Fig. 6.5, increasing $\Delta t^*_{lag_{L_1}}$ were found at increasing α.

Rather than investigate $\Delta t^*_{lag_{L_1}}$ and $\Delta t^*_{lag_{L_2}}$ separately, the goal of finding a correlation between the two lag times suggested the analysis of their ratio (also referred as "lag time spread ratio"). In addition, the fact that $\Delta t^*_{lag_{L_2}} \approx$const. for each case ($\Delta t_{lag_{L_2}} \approx \mathcal{O}(10^{-2})$ s) facilitated the interpretation of the influence of the slope on the delay times for sprinklers located streamwise, $\Delta t^*_{lag_{L_1}}$. Therefore, for each α angle, estimates of the relationship between $\Delta t^*_{lag_{L_1}}$ and $\Delta t^*_{lag_{L_2}}$ were assessed for each activation time contour line previously considered (t^*_{act} from 6 to 15), as following described. By dividing both right and left side of Eq. 6.1 for a given RTI, the value t^*_{act}/RTI represented by one activation pattern can be thought as:

$$\frac{t^*_{act}}{RTI} = \frac{t^*_{FA}}{RTI} + \frac{t^*_{lag}}{RTI} \tag{6.15}$$

For each segment L (L_1 and L_2) of a given activation pattern, we then assumed Eq. 6.15 at endpoint (1) (Eq. 6.16) and (2) (Eq. 6.17)

$$\frac{(t^*_{act})_{(1)}}{RTI} = \frac{(t^*_{FA})_{(1)}}{RTI} + \frac{(t^*_{lag})_{(1)}}{RTI} \tag{6.16}$$

$$\frac{(t^*_{act})_{(2)}}{RTI} = \frac{(t^*_{FA})_{(2)}}{RTI} + \frac{(t^*_{lag})_{(2)}}{RTI} \tag{6.17}$$

and we subtracted Eq. 6.17 from Eq. 6.16, thus obtaining Eq. 6.18, valid for both L_1 and L_2

$$\frac{\Delta t^*_{act}}{RTI} = \frac{\Delta t^*_{FA}}{RTI} + \frac{\Delta t^*_{lag}}{RTI} \tag{6.18}$$

Given the front arrival times available from the PLIF measurements, and assuming Δt^*_{act}=0 for two points of the same contour, we obtained:

$$-\Delta t^*_{FA} = \Delta t^*_{lag} \tag{6.19}$$

Equation 6.19 represented a general equation correlating the two endpoints of both L_1 and L_2. Finally, an RTI-independent time ratio, η, was defined by first applying Eq. 6.19 to both L_1 and L_2, as follows

$$-\Delta t^*_{FA_{L_1}} = \Delta t^*_{lag_{L_1}} \tag{6.20}$$

$$-\Delta t^*_{FA_{L_2}} = \Delta t^*_{lag_{L_2}} \tag{6.21}$$

and taking the ratio of Eq. 6.21 and 6.20 term by term, as follows

$$\eta = \frac{\Delta t^*_{lag_{L_2}}}{\Delta t^*_{lag_{L_1}}} = \frac{\Delta t^*_{FA_{L_2}}}{\Delta t^*_{FA_{L_1}}} \tag{6.22}$$

First, as one may note, Eq. 6.19 shows that the difference between lag times at the endpoints of a given length (L_1 or L_2) is equal and opposite to that between

the correspondent front arrival times (Eqs. 6.20 and 6.21). Therefore, in order to preserve the balance of the activation time (same for both endpoints of an activation pattern), the endpoint of L (L_1 or L_2) where the front arrival time was smaller corresponded to the point where the delay time was larger, and vice-versa.

Based on saltwater measurements, the flow streamwise (S_1) was faster on the upslope and slower on the downslope as expected. However, moving to higher slopes, the increasing skewness of the patterns and their trend to get closer to the impingement point on the downslope (Fig. 6.5) caused the upper endpoint of L_1 (intersection between the contour line and the S_1 axis) to move farther upslope (longer distance from the impingement point for the front to cover) and the lower endpoint closer and closer to the impingement point on the downslope (shorter distance from the impingement point). This effect due to increasing slopes, and particularly pronounced in the range $24° \leq \alpha \leq 40°$, produced larger front arrival time for the upper endpoint of L_1 and smaller front arrival time for the lower endpoint of a given activation pattern (t^*_{lag}=const.). On the other hand, in the $0° \leq \alpha \leq 18°$ slope range, given the reduced skewness of the activation patterns, more similar front arrival times between the two endpoints of L_1 were found.

In response to larger front arrival times on the upslope (particularly for $24° \leq \alpha \leq 40°$), smaller delay times for the virtual sprinklers were observed according to Eq. 6.1. It should be noted that smaller lag times (high heat sensor responsiveness) on the upslope are consistent with the theory by Hollman [141], which reports a convective heat transfer coefficient, $h = Re^{0.466} \approx \sqrt{Re}$ (for small cylinder shapes and $4 \leq Re \leq 4000$). In this case, the higher the velocity of the hot gas flowing over

the heat sensor and faster the response of the sprinkler, and this matches the higher velocity found on the upslope during saltwater experiments. On the other hand, for the same activation time, the sprinkler lag time increased in the downslope as increasing the inclination angle because of a shorter front arrival time for the lower endpoint of L_1.

In detail, for saltwater experiments, $\Delta t_{lag_{L_1}}$ slightly increased from 0.14 s to 0.19 s in the range $0° \leq \alpha \leq 18°$ (0.68 s to 0.96 s in the real fire scenario), while a major change was observed when increasing the slope in the range $24° \leq \alpha \leq 40°$ with $\Delta t_{lag_{L_1}}$ values from 2 s to 6.2 s (10.4 s to 31.2 s in the real fire scenario).

These results should be interpreted taking into consideration that this analysis was based on the spatial distribution of the activation patterns, t^*_{lag}=const. The scenario would be different if instead of the intersections of these lines with the main axes we would have used arbitrary points, symmetric with respect to the impingement point in the streamwise direction. In this case, based on the results shown in Fig. 6.5, we would have noticed that by increasing α, the delay in the activation between these two points would have increased, observing a late activation for the lower side point, compared to its symmetric on the elevated side of the plate (as observed by Chatterjee *et al.* [76,82]). Therefore, based on Eq. 6.1, a shorter activation time corresponded to a smaller front and lag times for the upslope streamwise point, and viceversa for the lower point.

The ratio η (Eq. 6.22) was hence investigated with respect to the activation time spread (representing the skewness of activation time contours), L_2/L_1, and to the inclination angle α, respectively (Fig. 6.8). The analysis for L_2/L_1 shown in

Fig. 6.8 (left) revealed that, by increasing α from 0^0 up to 40^0, the delay between the endpoints in the streamwise direction quantified by $\Delta t^*_{lag_{L_1}}$ increased compared to the delay along the spanwise direction, $\Delta t^*_{lag_{L_2}}$, which instead showed to be approximately constant ($\Delta t_{lag_{L_2}} \approx \mathcal{O}(10^{-2})$ s) for each slope.

In detail, such correlation was found to follow an exponential law given in Eq. 6.23 and shown in Fig. 6.8 (left).

$$\eta = \frac{\Delta t^*_{lag_{L_2}}}{\Delta t^*_{lag_{L_1}}} = B \cdot e^{-|\epsilon| \frac{L_2}{L_1}} \tag{6.23}$$

where B is a coefficient depending on the $\frac{\Delta t^*_{lag_{L_2}}}{\Delta t^*_{lag_{L_1}}}$ distribution, and symbol ϵ represents the angular coefficient (negative) for the curves displayed in Fig. 6.8 (left). The investigation continued by analyzing the absolute value $\mid \epsilon \mid$ with respect to the slope angle, α.

Values for $\mid \epsilon \mid$ were estimated for each α and found to increase quadratically with increasing slopes (Fig. 6.8 (right)), as shown in Eq. 6.24.

$$\mid \epsilon \mid = 1.54 \cdot 10^{-3} \alpha^2 - 9.22 \cdot 10^{-3} \alpha + 0.44 \tag{6.24}$$

In light of these results, the ϵ parameter was interpreted as the rate at which the streamwise lag time, $\Delta t^*_{lag_{L_1}}$, compares to the spanwise lag time, $\Delta t^*_{lag_{L_2}}$, at increasing slope angle. Particularly, according to Eq. 6.24, for lower slopes ($0° \leq \alpha \leq 10°$) this phenomenon occurs at a slower pace, whereas it gets faster when $\alpha > 18°$ (Fig. 6.8, right). These observations align well with the results previously discussed for the activation time contours (Fig. 6.5)—as discussed, an increasing slope causes the sprinklers to activate primarily in the streamwise direction (with a delayed activation on the downslope) rather than the spanwise, where both front arrival and delay

times are larger.

Equations 6.23 and 6.24, along with the analysis of the activation time spread ratio, contribute to the knowledge of the suppression systems (sprinkler) for inclined fires, which still lacks a defined sprinkler spacing strategy at varying slopes. In detail, these correlations represent a valuable engineering tool for preliminary sprinkler placement design.

In summary, while 10° to 18° inclined ceilings behave similarly to flat ceilings, ceilings inclined (α) from 24° to 40° have markedly delayed activation downslope and spanwise, and faster activation upslope. Further, as the degree of incline increases, downslope sprinklers activate with increasing delay, with upslope sprinklers activating faster. This suggests a favorable buoyancy component upslope that accelerates flow and reduces front arrival time, a phenomenon particularly pronounced among the higher range (24° to 40°) of slopes.

Analysis of activation contour lines exhibited a different rate of change of L_2/L_1 with respect to α: no change in the spread ratio in the low slope (0° to 18°) range, whereas L_2/L_1 decreased quadratically in the 24° to 40° range. With slopes greater than 24°, activation time spread ratio decreases quadratically with respect to α, meaning increasingly delayed activation of spanwise and downslope sprinklers and accelerated activation of symmetrical/upslope sprinklers.

Practically, this suggests that quick response sprinklers should be preferred in the lower side of sloped ceilings with $24° \leq \alpha \leq 40°$ in areas with multiple fire hazards. And, given the similarity between $0° \leq \alpha \leq 18°$ ceilings, sprinkler placement

can generally be applied similarly to flat horizontal ceilings.

Chapter 7: Discussion, Conclusions and Future Work

In this study, a quantitative saltwater modeling technique was used to investigate the dispersion of hot, buoyant flows. A dimensional analysis based on the analogy relating saltwater and fire-induced flows was applied to measurements taken with Particle Image Velocimetry (PIV) for velocity and Planar Laser Induced Fluorescence (PLIF) for flow concentration which enabled analysis of different aspects of interest for both an unconfined plume and a sloped ceiling jet.

Free Plume Resolution Study

PIV and PLIF imaging with a spatial resolution of $\sim 170\mu$m was first used to characterize and validate flow properties of a free plume. Good agreement was found between measurements, established turbulent point source plume theory [104], and previous studies from real pool fire experiments [101] and scaled saltwater tests [94, 97, 100, 108]. Probability density functions (PDFs) were recorded at different heights (x_3) and cross-stream locations (x_1) which provided qualitative insight into local turbulent mixing and entrainment.

Highly spatially-resolved saltwater measurements (25μm) were later designed based on the same flow setup (saltwater source strength, volumetric flow rate, etc.) used for the characterization and validation of the plume. A spatial resolution coars-

ening process was applied to these highly-resolved images using a pixelated, virtual interrogation window of varying size L inspired by the low-pass filter concept used in Large Eddy Simulations (LES). Although the virtual window technique operated inversely compared to an LES mesh-grid refinement for sensitivity analysis, the main goal, similar to that of a numerical simulation, was to determine a resolution threshold for converged statistics of the flow. The investigation provided intervals of resolution that could be used for the development of CFD models or to probe existing plume numerical studies. Based on the characteristics analyzed in most of the fire plume numerical studies (e.g. first and second order statistical moments), comprehensive guidelines on the resolution ranges for converged time-averaged velocity and density difference (first order statistics), flow scales turbulence intensities (second order statistics), and higher-order statistics, along with spatial resolutions to resolve more than the 80% of turbulence by the larger scales (kinetic energy resolution factor, M) were provided. Based on analysis of the results for both intermittent and fully-buoyant regions of the flow, it was determined that $L \leq 0.3D^*$ should be adequate to resolve the time-averaged concentration (temperature) of the flow and the centerline turbulence intensities. For the streamwise velocity, however, both first and second order statistical moments are found to be resolved at $L \leq 0.7D^*$. This also implies that for $L \leq 0.3D^*$, both velocity and temperature statistical moments of large-scale fire flows can be resolved along the centerline (from the intermittent region to the fully-buoyant region). For the purpose of modeling practical fire-induced flows (smoke transport), where velocity and temperature fields are assumed coupled by buoyancy forces (free convection), an intermediate resolution range of $L \leq 0.5D^*$

is suggested.

Eventually, on the basis of density difference higher order statistics, it was shown that the virtual window is able to operate as a low-pass filter to quantify the contribution of smaller (pixel-based standard deviation within the grid) and larger (pixel-based mean over the grid) scales over time. This provided a new methodology for establishing an engineering tool to probe numerical analyses and contribute to the development of new ones.

Sloped Ceiling Jet Flows

Saltwater modeling experiments were then used to quantify the flow field of a ceiling jet generated by the impingement of a steady fire plume onto an unconfined sloped surface with angles ranging from $\alpha = 0^\circ$ to $\alpha = 40^\circ$. The jet flow developing along an inclined plate was visualized employing PIV and PLIF single-laser sheet techniques. Preliminary observation of raw images revealed features of the flow at different slopes, further investigated through quantitative measurements. Upslope of the plate, it was found that, at increasing slopes, the buoyancy force acted on the ceiling jet to accelerate the bulk flow by means of a favorable gravity component along the plate, whereas a decreased perpendicular component inhibited entrainment with the fresh flow, causing the flow to appear denser at higher angles. On the downward side of the ceiling plate, where the gravity component (and therefore the buoyancy force) opposes the flow motion, the ceiling jet increasingly decelerated at increasing slopes. This provided conditions for a flow reversal phenomenon at a point (the penetration distance) where the flow reversed and the density difference was approximately zero. Consistent with past results from computational analy-

sis and small fire experiments, the penetration distance was found to be shorter at higher angles, whereas in the lower slope range investigated, that is α=0° and α=10°, such distance fell out of the ceiling plate boundaries. Additionally, from velocity and concentration plots, both transport characteristics exhibited an increasing asymmetrical behavior between upslope (S_1/H >0) and downslope (S_1/H <0) as the ceiling slope was increased. Increasingly asymmetrical velocity and density difference (temperature) distributions between the upslope and the downslope regions found for α >18° suggest scenarios where increasing activation delays are expected between the same devices located upslope and downslope of the impingement point due to activation times for similar detectors being controlled by near-field flow speed and temperature.

The sloped ceiling-jet boundary layers (momentum and thermal) were then studied in detail. The results obtained for the boundary layers confirmed that the ceiling jet flow development along an inclined ceiling is driven by the initial momentum of the impinging plume, similarly observed for flat ceilings [134, 135]. The δ_u (momentum) and δ_θ (thermal) boundary layer fit curves obtained allow for estimation of the extension of the jet flow underneath the ceiling where, in practical scenarios, a suppression system would operate. This information is therefore of great interest for sprinkler spacing and placement during the design phase, as it can provide a measure of the sprinkler height (or standoff distance from the ceiling) at which the sensitive element can trigger the sprinkler device for an early response. Fits were also provided for the full region of influnce of the jet layer beneath the ceiling, including the half-Gaussian layer below the boundary layer. In this region,

both velocity and temperature exponentially decrease from the maxima of their respective boundary layers. Least-squares fits were determined for $0° < \alpha < 40°$ as a function of the upslope, S_1/H, and the angle, α.

Saltwater measurements of velocity and density difference were later employed to estimate the depth of the ceiling layer (momentum L_u, thermal L_θ), given as the sum of the boundary layer (momentum δ_u and thermal δ_θ), where both velocity (momentum) and concentration (thermal) reach their maxima at the edge, and the half-Gaussian layer, where both flow characteristics decay exponentially from their peaks, respectively. The primary interest in estimating δ_u, δ_θ, L_u and L_θ at increasing slope angles was to provide a local extension for two operative scenarios for suppression devices as the ceiling jet develops along S_1/H. First, estimating where sprinkler elements can most quickly trigger suppression devices, i.e. the highest velocity and temperature (boundary layer) and second, assessing how activation can be delayed by lower values of both characteristic flow scales.

The investigation conducted on the boundary layer produced consistent results with those obtained from studies concerning both horizontal [94, 134, 135] and sloped ceilings [137] from small fire experiments to previous saltwater modeling experiments [94]. Even though further experiments should be conducted using different flow conditions (e.g. different saltwater source strengths), the results presented here suggest that the saltwater modeling technique could be a valid tool to characterize this region of the flow. In fact, the saltwater results illustrate how inclined ceiling jet flows can be assessed in a similar manner to analyses conducted on horizontal ceilings.

By increasing the slope, both momentum and concentration (thermal) boundary layers were observed to progressively become thinner. Alpert [133] and Cooper [134] previously claimed that, within a fire-induced ceiling jet, the boundary layer is dominated by the initial momentum of the impinging plume. Although these observations were originally formulated for horizontal ceilings, the saltwater boundary layers for slopes up to 40° were found to follow the same trends. As an example supporting this suggestion, the momentum boundary layer, δ_u, was found to follow $\delta_u \sim (S_1/H)^n$, with n ranging from 0.8 to 0.87 (for $0° \leq \alpha \leq 40°$), which is typical for a turbulent boundary layer in forced convection along a flat plate. The thinning of the boundary layers (δ_u, δ_θ) can then be interpreted as an effect of the increased velocity and concentration at higher slopes, i.e. an increased (Re). Similar to horizontal ceilings, sloped ceiling boundary layers can be assumed to be momentum-dominated [133, 134]. Correlations provided for δ_u and δ_θ can then be employed to design a fast activation sprinkler layout, placing the devices where these correlations predict ideal velocities and temperatures.

Eventually, analysis of the ceiling jet, S_1/H, was completed with relationships describing the edge of such region (L_u for velocity and L_θ for concentration) for upslope locations in the range $0 \lesssim S_1/H \leq 1.1$ varying the slopes from 0° to 40°. By means of a least-square regression method, $L_u = L_u(\alpha, S_1/H)$ and $L_\theta = L_\theta(\alpha, S_1/H)$ best fit curves (for velocity and concentration, respectively) were fit as explicit functions of the slope, α, and the upslope location, S_1/H, using measured data sets from each slope (α=0°, 18°, 24°, 40°), except for the case at α=30°. The latter was used as a test case to validate the curve fit to measured data, thus providing a visual

demonstration of the ability to predict the extension of a ceiling jet layer (L_u, L_θ) for a slope in the range 0° to 40°. Future measurements for any slope other than those investigated in the range of 0° to 40° should be able to validate this simple predicting tool which could be potentially applied to full-scale scenarios to design activation systems sensing lower temperatures and lower flow velocities (early fire activation/detection).

In addition, the results showed that, consistent with the observations discussed above for the boundary layers (included within the ceiling jet layer), both L_u and L_θ ceiling jet layers were fully buoyancy-dominated. In fact, this is the opposite of what is seen for the boundary layers: the higher the slope of the ceiling plate, the larger the extension of L_u and L_θ. This was interpreted as the effect of increasing slopes on the gravity (buoyancy) force components acting on the flow along the upslope and perpendicular to the wall. At higher angles, the reduction of the gravity force component along the perpendicular to the surface inhibited entrainment with fresh flow below the ceiling flow edge, while an increased gravity component upslope acted on the ceiling jet to accelerate the flow. Therefore, it was inferred that denser and faster ceiling jet flows at increasing slopes required larger regions underneath the ceiling to eventually merge the quiescent flow conditions.

Activation under sloped ceilings

Because these sloped ceiling-jet flows were observed to be asymmetrical, a multi-planar laser grid was generated around the impingement point illuminating the flow field along both spanwise and streamwise directions. The measured data estimated at a distance ξ (stand-off distance) from the surface, where sprinkler heads are vir-

tually set, enabled a two-dimensional contour of response time.

The ability of saltwatwer modeling to provide a two-dimensional, scaled representation of the activation time under a sloped ceiling with an inclination varying from 0° to 40° was investigated. Using a sprinkler activation model by Heskestad and Bill [91] for real fire scenarios, a "multi-planar" laser sheet grid was created to capture saltwater velocity, density difference, and front arrival time of the ceiling flow. This work involved a steady fire as a major idealization in the construction of this model, particularly valuable for sprinklers placed in the boundary layer (within 2% of H) of high ceilings [92, 93, 143] in the early-stage of a fire. By integrating dimensionless saltwater measurements into the activation model, two-dimensional activation time contours were plotted for each slope. This provided valuable information as to the effect of slope that may be reduced to simplified models useable as a critical design tool.

From the activation time contours, it was inferred that inclined ceilings at 10° and 18° angles have similar activation patterns as flat ceilings, while increasing α from 18° to 40° produced significant delays in activation downslope of the impingement point, whereas sprinklers activated faster upslope. This mostly occurs because of a favorable buoyancy component upslope that accelerates the flow and reduces the front arrival time for the upslope sprinkler, whereas the opposite occurs for the devices located downslope. This phenomenon becomes particularly pronounced in the higher range of slopes (from 24° to 40°), while the range 18° to 24° corresponds to a transition between the flat ceiling scenario and the one for larger slopes.

The saltwater modeling observations presented above have also been com-

pared against numerical fire simulations from Chatterjee *et al.* [76]. The upslope vs. downslope sprinkler activation delay, Δt_{act} as a function of $\Delta S_1/H$, for 0°, 18° and 30° slopes was found to compare well with the trend observed for the 0°, 18.4°, and 33.7° fire scenarios which were numerically modeled. However, the inadequacy of this scaled technique with a constant source, $\dot{m}^*_{sw}$ to accurately estimate activation delays below sloped ceilings for a variable fire source, $\dot{Q}(t)$, was inferred from the overestimated saltwater activation times compared to those from fire simulations. Nonetheless, given the small fire strength simulated by our measurements, ($\dot{Q} = 100$ kW), which better represents the early stage of a fire rather than its full growth phase (see Fig. 2.9 in [76] for reference), and the short front arrival times (20-30% of the t_{act}) found for each slope case, led to our assumption that our analysis is still valid for a quasi-steady fire scenario.

A L_2/L_1 skewness parameter for the activation patterns was introduced to correlate the activation time along the main axis, S_1, with that related to sprinklers located spanwise with respect to the impingement point (along S_2). The analysis of the so-called "activation time spread ratio", L_2/L_1, with respect to the ceiling slope, α, showed a common trend for all the activation patterns from t^*_{act}=6 to t^*_{act}=15. Each activation contour line exhibited a similar rate of change of L_2/L_1 with respect to α—approximately no change in the spread ratio was noticed in the low slope range (0° to 18°), whereas L_2/L_1 decreased quadratically in the 24° to 40° range. This provided valuable information about the unknown correlation between sprinklers activating streamwise (upslope and downslope) and those activating spanwise (characterized by a similar activation time to that of the downslope

sprinklers). In fact, by increasing the slope up to 18° from the horizontal, the activation delay between upslope sprinklers and those located (symmetrically) either downslope and spanwise stays unchanged (L_2/L_1 ≈const.). When assuming slopes greater than 24°, the skewness of the activation contours represented by the activation time spread ratio increases quadratically with the respect of α. This clearly indicates that the activation of the sprinklers located spanwise and downslope are delayed further compared to symmetrical sprinklers located upslope. These results could suggest fire safety strategies where quick response sprinklers may be preferred on the lower side of sloped ceilings with 24°$\leq \alpha \leq$40°), in areas with multiple fire hazards. On the other hand, given the similarity between cases at 0°, 10° and 18°, strategies already adopted for horizontal ceilings could be extended (in a first approximation) to scenarios with slopes up to 18°.

Based on a L_2/L_1 skewness parameter for the activation patterns, the analysis conducted for sprinkler lag time, t^*_{lag}, revealed that for devices located streamwise with respect to the impingement point, the time exponentially decreases with respect to the lag time found for sprinklers located spanwise. This was found to accelerate quadratically with increasing α, resulting in more skewed activation patterns below the ceiling when increasing inclination.

Future work

Highly spatially resolved saltwater measurements were designed to provide useful guidelines in development and validation of Large Eddy Simulations (LES) of unconfined plumes. Although saltwater modeling represents a validated and convenient approach to costly large scale fire experiments [94, 119], technical limitations re-

lated to laser techniques used for the experiments, namely PIV and PLIF, should be further investigated. The laser sheet thickness used for both PLIF and PIV measurements is subject to fluctuations due to the law of refraction (or Snell's law). When the laser crosses the saltwater, which has a different refraction index from that of the fresh water, the laser sheet steers at the interface between the two media. This variation in position is somewhat proportional to the interface radius of curvature of the medium crossed, therefore the turbulent interface of the plume (small radius of curvature) attenuates this variation. In addition, the presence of salt mass fraction gradients within the laser thickness are assumed small because of the symmetry of the plume, so that within the the probe volume (illuminated region) the related changes in the index of the refraction from point to point are small. All of the previous assumptions ensure that the laser sheet is aligned to cut through the plume centerline anyway, but the aforementioned small variations still make the laser sheet thickness fluctuate within a confidence interval. This produces uncertainties in the laser sheet thickness that can change the sampling volume from frame to frame and therefore affect the turbulence statistics for both velocity (PIV) and concentration (PLIF) measurements. While other major source of errors dealing with the flow apparatus and the preparation of the experiments are much more manageable, this aspect is difficult to quantify. Future work should focus on LES or DNS simulations recreating similar plume scenarios to compare and validate the results presented in this work.

The study on inclined ceiling jet flows provided useful information regarding the operative environment of suppression systems (sprinklers) on slopes. Given the

need to predict activation times based on ceiling jet velocity and concentration, distributions of both flow characteristics underneath the ceiling, namely the boundary layer and the ceiling jet layer, were investigated. The correlations established for δ_u, δ_θ, $L_u(S_1/H, \alpha)$ and $L_\theta(S_1/H, \alpha)$ were derived for a given saltwater source strength, $\dot{m}^*_{sw}$, designed to ensure a highly turbulent flow at the impingement point ($Gr_H \sim 10^{11}$). This allowed us to neglect molecular diffusion effects along the ceiling and assume dominant turbulent convective transport to preserve the similarity between saltwater and fire-induced ceiling jet flow. This assumption was verified by comparing the power laws found for the boundary layers, δ_u and δ_θ, typical of turbulent boundary layers. On the other hand, the results presented for δ_u and δ_θ on horizontal ceilings showed that a laminarization process occurred for S_1/H >0.65. For these locations, the images of the flow exhibited a stratification of the ceiling layer replacing the large turbulent structures dominating the flow upstream. This phenomenon, which was found to be disruptive with results from previous studies on horizontal fire-induced ceiling jets, was only qualitatively analyzed, lacking a proper quantitative analysis able to determine the likely cause for this phenomena. Based on previous observations from Yao [94, 97], who experienced similar effects for his saltwater experiments, saltwater ceiling flows are characterized by lower Gr (or Re) numbers when compared to hot gas ceiling jets, and therefore are more sensitive to a change in the Ri number. The Ri can be interpreted as the ratio between the potential energy associated with density differences (which inhibits mixing and entrainment) and the kinetic flow energy (which promotes mixing and entrainment) [94]. It is well established that the Ri for horizontal ceilings increases

with increasing radial distance from the impingement point [133], and this progressively reduces the entrainment downstream as buoyancy acts to stably stratify the ceiling layer and inhibiting further mixing [94]. Higher slopes should have a lower Ri along the upslope compared to the horizontal due to a higher velocity gradient orthogonal to the ceiling and lower density difference potential energy, because of a reduced orthogonal gravity component. This would explain why the laminarization effect was not observed for higher slopes. Future experiments should determine how the position where the flow begins to laminarize changes, based on various source strengths and ceiling heights. This will require an analysis of Re_H (or equivalently the Gr_H) at the impingement point based on different initial conditions (source strength, ceiling height, etc.), and local estimates of the Ri number along S_1/H to establish a general criterion for horizontal ceiling laminarization.

Future work on sprinkler activation should focus on conducting large-scale fire tests (or numerical simulations) able to confirm the slope effects on activation captured using the multi-grid PLIF/PIV laser technique. In order to provide guidelines for fire scenario protection schemes, the aspects neglected in the current analysis of saltwater experiments such as the presence of end-walls (vertical walls) and the use of different saltwater source strengths (simulating different fire strengths) and ceiling heights should be included. Given the results, effects due to increasing slopes were particularly pronounced for slopes $\alpha > 24°$ with a transition in the range $18° < \alpha < 24°$. In this study no slope angle within this transitional range was explored; therefore quantitatively investigating additional slope cases for $18° < \alpha < 24°$ would help to determine the threshold ceiling slope angle causing

a marked change in the activation patterns. This would better define a distinct sprinkler spacing strategy for each case.

A.1 Non-linear Least-Squares Method

Non-linear least squares is a statistical method used to fit a given set of m experimental data points (x_i, y_i), i=$1, \ldots, m$ (in pairs) with a non-linear model (function), y=$f(x,\boldsymbol{\beta})$, where $\boldsymbol{\beta}$=$(\beta_1, \beta_2, \beta_3, \ldots, \beta_n)$ represents a vector of n unknown parameters ($m \geq n$). This approach is used in regression analysis, often in non-linear regression modeling in which a curve is fit into a set of data, and its objective is to adjust the n parameters of the model function by successive iterations to eventually find the best fit for the data points.

Assume a set of m observations, (x_1, y_1),...,(x_m, y_m), and the curve (model function) introduced above, y=$f(x,\boldsymbol{\beta})$, that in addition to the independent variable x also depends on n parameters of the $\boldsymbol{\beta}$ vector. By definition, the measure of the fit of a model to a data point is given by its residual (or sample prediction error), r_i, defined as the difference between the actual experimental observation, y_i, and the model prediction, $f(x_i, \boldsymbol{\beta})$

$$r_i = y_i - f(x_i, \boldsymbol{\beta}) \tag{1}$$

for i=$(1, 2, 3, \ldots, m)$. The least-squares determines the optimal $\boldsymbol{\beta}$ vector by minimizing the sum of squared residuals, S

$$S = \sum_{i=1}^{m} r_i^2 \tag{2}$$

The minimum of S occurs when the gradient with respect to $\boldsymbol{\beta}$ is zero. Since the model contains n parameters there are n gradient equations that must be satisfied:

$$\frac{\partial S}{\partial \beta_j} = 2\sum_{i=1}^{m} r_i \frac{\partial r_i}{\partial \beta_j} \quad j = (1, 2, 3, \ldots, n) \tag{3}$$

In case of a nonlinear function f, the derivatives $\partial r_i/\partial \beta_j$ are functions of both the independent variable and the parameters, so these gradient equations do not have a closed solution. Therefore, an iterative procedure of refinemnet for the parameters is adopted, that is, the values are obtained by successive approximation,

$$\beta_j \approx \beta_j^{k+1} = \beta_j^k + \Delta\beta_j \tag{4}$$

Symbol k represents the current iteration and the vector of increments, $\Delta\boldsymbol{\beta}$, is known as the shift vector. At each iteration the model is approximated using a first-order Taylor polynomial expansion about $\boldsymbol{\beta}_j^k$ as

$$f(x_i, \boldsymbol{\beta}) \approx f(x_i, \boldsymbol{\beta}^k) + \sum_j \frac{\partial f(x_i, \boldsymbol{\beta}^k)}{\partial \beta_j}(\beta_j - \beta_j^k) = f(x_i, \boldsymbol{\beta}^k) + \sum_j \boldsymbol{J}_{ij}\Delta\beta_j \tag{5}$$

and the Jacobian, $\boldsymbol{J_{ij}}$, is introduced as a function of both the independent variable (i subscript) and the parameters (j subscript), so it changes at each iteration. Therefore, it appears that $\partial r_i/\partial \beta_j = -J_{ij}$ and the residuals are given as follows

$$\Delta y_i = y_i - f(x_i, \boldsymbol{\beta}^k) \tag{6}$$

$$r_i = y_i - f(x_i, \boldsymbol{\beta}) = (y_i - f(x_i, \boldsymbol{\beta}^k)) + (f(x_i, \boldsymbol{\beta}^k) - f(x_i, \boldsymbol{\beta})) \approx \Delta y_i - \sum_{s=1}^{n} \boldsymbol{J}_{is}\Delta\beta_s \tag{7}$$

Substituting Eqs. 7 into Eqs. 3, Eqs. 3 become

$$-2\sum_{i=1}^{m} J_{ij}(\Delta y_i - \sum_{s=1}^{n} J_{is}\Delta\beta_s) = 0 \tag{8}$$

Bibliography

[1] Klote, J. H., Klote, J. H. and McLean, *Atrium smoke management*, Fire Protection Engineering, (7), 2000.

[2] A. F. A. Gawad, H. A. Ghulman, *Prediction of Smoke Propagation in a Big Multi-Story Building Using Fire Dynamics Simulator (FDS)*, American Journal of Energy Engineering, Special Issue: Fire, Energy and Thermal Real-life Challenges, Vol. 3, No. 4-1, 2015, pp. 23-41.

[3] P. Maisto, M. J. Gollner, A. W. Marshall, *Salt-Water Modeling to Probe Sub-Grid Scale Turbulent Mixing of Fire Plumes*, 9$^{\text{th}}$ U.S. National Combustion Meeting, Cincinnati, OH, 2015.

[4] P. Maisto, M. J. Gollner, A. W. Marshall, *Characterization of Sloped Ceiling Jet Flow Using Laser-Assisted Saltwater Modeling Technique*, 10$^{\text{th}}$ U.S. National Combustion Meeting, College Park, MD, 2017.

[5] K.A. Watson, K.M. Lyons, C.D. Carter, J.M. Donbar, *Simultaneous two-shot CH planar laser-induced fluorescence and particle image velocimetry measurements in lifted CH4/air diffusion flames*, Proceedings of the Combustion Institute Volume 29, Issue 2, 1905-1912, 2002.

[6] D. W. Stroup, D. D. Evans, *Use of computer fire models for analyzing thermal detector spacing*, Fire Safety Journal, Volume 14, Issues 12, 33-45, 1988.

[7] P. Maisto, M. J. Gollner, A. W. Marshall, *Predicting Detector Response Time Using Saltwater Modeling on Sloped Ceilings*, 16$^{\text{th}}$ International Conference on Automatic Fire Detection-AUBE 17 & Suppression, Detection and Signaling Research and Applications Conference-SUPDET 2017, College Park, MD, 2017.

[8] Y. Oka, O. Imazeki, O. Sugawa, *Temperature profile of ceiling jet flow along an inclined unconfined ceiling*, Fire Safety Journal, 45, 221-227, 2010.

[9] P. Maisto, A. W. Marshall, M. J. Gollner, *Quantitative saltwater modeling for validation of sub-grid scale LES turbulent mixing and transport models for fire*, 68th Annual Meeting of the APS Division of Fluid Dynamics, Volume 60 , 21, Boston, 2015.

[10] P. Maisto, A. W. Marshall, M. J. Gollner, *A Virtual Study of Grid Resolution on Experiments of a Highly-Resolved Turbulent Plume*, 70th Annual Meeting of the American Physical Society Division of Fluid Dynamics, Denver, CO, 2017.

[11] Rouse H., Yih C.S., Humphries H.W., *Gravitational convection from a boundary source*, Tellus, 1952, 4, 20210.

[12] Morton B.R., Taylor G.I., Turner J.S., *Turbulent gravitational convection from maintained and instanteous sources*, Proc. Royal Soc. London, Ser. A, 1956, 234, 123.

[13] R. J. M. Bastiaans, C. C. M. Rindt, F. T. M. Nieuwstadt, A. A. van Steenhoven, *Direct and large-eddy simulation of the transition of twoand three-dimensional plane plumes in a confined enclosure*, International Journal of Heat and Mass Transfer 43 (2000) 2375-2393.

[14] P.E. DesJardin, T.J. O'Hern, and S.R. Tieszen, *Large eddy simulation and experimental measurements of the near-field of a large turbulent helium plume*, Phys. Fluids, 16:18661883, 2004.

[15] M. V. Pham, F. Plourde, and K. S. Doan, *Direct and large-eddy simulations of a pure thermal plume*, Phys. Fluids 19, 125103 (2007).

[16] A. J. Smagorinsky, *General circulation experiments with the primitive equations*, Mon. Weather Rev. 91, 99, (1963).

[17] Germano, U. Piomelli, P. Moin, and W. H. Cabot, *A dynamic subgridscale eddy viscosity model*, Phys. Fluids A 3, 1760, (1991).

[18] Burton, G. C., *Large eddy simulation of a turbulent helium-air plume using the nLES method*, Center for Turbulence Research, Stanford University and NASA-Ames Research Center, Stanford, CA, (2009)

[19] Cetegen, B. M., Ahmed, T. A.,*Experiments on the periodic behavior of buoyant plumes and pool fires*, Combustion and Flame, 93:157184 (1993)

[20] Cetegen, B. M., Kasper, *Experiments on the oscillatory behavior of buoyant plumes of helium and helium-air mixtures*, Physics of Fluids, 8:29742984 (1996)

[21] Nicolette, V. F., Tieszen, S. R., Domino, S. P., Black, A. R., O'Hern, T. J., *A Turbulence model for buoyant flows based on vorticity generation*, Technical Report SAND2005-6273, Sandia National Laboratory, Albuquerque, NM (2005)

[22] Tieszen, S. R., Domino, S. P., Black, A. R., *Validation of a simple turbulence model suitable for closure of temporally-filtered Navier-Stokes equations using a helium plume*, Technical Report SAND2005-3210, Sandia National Laboratory, NM (2005)

[23] Yokoi S., *Study on the prevention of fire-spread caused by hot upward current*, BRI Report, June, 1960.

[24] Hasemi Y., Tokunaga T., *Flame geometry effects on the buoyant plumes from turbulent diffusion flames*, Fire Sci Technol 1984;4:1526.

[25] Cox G, Chitty R., *Some source dependent effects of unbounded fires*, Combust Flame 1985;60:21932.

[26] Heskestad G., *Luminous heights of turbulent diffusion flames*, Fire Safety J 1983;5:1038.

[27] Delichatsios M. A., *Air entrainment into buoyant jet flames and pool fires*, Combust Flame 1987;70:3346.

[28] Kung H., Stavrianidis P., *Buoyant plumes of large-scale pool fires* 19$^{\text{th}}$ Symposium on Combustion, 1982.

[29] Hamins A, Konishi K, Borthwick P, Kashiwagi T., *Global properties of gaseous pool fires*, 26$^{\text{th}}$ Symposium on Combustion, Napoli, Italy, 1996. p. 142936.

[30] Beyler C. L., *Fire plumes and ceiling jets*, Fire Safety J. 1986; 11:5375.

[31] Zukoski E. E., *Properties of fire plumes*, In: Cox G., editor, Combustion fundamentals of fire. San Diego: Academic Press, 1995. p. 34.

[32] Quintiere J. G., Grove B. S., *A unified analysis for fire plumes*, 27$^{\text{th}}$ Symposium on Combustion, Boulder, CO, USA, 1998. p. 275766.

[33] Tamanini F., *Reaction rates, air entrainment and radiation in turbulent fire plumes* Combust Flame 1977; 30:85101.

[34] You H. J., Faeth G. M., *Turbulent combustion: buoyant axi-symmetric turbulent diffusion flames in still air*, Combust Flame 1982;44:261.

[35] Crauford N. L., Liew S. K., Moss J. B., *Experimental and numerical simulation of a buoyant fire*, Combust Flame 1985;61:55.

[36] Adiga K. C., Ramaker D. E., Tatem P. A., Williams F. W., *Modeling pool-like gas flames of propane*, Fire Safety J. 1989; 14:24150.

[37] Hossain M. S., Rodi M. A., *Turbulence model for buoyant flows and its application to vertical buoyant jets*, In: Rodi W, editor. Turbulent jets and flames. New York: Pergamon Press, 1982. p. 12178.

[38] Nam S., Bill R. G., *Numerical simulation of thermal plumes*, Fire Safety J., 1993;21:23156.

[39] Sinai Y. L., Owens M. P., *Validation of CFD modeling of unconfined pool fires with crosswind: flame geometry*, Fire Safety J. 1995; 24:134.

[40] Miles S., Kumar S., Cox G., *The balcony spill plumeSome CFD simulations*, Fire Safety Science Proceedings of 5th International Symposium, Tsukuba, Japan, 1997. p. 23747.

[41] Madrzykowski D., *The future of fire investigation*, Fire Chief, October, 2000.

[42] K.B. McGrattan, H.R. Baum, and R.G. Rehm, *Large eddy simulations of smoke movement*, Fire Saf. J., 30:161178, 1997.

[43] X. Zhou, K.G. Luo, and J.J.R. Williams, *Study of density effects in turbulent buoyant jets using large-eddy simulation*, Theoret. Comput. Fluid Dynamics, 15:95120, 2001.

[44] X. Zhou, K.G. Luo, and J.J.R. Williams, *Vortex dynamics in spatio-temporal development of reacting plumes*, Combust. and Flame, 129:1129, 2002.

[45] X. Zhou, K.G. Luo, and J.J.R. Williams, *Large-eddy simulation of a turbulent forced plume*, European J. Mechanics, B/Fluids, 20:233254, 2001.

[46] Baum H. R., McGrattan K. B., Rehm R. G., *Three dimensional simulations of fire plume*, Fire Safety ScienceProceedings of the 5th International Symposium, Tsukuba, Japan, p. 51122.

[47] W. K. George Jr., R. L. Alpert, F. Tamanini, *Turbulence measurements in an axisymmetric buoyant plume*, International Journal of Heat and Mass Transfer, Volume 20, Issue 11, November 1977, Pages 1145-1154.

[48] Papanicolaou, P.N., E. J. List, *Investigations of round vertical turbulent buoyant jets*, J. Fluid Mech. (1988), vol. 195, pp. 341-391

[49] G. Maragkos, P. Rauwoens and B. Merci, *Application of FDS and FireFOAM in large eddy simulations of a turbulent buoyant helium plume*, 7^{th} Mediterranean Combustion Symposium, 11-15 September 2011, Sardinia, Italy

[50] T.G. Ma, J.G. Quintiere, *Numerical simulation of axi-symmetric fire plumes: accuracy and limitations*, Fire Safety Journal 38 (2003) 467492.

[51] Nakagome H., Hirata M., *The structure of turbulent diffusion in an axisymmetrical thermal plume*, Heat Transfre and Turbulent Buoyant Convection, (Spalding and Afgan Eds.) McGraw-Hill, NY. 367-372 (1977).

[52] N. E. Kotsovinos, *Temperature measurements in a turbulent round plume*, International Journal of Heat and Mass Transfer Volume 28, Issue 4, April 1985, pp. 771-777.

[53] J. G. Quintiere, *Fundamentals of Fire Phenomena*, John Wiley and Sons Ltd, 2006.

[54] A.N. Kolmogorov, *The local structure of turbulence in incompressible viscous fluid for very large reynolds numbers*, Dokl. Akad. Nauk SSSR, 30:299303, 1941.

[55] Sagaut P., *Large Eddy Simulation for Incompressible Flows*, 3^{rd} Ed., Springer, 2006.

[56] Pope, S.B., *Ten questions concerning the large-eddy simulation of turbulent flows*, New Journal of Physics 6 (1) (2004) 35.

[57] J.W. Deardorff, *Numerical Investigation of Neutral and Unstable Planetary Boundary Layers*, Journal of Atmospheric Sciences, 29:91115, 1972.

[58] Olsen M.G., Adrian R.J., *Out-of-focus effects on particle image visibility and correlation in microscopic particle image velocimetry*, Exp Fluids 29:S166S174. doi:10.1007/s003480070018, 2000.

[59] J. Way and P. A. Libby, *Application of hot-wire anemometry and digital techniques to measurements in turbulent helium jet*, AIAA J. 9, 1567 1573 (1971).

[60] J. Wygnanski and H. E. Fiedler, *Some measurements in the self-preserving jet*, J. Fluid Mech. 38, 577 612 (1969).

[61] L. P. Chua, *Measurements in a turbulent circular jet*, Ph.D. Thesis, University Newcastle (Australia) (1989).

[62] F. H. Champagne and I. J. Wygnanski, *An experimental investigation of coaxial turbulent jets*, Int. J. Heat Trans., 1445-1464 (1971).

[63] M. Amielh, T. Djeridane, F. Anselmet and L. Fulachier *Velocity near-field of variable density turbulent jets*, Int. J. Heat Mass TransIer. Vol. 39, No. 10, pp. 2149-2164, 1996.

[64] T. J. O'Hern, E. J. Weckman, A. L. Gerhart, S. R. Tieszen, R. W. Schefer, *Experimental study of a turbulent buoyant helium plume*, J. Fluid Mech., vol. 544, pp. 143171, 2005.

[65] I. Amidror, *Scattered data interpolation methods for electronic imaging systems: a survey*, Journal of Electronic Imaging. Vol. 11, No. 2, pp. 157176, 2002.

[66] S. B. Pope, *Turbulent Flows*, Cambridge University Press, 2000.

[67] www.lavision.de

[68] www.photonics.com

[69] P. Ruffino, M. diMarzo, *The simultaion of fire sprinklers thermal response in presence of water droplets*, Fire Safety Journal 39, 721-736, 2004.

[70] J. A. Milke, A. J. Campanella, C. T. Childers, B. D. Wright, *Performance of Smoke Detectors and Sprinklers in Residential and Health-Care Occupancies*, Department of Fire Protection Engineering University of Maryland, 2010.

[71] K. Frank, M. Spearpoint, G. Baker, C. Wade, P. Collier, C. Fleischmann, *Measuring modified glass bulb sprinkler thermal response in plunge and compartment fire experiments*, Fire Safety Journal, Vol. 91, 662-670, 2017.

[72] Schifiliti R.P., Custer R.L.P., Meacham B.J., *Design of Detection Systems*, In: Hurley M.J. *et al.* (eds) SFPE Handbook of Fire Protection Engineering. Springer, New York, NY, 2016.

[73] S. Sako, Y. Hasemi, *Response Time of Automatic Sprinklers below a Confined Ceiling*, Fire Safety Science, 2, 613-622, 1989.

[74] J. Dinaburg, D. T. Gottuk, *Fire Detection in Warehouse Facilities*, Fire Detection in Warehouse Facilities. Springer Briefs in Fire. Springer, New York, NY, 2013.

[75] F. P. Incoprera, D. P. Dewitt, T. L. Bergman, A. S. Lavine, *Fundamentals of Heat and Mass Transfer*, 6th Edition, John Wiley & Sons (2007).

[76] P. Chatterjee, K.V. Meredith, *Numerical Modeling of Sprinkler Activation and Spray Transport Under Sloped Ceilings*, FM Global Research Technical Report, ID 0003055093, Boston MA 02062 (2015).

[77] H.C. Kung, R.D. Spaulding, P. Stavrianidis, Fire Induced Flow Under a Sloped Ceiling, Fire Safety Science, 3, 271-280, (1991)

[78] Y. Wu, J.P. Stoddard, P. James, G.T. Atkinson, *Effect of slope on control of smoke flow in tunnel fires*, Fire Safety Journal, 5, 12251248 (1997)

[79] Y. Oka, O. Imazeki, *Temperature distribution within a ceiling jet propagating in an inclined flat-ceilinged tunnel with natural ventilation*, Fire Safety Journal, 71, 20-33 (2015)

[80] Gollner, M., Overholt, K., Williams, F., Rangwala, A. and Perricone, J., *Warehouse commodity classification from fundamental principles. Part I commodity and burning rates*, Fire Safety Journal, Volume 46, Issue 6, August 2011, pp 305-316

[81] K.E. Isman, *Challenges for the Fire Sprinkler Industry*, Fire Protection Technology Science, (2012)

[82] P. Chatterjee, K.V. Meredith, Y. Wang, *Temperature and velocity distributions from numerical simulations of ceiling jets under unconfined, inclined ceilings*, Fire Safety Journal, (2017)

[83] Y. Oka, M. Ando, *Temperature and velocity properties of a ceiling jet impinging on an unconfined inclined ceiling*, Fire Safety Journal, 55, 97-105 (2013)

[84] O. Sugawa, *Simple Estimation Model on Ceiling Temperature and Velocity of Fire Induced Flow under Ceiling*, Fire Science and Technology, 21-1, 57-67 (2001)

[85] O. Sugawa, T. Hosozawa, N. Nakamura, A. Itoh, Y. Matsubara, *Flow Behavior under Sloped Ceiling*, 15th Meeting of the UNJR Panel on Fire Research and Safety, 2 (2000)

[86] E. Carlsson, *Comparison of Sprinkler Activation in Flat and Sloping Ceilings using FDS 6*, Report 5404, Lund University, (2013).

[87] G. Heskestad, M. A. Delichatsios, *Environments of Fire Detectors Phase I: Effect of Fire Size, Ceiling Height and Material, Measurements and Analysis*. Nbs-gcr-77-86 and Nbs-gcr-7795, 1-2, NIST, (1977).

[88] S.P. Jankiewicz, *Predicting Smoke Detector Response Using a Quantitative Salt-Water Modeling Technique*, M.S. Thesis, University of Maryland, College Park, 2004.

[89] G. Heskestad, *Physical Modeling of Fire*, Journal of Fire and Flammability, 6, 253 (1975).

[90] G. Heskestad, *Generalized Characteristics of Smoke Entry and Response for Products-of Combustion Detectors*, 7$^{\text{th}}$ International Conference on Problems of Automatic Fire Detection, Rheinish-Westfalischen Technischen Hochschule, Aachen, Germany, (1975).

[91] G. Heskestad, R. G. Bill Jr., *Quantification of Thermal Responsiveness of Automatic Sprinklers Including Conduction Effects*, Fire Safety Journal, 14, 1-2, 113-125 (1988).

[92] R.L. Alpert, *Fire Induced Turbulent Ceiling-Jet*, Factory Mutual Research Corporation, Norwood MA, FMRC Serial No.19722-2, 35 (1971).

[93] R.L. Alpert, *Calculations of Response Time of Ceiling Mounted Fire Detectors*, Fire Technology, 8, 3, 181-195 (1972).

[94] X. Yao, *Characterization of Fire Induced Flow Transport Along Ceilings Using Saltwater Modeling*, Ph.D. Dissertation, University of Maryland, College Park, MD, USA, 2006.

[95] Shabbire, A., George, W.K., *Experiments On a Round Turbulent Buoyant Plume*, J. Fluid Mech., 1994. 275: p. 1-32.

[96] Sangras, R., and Faeth, G.M., *Buoyant Turbulent Jets and Plumes: III. Round turbulent Nonbuoyant Starting Jets and Puffs and Buoyant Starting Plumes and Thermals*. Report No. GDL/GMF-99-03, 1999.

[97] X. Yao , T. Ma, A.W. Marshall, A. Trouvé, *Mixing and Turbulent Transport in Unconfined and Impinging Plumes*, 10^{th} International Fire Science and Engineering Conference - interflam, Edinburgh, Scotland (2004).

[98] X. Yao, A.W. Marshall, *Characterizing turbulent ceiling jet dynamics with salt-water modeling*, Fire Saf. Sci., 8, 927-938 (2005).

[99] X. Yao, A.W. Marshall, *Quantitative salt-water modeling for fire-induced flows*, Fire Saf., 41, 497-508 (2006).

[100] T. G. Layton, *Detailed Measurements of Fire-Induced Mixing Phenomena*, M.Sc. Thesis, University of Maryland, College Park, MD, USA, 2014.

[101] B.J. McCaffrey, *Purely Buoyant diffusion Flames: Some Experimental Results*, Center For Fire Research, 1979.

[102] Thomas, P.H., Hinkley, P.L., Theobald, C.R. and Simms, D.L., *Investigations into the Flow of Hot Gases in Roof Venting*, Fire Research Technical Paper No. 7, HMSO, London (1963).

[103] Tangren, E. N., Sargent, W. S. and Zukoski, E. E., *Hydraulic and Numerical Modeling of Room Fires*, California Institute of Technology, Pasadena, California (1978).

[104] Zukoski, E.E, *Prediction of Smoke Movement in Buildings*, California Institute of Technology, Pasadena, California (1978).

[105] K.D. Steckler, H.R. Baum, and J.G. Quintiere, *Salt Water Modeling of Fire Induced Flows in Multi-Compartment Enclosures*, NBSIR 86-3327, Gaithersburg, MD: National Bureau of Standards (1986).

[106] A.A. Kelly, *Examination of Smoke Movement in a Two-Story Compartment Using Salt Water and Computational Fluid Dynamics Modeling*, M.S. Thesis, Dept. Fire Protection Engineering, University of Maryland, College Park, MD (2001).

[107] Clement, J.M., and Fleischman, C.M., *Experimental Verification of the Fire Dynamics Simulator Hydrodynamic Model*, Fire Safety Science - Proceedings of the Seven International Symposium, 2002, 839-851.

[108] Ling, Y.E., *Wind-driven plume dispersion near a building*, M.S. Thesis, University of Maryland, College Park, 2008.

[109] C. C. Siang, *Characterizing Smoke Dispersion along Beamed Ceilings Using Salt-Water Modeling*, M.S. Thesis, University of Maryland, College Park, 2010.

[110] Keane, R., Adrian, R., *Optimization of particle image velocimeters.Part I: Double pulsed systems*, Meas. Sci. Technol. 1, 1202-1215 (1990).

[111] E.K. Budnick, Estimating Effectiveness of State-of-the-Art Detectors and Automatic Sprinklers on Life Safety in Residential Occupancies, Fire Technology, 20, 3, (1984)

[112] B. Zohuri,*Dimensional Analysis and Self-Similarity Methods for Engineers and Scientists*, Springer, 2015.

[113] Schlichting, H., Gersten, K., *Boundary Layer Theory*, Springer, 8th Edition.

[114] Kundu, P.K., Cohen, I.M., Hu, H.H., Publishers, E.S., Fluid Mechanics. Academic Press, San Diego (2002).

[115] Joseph, D.D., *Stability of fluid motions I*, Volume 27. Springer Science & Business Media, 2013.

[116] Merker, G.P., *Konvektive Wärmeübertragung*, Springer-Verlag, 2013.

[117] Lee, J.H.W., Chu, V.H., *Turbulent jets and plumes: A Lagrangian approach*, Springer, 2003.

[118] Rehm, R., Baum, H., *The equations of motion for thermally driven buoyant flows*, Journal of Research of the NBS 83, 297308, 1978.

[119] J.Q. Quintiere, Scaling Applications in Fire Research, Fire Safety Journal, 15, 3-29 (1989)

[120] Morton, B., Taylor, G., Turner, J., *Turbulent gravitational convection from maintained and instantaneous sources*, in: Proceedings of the Royal Society of London A: Mathematical, physical and engineering sciences, The Royal Society. pp. 123, 1956.

[121] Morton B., *Forced plumes*, Journal of Fluid mechanics 5, 151163, 1959.

[122] Papanicolaou, P.N., *Mass and momentum transport in a turbulent buoyant vertical axisymmetric jet*, Ph.D. Dissertation. California Institute of Technology Pasadena/CA, USA, 1984.

[123] Heskestad, G., *Virtual Origins of Fire Plumes*. Fire Safety Journal, 1983. 5: p. 109-114.

[124] Webster, D.R., Roberts, P.J.W., and Ra'ad, L., *Simultaneous DPTV/PLIF Measurements of Turbulent Jet*. Experiments in Fluids, 2001. 30: p. 65-72.

[125] Arcoumanis, C., McGuirk, J.J. and Palma, J.M.L.M., *On The Use Of Fluorescent Dyes For Concentration Measurements in Water Flows*. Experiments in Fluids, 1990. 10: p. 177-180.

[126] Houcine, I., Vivier, H., Plasari, E., David, R. and Villermaux, J., *Planar Laser Induced Fluorescence Technique For Measurements of Concentration Fields in Continuous Stirred Tank Reactors*. Experiments in Fluids, 1996. 22: p. 95102.

[127] Guilbault, G.C., *Practical Fluorescence*. 1973: New York: Marcel Dekker.

[128] Walker, D.A., *A Fluorescence Technique for Measurement of Concentration in Mixing Liquids*. Journal of Physics E: Sci Instrum, 1987. 20: p. 217-224.

[129] Wolf, A.V., Brown, M.G. and Prentiss, P.G., *Concentrative Properties of Aqueous Solutions: Conversion Tables in Handbook of Chemistry and Physics*, 60^{th} Edition. 1979-1980. p. D-261-262.

[130] H.Z. You, G.M. Faeth, *Am Investigation on Fire Impingement on a Horizontal Ceiling*, National Bureau of Standards Technical Report, Rpt. No.NBS-GCR-79-188, October 1978.

[131] E.E Zukoski, T. Kubota, *An Experimental Investigation of the Heat Transfer from Buoyant Plume to a Horizontal Ceiling-part 2, Effects of Ceiling Layers*, National Bureau of Standards Technical Report, Rpt. No.NBS-GCR-77-98, October 1975. 16

[132] Veldman, C.C., Kubota, T., and Zukoski, E.E., *An Experimental Investigation of the Heat Transfer from a Buoyant Gas Plume to a Horizontal Ceiling - Part 1. Unobstructed Ceiling*, National Institute of Standards and Technology Report NBS-GCR-77-97, 1975.

[133] Alpert, R.L., *Turbulent Ceiling-Jet Induced by Large-Scale Fires*, Combustion Science and Technology, 1971. 11: p. 197-213.

[134] Cooper, L.Y., and Woodhouse, A., *The Buoyant Plume-Driven Adiabatic Ceiling Temperature Revised*, Journal of Heat Transfer, 1986. 108: p. 822826.

[135] Motevalli, V., and Mark, C., *Characterizing the Unconfined Ceiling Jet under Steady-State Conditions: A Reassessment*, Fire Safety Science - Proceedings of the Third International Symposium, 1991: p. 301-312.

[136] M. Poreh, Y.G. Tsuei, J.E. Cermak, *Investigation of A Turbulent Radial Wall Jet*, ASME Journal of Applied Mechanics, 457-463 (1967).

[137] Oka, Y., Matsuyama, K., *Scale Similarity on Ceiling Jet Flow*, Fire Safety Journal, 61, 2013, 289-297.

[138] G. Heskestad and T. Hamada, F. Safety J., 21, p. 69, (1993).

[139] Heskestad, G., *The sprinkler response time index (RTI)*, Technical Conference on Residential Sprinkler Systems, Factory Mutual Research Corp , 1981.

[140] G. Heskestad and H. Smith, FMRC Serial Number 22485, Factory Mutual Research Corp., Norwood, MA (1976).

[141] J.P. Hollman, Heat Transfer, McGraw-Hill, New York (1976).

[142] K.B. McGrattan, A. Hamins, D.W. Stroup, *Sprinkler, Smoke and Heat Vent, Draft Curtain Interaction: Large Scale Experiments and Model Development*, International Fire Sprinkler-Smoke and Heat Vent-Draft Curtain Fire Test Project, NISTIR 6196-1 (1998).

[143] D.D. Evans, D.W. Stroup, Fire Tech Journal, 22, 54 (1986)

[144] P.J. DiNenno, D. Drysdale, C.L. Beyler, W.D. Walton, J.R. Hall, J.M. Watts, *SFPE Handbook of Fire Protection Engineering*, 3rd Edition, 2002.

[145] Alpert R.L., *Ceiling Jet Flows*, In: Hurley M.J. et al. (eds) SFPE Handbook of Fire Protection Engineering. Springer, New York, NY, Edition, 2016.

[146] G. Heskestad, *Similarity Relations for the Initial Convective Flow Generated by Fire*, ASME Paper No. 72-WA/HT-17, American Society of Mechanical Engineers, New York (1972).

[147] NFPA 72, National Fire Alarm Code, National Fire Protection Association, Quincy, MA (1999).